

# **Multiple Packer Techniques for In Situ Stress Measurement in Hard Soils-Soft Rocks**

by

Nadia Shafie Zadeh

A thesis submitted in partial fulfillment of the requirements for the degree of

Doctor of Philosophy

in

Geotechnical Engineering

Department of Civil and Environmental Engineering  
University of Alberta

©Nadia Shafie Zadeh, 2016

## ABSTRACT

Caprock Integrity analysis is the most critical stage in any thermal enhanced oil recovery (EOR) project. One of the primary input data for conducting a reservoir-geomechanical analysis to assess the mechanical and hydraulic integrity of the caprock is the in situ stress state within the caprock. Among the methods that have been developed for in situ stress measurements, micro-hydraulic fracturing has been extensively applied by the petroleum industry. A common technique to carry out stress tests in impermeable and weak rocks like clay shale is to combine sleeve fracturing with the micro- fracturing test. The initial sleeve fracturing stage is intended to avoid premature initiation of a fracture at the packer level. Interpretation of data using this method, however, reveals illogical magnitudes of the minimum stress in hard soil-soft rock such as clay shales, at least for tests conducted in northeastern Alberta. Two micro-hydraulic fracturing tests conducted in two different projects: one shallow SAGD project and one CSS project, are analyzed in this research. Comprehensive analyses and characterization of Clearwater clay shale completed and through the use of an inverse analysis technique, constitutive parameters for a modified Cam Clay model were selected. For the CSS project, the paucity of laboratory data on the clay shales of the Joli Fou Formation required the development of a unique tool for calibration and optimization of its geomechanical properties. The rate of excess pore pressure development or drainage conditions during the sleeve fracturing test have been studied to better understand how permeabilities and loading rate influence packer-induced stresses during sleeve fracturing test. This research also includes the evaluation of the pressure transmissibility of the packer elements both analytically and numerically during hydraulic fracturing test and the optimal pressure regarding the relevant internal pressure to maintain an efficient seal to prevent leakage and unsuccessful test

introduced. Fluid-structure interaction analyses using a co-simulation technique was conducted to evaluate the principal stress components of caprock in both SAGD and CSS projects. Finally, the main source issue of unreliable micro hydraulic fracturing test data conducted in hard soil- soft rock diagnosed using the simulation of the fracture mechanism, XFEM technique and the analyses gained from the fracture behavior studies provided valuable insight into the modified suggested method.

**TO MY FAMILY WITH SINCERE GRATITUDE**

## ACKNOWLEDGEMENTS

I would like to express my appreciation and gratitude to the following individuals:

Dr. Rick Chalaturnyk for his nurturing supervision, patience and significant professional pieces of advice from conception to completion of this work,

Dr. Norbert Morgenstern for his support and providing beneficial insight and guidance,

Dr. Bruce Carter, Dr. Klaus Wolf, Dr. Michele Calvello, Dr. Samer Adeeb, Vincent Pisis, and Erfan Saberhosseini for providing technical assistance and many enlightening discussions,

Hope Walls for her patience and support,

My parents for being living expression of love and for their unshakable faith in me that gives me strength along my journey,

My sisters- Nazila, Nora and Niki- for their infectious enthusiasm and uplifting energy, and for being a constant source of love and happiness during these years,

All my friends, especially Lee Cardwell, for being a source of encouragement.

# TABLE OF CONTENTS

<b>CHAPTER 1 INTRODUCTION</b> .....	1
INTRODUCTION .....	2
BACKGROUND .....	3
STEAM ASSISTED GRAVITY DRAINAGE (SAGD) .....	3
CYCLIC STEAM STIMULATION (CSS) .....	4
MULTIPLE FIELD STRESS MEASUREMENT TECHNIQUES .....	7
RESEARCH MOTIVATION .....	9
RESEARCH OBJECTIVE .....	10
SCOPE OF RESEARCH .....	10
METHODOLOGY .....	11
THESIS OUTLINE .....	12
<b>CHAPTER 2 COMPREHENSIVE ANALYSES OF FIELD DATA</b> .....	15
INTERPRETATION CHALLENGES FOR IN SITU STRESS FROM MICRO-FRAC TESTS IN SOFT ROCKS/HARD SOILS .....	16
CLEARWATER WEST LP-SAGD PILOT PROJECT .....	16
INTRODUCTION .....	16
GEOLOGICAL DESCRIPTION OF SAGD PROJECT .....	17
IN SITU STRESS TESTING PROCEDURE .....	18
INTERPRETATION METHODOLOGY .....	19
RESULTS FROM MICRO-FRAC TEST CONDUCTED IN HSSR .....	22
DISCUSSION ON INTERPRETATION METHODS .....	24
PRIMROSE/WOLF LAKE CSS PROJECT .....	27
GEOLOGICAL DESCRIPTION OF FIELD CASES .....	28
DATA INTERPRETATION .....	28
DISCUSSION .....	29
CONCLUSION .....	30
<b>CHAPTER 3 COMPREHENSIVE ANALYSES OF LABORATORY DATA</b> .....	32
LABORATORY DATA ANALYSES .....	33
GEOTECHNICAL CHARACTERIZATION OF CLEARWATER CLAY SHALE AND COMPARISON OF THE PROPERTIES WITH OTHER CRETACEOUS CLAY SHALES IN NORTH AMERICA ..	34
INTRODUCTION .....	34

GENERAL GEOLOGY.....	35
DATA COLLECTION AND METHODS .....	36
INDEX PROPERTIES.....	39
PARTICLE SIZE DISTRIBUTION (PSD).....	41
MINERALOGY .....	41
HYDRO-GEOMECHANICAL PROPERTIES.....	42
UNCONFINED COMPRESSIVE STRENGTH (UCS).....	42
SHEAR PARAMETERS.....	43
PERMEABILITY .....	51
CONSOLIDATION BEHAVIOUR.....	52
SWELLING BEHAVIOUR .....	54
MODIFIED CAM CLAY CONSTITUTIVE MODEL .....	56
THE CRITICAL STATE LINE (CSL) AND YIELD SURFACE .....	59
DISCUSSION.....	63
JOLI FOU CLAY SHALE FORMATION .....	65
CALIBRATION OF MODIFIED CAM CLAY (MCC) MODEL USING INVERSE ANALYSIS FOR JOLI FOU CLAY SHALE FORMATION .....	65
INTRODUCTION.....	65
INVERSE ANALYSES .....	66
GRADIENT METHOD.....	67
NUMERICAL SIMULATION OF TRIAXIAL TESTS.....	69
CALIBRATION SCHEME AND INPUT PARAMETERS STATISTICS .....	70
ANALYSES AND DISCUSSION .....	72
VERIFICATION AND VALIDATION OF THE PROCEDURE.....	73
CONCLUSION.....	75
<b>CHAPTER 4 A FLUID-STRUCTURE INTERACTION ANALYSIS OF PRESSURIZING THE PACKER IN SLEEVE FRACTURING TEST .....</b>	<b>76</b>
A FLUID-STRUCTURE INTERACTION ANALYSIS.....	77
SENSITIVITY ANALYSIS OF DRAINAGE CONDITIONS AS A FUNCTION OF PERMEABILITY AND LOADING RATE IN PACKER-INDUCED STRESSES DURING MICRO HYDRAULIC FRACTURING TESTS IN CLAY SHALE .....	77
INTRODUCTION.....	78
MECHANICAL ANALOGY.....	79

DESCRIPTION OF MECHANICAL BEHAVIOUR OF THE FORMATION .....	81
MECHANICAL DESCRIPTION OF POROELASTIC FORMATION .....	81
DEVELOPMENT OF NUMERICAL MODEL.....	82
RESPONSE TO PACKER LOADING WHEN FORMATION FULLY DRAINED VS. PURELY UNDRAINED .....	84
ANALYSIS OF DRAINAGE CONDITIONS.....	86
SENSITIVITY TO FORMATION PERMEABILITY .....	87
SENSITIVITY TO DIFFERENT MONOTONIC LOADING RATES.....	88
CONCLUSIONS.....	92
INFLUENCE OF PACKER PROPERTIES DURING IN SITU STRESS TESTING.....	94
INTRODUCTION.....	94
HYPERELASTIC CONSTITUTIVE MODEL .....	96
SOURCES OF PRESSURE TRANSMISSIBILITY REDUCTION.....	99
MATHEMATICAL CALCULATION OF PRESSURE TRANSMISSIBILITY .....	102
NUMERICAL EXPERIMENTS.....	105
CONCLUSIONS.....	113
FLUID-STRUCTURE INTERACTION ANALYSES OF SLEEVE FRACTURING TEST TO EVALUATE HORIZONTAL STRESS COMPONENTS OF CAP ROCK USING INVERSE TECHNIQUE .....	115
INTRODUCTION.....	115
ANALYSIS APPROACH USING FSI ANALYSES.....	117
DEFINING THE DOMAIN MODELS .....	119
SOLUTION METHODOLOGY .....	121
GEOLOGICAL DESCRIPTION OF CSS AND SAGD PROJECTS.....	122
LP-SAGD PROJECT SITE.....	122
CSS PROJECT SITE .....	124
RESULTS AND DISCUSSION.....	126
LP-SAGD PROJECT SITE.....	126
CSS PROJECT SITE.....	132
CONCLUSION.....	137
<b>CHAPTER 5 FRACTURE MECHANISUM DURING MICRO HYDRAULIC FRACTURING TEST</b> .....	<b>139</b>

FRACTURE MECHANISM DURING MICRO HYDRAULIC FRACTURING TEST USING FULLY- COUPLED HYDRAULIC FRACTURING SIMULATION (XFEM) .....	140
INTRODUCTION .....	140
ROCK FRACTURE MECHANICS THEORY .....	140
MICRO FRAC TEST AND FACTORS AFFECTING TEST RESULTS .....	149
XFEM THEORY .....	152
SIMULATION OF MICRO HYDRAULIC FRACTURING .....	155
LP-SAGD PROJECT SITE .....	155
CSS PROJECT SITE .....	161
DISCUSSION .....	166
<b>CHAPTER 6 CONCLUSION</b> .....	168
SUMMARY AND CONCLUSION .....	169
<b>REFERENCES</b> .....	173
<b>APPENDIX I</b> .....	191
AOS MICRO-FRAC TEST AT THE DEPTH OF 63 M IN WELL AA/03-22-088-08W4 .....	191
<b>APPENDIX II</b> .....	196
CNRL MICROFRACTURE AT 337 M IN WELL 11-11-67-3W4 .....	196

## LIST OF TABLES

### CHAPTER 2

Table 1. All the data obtained from various methods of interpretation of micro-hydraulic fracturing test.....	27
---	----

Table2. All the data obtained from various methods of interpretation of micro-hydraulic fracturing test at 337 m in well 11-11-67-3W4.....	31
--	----

### CHAPTER 3

Table 1. Generalized classification of Sedimentary units of Clearwater clay shale Member.....	38
---	----

Table 2. Index properties of Clearwater Formation clay shale samples.....	39
---	----

Table 3. Atterberg limits test results of Clearwater clay shale samples.....	40
--	----

Table 4. Index properties of different Cretaceous clay shales.....	40
--	----

Table 5. Summary of Combined Bulk and Clay XRD Analysis.....	42
--	----

Table 6. Uniaxial compressive strength of different Cretaceous clay shales.....	43
---	----

Table 7. Summary of direct shear test results of Clearwater Formation Samples.....	49
--	----

Table 8. Summary of permeability tests results.....	53
---	----

Table 9. Summary of values of compression and swelling indices of different shales.....	58
---	----

Table 10. Isotropic compression test results for Clearwater shale.....	59
--	----

Table 11. Summary of values of soil constants of different Clays.....	61
---	----

Table 12. Description of the modeled samples.....	71
---	----

Table 13. Initial and calibrated input parameters.....	73
--	----

### CHAPTER 4

Table 1. Different sets of Hyperelasticity constitutive model's parameters used for modeling.....	108
---	-----

Table 2. Description of different numerical modeling cases.....	108
---	-----

Table 3. Summary of the results of the modeling.....	109
--	-----

Table 4. Steel properties used for couplings and mandrel.....	126
---	-----

Table 5. Properties used for Clearwater clay shale model.....	126
---	-----

Table 6. Properties used for Joli Fou clay shale model.....	132
---	-----

### CHAPTER 5

Table 1. Micro hydraulic fracturing test operation data for SAGD.....	156
---	-----

Table 2. Micro hydraulic fracturing test operation data for CSS project.....	161
--	-----

Table 3. Quasi-brittle shale properties used by Haddad and Sepehrnoori .....	166
--	-----

## LIST OF FIGURES

### CHAPTER 1

Figure 1. Steam-assisted gravity drainage (SAGD) process.....	4
Figure 2. Cyclic steam stimulation (CSS) process.....	5

### CHAPTER 2

Figure 1. Arrangement of packers during the sleeve fracture and micro-frac tests stages.....	19
Figure 2. Complete packer inflation pressure time record for sleeve fracturing stages of micro-frac test for Clearwater West LP-SAGD Pilot Project.....	23
Figure 3. Recorded pressure history during the micro-frac test in Clearwater Formation at 63 m depth.....	24
Figure 4. Reconciliation plot of all data obtained from various methods of interpretation for Clearwater West LP-SAGD Pilot Project.....	27
Figure 5. Pressure versus time curve from in situ stress test for Joli Fou clay shale at depth of 337 m for Primrose/Wolf Lake CSS project.....	31
Figure 6. Recorded pressure history during the micro-frac test in Joli Fou clay shale at depth of 337 m for Primrose/Wolf Lake CSS project.....	32
Figure 7. Reconciliation plot of all data obtained from various methods of interpretation for test at 337 m in well 11-11-67-3W4.....	32

### CHAPTER 3

Figure 1. Location map of main heavy oil and bitumen deposits, Alberta, Canada.....	36
Figure 2. Geological cross -section of Clearwater and McMurray Formations in Northern Alberta.....	37
Figure 3. Lower cretaceous stratigraphy.....	38
Figure 4. Plasticity chart of Clearwater clay shales.....	40
Figure 5. Particle size distribution over a range of Clearwater clay shale samples.....	41
Figure 6. UCS versus depth.....	45
Figure 7. UCS versus moisture content.....	45
Figure 8. UCS versus void ratio.....	45
Figure 9. UCS versus clay fraction.....	45
Figure 10. Porosity versus moisture content.....	45
Figure 11. Depth versus moisture content.....	45
Figure 12. Unconsolidated-undrained triaxial test result.....	46
Figure 13. Consolidated-undrained triaxial tests result.....	47
Figure 14. Consolidated-drained triaxial tests result.....	48

Figure 15. (a) Deviatoric Stress vs. Axial Strain, (b) Volumetric Strain vs. Axial Strain from consolidated drained triaxial compression tests. Positive volumetric strain indicates pore volume increase during shear.....	48
Figure 16. Schematic direction of the direct shear test samples.....	49
Figure 17. Clearwater Formation direct shear tests, Parallel to bedding plane– Mohr-Coulomb Failure Envelopes, The area between dotted lines represent $\pm$ standard deviation.....	49
Figure 18. Clearwater Formation direct shear tests, Perpendicular to bedding plane– Mohr-Coulomb Failure Envelopes, The area between dotted lines represent $\pm$ standard deviation.....	50
Figure 19. Clearwater Formation - Integrated interpretation of shear strength envelope.....	50
Figure 20. Pre-shear variation of brine permeability for Clearwater triaxial specimens.....	53
Figure 21. Variation of average brine permeability for Clearwater specimens during the triaxial test.....	54
Figure 22. Variation of brine permeability for different Clearwater specimens during the triaxial test.....	54
Figure 23. Comparison of Scanning Electron Microscope (SEM) analysis of two Clearwater clay shale samples with different structures.....	54
Figure 24. Swelling behavior of Clearwater clay shale.....	56
Figure 25. Elastic-plastic behavior of material in isotropic compression and swelling .....	57
Figure 26. Yield curves as predicted from Cam-Clay constitutive model.....	58
Figure 27. Isotropic compression test results for Clearwater clay shale sample....	59
Figure 28. Effective stress path during drained shearing of Clearwater shale for different consolidation stresses and critical state line.....	60
Figure 29. Limit state curves of Clearwater clay shales, for large strain envelope.	62
Figure 30. The complete state boundary surface in $q'/p'_e$ versus $P'/p'_e$ space....	62
Figure 31. Plasticity of various formations in western Canada.....	64
Figure 32. Definition of an inverse process.....	67
Figure 33. Inverse analysis coupling UCODE and FLAC.....	70
Figure 34. Triaxial test simulation (a) Geometry, boundary conditions and loading, (b) Finite difference mesh.....	71
Figure 35. Stress- Strain curves for drained triaxial tests, comparison between laboratory results and simulated results using initial value of parameters and calibrated ones.....	73
Figure 36. Least square objective function for initial and calibrated models.....	74
Figure 37. Error variance for initial and calibrated models.....	74
Figure 38. Composite scaled sensitivity for initial and calibrated models.....	74

Figure 39. Stress- Strain curves for drained triaxial test, comparison between laboratory results and simulated results using calibrated parameters.....	75
--	----

**CHAPTER 4**

Figure 1. Schematic illustration of equivalent mechanical model for undrained response.....	80
Figure 2. Schematic illustration of equivalent mechanical model for drained response.....	81
Figure 3. Schematic illustration of equivalent mechanical model for partially drained response.....	81
Figure 4. The finite elements discretization of the region under study.....	84
Figure 5. Contours of the resulting radial effective stress (right) and pore pressure (left) under undrained condition in the formation, with displacement after pressurization of the packer.....	85
Figure 6. Contours of the resulting radial effective stress (right) and pore pressure (left) under drained condition in the formation with displacement immediately after packer pressurization.....	85
Figure 7. Contours of the resulting radial effective stress and pore pressure under drained formation condition, with displacement after dissipation of pore pressure.....	86
Figure 8. No-deformed and deformed mesh and maximum radial displacement after packer pressurization under undrained (left) and drained (right) conditions at the packer loading step.....	86
Figure 9. Effects of permeability on radial stress and pore pressure in undrained, partially drained, and drained conditions.....	88
Figure 10. Stress distribution along radial distance from midpoint of packer-formation interface for an applied pressure of 10 MPa and different permeabilities.....	90
Figure 11. Drainage conditions with regard to permeability and loading rate.....	92
Figure 12. Effect of loading rate on effective radial stress and pore pressure for 0.1 and 1.5 MPa/min loading rates.....	92
Figure 13. Micro hydraulic fracturing test.....	96
Figure 14. Apparent shear modulus of typical polymer as a function of temperature.....	97
Figure 15. Semi-circular element cut from the tube in cylindrical coordinate system, z-axis is normal to the page.....	102
Figure 16. The finite element discretization of the region under study, (a) pressurizing the packer with rigid casing, (b) Pressurizing the packer with steel casing.....	106

Figure 17. Observational elements and point used for monitoring the radial/contact pressure on the packer and casing and displacement on the sliding coupling, shown in deformed shape after pressurizing.....	107
Figure 18. Packer and casing pressure for different cases with 25 MPa inflation pressure.....	109
Figure 19. Packer and casing pressure for different cases with 20 MPa inflation pressure.....	110
Figure 20. Sliding coupling displacement in different cases.....	110
Figure 21. Lift-off/touch pressure and Pressure Transmissibility coefficient for different cases.....	111
Figure 22. The Z axial displacement of the sliding coupling when the expansion ratio is high (with (right) and without (left) showing mandrel (case#11), the maximum displacement is about 3 cm.....	113
Figure 23. Contact pressure on the steel calibration casing when applied inflation pressure is 20 MPa (case#9), the average value of contact pressure is 16 MPa.....	113
Figure 24. Attempted sleeve fracturing test before micro hydraulic fracturing.....	118
Figure 25. Mechanical Domain in Details.....	120
Figure 26. CFD Domain with Details.....	120
Figure 27. Interaction Surface between CFD and Mechanical Domains.....	121
Figure 28. Stress Magnitude constraints for each faulting regime, Clearwater Clay Shale Formation at 63 m.....	124
Figure 29. Stress Magnitude constraints for each faulting regime, Joli Fou Clay Shale Formation at 337 m.....	125
Figure 30. Pressure versus time curve from in situ stress test for Clearwater clay shale at depth of 63 m.....	127
Figure 31. Pressure –Time curve for $\sigma_H=1.6$ and $\sigma_h=1.1$ .....	129
Figure 32. Pressure –Time curve for $\sigma_H=1.7$ and $\sigma_h=0.87$ .....	129
Figure 33. Pressure –Time curve for $\sigma_H=1.24$ and $\sigma_h=0.9$ .....	129
Figure 34. Pressure –Time curve for $\sigma_H=1.66$ and $\sigma_h=1$ .....	129
Figure 35. Pressure –Time curve for $\sigma_H=1.66$ and $\sigma_h=0.98$ .....	129
Figure 36. Pressure –Time curve for $\sigma_H=4.5$ and $\sigma_h=2$ .....	129
Figure 37. Pressure –Time curve for $\sigma_H=1.1$ and $\sigma_h=0.74$ .....	129
Figure 38. Pressure –Time curve for $\sigma_H=1.03$ and $\sigma_h=0.76$ .....	129
Figure 39. Pressure –Time curve for $\sigma_H=1.61$ and $\sigma_h=0.91$ .....	130
Figure 40. The point that circumferential stress changes from compression to tension and its equivalent pressure on the packer.....	130
Figure 41. Deformation and plastic strain profile at the end of the sleeve fracturing test at 63 m depth.....	131
Figure 42. Displacement, velocity and pressure profiles of CFD domain.....	131

Figure 43. Pressure versus time curve from in situ stress test for Joli Fou clay shale at depth of 337 m.....	133
Figure 44. Pressure –Time curve for $\sigma_H=5.9$ and $\sigma_h=4.5$ .....	134
Figure 45. Pressure –Time curve for $\sigma_H=6.5$ and $\sigma_h=6$ .....	134
Figure 46. Pressure –Time curve for $\sigma_H=6.5$ and $\sigma_h=4.75$ .....	134
Figure 47. Pressure –Time curve for $\sigma_H=6.5$ and $\sigma_h=5$ .....	134
Figure 48. Pressure –Time curve for $\sigma_H=7$ and $\sigma_h=5$ .....	134
Figure 49. Pressure –Time curve for $\sigma_H=6.7$ and $\sigma_h=4.75$ .....	134
Figure 50. Pressure –Time curve for $\sigma_H=5.75$ and $\sigma_h=5.25$ .....	134
Figure 51. Pressure –Time curve for $\sigma_H=6$ and $\sigma_h=4.5$ .....	134
Figure 52. Pressure –Time curve for $\sigma_H=6.25$ and $\sigma_h=4.5$ .....	135
Figure 53. The point that circumferential stress changes from compression to tension and its equivalent pressure on the packer.....	135
Figure 54. Total deformation of the packer element (left) and formation (right) at the end of the test.....	136
Figure 55. Maximum plastic strain on the borehole wall after pressurizing the packer.....	136
Figure 56. Displacement, velocity and pressure profiles of CFD domain.....	137

## CHAPTER 5

Figure 1. Fracture parameters: aperture, width and fluid flow.....	146
Figure 2. The three basic modes of loading for a crack and corresponding crack surface displacements.....	147
Figure 3. Schematic illustration of the definition of the kink angle.....	148
Figure 4. Concept of phantom nodes in XFEM.....	154
Figure 5. Traction-separation cohesive law for XFEM procedures.....	155
Figure 6. Maximum formation displacement after first cycle of sleeve fracturing loading step.....	158
Figure 7. Fracture opening of enrichment element after 2 cycles of injection, SAGD project, opening in X-plane view cut (left), opening in Z-plane view cut (right).....	158
Figure 8. Crack element in the enriched region, SAGD project, Crack element in X-plane view cut (left), Crack element in Z-plane view cut (right).....	159
Figure 9. The length of the disturbed zone during the drilling and sleeve fracturing test, SAGD project.....	159
Figure 10. Minimum redistributed stress for the first and second element at the cracked element in the enriched region in FSI model.....	160
Figure 11. Maximum formation displacement after first cycle of sleeve fracturing loading step, CSS Project.....	162

Figure 12. Fracture opening of enrichment element after 2 cycles of injection, CSS project, opening in X-plane view cut (left), opening in Z-plane view cut (right)..... 163

Figure 13. Crack element in the enriched region, CSS project, Crack element in X-plane view cut (left), Crack element in Z-plane view cut (right)..... 163

Figure 14. The length of the disturbed zone during the drilling and sleeve fracturing test, CSS project..... 164

Figure 15. Boundary that the nature of loop stress changes from tension to compression during sleeve fracturing test, the length of tensile crack , CSS project..... 164

Figure 16. Minimum redistributed stress for the first and second element at the cracked element in the enriched region in FSI model..... 165

Figure 17. Fracture propagation in micro hydraulic fracturing test in quasi-brittle shale (harder material than clay shale)..... 167

## CHAPTER 1 INTRODUCTION

WITH THEM THE SEED OF WISDOM DID I SOW,  
AND WITH MY OWN HAND LABOUR'D IT TO GROW:  
AND THIS WAS ALL THE HARVEST THAT I REAP'D---  
"I CAME LIKE WATER, AND LIKE WIND I GO."

"KHAYYAM"

## INTRODUCTION

Argillaceous formations, which are known as hard soil-soft rock (HS-SR), are presently being studied in several countries as caprock for reservoirs and potential host rocks for underground gas storage and geological disposal of radioactive waste. This class of materials is well known for creating a variety of civil engineering problems ranging from the diagnosis of geological and groundwater conditions, a collection of undisturbed samples, the determination of characteristic material properties, stability of slopes and excavations, construction of compacted shale embankments and performance of underground openings. Much of the engineering experience with clay shales has been developed over the past 50 years from the construction of dams and slopes, all of which take place at relatively shallow depths. The investigation of caprock integrity thermal recovery processes such as SAGD (Steam Assisted Gravity Drainage) and CSS (cyclic steam stimulation) or caprock integrity for CCS (Carbon Capture and Storage) projects, however, will usually take place at much greater depths. With limited access to these formations at depth (i.e., only through boreholes), detailed characterization of these formations is challenging. Caprock integrity assessments, in general, include geological studies for the caprock, in situ stress determination, constitutive property characterization and numerical simulations. The two key requirements to ensure caprock integrity are the hydraulic integrity and mechanical integrity (Yuan et al., 2011) and their assessment generally involves material property or constitutive property determination and reservoir-geomechanical numerical simulation studies comparing the prevailing stress condition against the material strength.

A critical element of these evaluations is the in situ stress conditions existing within the caprock. Substantial effort has been invested over the last 5 to 6 years on the measurement of the in situ stress for in situ thermal recovery projects in northeastern Alberta. For instance, in SAGD, CSS and CCS projects, micro-frac data has been acquired in the caprock in order to quantify the in situ stress state before any in situ thermal recovery process begins (Khan (2010), Collins et al (2011), Yuan et al (2011), Khan et al (2011), Uwiera-Gartner et al (2011), Mishra et al (2011)). The increased activity has been driven by a caprock failure even in an SAGD project in 2006 that, amongst other factors, was believed to have been caused by steam injection above the in situ stress magnitudes.

While conventional micro-frac tests have been extensively conducted, in both open borehole and cased holes, there have been a significant number of test programs conducted using multiple packer tools such as MDT® (modular dynamic tester) and RCI® (reservoir characterization instrument). For micro-frac testing, MDT has been used by industry for more than a decade to obtain measurements of far field stress magnitudes (Desroches (1994, 1995), Thiercelin (1994, 1996), Fourmaintraux (2005), Cantini (2005)).

## **BACKGROUND**

The acquisition of reservoir geomechanical data such as in-situ stresses are important to a wide range of applications including well stimulation and reservoir management issues such as optimal placement of CO<sub>2</sub> injectors (CCS projects), disposal of radioactive waste and unconventional resources recovery including thermal recovery of bitumen (SAGD, CSS), and shale gas. The following sections provide background information for three of the major research themes contained in this research: 1) the SAGD thermal recovery process; 2) the CSS thermal recovery process and 3) the multiple field stress measurement techniques with a special consideration in micro-fracturing technique based on multiple packer techniques.

### **STEAM ASSISTED GRAVITY DRAINAGE (SAGD)**

Among various in situ recovery techniques, the SAGD process has been verified to be the most promising thermal recovery method for economic recovery of heavy oil and bitumen from the enormous oil-sand deposits in northeastern Alberta, Canada. SAGD is a uniquely Canadian technology that is poised to make an enormous contribution to energy production in North America and to the Canadian economy. Northern Alberta oil sands, encompassing the Athabasca, Peace River and Cold Lakes areas, are the largest oil sands deposits in the world that cover a surface area of more than 140,200 km<sup>2</sup> with an estimated initial oil in place of 1.7 trillion barrels.

The concept of the SAGD process is shown in Figure 1. The mechanism by which the process proceeds is a reduction of the viscosity of the heavy oil within bitumen by the injection of steam into the reservoir and subsequent flow of heated bitumen by gravity to the production well below. In this process, two horizontal wells are drilled one well above the other and separated by distance (usually 5 m) near the bottom of the oil bearing

formation. The top well is used to inject steam into the oil sands (injector), heating up the oil (up to 200 degrees Celsius) and allowing it to drain into the bottom well (collector). The combined influence of temperature and pore pressure changes from the injection of steam produce a complex evolution of effective stress changes within the reservoir. The resulting deformation from this process induces deformations (and associated stress changes) in the overlying caprock and with the addition of pore pressure diffusion into the caprock create conditions that may potentially lead to failure within the caprock.

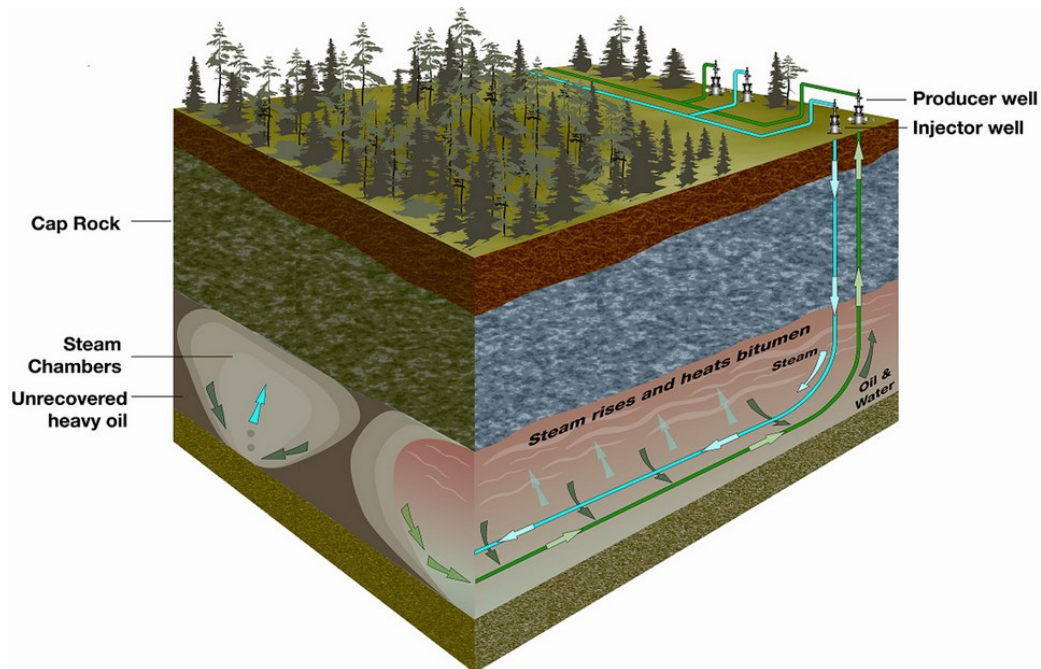


Figure 1. Steam-assisted gravity drainage (SAGD) process (<http://www.desiderataenergy.com>)

### CYCLIC STEAM STIMULATION (CSS)

Cyclic steam stimulation is another thermal recovery method that involves a periodic injection of high pressure steam into the payzone or reservoir with the purpose of heating the heavy oil near the wellbore in which one wellbore plays the role as both injector and collector. CSS consists of three stages as shown in Figure 2. Steam injection is the first stage in which high pressure steam is injected through the vertical wellbore for a certain amount of time to heat the heavy oil in the reservoir. The second stage is the soak phase in which the wellbore is shut down and the reservoir is allowed to soak for some time,

though not for more than a few days. During this period, the reservoir is heated by the steam and consequently causes the reduction of viscosity in heavy oil. In addition to heating the bitumen, the high pressure steam creates fractures within the reservoir thereby increases permeability and fluid flow. The third stage is production in which the wellbore is opened and put into production. This process repeats till production falls below an economic threshold.

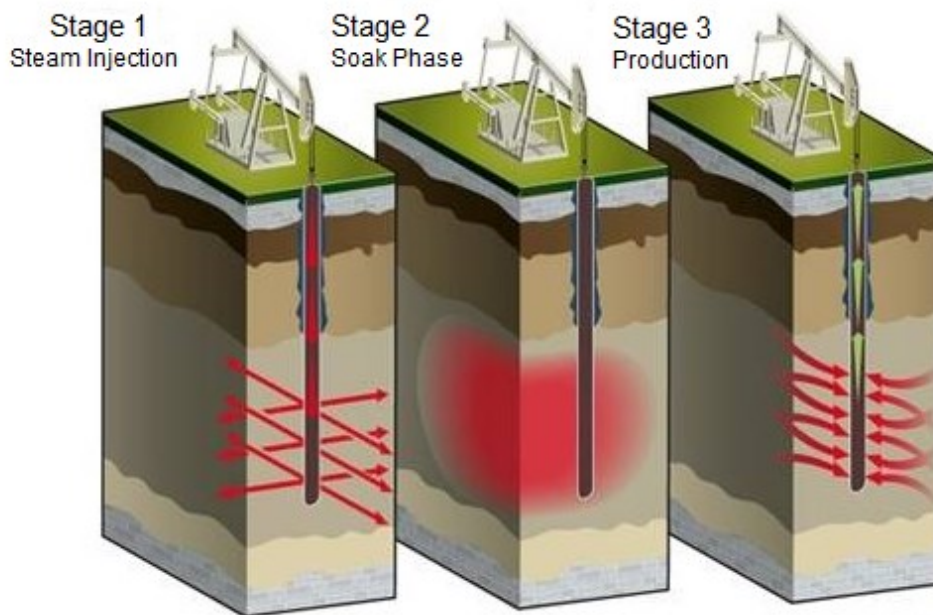


Figure 2. Cyclic steam stimulation (CSS) process (<http://www.aapgsuez.net>)

The selection of a maximum steam injection pressure is a critical element in the design and operation in SAGD and CSS projects. Caprock integrity assessments provide one constraint on the selection of the maximum steam injection pressure to ensure it does not potentially risk a loss of confinement of the steam chambers or heated zone. Hydraulic and mechanical integrity are the two most important design characteristics of caprock that must be maintained during the life of an SAGD or CSS project. The hydraulic seal must be laterally continuous and have low vertical transmissibility to ensure that there is a minimal possibility of escape for reservoir fluid through the caprock into the shallow groundwater aquifer or the ground surface over the life of the project. The induced deformation and potential failure of the caprock during thermal operations may introduce new hydraulic conduits and thus compromise its hydraulic integrity.

Consequently, assessment of hydraulic integrity is intimately linked to the mechanical behavior of the caprock. The caprock must have adequate strength and deformation properties to adequately resist the pressure, temperature, and deformation imposed by SAGD or CSS process, which is directly related to its mechanical integrity. Loss of caprock integrity, both hydraulic and mechanical, may lead to a breach of the caprock and release of steam/bitumen into overlying potable water zones or to the ground surface.

The consequences of caprock failure could be catastrophic. For instance, in May 2006, the SAGD industry experienced an unexpected and disastrous caprock failure and subsequent steam release incident at the Joslyn Creek SAGD project, located about 60 kilometers north of Fort McMurray. The steam release caused a surface disturbance about 125 by 75 meters. Surface uplift and subsidence zones are present in the vicinity of the main steam release zone.

Designing against this type of failure is completed using numerical analyses of the SAGD or CSS process. Inputs to these analyses include the operational parameters, geological model, a constitutive behavior of the formations and the initial in situ stress state. Determination of the initial in situ stress state is obtained by conducting micro-frac tests at several locations to enable the  $\sigma_v$ ,  $\sigma_{Hmax}$  and  $\sigma_{Hmin}$  distribution to be computed for each major formation. As companies strive to operate at a maximum steam injection pressure, accurate knowledge of the in situ stress state within the caprock becomes a critical element in designing a safe project.

The complex constitutive behavior of the clay shales that comprise the caprock for most SAGD and CSS projects in northeastern Alberta poses diverse problems for geotechnical investigations involving in situ stress measurement testing. It is well accepted that the vertical stress gradient at shallow depths (less than 500 m) ranges from 20 to 22 kPa/m and on average it is equal to 21 kPa/m. Consequently, a properly executed/interpreted micro-frac test should never measure  $\sigma_{Hmin}$  larger than the density-derived  $\sigma_v$ . Yuan (2011) reported some MDT tests conducted for the target shallow reservoir by three different service providers on four different wells. Fracture closure pressures at 24 to 36 kPa/m were reported to the ERCB (ERCB, 2010). Doubts should be raised about these values because they are larger than the density-derived  $\sigma_v$  around 21 kPa/m. Indeed, subsequent analyses led to a conclusion that most measurements provided data of very low confidence and were deemed inconclusive although one measurement did provide a

closure pressure gradient of 20.6 kPa/m. Similar values have been reported by Chevron Canada Resources (2008) at two SAGD shale caprock boreholes and one gas storage shale caprock borehole in which MDT test interpreted fracture closure pressures between 30 and 34 kPa/m were reported.

The primary challenge of multiple packer techniques like the MDT micro-frac test in clay shales is their mechanical behavior, which has a sharp contrast to the assumption of any hydraulic-based tests. Like any hydraulic-based tests, the expectation of rock behavior is elastic up to the point of fracture initiation. By contrast, clay shales exhibit inelastic manner and frequently behave non-linear and plasticity so the pressure response during the test can suffer poor reliability. Reviewing the mechanical behavior of HS-SR materials is pointed out that even if inelastic strains dominate the stress-strain relationship, an elastic behavior is nevertheless present upon unloading, this elasticity being, most of the times, nonlinear and anisotropic although no technique or calculation model takes into account this particular mechanical behavior for stress measurements. Additional testing problems besides that of plastic behavior of the formation in these layers include poor packer sealing, fracture by-pass, low fluid filtration, and the presence of natural defects which may cause other sources of problems especially in multiple packer techniques with problems of non-uniform strain levels and disturbed stress fields around the apparatus. Geotechnical engineers are used to viewing geological materials as either a rock, with engineering behavior primarily controlled by fissures and joints or as a soil whose behavior is highly susceptible to the fabric and water content of the intact material. However, clay shales are intermediate between rock and soil regarding porosity, strength, and compressibility, and typically exhibit properties of both. These unusual properties of clay shales cause difficulties in analyzing their behavior.

### **MULTIPLE FIELD STRESS MEASUREMENT TECHNIQUES**

Over the past 30 years, various techniques for measuring in situ stresses in rocks and soils have been developed and improved over time. These techniques can be divided into six main groups for rocks:

- 1) hydraulic methods (e.g., hydraulic fracturing, sleeve fracturing, and hydraulic tests on pre-existing fractures (HTPF));

- 2) relief methods (e.g., surface relief methods, undercoring, borehole relief methods such as overcoring, borehole slotting, and relief of large rock volumes);
- 3) jacking methods (flat jack and curve jack methods);
- 4) strain recovery methods (e.g., anelastic strain recovery (ASR), differential strain curve analysis (DSCA));
- 5) borehole breakout methods (e.g., calliper and diameter analysis, borehole televiewer analysis); and
- 6) Others such as fault slip data analysis, earthquake focal mechanisms, indirect methods such as Kaiser Effect, and inclusions in time-dependent rock, measurement of residual stresses).

For soils, measurement of in situ stress could be divided into four main methods:

- 1) pressuremeter;
- 2) flat dilatometer (DMT);
- 3) spade total stress cells; and
- 4) hydraulic fracturing.

This research study examines the use of hydraulic fracturing as an in situ stress measurement method in combination with dual packer techniques. Numerous field studies in which hydraulic fracturing stress measurements were compared with other stress results (Haimson and Fairhurst, Von Schonfeldt (1970), Roegiers (1974), Haimson (1975, 1978, 1981, 1983, 1984), Doe et al (1983), Li Fang-Quan (1983), Bredehoeft (1976), Haimson and Voight (1977), Gay (1980), Bell and Gough (1983), Hickman (1985)) have shown it to be a valid and valuable method for determining the minimum in situ stress. Among all the methods for in situ stress measurements, hydraulic fracturing, as first introduced by Clark (1949), has been the most common method applied in the petroleum industry for both rocks and soils.

The analysis of hydraulic fracture theory in rock began with the work of Scott, Bearden and Howard (1953), Hubbert and Willis (1957) and the petroleum industry has been a major sponsor of research in the application of this method for petroleum extraction. Scheidegger (1962) was the first scientist to propose a method for determining the three principal stresses in the Earth's upper crust directly by analyzing the bottom hole pressure charts obtained from the hydra-fracturing (old term for hydro-fracturing) process of oil

wells. Refinements were added by series of researchers (Dunlap (1963), Kehle (1964), Fairhurst (1964), Haimson (1968)) until Haimson and Fairhurst (1970) made the statement that hydraulic fracturing may soon cease to be a potential method and become a practical tool for stress determination. After that, hydraulic fracturing increased the understanding of the state of stresses in the Earth's crust (Bredehoeft et al. (1976), Haimson (1976, 1978, 1980), Rice and Cleary (1976), Rummel et al.(1977), Medlin and Masse (1977, 1979), Zoback et al.(1980), Alexander, Warpinski, Warren (1983), Kuriyagawa et al.(1983), Nelson (1987), Teufel and Warpinski (1987), Detournay et al.(1987, 1988), Desroches (1994, 1995), Thiercelin (1994, 1996), Fourmaintraux (2005), Cantini (2005)).

Bjerrum and Andersen (1972) proposed hydraulic fracturing as a means for measuring in situ stress in soils. A review of laboratory simulated hydraulic fracturing experiments by Nobari et al.(1973), as reported by Jaworski (1979, 1981), and Widjaja et al. (1981) revealed two common characteristics of hydraulic fracture behaviour in soils: (a) hydraulic fracture occurs when the tangential effective stress reduces to the soil tensile strength on the plane of maximum tensile stress and  $P_f$  as breakdown pressure is primarily a function of the induced in situ stresses, soil tensile strength and ambient pore pressure; and (b) fractures are perpendicular to the minimum principal stress when the in situ stresses are non-hydrostatic. As with hydraulic fracturing tests in rock, tests in soils have been found to be affected by injection rate, permeability, mechanical properties of soils, and test parameters like borehole diameter. Different field test verifications have been conducted by Massarsch et al. (1975), Tavenas et al. (1975), Lefebvre et al. (1981), Chan (1986), Murdoch et al. (1991) and have revealed challenges with the interpretation of the results.

## **RESEARCH MOTIVATION**

Determination of the in situ stress state in many projects such as SAGD, CSS and CCS is critically important. Although the MDT tool has been used broadly for in-situ stress state determination, most previous research related to the application of this method has focused on the field of conventional rock mechanics. In-situ stress measurement in hard soil/soft rock formations such as the Clearwater Formation appears to have received little attention. As noted above, unrealistic stress gradients are interpreted from MDT tests in this class of material. To both better understand how these unrealistic in situ stress estimates result from MDT tests and extract valuable in situ stress interpretations from

the current, reasonably extensive databases of MDT measurements would be valuable contributions to improved thermal recovery project designs. Numerical analyses for simulation of the test in this kind of material are crucial with considering (a) a suitable geomechanical constitutive model which represents their behavior during the test which may have a significant effect on the formation's geomechanical response and (b) the interaction between MDT tool and the formation in concern. The impact of interaction between MDT tool and formation during the sleeve-fracturing test before and after hydraulic fracture as well as the amount of the induced stresses and the nature of them for defining the best method of analyzing the data are primary motivating factors of this study.

### **RESEARCH OBJECTIVE**

It is postulated that the complex constitutive behavior of the clay shale formations overlying the oil sands during the MDT micro-frac tests is the fundamental reason for the non-realistic stress estimates. The objective of this research is to examine numerically, the soil- structure interaction behavior between the MDT tool (a multiple packer tool) and clay shale formation to provide new insight into in situ stress interpretation using this measurement technique. Three key factors are considered in the research: 1) drainage condition as a function of permeability and loading rate; 2) constitutive behavior of the formations and 3) properties of the packer elements. The other objective of this research is investigation of fracture mechanism of micro hydraulic fracturing test.

### **SCOPE OF RESEARCH**

An exhaustive data set of experimental results for clay shales from Total Canada's Griffon SAGD Project and ConocoPhillips's Surmont SAGD Project area will be re-analyzed and incorporated into this research study. Consequently, it is not expected that additional laboratory experiments will be required for the research. Several MDT test datasets have been provided for the Primrose/Wolf Lake CSS project from CNRL and MDT dataset from Alberta Oil Sands Clearwater West LP-SAGD Pilot Project will be utilized for initially workflow verification. It is also expected that no formal numerical simulation codes will be written as commercial software (CFD, ABAQUS2D/3D, UCODE, FLAC2D, and ABAQUS XFEM) will be used for fluid flow and geomechanical simulations and inter-code programming will be completed with Python and C++.

## METHODOLOGY

The research methodology that will be applied to achieve the research objectives has three components: 1) the comprehensive analysis of field test results; 2) the analysis of the laboratory tests conducted on clay shales samples; and 3) analytical and numerical simulations of the micro-frac tests using multiple packer technique. The following research tasks will be undertaken:

- A critical analysis of field test data obtained from this technique from Clearwater formation for Clearwater West LP-SAGD Pilot Project (Alberta Oil Sands Inc.), and from Joli Fou Formation for Primrose/Wolf Lake CSS project from CNRL will be analyzed according to the conventional test interpretation methods. The first data related to shallow depth (63 m) and the second data sets related to depth of 337 m.
- No laboratory tests were conducted in the current research; however, geomechanical laboratory test results obtained by previous researchers are reanalyzed to determine the mechanical behavior of Clearwater Formation clay shales. This formation was considered to be the caprock for Clearwater West LP-SAGD Pilot Project area. Initial research efforts were given to extracting Cam-Clay constitutive parameters from the experimental results, which will be considered as the constitutive behavior of clay shale. For the Joli Fou Formation, however, because of the paucity of laboratory data from Primrose/Wolf Lake CSS project, these parameters were calibrated and optimized using the inverse analyses techniques with the actual data from triaxial tests using two software platforms: UCODE (from USGS) and FLAC2D (from Itasca).
- Modelling the fracture without knowing the stress regime is a challenging phase of accurate simulation for both sleeve fracturing and hydraulic fracturing parts. It required a comprehensive review of advantages and disadvantages of the tools available for doing the numerical part of two different stages of the test with together. ABAQUS, CFD and XFEM (from Dassault Systems Simulia Corp) have been chosen for this stage of the numerical analysis.
- Numerical modelling was conducted in different stages of the test, for sleeve fracturing and hydro-fracturing phases separately. The former stage was studied by coupling ABAQUS to CFD using the co-simulation technique with CSE to

investigate the fluid-mechanical interaction and stress/strain profiles on the formation during the pressurizing the packer at this phase and study the magnitude and nature of induced stresses resulting from this phenomenon. Before that, preliminary numerical modelling was conducted to investigate the packer pressurization stage and its influence on the change of stresses around the affected area in clay shales. At this stage, the effect of drainage condition and loading rate for pressurizing the packer was also investigated. This part is mechanical only, without considering fluid effects in the formation.

- The initial boundary conditions required for the numerical modelling of the hydraulic fracturing stage of the test was determined from the numerical modelling of the sleeve fracturing (previous phase). Numerical modelling was utilized to provide an evaluation of fracture initiation and propagation during the cyclic loading of the test. There are various unknown parameters during the test, which may have huge effects on the interpretation of the results. In the second stage, the hydro-fracturing part in which the fluid is injected directly to the test interval, parametric studies and also sensitivity analyses of different condition of surrounding materials were completed. Conducting initial numerical stress-strain analyses of packer loading in sleeve fracturing will be completed by simulation of hydraulic fracturing using XFEM.

## THESIS OUTLINE

The structure of this thesis will be completed in paper format, and selected manuscripts will be submitted for peer review. It is anticipated that seven manuscripts will be completed based on laboratory investigations, analytical developments, and numerical modelling. Below is a list of the topic and a brief description of each anticipated chapter where each will provide a relevant literature review.

- **Chapter 1 Introduction**: Contains a brief background, the big picture, and the structure of the research.
- **Chapter 2 Analysis of open-hole in-situ stress measurement using the micro-hydraulic fracturing technique: Focus on the fracture closure pressure**: this chapter will present interpretation of field data of the multiple packer technique from SAGD

and CSS project areas according to the classic interpretation methods. The results will be discussed and analyzed in the format of a paper.

- **Chapter 3 Inverse Analyses Techniques for calibration/optimization of critical state material parameters of clay shale:** Experimental data conducted on Clearwater Clay shale in different SAGD and CSS project areas will be reanalyzed for extracting the geomechanical parameters of this material. Moreover, this chapter presents a procedure to estimate geomechanical parameters from laboratory test results using inverse analysis. The procedure is applied to calibrate the Modified Cam-Clay parameters using compression triaxial, one-dimensional consolidation and isotropic compression test results from clay shale samples. A finite difference code (FLAC2D) and an inverse analysis algorithm (UCODE) are combined to minimize the difference between the numerical prediction of the stress-strain response and the experimental data. It is anticipated that two papers will be written out of the results.
- **Chapter 4 A fluid-structure interaction analysis of pressurizing the packer in sleeve fracturing stage of MDT test:** Numerical simulations of pressurizing the packers as pressure boundary condition analysis during either sleeve fracturing or isolating the test interval stage of micro-fracturing test as the first and second phases of the procedure will be conducted on the borehole wall in clay shale under different drainage conditions as a function of loading rate and permeability. In this chapter, furthermore, the performance of the packers during the loading and its effect on the formation will be evaluated using the fully coupled fluid-structure interaction solution provided by the ABAQUS co-simulation capability. Three papers will cover the results of these investigations.
- **Chapter 5 Fracture mechanism in clay shales during the micro-fracturing test using multiple packer technique:** Clay shale formations often contain natural fractures, and complex hydraulic fracture networks may form during the test. The complex fracture network is strongly influenced by the interaction between the hydraulic fracture and pre-existing fractures which depends on in-situ stresses, rock mechanical properties, the properties of the fractures, and the hydraulic fracturing test parameters such as fluid properties and injection rate. In this paper, the fracture initiation condition association with limited injection rate would be discussed, and fracture propagation and progressive failure mechanism would be investigated.

- **Chapter 6 Conclusion:** A review of the research program and general conclusions of each chapter along with recommendations and suggestions for further studies and the next steps of this research are included in this chapter.

## CHAPTER 2 COMPREHENSIVE ANALYSES OF FIELD DATA

“STRANGE, IS IT NOT?  
THAT OF THE MYRIADS WHO BEFORE US PASS’D THE DOOR OF DARKNESS  
THROUGH.  
NOT ONE RETURNED TO TELL US OF THE ROAD, WHICH TO DISCOVER WE  
MUST TRAVEL TOO”

“KHAYYAM”

## **INTERPRETATION CHALLENGES FOR IN SITU STRESS FROM MICRO-FRAC TESTS IN SOFT ROCKS/HARD SOILS<sup>1</sup>**

Clearwater clay shale formation plays a role as caprock for Clearwater West LP-SAGD Pilot Project (Alberta Oil Sands Inc.) from Athabasca deposit, and Joli Fou clay shale formation is a major caprock for Primrose/Wolf Lake CSS project (CNRL) from Cold Lake deposit. These two projects are approximately 350 km apart from one another. The MDT data sets for these two sites have been analyzed according to the conventional test interpretation methods. The first data sets related to shallow depth (63 m) and the second data sets related to the depth of 337 m (lower elevation). The data will be discussed in two different sections individually.

### **CLEARWATER WEST LP-SAGD PILOT PROJECT**

#### **INTRODUCTION**

Measurement of the magnitude and orientation of the minimum horizontal stress is a fundamental element in determining the far-field stress distribution in the subsurface. For thermal oil recovery projects such as steam assisted gravity drainage (SAGD), where steam is injected at elevated pressures, knowledge of in situ stresses, particularly the minimum horizontal stress within the overlying seals of the reservoir or caprock, is critical for selecting the maximum steam injection pressure. Micro-hydraulic fracturing tests are the most common method used for stress measurement in a borehole at depth. These tests generate a pressure response obtained during the cyclic fluid injection/shut-in periods that allow interpretation of the initiation, propagation and closure of an induced hydraulic fracture. The pressure response is generated by injecting fluids at a constant rate into a region of the borehole sealed between two inflatable packers.

For SAGD projects in the northeastern region of Alberta, the Clearwater Formation is generally identified as the caprock. The Clearwater Formation consists primarily of black and green shale, with some interbedded grey and green sandstone and siltstone (Glass, 1997). The properties of these lithologies place them in the complex transitional range of

---

<sup>1</sup> A part of this chapter related to LP-SAGD pilot project was presented at the "SHALE ENERGY ENGINEERING CONFERENCE" held in Pittsburg, PA, July 21-23, 2014. The paper was selected for presentation at the symposium by the conference technical committee based on a technical and critical review of the paper by a minimum of two technical reviewers. It has been published in conference proceeding.

geological materials described as either “hard soils” or “soft rocks” (HSSR). An appropriate classification for HSSR can be found in Hawkins and Pinches (1992).

Micro-frac testing within these HSSR lithologies can sometimes be difficult. Occasionally the induced fractures will migrate along the packer elements used to seal the testing interval. To alleviate issues such as this, field test procedures have been implemented where an initial “induced” fracture at the borehole wall is created using the inflation of one of the packers – typically referred to as a “sleeve” fracturing stage. The intent of this process is to create a discontinuity at the borehole wall that will serve as the initiation point for the hydraulic fracture generated during the mini-frac test. These multiple test stages within an HSSR lithology have unfortunately lead to complex stress paths around the borehole, complex behavior during fluid injection and difficulty in interpreting the fracture closure pressure, which is required for interpreting the minimum in situ stress. The following sections discuss a series of mini-frac tests conducted using the multistage packer technique for in situ stress measurement test performed in Clearwater Formation and highlights the issues surrounding the interpretation of the minimum in situ stress.

#### **GEOLOGICAL DESCRIPTION OF SAGD PROJECT**

In northeast Alberta, bitumen resources are at relatively shallow depths located about 100 meters below ground surface. The stratigraphic section in the project area consists of Devonian, Cretaceous, and Quaternary sediments overlying the Precambrian basement. The Devonian-aged strata underlie the prospective Cretaceous reservoir sediments and are separated by the sub- Cretaceous unconformity. The Cretaceous sediments are in turn overlain by a thin veneer of Quaternary sediments. The characteristics of these stratigraphic units are described in detail by Andriashek (2003), Bachu et al. (1993) and Porter et al. (1982). The stratigraphic and geomechanical unit of interest is the Clearwater Formation, defined as the caprock for this project, and which is subdivided into the lower Wabiskaw Member and the Clearwater shale. This unit is lower Cretaceous-aged, and conformably overlies the McMurray Formation (reservoir).

According to project operator (AOS, 2010), the Clearwater shale is pervasive in this area, conformably overlying the Wabiskaw Member, and is unconformably overlain by Quaternary sediments. The top of the Clearwater shale occurs at depths of 10 to 14 meters with the thickness of the Clearwater shale in the Project area typically ranging

from 52 to 56 meters. The Clearwater shales are thick and laterally extensive throughout this area, and are expected to provide an excellent cap rock for SAGD production.

### **IN SITU STRESS TESTING PROCEDURE**

Micro-frac testing conducted in this project were performed with a multiple packer tool that allowed both the sleeve and hydraulic fracturing stages of the micro-frac test to be conducted with a test interval or depth. Figure illustrates the configuration of the packer tool during these stages. The hydraulic fracturing stage of the micro-frac test consisted of a series of injection/shut-in cycles. The following provides a summary of the test stages:

- **Sleeve Fracturing Cycle:** The test should be started by pumping fluid at a constant rate into one of the packers of the tool, up to the maximum allowable pressure the packer can sustain which will result in initiation of a stable fracture. Fracture initiation is recognized either by a breakdown or by a pressure plateau. The packer can then be deflated and the tool positioned so that the interval is at the level of the created fracture. This procedure ensures that fracture extension will start at the interval level.
- **Packer Inflation:** Once the tool has been properly positioned, the test interval is isolated by pressurizing the straddle packer arrangement until the pressure in the test interval starts to rise. The subsequent pressure decline is then observed to check the quality of the packer seal. Packers are further pressurized if the seal is not satisfactory.
- **Leak-Off Cycles:** Fluid is then injected in the interval at a constant flow rate. The wellbore is pressurized to a pressure below the breakdown of the formation. The goal is to check that the downhole pump can deliver enough flow rates to overcome fluid diffusion through the mudcake and into the formation.
- **Hydraulic Fracturing Cycles:** Fluid is again injected into the interval at a constant flow rate and the fracture is then extended. After the propagation, the injection is continued until the pressure stabilizes. The injection is then stopped and the pressure allowed decaying to a pressure level that ensures that the fracture is closed. The value of the stress acting normal to the fracture surface is determined by monitoring the initiation, propagation, closure, and reopening of the induced fracture. In general the fracture grows perpendicularly to the direction of the minimum stress. A stress test usually comprises two to five such cycles. Once the operator is satisfied that good

quality data were acquired, packers are deflated and the tool is moved to the next interval.

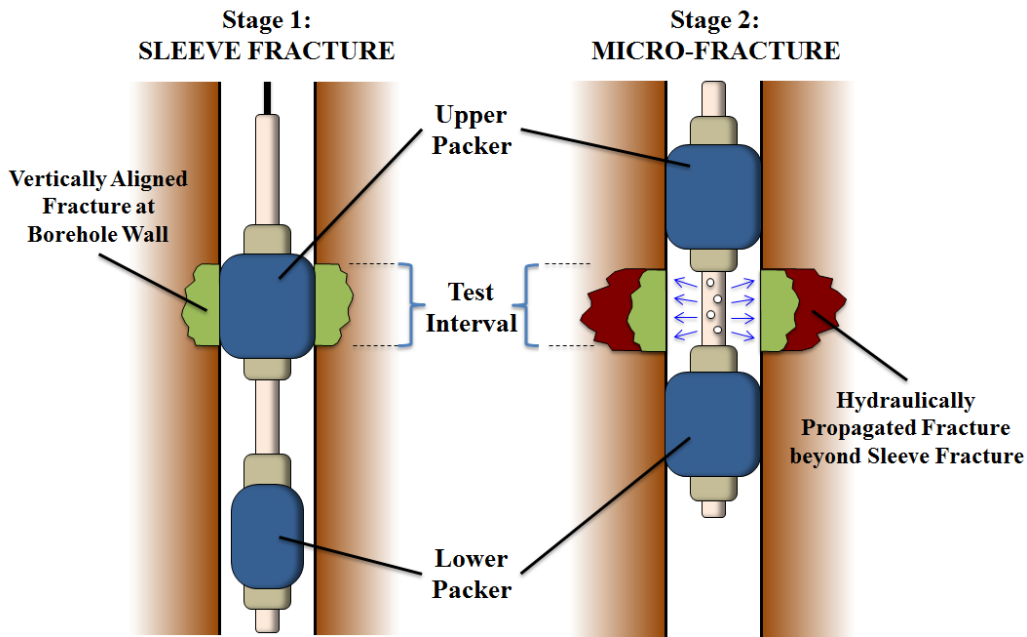


Figure 1. Arrangement of packers during the sleeve fracture and micro-frac tests stages

#### INTERPRETATION METHODOLOGY

A variety of interpretation techniques have been developed to estimate the magnitude of the minimum principal stress from the pressure records obtained during the micro-frac test. The following pressures (if measurable) are used in these interpretation techniques: breakdown pressure, propagation pressure, instantaneous shut-in pressure (ISIP), closure pressure, reopening pressure and rebound pressure.

The goal of stress testing with the micro-hydraulic or mini-frac techniques is to create a fracture that provides an estimate of the closure stress as close as possible to the minimum in situ stress. Theoretically, the width of the created fluid-filled fracture will become zero if the pressure of the fluid in the fracture is equal to the total stress acting on the fracture surface. The value of this pressure is called the closure stress and would ideally equal the in situ minimum stress. Unfortunately, measurement or interpretation of the closure stress is challenging since the constant fluid pressure in the fracture cannot be attained in practice. What is measured is the pressure at which the fracture initiates, propagates, closes and opens in the near-well region of the borehole. Consequently, estimates of the closure stress (or pressure) are detected by examining the flow regimes

associated with the abrupt changes in fracture conductivity when the fracture opens or closes over the several stages of the testing program. At each stage, various estimates of the closure pressure are determined. Reconciling estimates over all cycles provides an estimation of the closure stress and the minimum in-situ stress.

Methods have been used for determination of minimum in situ stress using variants of pressure-time data analysis in this research are as follows:

(a) Pressure versus square root of shut-in time: this method was proposed by Nolte (1982), assumes that after fluid injection into the formation is stopped, the pressure decline due to fluid leak-off should be linear as long as the fracture remains open. This method is often used in conjunction with the log-log plot of pressure-time data. On the log-log plot, the fracture linear flow regime is identified by its characteristic half slope. This plot indicates if the closure stress has been identified accurately on a pressure versus square root of time plot. A plot of pressure versus the square root of time since shut-in is usually a declining straight line, but once the fracture closes there would be a deviation from the straight line. This point is taken as the closure stress or the minimum in situ stress. The other common variant of pressure versus shut-in time plot used is P versus Nolte G-function (Nolte (1979), Castillo (1987), Syfan et al. (2007)).

(b) Tandem square root or linear flow plot: in linear flow plots, the bottomhole pressure is plotted against  $\sqrt{(T_{inj}+dt)}-\sqrt{dt}$ . This type of plot superimposes pressure for the linear flow during injection on the one during fall-off. The fundamental assumption is that until the occurrence of fracture closure, the flow is linear, and soon after that, the flow becomes non-linear.

(c) Log pressure versus time since shut-in: often the log of the bottomhole pressure plotted against the time since shut-in. This type of the plot is based on an exponential leak-off after the closure. Thus the inflection point on the slope of the curve is taken to be equal to the ISIP or minimum in situ stress (Warpinski (1989)).

(d) Log dP versus log dt plot: this plot is based on an exponential leak-off after closure (Whitehead et al. (1989)). The plot is often used in reservoir engineering to estimate the duration of wellbore storage. The end of wellbore storage is followed by linear or bilinear flow in the fracture as long as the fracture remains open. When fracture begins to close, the dP versus dt curve deviates from the straight line. The dP value corresponding to this

deviation from the straight line denotes the closure of the fracture. Once this value  $dP$  is known, the ISIP or minimum in situ stress can be obtained.

(e) Pressure decay rate: the pressure decay following the cessation of fluid injection is caused by an extension of the fracture as well as the leak-off of the injection fluid from the fracture into the formation. As these processes continue, the pressure eventually reaches a value which is equal to the far field stress normal to the fracture causing the fracture to close. This method is based on the assumption that the pressure decay consists of two distinct stages: a stage of linear flow when the fracture is still open; and the other stage of radial flow following the fracture closure. The pressure change per unit time ( $dP/dt$ ) plotted against pressure ( $P$ ) thus results in a bi-linear curve representing the opened and closed fracture pressure regime. The point of intersection of these two linear curves is considered to be the closure stress or minimum in situ stress (Lee and Haimson (1989)).

(f) Fracture reopening test: minimum in situ stress can be estimated from fracture reopening tests. On subsequent fluid injection at a constant rate following the initial breakdown of the formation, the slope of the pressure versus time curve should be constant till the fracture reopens. Deviation from the straight line would occur when the fracture reopens. The point of deviation is considered as the reopening pressure and theoretically is the upper limit of the minimum in situ stress (Whitehead et al (1989)).

(g) Horner plot: the Horner plot is a plot of pressure versus  $\log (T_{inj}+dt)/dt$ . The plot was originally used in reservoir engineering for pressure decline analysis. McLennan and Roegiers (1981) suggested that when the pressure fall-off data are plotted on a Horner plot, a change in slope can occur where the fracture closes. This method assumes that till the fracture has closed completely and the pressure transient effects are controlled by radial flow, a straight line will be observed on the Horner plot; prior to the fracture closure the relationship is believed to deviate from a straight line. They also indicated that following situations can be observed when Horner plots are used to determine the minimum stress. A description of the methodology followed for each of these methods can be found in Barree et al. (2009).

## RESULTS FROM MICRO-FRAC TEST CONDUCTED IN HSSR

To illustrate the issues with micro-frac testing in HSSR, the following section will describe and interpret the results obtained from a micro-frac test conducted at a depth of 63 m in Well AA/03-22-088-08W4. The test consisted of two stages: 1) sleeve fracturing and 2) hydraulic fracturing and each stage are discussed below.

### 1) Sleeve fracturing

Figure 2 provides a summary plot of the complete pressure history during the sleeve fracturing stages of the micro-frac test. This figure also illustrates the slope change in the pressure-time plot for two cycles, which are used for interpreting the potential formation breakdown pressure. As noted in Figure , the breakdown pressures were estimated to range from 13.5 MPa and 14.2 MPa.

One of the issues that may complicate stress interpretations during this stage of the test in HSSR materials is creep and stress relaxation processes. The Clearwater Formation shales within this test interval, like many soft shales, when subjected to a sustained loading can undergo significant creep strains. Conversely, stress relaxation may occur if the inflated packers are held constant for a period of time and under a fixed deformation, there is a time-dependent reduction in stress. Stress relaxation can be considered as the reverse of creep and conceptually, creep is pressure controlled and relaxation is volume controlled. As noted in Figure 2, eleven points were identified in the two sleeve fracturing stages where both creep and/or stress relaxation effects may play a role in modifying both boundary conditions of the test.

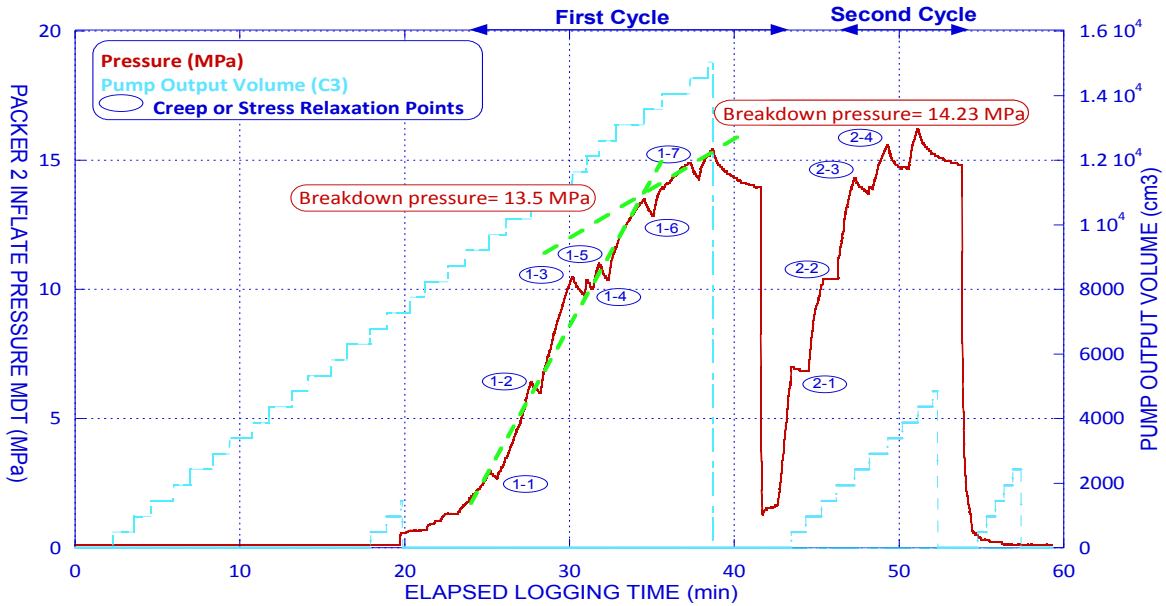


Figure 2. Complete packer inflation pressure time record for sleeve fracturing stages of micro-frac test for Clearwater West LP-SAGD Pilot Project

## 2) Micro-hydraulic fracturing

After the sleeve fracturing stage, the upper and lower packers of the tool are moved to straddle the 63 m depth to perform leak-off and micro-frac tests. One leak-off test was performed with relatively slow leak-off, which indicated low formation permeability. Figure 3 illustrates the injection rate and pressure versus time record for the micro-frac test. The micro-frac test sequence analyzed in this paper comprised two fracturing cycles. The initial leakoff test, the first injection and fall off test, the second injection and fall off test and the first and second rebound stages of the test are summarized in Figure The first and second injection cycles have been analyzed using the methods listed above to determine the reopening, fracture propagation, ISIP and fracture closure pressure. Data interpretation using different classical methods for determination of ISIP, reopening pressure and closure pressure for the first and second cycle of hydraulic fracturing test are illustrated in Appendix I.

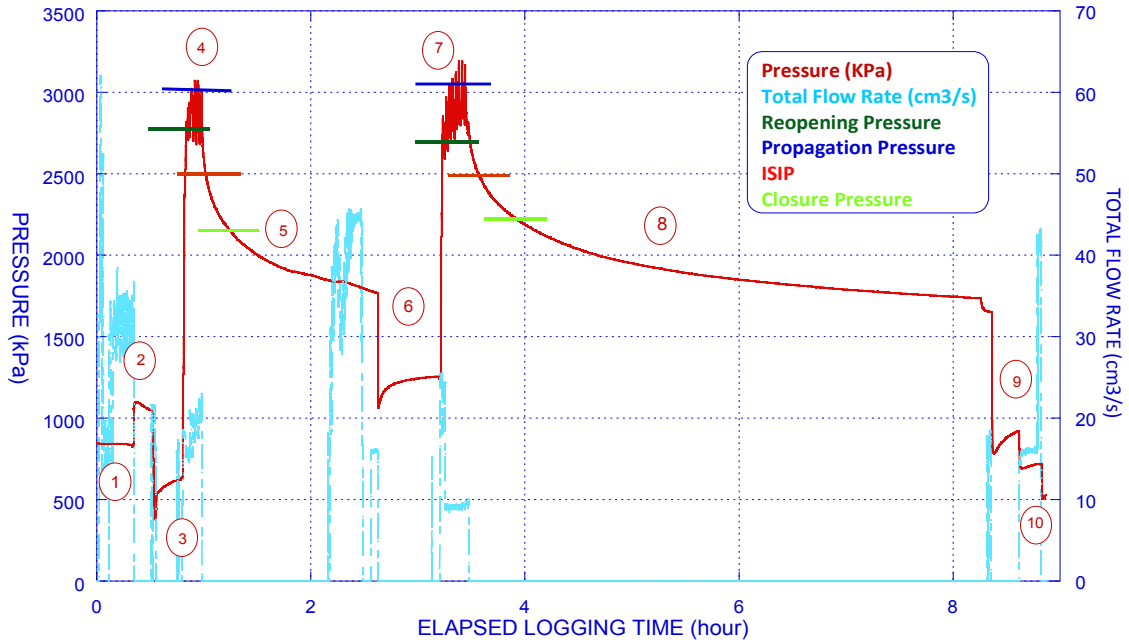


Figure 3. Recorded pressure history during the micro-frac test in Clearwater Formation at 63 m depth. Circles refer to the following stages: 1) upper and lower packer inflation, 2) leakoff test, 3) drawdown, 4) first cycle, 5) first falloff, 6) flowback, 7) second cycle, 8) second falloff, 9) flowback and 10) packer deflation

## DISCUSSION ON INTERPRETATION METHODS

A review of the flow regime identification methodologies is beyond the scope of this study but understanding flow regimes is an important element in understanding the downhole formation response to fluid injection. Increasingly more sophisticated pressure transient analysis techniques are being utilized for estimating ISIP and fracture closure pressures (Powless, 2013). One fundamental method for detecting flow regimes in the presence of the fracture is by plotting the log of pressure versus the log of time. For both cycles, the unit, half and almost zero slope could be observed (Figures A.I.8 and A.I.16) which indicated the wellbore storage and skin effect, fracture/formation linear flow and bilinear or pseudoradial flow regime respectively.

Although the reopening pressure is normally considered as an upper bound of minimum stress (Ratigan 1992, Ito et al. 1993, Detournay et al. 1994), the use of this pressure as a measure of  $\sigma_{\min}$  can be unreliable especially in nearly impermeable materials. Sensitivity of the reopening pressure to the pumping rates and the residual permeability of the existing fracture, assuming it was formed during the sleeve fracturing stage and that it

was mechanically closed during the previous shut-in period, are the factors that can influence the reopening pressure and result in an overestimate of  $\sigma_{\min}$ .

All data obtained from various methods of interpretation are summarized in Table and Figure 4, which allow estimating the lower and upper limits of minimum in situ stress and its gradient. Fracture closure pressure is the most suitable measurement for estimating  $\sigma_{\min}$  and as shown in Figure 4, ranges between 2.03 to 2.53 MPa in the 1st cycle and 2.09 to 2.47 MPa in the 2nd cycle. Assuming equal validity for each of the interpretation methods,  $\sigma_{\min (1st)} = 2.33 \pm 0.20$  MPa and  $\sigma_{\min (2nd)} = 2.31 \pm 0.14$  MPa. Recalling that the test depth interval was 63 m, this stress estimate can be converted to a stress gradient. Based on all the closure measurements, the stress gradient computed for this test interval is  $\sigma_{\min} = 35.6 \pm 2.5$  kPa/m.

The magnitude of this estimate for  $\sigma_{\min}$  is problematic. Based solely on formation bulk density estimates alone, the gradient of the in situ vertical stress should be approximately 21 kPa/m. If both horizontal stresses are substantially higher than the vertical stress, the micro-frac test should have yielded an estimate of  $\sigma_{\min}$  close to 21kPa/m. If one of the horizontal stresses was less than the vertical stress, the micro-frac test should have yielded a minimum stress gradient estimate lower than 21kPa/m. Clearly, this is not the case over the two cycles analyzed in this test and this result has been found in many other tests deploying the same multi-packer technique in HSSR.

There are several hypotheses for why such high minimum in situ stress gradients are generated. For instance, impermeable formations pose several challenges for stress testing. First, as mentioned previously, a fracture must be initiated in the interval during sleeve fracturing test which itself induces stresses in vicinity of the borehole wall. The area of influence of this stress change may extend out as far as ten times the borehole radius. Second, classic test interpretation methods may no longer be valid because it is based on the assumption that sufficient fluid will leak from the fracture face(s) to close it during the limited time of shut-in periods. If the formation has very low permeability, the fracture may not close during the test.

Based on regional data for the Clearwater Formation, permeability would be approximately 10-15  $\mu$ D, which is a low permeability. In such cases, a pressure decrease is still observed after shut-in, as in a typical hydraulic fracturing cycle, but it corresponds

only to the dissipation of stored energy to further extend the fracture and cannot be directly interpreted for the estimation of closure pressure.

For example, even if closure of the fracture for these two test cycles can be identified at 2.3 or 2.5 MPa, the pressure decline exhibits a peculiar behavior of shale which does not lend itself to an explicit determination of the closure pressure, at least not with the range of interpretation methods used in this analysis.

As well, during pumping cycles following fracture creation the pressure record may exhibit features similar to those characteristics of the reopening of a closed fracture. These features, however, correspond only to the loading of an already open fracture before propagation and cannot be directly interpreted for  $\sigma_{\min}$ .

Furthermore, stresses around the borehole are higher than the far-field in-situ stress condition as a result of induced stresses from the drilling phase and also sleeve fracturing stage. Therefore, a proper micro-fracturing test should inject enough volume of fluid to ensure fracture propagation extends beyond this altered-stress zone. For the current micro-frac test a relatively small volume of 30 L of fluid was injected into the formation. This small injection volume did not extend the fracture beyond the altered stress zone and is likely the main reason for incorrect high fracture closure pressure, reflecting the near well stress field rather than the far field stress state.

Table 1. All the data obtained from various methods of interpretation of micro-hydraulic fracturing test

Method of Interpretation	First Cycle			Second Cycle		
	Reopening Pressure (MPa)	ISIP (MPa)	Closure Pressure (MPa)	Reopening Pressure (MPa)	ISIP (MPa)	Closure Pressure (MPa)
P-Sqrt (Tinj)	2.78	-	-	2.73	-	-
P- dt	-	2.65	-	-	2.52	-
Log dp- Log dt	-	2.65	-	-	2.51	-
P-Log((Tinj+dt)/dt) (Horner Plot)	-	-	2.52	-	-	2.47
Log dp- Log dt	-	-	2.03	-	-	2.09
dP/dt- P	-	2.46	-	-	2.51	-
P- G Function	-	2.55	2.27	-	2.58	2.3
P-[Sqrt(Tinj+dt)-Sqrt(dt)]	-	2.68	2.51	-	2.51	2.3
P-Sqrt(dt)	-	-	2.3	-	-	2.35

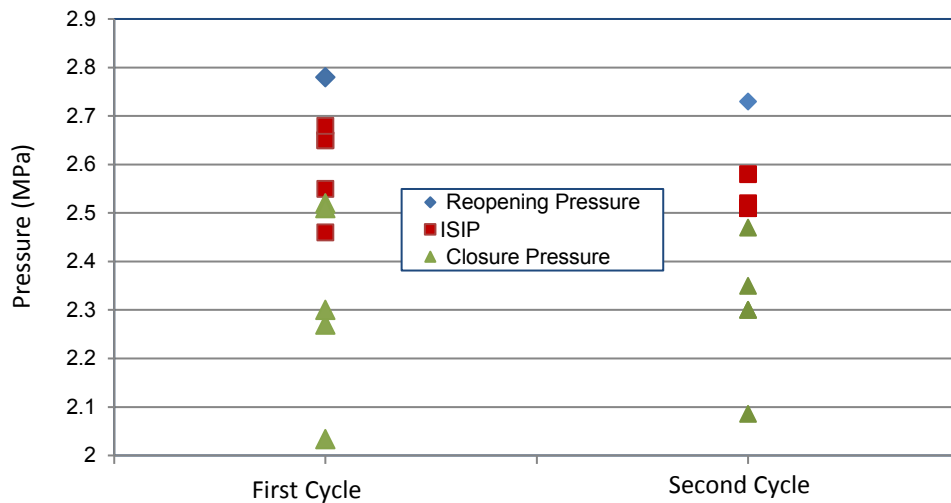


Figure 4. Reconciliation plot of all data obtained from various methods of interpretation for Clearwater West LP-SAGD Pilot Project

## PRIMROSE/WOLF LAKE CSS PROJECT

The Primrose/Wolf Lake area of northeastern Alberta employs high-pressure cyclic steam stimulation (HPCSS) process to recover bitumen from the Clearwater Formation. Primrose East is located in Township 67, Ranges 2 and 3, West of the 4th Meridian, approximately 350 kilometres (km) northeast of Edmonton, inside the Cold Lake Air Weapons Range. The purpose of this part of engineering analysis is to assess the rock stresses above the reservoir and in the caprock in Wells 11-11-67-3W4 in CNRL Primrose/Wolf Lake CSS project area, in 337m. The stress analyses were done on micro-frac data to quantify the

driving forces that exist in situ and to determine least principal stress or closure pressure on the Joli Fou Formation of Colorado Group.

## **GEOLOGICAL DESCRIPTION OF FIELD CASES**

The caprock overlying the Clearwater Formation reservoir in this setting comprises the Lea Park Formation, the Colorado Group and Mannville Group consists of the Grand Rapids Formation and non-reservoir Clearwater Formation. The micro-frac test interval is in the first formation of Colorado Group related to the upper Cretaceous (ERCB, 2013).

The Colorado Group is a shale interval with a thickness of 170 m for wells 11-11. The variable thickness of these shales is the result of post-Cretaceous erosion combined with subsidence. This shale is the seal for fluids (including gas) in the Clearwater and Grand Rapids Formations. Similarly, it is an effective barrier to communication between any fluids associated with production from or injection into the Clearwater or Grand Rapids and fluids of the Quaternary freshwater aquifers. The Colorado Group consists of the following units (ERCB, 2013):

- Joli Fou Formation—consists of dark gray, noncalcareous shale with very thin interbeds of siltstone and sandstone;
- Viking Formation—consists of upward coarsening silty and fine-grained sand.
- Westgate Formation—consists of a wedge of noncalcareous mudstone and siltstone. The gray mudstone dominates the top and base intervals, whereas upward coarsening intervals of siltstone to sandstone is mainly concentrated in the middle part of the formation.
- Fish Scales Formation—consists of well-laminated claystone and mudstone and is approximately 6 m thick.
- Belle Fourche Formation—consists of noncalcareous to slightly calcareous mudstone and siltstone.
- Second White Speckled Shale Formation—consists of calcareous claystone to siltstone and is distinctively fissile in core.
- Upper Colorado Group shale—consists of the Verger Member (about 4 m thick), the Cold Lake Member (about 21 m thick), and the First White Specks Member which are predominantly shale.

## DATA INTERPRETATION

### 1) Sleeve fracturing

A sleeve fracture was performed at 337 m and the slope change on the first and second attempts can be observed in pressure vs. time plot illustrated in Figure 5. This is an indication of successful sleeve fracture in the formation at this depth, and the complete breakdown was achieved at around 20 MPa. As it is clear, the breakdown pressure at the second cycle is less than the one in the first cycle which mentioned complete breakdown was achieved.

### 2) Hydraulic Fracturing

After three leak-off tests, a total of four closure pressure tests were performed. Figure 6 illustrates the injection rate and pressure versus time record for the micro-frac test. The micro-frac test sequence analyzed in this test interval comprised four fracturing cycles. Summary of the result interpretation shows in Table 2 and Figure 7. Appendix II illustrated all plots used for analyses.

## DISCUSSION

For understanding the flow regimes in the presence of the fracture, the log-log plot of pressure versus time should be investigated. The unit, half and almost zero slopes could be observed which indicated the wellbore storage and skin effect, fracture/formation linear flow and bilinear or pseudo-radial flow regime respectively (Appendices II).

If closure pressure is considered as a good estimate of two extreme levels of the minimum in situ stress, the gradient of minimum in situ stress resulting from interpretation of the test data for this test interval is 27 kPa/m as the minimum and 33 kPa/m as the maximum and 30 kPa/m as mean. None of the unsleeved fractured test intervals was successfully done. Therefore there is no result from non-sleeved station to be analyzed. Lessons learnt from practical experiences show, in general, the gradient of in situ vertical stress at the shallow depths ranges from 20 to 22 kPa/m and on average it is equal to 21kPa/m. Doubts should be raised about these values because they are larger than the density-derived in situ vertical stress around 21 kPa/m.

## CONCLUSION

The data acquired from multi-packer micro-hydraulic fracture tests was analyzed and discussed. The results demonstrate that although the micro-frac tests are regularly used in the petroleum industry, special attention must be paid to the unique conditions of the caprock in the oilsands development and consequent demands for high-quality data and accurate interpretation. Issues surrounding stress alterations in the near wellbore region, low permeability and low injection volumes were shown to contribute to incorrect estimates of the far field minimum in situ stress.

Inversion with a fully coupled hydraulic fracturing model will be conducted to investigate the hypotheses mentioned above concerning the minimum in situ stress estimates. A second approach consists of conducting a flow-back/rebound cycle at the end of each hydraulic fracturing cycle. When the pressure stabilizes at the end of the rebound part of the cycle, the pressure in the fracture is closer to the closure pressure and is the best estimate for the closure stress in such formations. Multiple cycles and flow-back technique can specifically help to define the closure pressure for low permeability materials like clay shale.

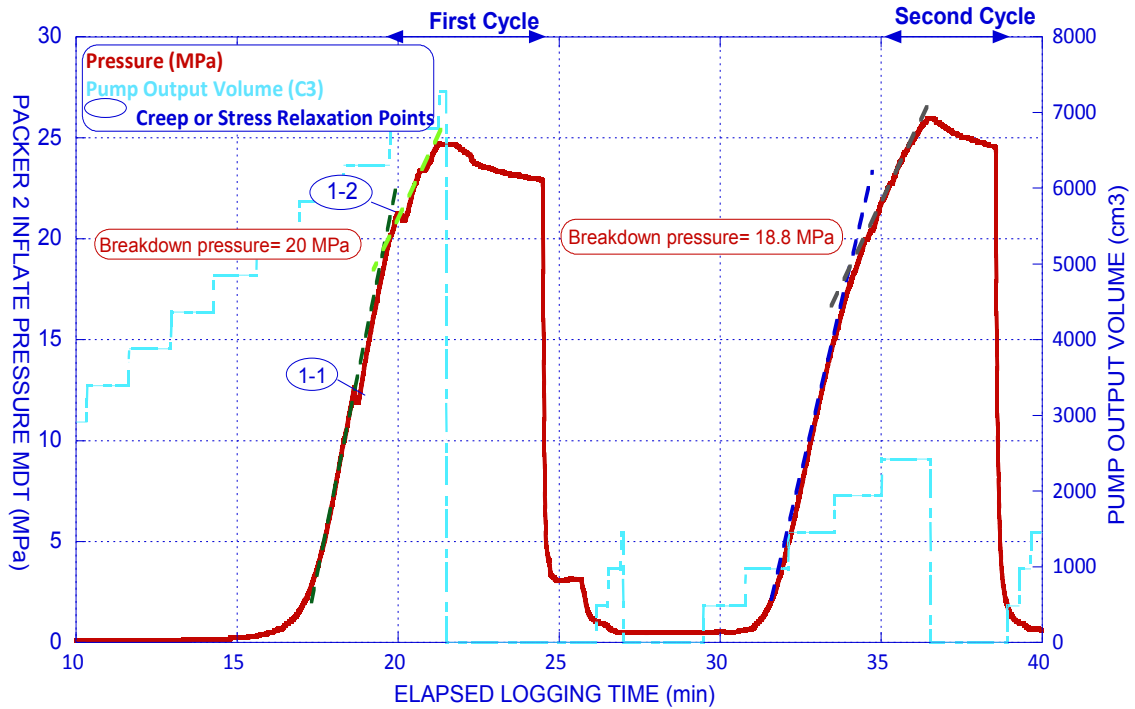


Figure 5. Pressure versus time curve from in situ stress test for Joli Fou clay shale at depth of 337 m for Primrose/Wolf Lake CSS project

Table2. All the data obtained from various methods of interpretation of micro-hydraulic fracturing test at 337 m in well 11-11-67-3W4

Method of Interpretation		$P\text{-}\sqrt{t}(T_{inj})$	$P\text{-}dt$	$\text{Log } dp\text{-} \text{Log } dt$	$P\text{-}\text{Log}(T_{inj}+dt)/dt$	$\text{Log } dp\text{-} \text{Log } dt$	$dp/dt - P$	$P\text{-}G \text{ Function}$	$P\text{-}[\sqrt{t}(T_{inj}+dt)\text{-}\sqrt{t}(dt)]$	$P\text{-}\sqrt{t}(dt)$
First Cycle	Reopening Pressure (MPa)	12								
	ISIP (MPa)		11.4	11.45						
	Closure Pressure (MPa)				11.8	11.3		11.3	11.4	11.4
Second Cycle	Reopening Pressure (MPa)	12.8								
	ISIP (MPa)		9.4	9.5			9.1		9.4	
	Closure Pressure (MPa)				9.2	10.9		9.2	9.1	9.3
Third Cycle	Reopening Pressure (MPa)	11								
	ISIP (MPa)		10.5	9.6			10.1		10.5	
	Closure Pressure (MPa)				9.85	9.87		9.8	9.9	10.2
Fourth Cycle	Reopening Pressure (MPa)	11.4								
	ISIP (MPa)		10				10		10.55	
	Closure Pressure (MPa)				10	9.75		9.8	9.94	10

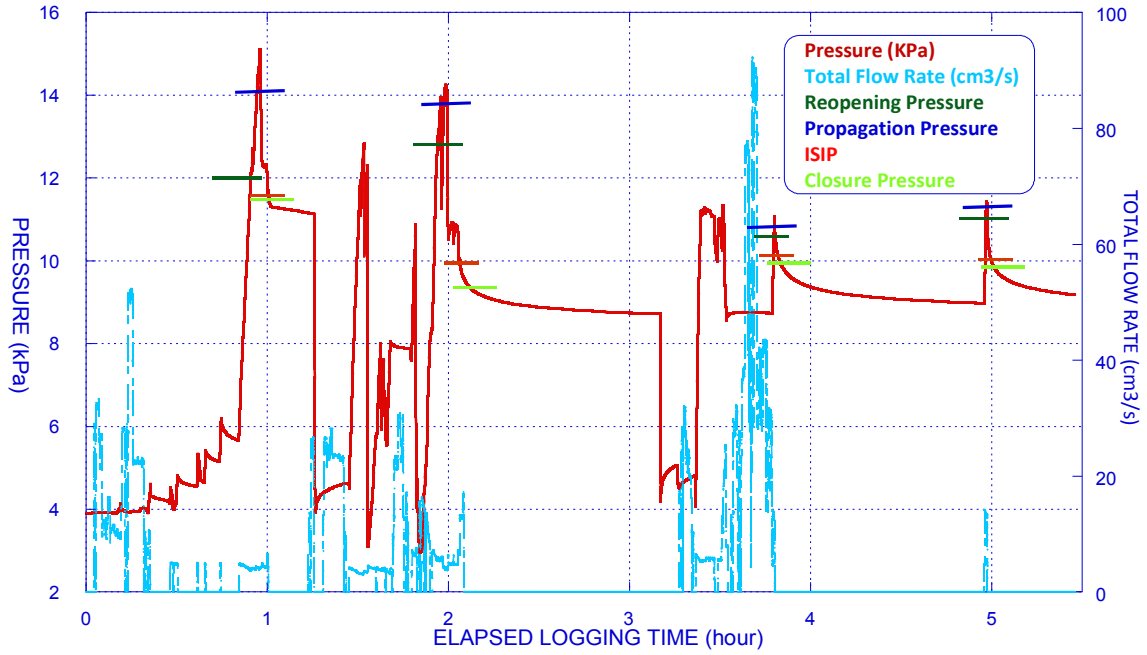


Figure 6. Recorded pressure history during the micro-frac test in Joli Fou clay shale at depth of 337 m for Primrose/Wolf Lake CSS project

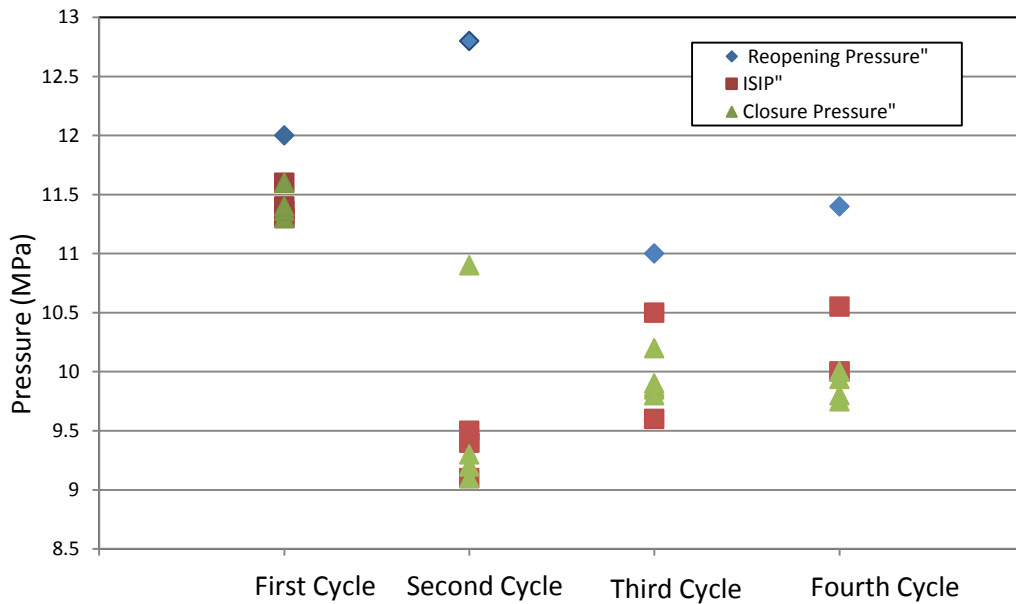


Figure 7. Reconciliation plot of all data obtained from various methods of interpretation for test at 337 m in well 11-11-67-3W4

**CHAPTER 3 COMPREHENSIVE ANALYSES OF LABORATORY  
DATA**

**MYSELF WHEN YOUNG DID EAGERLY FREQUENT  
DOCTOR AND SAINT, AND HEARD GREAT ARGUMENT  
ABOUT IT AND ABOUT: BUT EVERMORE  
CAME OUT BY THE SAME DOOR AS IN I WENT.**

**“KHAYYAM”**

## LABORATORY DATA ANALYSES

To tackle any numerical modeling project, input data plays a crucial role. One of the data sets that needs to be precisely considered is geomechanical parameters of material subjected to study. It is well-known that cretaceous clay/clay shales and mudstones which has been categorized as hard soil-soft rock (HS-SR) group are a difficult engineering material but they are the most common materials as caprock for reservoirs and potential host rocks for underground gas storage and geological disposal of radioactive waste.

Cementation develops in the process of lithification, but its magnitude is not great. The combination of compaction and cementation results in lithification. In the case of HS-SR, the process of lithification is not completed resulting in a material with a higher porosity than that of a rock. The cementing agents and clay minerals involved are often affected by chemical changes, resulting in a structural breakdown of rock. The processes of disintegration and decomposition of rocks arise as a result of weathering. Weathering weakens hard rock to various extents, and the physical and mechanical characteristics of weathered soft rock vary remarkably with type of rock matrix and the degree of weathering. The unique characteristics of these materials can be attributed to a combination of several processes occurring during not only deposition but also subsequent unloading. Several factors which are responsible for the present behaviour of stiff clays and mudstones, such as lithology, compaction, and bonding, were developed prior to the unloading of the original material. Lithology includes the mineralogy and the amount of clay fraction present, as well as the degree of compaction, and the extent and strength of internal bonding. An increase in the clay fraction and the percentage of montmorillonite results in increases in the plasticity and swelling potential and a decrease in the residual strength. The purpose of this section is to review the geomechanical behaviour of specifically Clearwater clay shale and Joli Fou clay shale formations with a concentration on the data required for the numerical studies.

## GEOTECHNICAL CHARACTERIZATION OF CLEARWATER CLAY SHALE AND COMPARISON OF THE PROPERTIES WITH OTHER CRETACEOUS CLAY SHALES IN NORTH AMERICA<sup>2</sup>

**Abstract:** Over the last thirty years, laboratory testing has been conducted to investigate the geotechnical properties of Clearwater clay shales from the Clearwater Formation in northeast Alberta. These properties are necessary for characterization of the overburden zones above in situ oil sands mines and assessment of caprock integrity in steam assisted gravity drainage (SAGD) projects. In general, caprock integrity assessments include caprock geological studies, in situ stress determination, constitutive property characterization, and numerical simulations, which allow operators to ensure that steam injection pressure does not cause any risk to the confinement of steam chambers. The aim of this study is to identify and provide the representative parameters that can enhance understanding of the geotechnical behaviour of the Alberta Clearwater Formation clay shale. Moreover, it illustrates how the results can be used to extract constitutive model parameters for modelling the behavior of this class of material. The parameters are also used for complex reservoir-geomechanical simulation for caprock integrity. These parameters are also compared with other Cretaceous clay shale counterparts in North America.

### INTRODUCTION

Problems associated with clay shales have been consistently experienced in many industrial projects (geotechnical or petroleum related projects). Cretaceous clay shales are widely deposited in North America. According to Scott and Brooker (1968), a large area of Western Canada is underlain by formations of the Upper Cretaceous period consisting of overconsolidated clay shale such as the Clearwater Formation. Figure 1 illustrates the main oil sands deposits in Northern Alberta, encompassing the Athabasca, Peace River, and Cold Lake areas. The Clearwater Formation is one of the main formations considered as caprock in situ recovery projects for the Athabasca oil sands area. Caprock integrity is of foremost concern with respect to in-situ thermal recovery methods in the

---

<sup>2</sup> A version of this section was published in Journal of Canadian Petroleum Technology, "Geotechnical Characterization of Clearwater Clay Shale and Comparison of the Properties with Other Cretaceous Clay Shales in North America", SPE-178916-PA

petroleum industry. In SAGD and CSS projects, caprock integrity is a critical element in the safe, economical, and environmentally-friendly operations of these projects. Understanding the geotechnical behavior of the caprock is crucial to assessing its integrity.

The aim of this research is to synthesize a wide range of geomechanical testing results for the fine-grained materials of the Clearwater Formation to develop a deeper understanding of the constitutive properties of this class of materials. It should be mentioned that samples come from different locations within the Fort McMurray region in northeastern Alberta. As most of these testing programs have been proprietary, the exact locations of the samples have been deliberately omitted.

## **GENERAL GEOLOGY**

The Clearwater Formation is an overconsolidated clay shale marine sequence deposited during the Cretaceous period. It is subdivided into a number of stratigraphic units based on characteristics of their lithology, stratigraphy, and depositional environment. Figures 2 and 3 show the cross section and the geological stratigraphy of the Cretaceous Clearwater Formation in Northern Alberta. This Cretaceous clay shale interval ranges from about ten metres to several hundred metres below the surface, dependent on different locations. Table 1 shows a generalized classification of the major sedimentary units of the Clearwater Formation (based on TEPCA 2008 facies chart). It should be mentioned that other organizations may utilize different nomenclature for facies identification. It should be mentioned that the data to be discussed do not belong to a specific depositional unit but reflects the wide range of plasticity exhibited in the Clearwater Formation as a whole. The formations of Cretaceous clay shales are usually interbedded with siltstone, sandstone, limestone, and bentonite (Scott and Brooker, 1968). This laminated and interbedded nature causes shales to behave anisotropically, and localized shale failures may develop along weaker layers and bentonitic layers because of shearing along bedding planes during stress changes related to deposition, faulting, glaciation, and erosion (Mollard, 1977).



Figure 1. Location map of main heavy oil and bitumen deposits, Alberta, Canada

The Clearwater Formation has been exposed to a variety of epigenetic processes. Vertical stresses can be easily determined from depth, bulk densities, and pore pressures. However, horizontal stresses are more difficult to quantify. Changes in vertical and horizontal stresses are influenced by previous loading history, and particularly by loading during deposition and unloading during an erosion sequence, such as excavation or glacial melting. Joints, fissures, and shear surface can originate in many ways, and shearing along bedding surfaces is particularly ubiquitous (Morgenstern et al., 1977). The characteristics of these stratigraphic units are described in detail by Andriashek (2003), Bachu et al. (1993), and Porter et al. (1982).

#### DATA COLLECTION AND METHODS

A group of tests assessed the hydro-geomechanical properties of Clearwater clay shale specimens recovered from various locations in Fort McMurray, Alberta. Characterization tests conducted on the test specimens provide values of specific gravity, bulk density, void ratio (porosity), moisture content, particle size distribution, and Atterberg Limits. The hydro-geomechanical testing program consisted of isotropically consolidated triaxial compression, direct shear (both

along and across bedding), one-dimensional compression, and unconfined compressive strength tests. Thermal tests such as thermal expansion and thermal conductivity have also been conducted but are not reported in this paper. Sample depths varied from 24 to 384 metres.

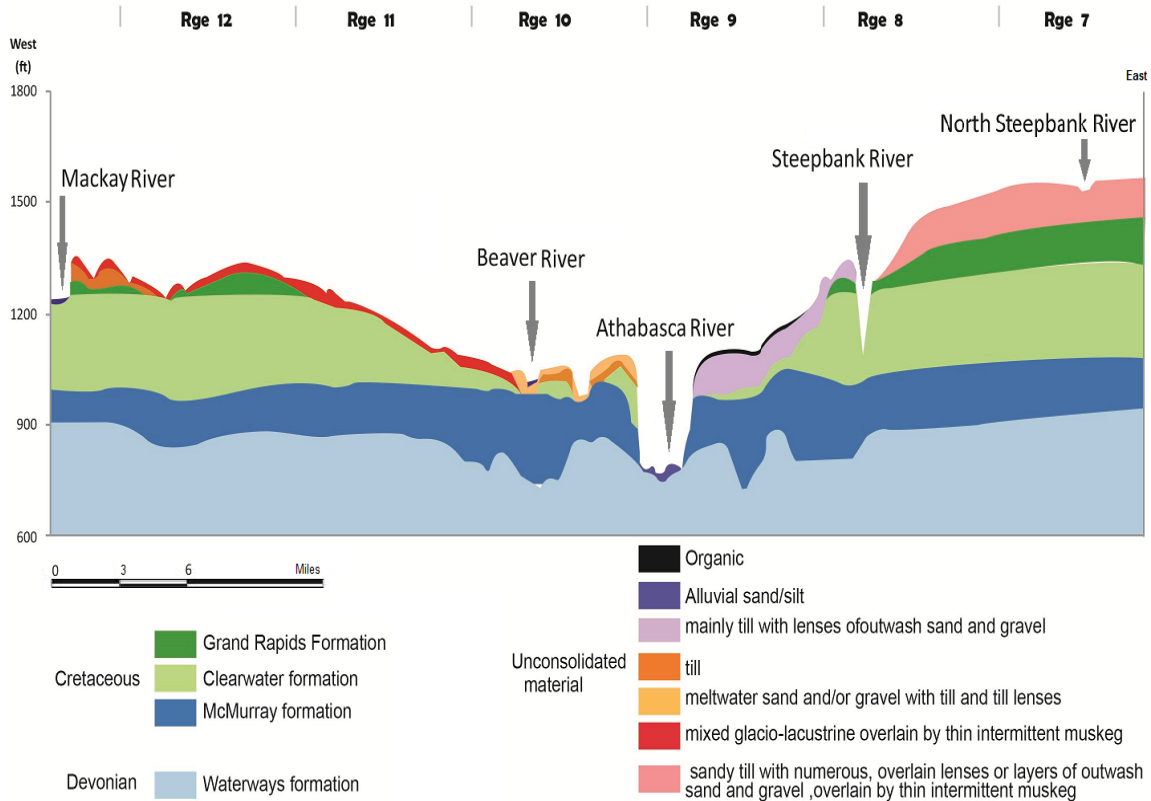


**Figure 2. Geological cross -section of Clearwater and McMurray Formations in Northern Alberta**

As the geological sections from the field are not available, the specific depositional units have not been determined. However, their behavior allows the samples to be categorized as having various proportions of sand or clay that can, in a broad sense, be related to the depositional units.

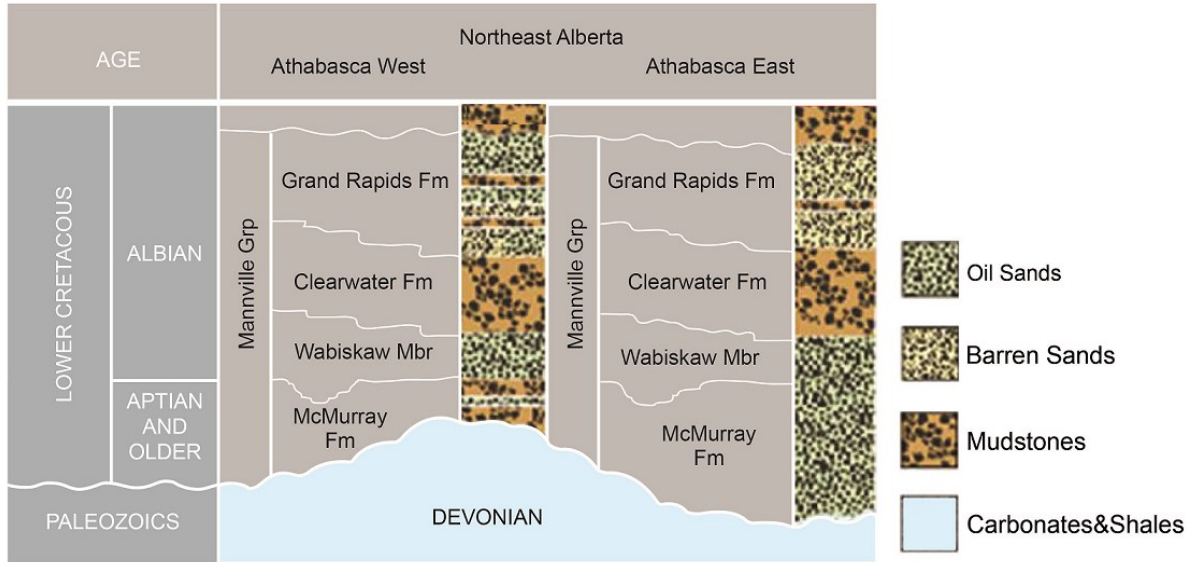


Figure 3. Lower cretaceous stratigraphy

Table 1. Generalized classification of Sedimentary units of Clearwater clay shale Member (TOTAL E&P JOSLYN Ltd, 2010)

Period	Formation/ Epoch	Formation Member	Depositional Unit	
Cretaceous	Clearwater	Clearwater	<b>Kc5:</b> Grey-brown, waxy clay with minor glauconitic sand-silt component, particularly near the erosional contact with the overlying Grand Rapids Formation	
			<b>Kc4:</b> Dark grey shale with silt-sand laminae/lenses. Lower contact is commonly marked by black, fissile low density clay	
			<b>Kc3:</b> Greyish-black shale with local low-angle, parallel bedded to x-bedded, glauconitic sandy silt. Lower contact is marked by a dual indurated bed and bound by a black, fissile, low-density clay cap	
			<b>Kc2:</b> Dark grey shale with moderate to common silt lenses, Local thin beds of low density clay, Thin, locally indurated beds. Lower contact may be marked by a thin interval of glauconitic shale and capped by a dual indurated bed	
			<b>Kc1:</b> Black, fissile, low-density clay with rare to moderate silt laminae/lenses. Upper contact is commonly marked by an indurated bed	
		Transgressive Marker (T21) Maximum Flooding Surface		
		Wabiskaw	Kcw3	
			Transgressive Marker (T15)	
			Kcw2	
			Transgressive Marker (T11)	
Kcw1				

## INDEX PROPERTIES

Table 2 summarizes the values of bulk and dry density, specific gravity, void ratio, porosity, and degree of saturation. For more information about the statistical variables and methods of calculation, check Navidi (2010). All tests were conducted as per ASTM standards. Tests on over 100 Clearwater clay shale specimens show that this material has, on average, specific gravity of 2.71, bulk density of 2.129 g/cm<sup>3</sup>, initial void ratio of 0.51 (which corresponds to an initial porosity of 33.6%), and degree of saturation of 87.5%.

**Table 2. Index properties of Clearwater Formation clay shale samples**

		$\rho_{\text{bulk}}$ (kg/m <sup>3</sup> )	$\rho_{\text{dry}}$ (kg/m <sup>3</sup> )	$G_s$	$e_0$	n(%)	$S_r$ (%)
Statistical Analyses	Number of Samples	106	106	102	102	102	95
	Maximum	2260	1884	2.80	0.79	44.1	99
	Minimum	1600	1037	2.48	0.3	23.1	80.45
	<b>Average</b>	<b>2129</b>	<b>1585</b>	<b>2.71</b>	<b>0.51</b>	<b>33.57</b>	<b>87.5</b>
	Standard Deviation	83.13	302	0.06	0.08	3.34	5.14
	Percentage of Confidence	95%	95%	95%	95%	95%	95%
	Coefficient of Variation (%)	0.04	0.19	0.02	0.15	0.1	0.06
	Level of Significance (t0.05)	1.98	1.98	1.98	1.98	1.98	1.99
	Error of Mean (SX)	8.074	29.33	0.006	0.015	0.681	0.99
	<b>Confidence Interval for Average (<math>\pm</math>)</b>	<b>15.99</b>	<b>58.1</b>	<b>0.013</b>	<b>0.030</b>	<b>1.348</b>	<b>2.089</b>

Atterberg Limits describe the consistency of fine-grained materials, with varying moisture content defining a boundary between two states of the materials. For instance, the Plastic Limit describes the boundary between semi-solid and plastic states. Atterberg Limits directly correlate with shear strength (O’Kelly (2013), Widodo et al, (2014)). Atterberg Limits tests were conducted as per ASTM D 4318. Figure 4 shows the plasticity chart of Clearwater clay shale samples. Almost all data plot between the A-line and the U-line. Ranges of Atterberg Limits indicate the nature of clay minerals presented in fine-grained materials such as clay shale. Figure 4 shows that most of the samples are categorized as medium to high plasticity. Table 3 summarizes the values of this set of properties reflecting the full suite of materials encountered in the Clearwater Formation. Table 4 summarizes the index properties of different Cretaceous clay shales associated with various projects.

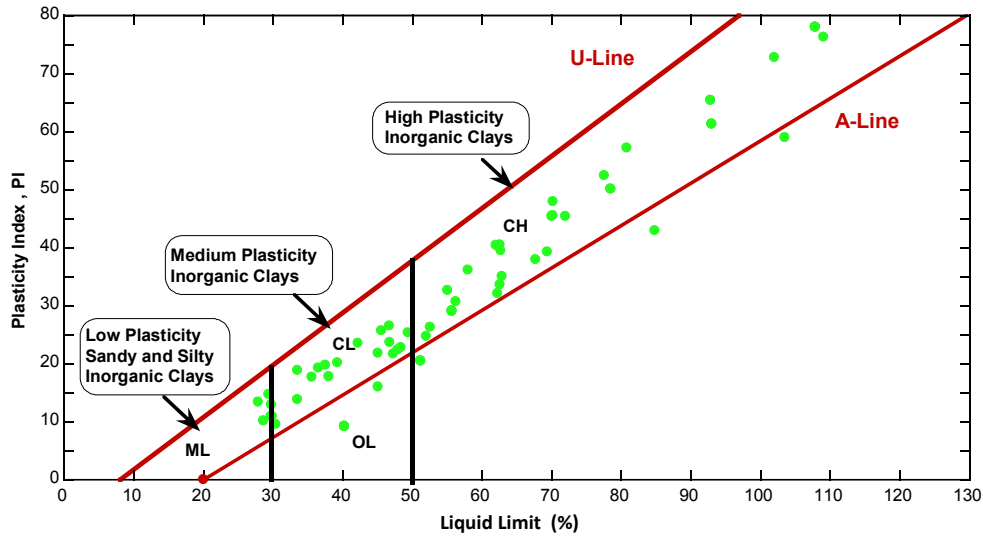


Figure 4. Plasticity chart of Clearwater clay shales

Table 3. Atterberg limits test results of Clearwater clay shale samples

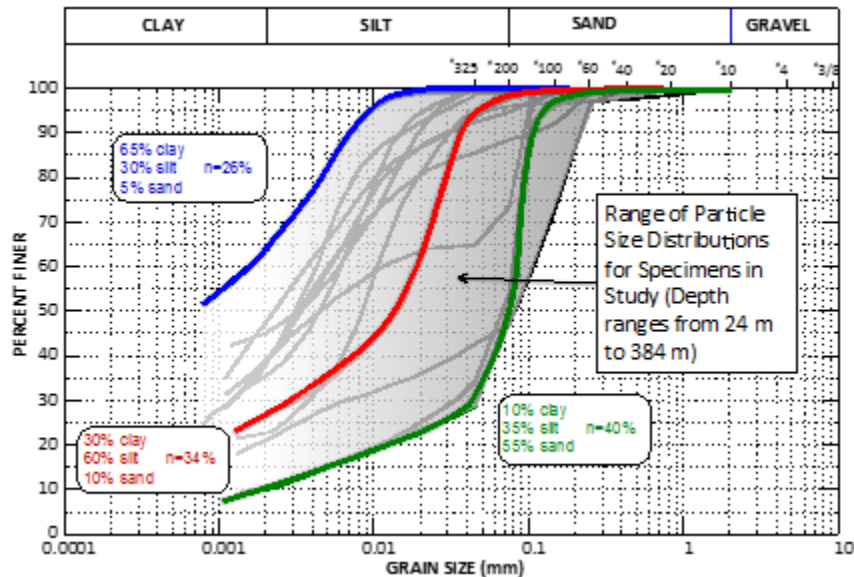
		W <sub>L</sub> (%)	W <sub>P</sub> (%)	I <sub>p</sub> (%)	w (%)
Statistical Analyses	Number of Samples	80	80	80	65
	Maximum	109.1	44.5	78	24.3
	Minimum	27.9	14.5	9.2	7.63
	<b>Average</b>	<b>61</b>	<b>26.2</b>	<b>35.5</b>	<b>18</b>
	Standard deviation	24.1	5.6	21.3	3.27
	Percentage of Confidence	95%	95%	95%	95%
	Coefficient of Variation (%)	0.39	0.21	0.6	0.19
	Level of Significance (t0.05)	1.99	1.99	1.99	2.00
	Error of Mean (SX)	2.69	0.63	2.38	0.41
	<b>Confidence Interval for Average (±)</b>	<b>5.36</b>	<b>1.25</b>	<b>4.73</b>	<b>0.81</b>

Table 4. Index properties of different Cretaceous clay shales

Formation	w (%)	W <sub>L</sub> (%)	I <sub>p</sub> (%)	Reference
Bearpaw, Canada	19 (10-27)	120 (50-150)	95 (30-130)	Clough et al. (1979), Peterson (1954)
Bearpaw, USA	14 (11-20)	-	-	Fleming et al. (1970)
Taylor	16 (3-38)	65 (34-151)	43 (17-112)	Hsu (1989)
Pierre	23 (15-38)	122 (55-204)	95 (35-175)	Fleming et al. (1970), Scully (1973)
Claggett	14 (10-18)	110 (54-241)	86 (34-205)	Fleming et al. (1970)
Colorado	9 (6-15)	-	-	Fleming et al. (1970)
Edmonton	20 (10-20)	40-100	20-25	Sinclair and Brooker (1967)
Clearwater	18 (8-24)	61 (28-109)	36 (9-78)	

## PARTICLE SIZE DISTRIBUTION (PSD)

The particle size distribution gives an idea of the composition of soil based on the average size of various constituent particles. Once the mechanical properties of a particular material are obtained, the particle size distribution curve can be related to those properties, and a distribution curve may serve as a common reference for future estimates of mechanical properties of materials with similar particle sizes. Particle size distribution analysis was conducted according to ASTM D422. Hydrometer 152H was used during the test. Looking at the PSD of all samples, it is evident that in general, more than 50% (and up to 95%) of the material passes through a sieve of size 200, and from 5% to 55% of clay particles pass through a sieve of size  $2\mu\text{m}$  in all cases (Figure 5). Thus, the soil is categorized as fine-grained. Figure 5 shows the further classification of the soil (as per Unified Soil Classification System (USCS) based on the Atterberg Limits. According to the geological classification of mudrocks suggested by Ingram (1953) and Gamble (1971) this material classified as silty shale (over 2/3 silt of grain size of mud fraction).



these samples ranges from 11.55 % to 48.4 % of the total rock volume. The wide range of proportions of clay content shows that the samples belong to different subdivisions with various lithologies (Tables 1). This is also evident in the PSD plot. The clay fraction XRD results indicate that these samples consist mainly of illite, chlorite, and kaolinite, with less smectite (montmorillonite). Table 5 summarized some of the bulk and clay x-ray diffraction results for Clearwater clay shale samples.

**Table 5. Summary of Combined Bulk and Clay XRD Analysis**

Sample ID.	Type of Analysis	Weight %	Clays														Total Clay	
			Qtz	Plag	K-Feld	Cal	Dol	Anhy	Pyr	Musc	Bar	Sider	Kaol	Chl	Ill	ML		Smec
1 210.75 m	Bulk Fraction	73.02	57	2	1	0	21	0	4	0	0	0	4	0	11	0	0	15
	Clay Fraction	26.98	13	0	0	0	0	0	0	0	0	0	16	16	55	0	0	87
	Bulk & Clay	100	45	2	1	0	15	0	3	0	0	0	7	4	23	0	0	34
2 226.45 m	Bulk Fraction	81.02	52	6	1	0	26	0	2	0	0	0	5	0	9	0	0	14
	Clay Fraction	18.98	6	0	0	0	0	0	0	0	0	0	17	10	57	0	10	94
	Bulk & Clay	100	43	5	1	0	21	0	1	0	0	0	7	2	18	0	2	29
3 212.6 m	Bulk Fraction	83.43	50	2	1	0	28	0	2	0	0	0	6	0	11	0	0	17
	Clay Fraction	15.57	6	0	0	0	0	0	0	0	0	0	28	16	50	0	0	94
	Bulk & Clay	100	42	2	1	0	24	0	2	0	0	0	9	3	17	0	0	29
4 218.75 m	Bulk Fraction	57.37	31	1	0	0	0	0	5	0	0	0	9	0	49	0	7	65
	Clay Fraction	42.63	6	0	0	0	0	0	0	0	0	0	19	8	51	0	16	94
	Bulk & Clay	100	19	1	0	0	0	0	3	0	0	0	13	3	50	0	11	77
5 214.9 m	Bulk Fraction	77.81	52	3	1	0	25	0	4	0	0	0	5	0	10	0	0	15
	Clay Fraction	22.19	6	0	0	0	0	0	0	0	0	0	26	13	55	0	0	94
	Bulk & Clay	100	41	3	1	0	19	0	3	0	0	0	10	3	20	0	0	33

## HYDRO-GEOMECHANICAL PROPERTIES

A suite of tests (discussed in the following section) has been conducted to evaluate the hydro-geomechanical properties of Clearwater clay shale specimens. It consists of UCS, triaxial tests, direct shear tests, one-dimensional consolidation tests, and isotropic consolidation tests.

### UNCONFINED COMPRESSIVE STRENGTH (UCS)

A total of 31 UCS tests have been analyzed. Core samples were cut and trimmed to a length to diameter ratio of 2:1 in a moisture room using cutting ring and in some cases the diamond cutter. It was also important to ensure both ends of the samples were flat, parallel, and perpendicular to the vertical axis. To further ensure that samples did not hydrate or further desiccate during preparation, mineral oil was lightly applied on trimmed surfaces of the specimen. After photographing and measuring sample dimensions and weight, samples were placed in the INSTRON loading frame and the ram

brought in contact with the sample. The axial loading strain rate was set to 0.5% per minute and the compressive load and strain values are recorded for determination of the peak strength. The average unconfined compressive strength from the UCS tests was  $1080 \pm 170$  kPa with 95% of confidence. Table 6 shows the difference between this value and its counterparts for different formations. Data of uniaxial compressive strength versus depth, water content, void ratio, and clay fraction are given in Figures 6 to 9, respectively. There is a general trend of uniaxial compressive strength decreasing as water content, void ratio, and clay fraction increase although the results do not show an acceptable coefficient of regression (for all cases, it is below 0.5). Although the UCS test is relatively simple, it requires meticulous sample preparation. For weak rocks like clay shale, further difficulties arise concerning good quality sample collection. Petrographic and physical features including structure, texture, and mineral composition of clay shale are intrinsic properties that control the UCS of the rock. On one hand, the lack of confining pressure during the UCS test and on the other hand, the rock micro-fabric and presence of micro-fractures which is a part of its natural structure can lead to variation in UCS and as a result, the scatter values for this mechanical property. Figures 10 and 11 show the data of water content versus depth and porosity. Water content increases with increasing porosity.

**Table 6. Uniaxial compressive strength of different Cretaceous clay shales**

<b>Formation</b>	<b>Bearpaw, Canada</b>	<b>Taylor</b>	<b>Pierre</b>	<b>Claggett</b>	<b>Edmonton</b>	<b>Clearwater</b>
<b>UCS (MPa)</b>	1-2.8	3.2 (0.5-12.7)	1.4 (0.8-2.6)	2.5 (2.3-5)	0.75	1.1 (0.3-1.9)
<b>Reference</b>	Peterson (1954)	Hsu (1989)	Fleming et al. (1970), Scully (1973)		Hanna and Little (1992)	

## **SHEAR PARAMETERS**

Four unconsolidated-undrained triaxial tests (UU), four consolidated-undrained triaxial tests (CU), and 24 consolidated-drained triaxial tests (CD) have been studied at different effective confining stresses. Drained triaxial tests were conducted at different overconsolidation ratios, from normally consolidated to heavily overconsolidated (ranging from 1 to 13). The overconsolidation ratio mentioned above refers to the laboratory scale and it does not have anything to do with the preconsolidation pressure in geological scale, which will be discussed later in consolidation behaviour section. OCR

here demonstrates the ratio of maximum confining pressure that sample has experienced during isotropic consolidation process over the confining pressure at which sample sheared. Sample preparation for triaxial tests is exactly the same procedure mentioned in UCS tests.

In order to saturate the samples, it was necessary to create a pore water solution matched the ionic strength of the in situ water condition. A salinity of 3,000 ppm was chosen for Clearwater samples based on laboratory experiments. For triaxial tests, all drainage lines were saturated with that brine fluid. Samples were placed in triaxial cell with two saturated sintered stainless porous stones at both ends and wrapped with a filter paper to have a better drainage during the test. Two layers of latex membrane have been placed carefully over the samples by using membrane stretcher then sealed with two O-rings on both pedestals. After assembling the top part of triaxial cell and using loading ram, the full cell has been placed under high-pressure triaxial loading frame. The cell confining pressure lines have been saturated and cell has been filled up with silicon oil and connected to the pump. Both top and bottom pore pressure lines have been saturated with brine fluid and connected to the backpressure pump. LVDT has been attached to the loading ram and connected to the top of triaxial cell to monitor the vertical strain. Readings from backpressure transducer, backpressure volume, cell pressure transducer, load cell transducer, and LVDT have been constantly recorded. Cell pressure and back pressure have been increased incrementally to mean effective confining stress and system has been held for at least 12 hours to achieve back saturation for the samples. By closing the backpressure valve and increasing confining pressure slowly and incrementally, the in-situ effective stress level has been reached for each sample according to its depth. The confining pressure and backpressure values are recorded and used to calculate the degree of saturation (B-value) for the samples. The ratio of pore pressure change to the change in confining pressure indicates the pore pressure coefficient or B-value, which is an indicator of degree of saturation for samples. For all testes, this value was at least 0.98 which showed that all samples under study were fully saturated during triaxial tests. Isotropic consolidation was the next step for CU and CD tests. According to the depth of the samples, the mean in situ effective stress has been calculated and samples have been consolidated to that level in several incremental stages.

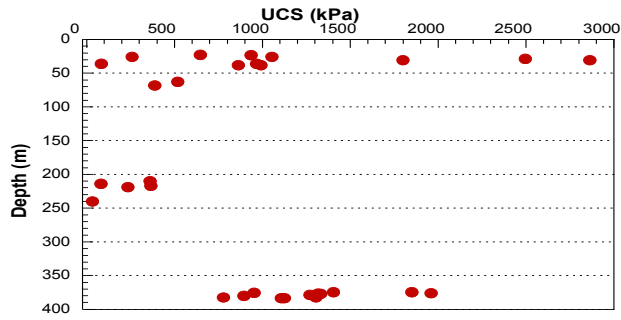


Figure 6. UCS versus depth

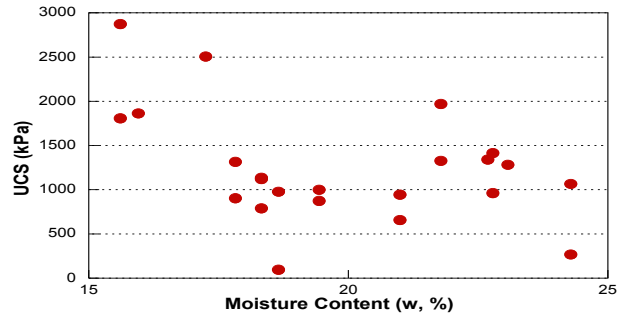


Figure 7. UCS versus moisture content

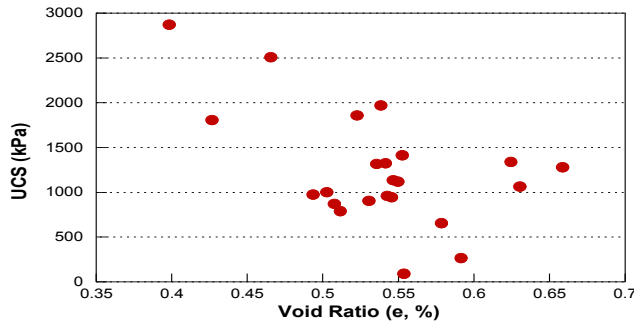


Figure 8. UCS versus void ratio

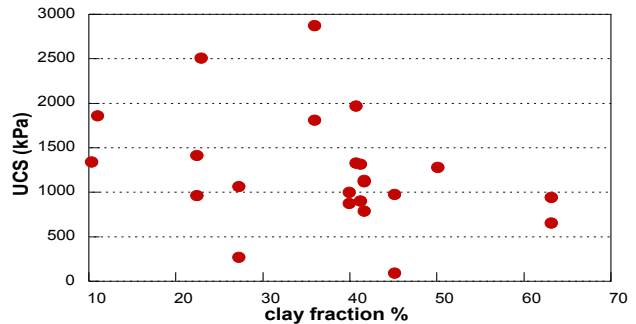


Figure 9. UCS versus clay fraction

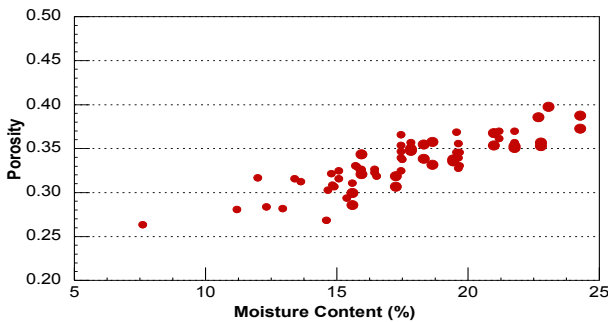


Figure 10. Porosity versus moisture content

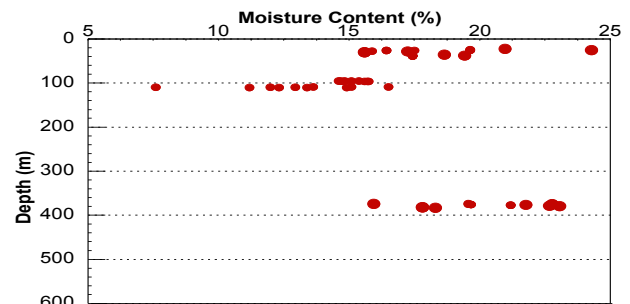


Figure 11. Depth versus moisture content

For that purpose, in each increment, backpressure valve has been closed, confining pressure has been increased then backpressure valve has been opened and let the sample to consolidate. Volume change in back pressure pump has been monitored and once back pressure pump volume was constant, this cycle has been repeated till the sample was isotropic consolidated at its in situ stress level. Then the loading ram has been moved down very slowly ( $\sim 0.004\%/min$ ) to contact with sample and then let the system be stabilized for a period of time before shearing. For CD tests, the backpressure valve was left open to allow the fluid to flow in and out of the sample and the volume change of the

backpressure fluid was recorded. For CU tests, the backpressure valve was closed. Axial stress was applied and increased slowly at a very low axial strain rate until the sample failed and reached steady state. Axial load, axial strain, pressure and volume change in both top and bottom pressure pumps, confining pressure, differential pressure values in drained tests were all recorded during shearing stage.

Figure 12 shows the UU tests result, with undrained shear strength equal to 1.85 MPa. Considering this parameter for classification suggested by Morgenstern and Eigenbrod (1974) and Botts (1986), this material categorized as silty shale/clayey shale since it is fissile with  $c_{uo}$  equal 1.85 MPa (268 psi).

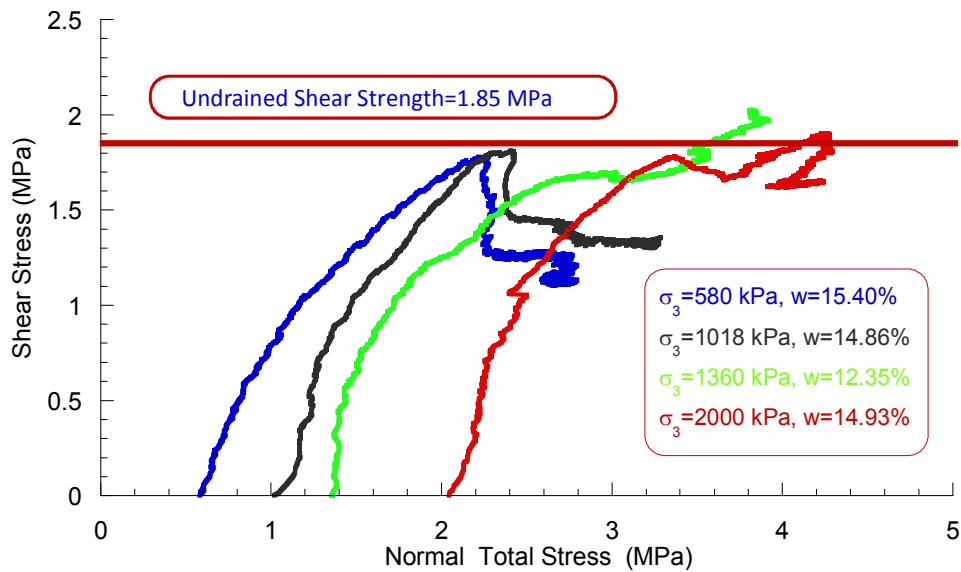


Figure 12. Unconsolidated-undrained triaxial test result

The magnitudes of shear parameters resulting from consolidated-undrained triaxial tests (CU) are 150 kPa and  $30^\circ$  for cohesion and friction angle, respectively (Figure 13). The failure envelope obtained from consolidated-drained triaxial tests (CD) of normally consolidated and overconsolidated samples shows two distinct branches. However, Figure 14 clearly shows that the slopes of these two lines are very close. According to Figure 14, the shear parameters for normally consolidated and overconsolidated samples are  $c_{n/c'} = 0$  kPa,  $\phi_{n/c'} = 31^\circ$  and  $c_{o/c'} = 200$  kPa,  $\phi_{o/c'} = 30^\circ$ , respectively. Figure 15 indicates deviatoric stress versus axial strain for some Clearwater clay shale samples under consolidated-drained triaxial tests.

Twenty-eight direct shear tests have been conducted with different normal stresses ranging from 500 to 3770 kPa. Samples of 63mm diameter and 36mm height were hand cut using a sharp knife and a ring cutter. The final sample dimensions and weight were recorded prior to the sample being carefully placed in the shear box and fixed into position. Two saturated sintered stainless steel porous stones were placed at the top and bottom of the samples. A seating load of 50kPa was then applied and an LVDT used for recording vertical displacement of the samples was secured to the top cap. The shear box was filled with 3000ppm salinity fluid and the saturation, swelling and consolidation behavior were monitored. The vertical stress was increased incrementally to reach the desired in-situ stress level, while allowing for a reasonable time for consolidation to take place. The consolidation process resulted in change of height of sample. The horizontal shear test was started while recording horizontal, vertical displacement, and shear load. A horizontal strain rate of about 0.0001inch/min was used to ensure excess pore pressure would dissipate during the drained shear test. All readings were recorded until the horizontal (or shear) load peak was exceeded to a sufficient degree and then the direction of travel was reversed while recording the readings. Forward and reverse shearing was repeated at least three additional times.

Ten tests conducted parallel to bedding and eighteen tests perpendicular to bedding were selected for analysis (Figure 16). Figures 17 and 18 and Table 7 summarize the results of these tests.

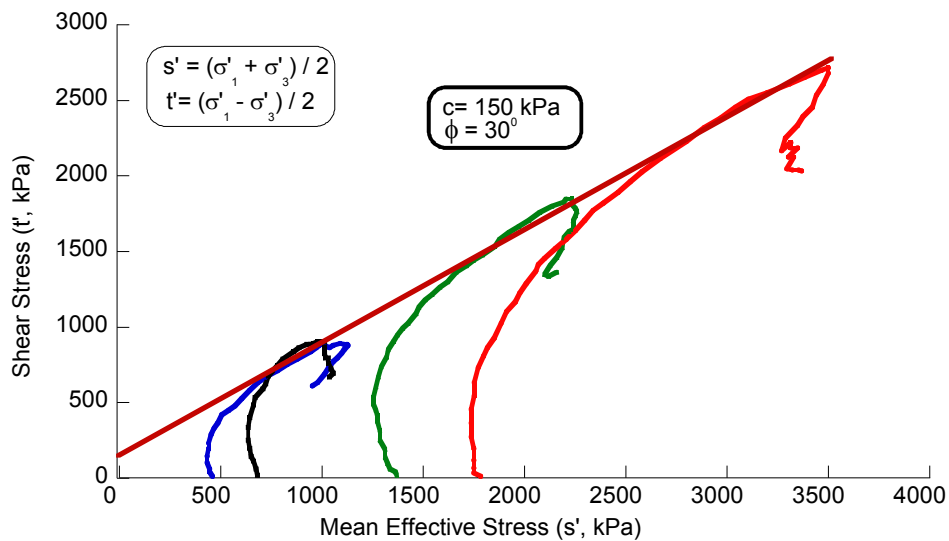


Figure 13. Consolidated-undrained triaxial tests result

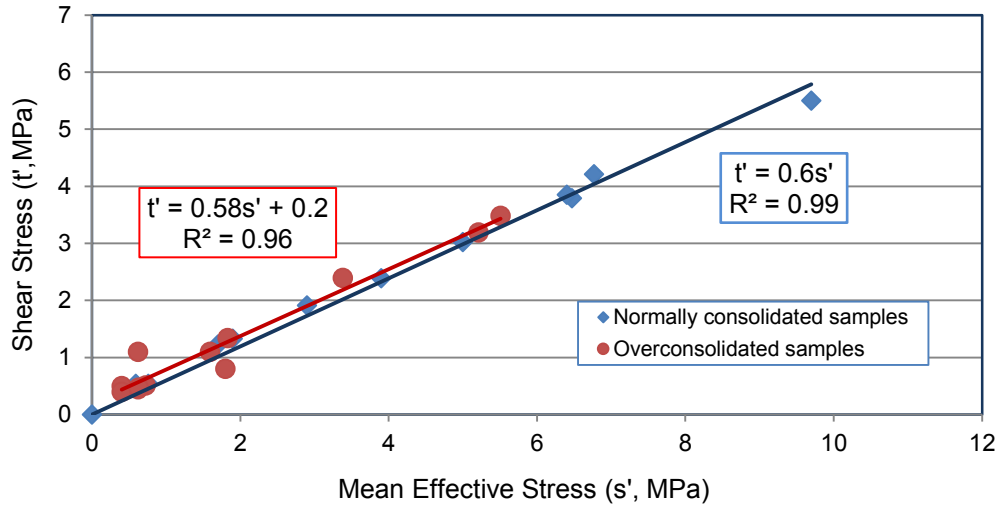


Figure 14. Consolidated-drained triaxial tests result

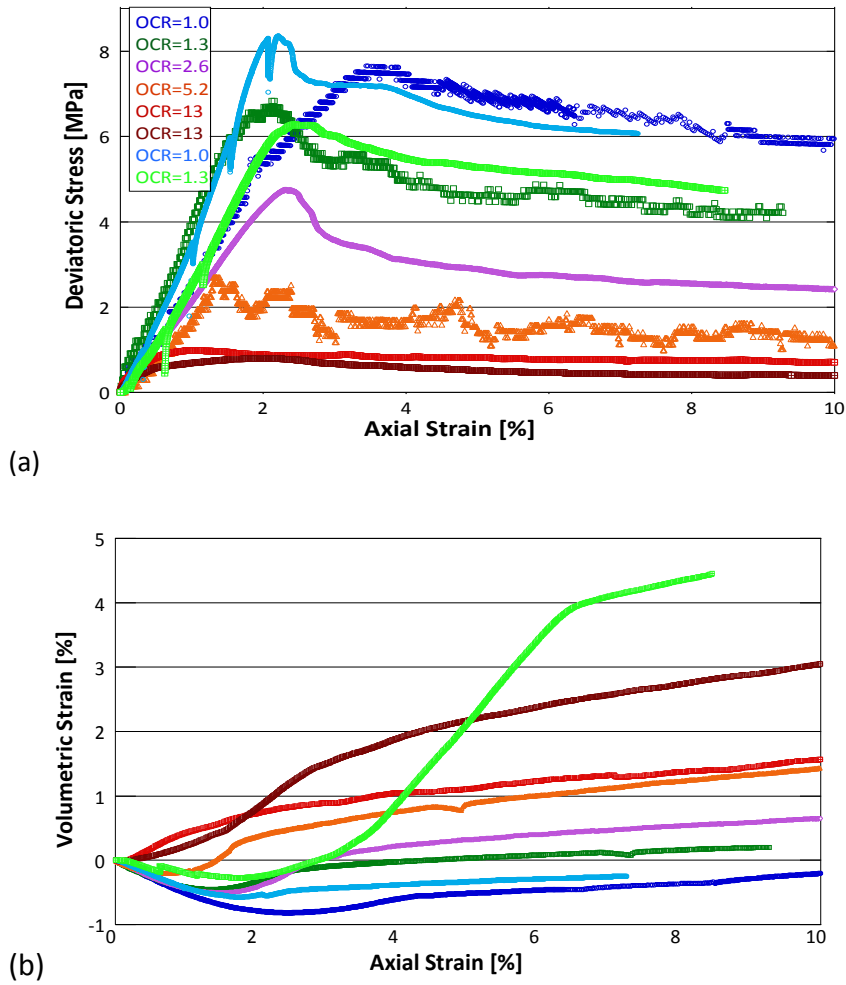


Figure 15. (a) Deviatoric Stress vs. Axial Strain, (b) Volumetric Strain vs. Axial Strain from consolidated drained triaxial compression tests. Positive volumetric strain indicates pore volume increase during shear.

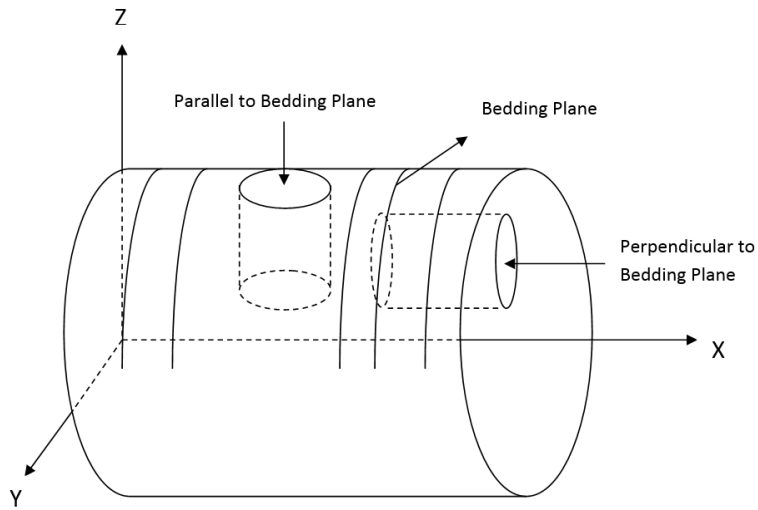


Figure 16. Schematic direction of the direct shear test samples

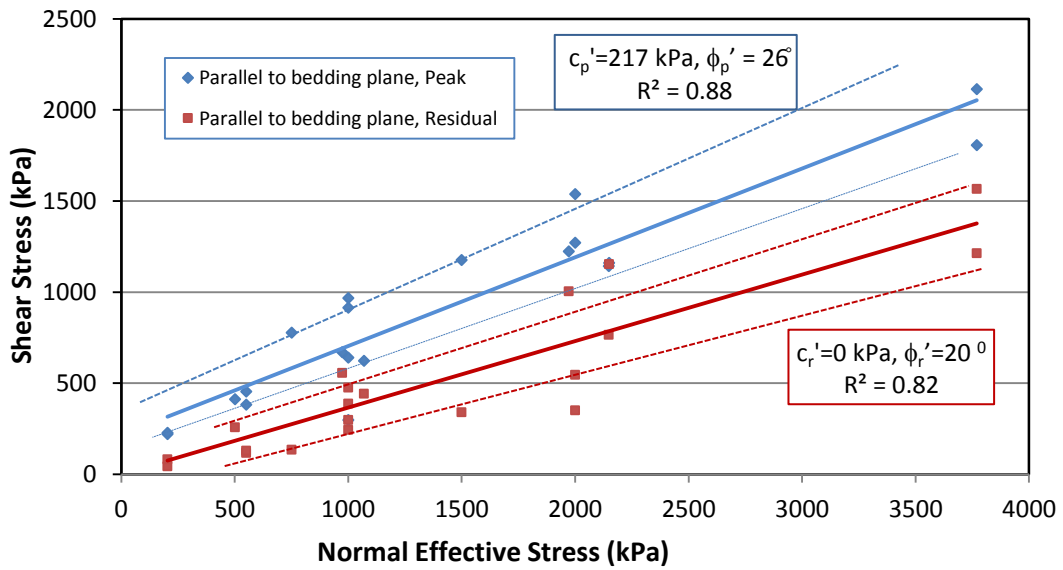


Figure 17. Clearwater Formation direct shear tests, Parallel to bedding plane– Mohr-Coulomb Failure Envelopes, The area between dotted lines represent  $\pm$  standard deviation

Table 7. Summary of direct shear test results of Clearwater Formation Samples

# of Tests	Orientation relative to bedding plane	$c_p'$ (kPa)	$\phi_p'$ ( $^\circ$ )	$c_r'$ (kPa)	$\phi_r'$ ( $^\circ$ )
18	Parallel	217	26	0	20
10	Perpendicular	64	35	0	28

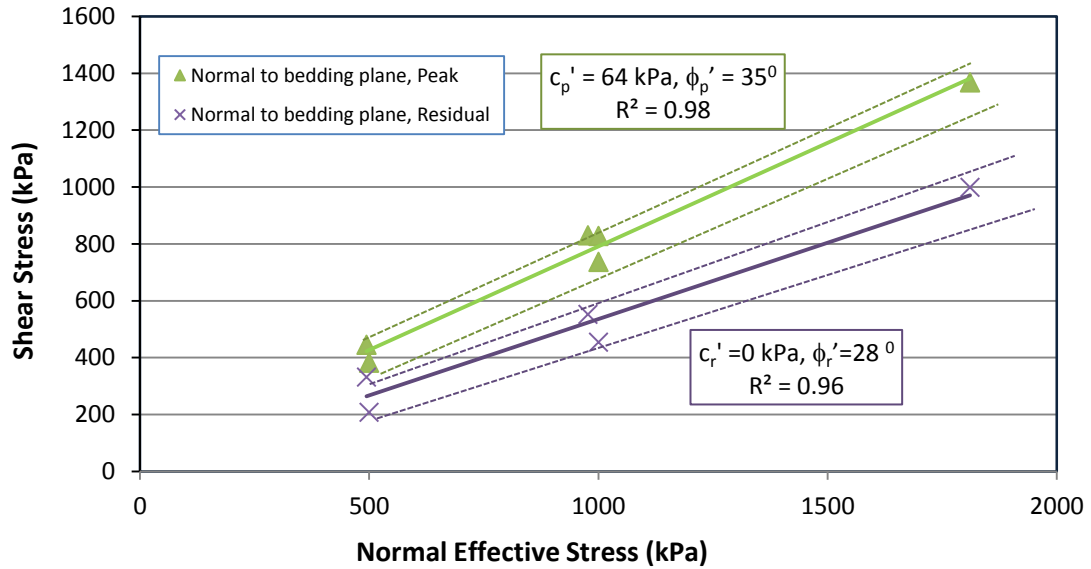


Figure 18. Clearwater Formation direct shear tests, Perpendicular to bedding plane– Mohr-Coulomb Failure Envelopes, The area between dotted lines represent  $\pm$  standard deviation

A composite integrated failure envelope for Clearwater Formation clay shale was developed (Figure 19). This figure summarized all CU and CD triaxial test results in a single chart. The peak and residual criteria for overconsolidated and normally consolidated samples are suggested.

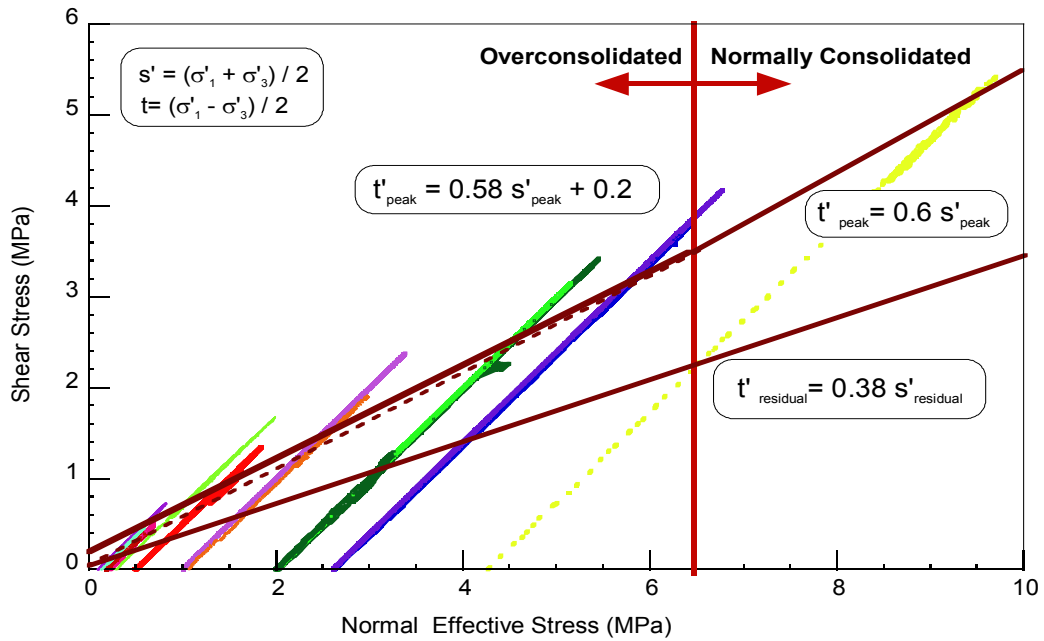


Figure 19. Clearwater Formation - Integrated interpretation of shear strength envelope

For direct shear testing, the parallel and normal to bedding plane test results fall within the upper and lower limit of triaxial shear strength results and the peak value of direct shear strength results match with the peak value of triaxial strength results at low mean effective stress zone. Moreover, the interpretation of a peak failure envelope suggests a bilinear envelope with a transition point between overconsolidated and normally consolidated states occurring around a normal effective stress of 6.5 MPa. This is in agreement with the preconsolidation stress calculated in “consolidation behavior” section in this paper. It should be noted that these are averaged results over the range of specimen depths used in this study. Conceptually, these results suggest that at effective stresses below approximately 6.5 MPa, anisotropy in shear strength normal and perpendicular to bedding may be an important component in the constitutive behavior of Clearwater Formation clay shale.

## **PERMEABILITY**

Permeability tests were conducted at different stages of triaxial tests, with different values of confining stress and OCR at maximum loading, before shearing, at peak, and after shearing for some samples, and before and after shearing for others. Drained triaxial compression tests with continuous permeability measurement were conducted at in situ conditions for all samples. The constant gradient or head method was used for all permeability measurements, following ASTM D5084. Both top and bottom pressures of the samples and the differential pressure across them were recorded and used to determine the permeability value. The data-logging system recorded for a period of time prior the tests and then close the by-pass valve that across the top and bottom drainage lines. In order to establish upward flow through the specimen, a constant differential fluid pressure,  $\Delta P$ , was set across the specimen by adjusting the upstream and downstream pumps. This differential pressure was maintained until a constant flow rate was established through the specimen. This technique was used for both initial, pre-shear permeability measurements as well as measurements during the shearing stages of the triaxial tests and at the end of the triaxial test. Very low strain rates (less than 0.5%/day) were utilized in triaxial tests where permeability measurements were made continuously during the loading of the specimen. Axial load, axial strain, pressure and volume change in both top and bottom pressure pumps, confining pressure, and differential values are

constantly recorded during shearing. In most tests, triaxial compression tests were completed once the specimens exceeded 10% axial strain.

Table 8 summarizes the fourteen permeability test results for Clearwater Formation specimens tested in this study. Figure 20 illustrates the relation between permeability and confining pressure. While the results show scatter, primarily due to inter-sample variability, the expected behavior of decreasing initial permeability with increasing confining pressure was found. The permeability variation during the shear stages of the tests is summarized in Figure 21. Figure 21 illustrates the average behavior over all specimens and shows average trend (red) and the minimum (green) and maximum (blue) trends to provide a measure of the variation in the results. Up to peak strength, the permeability of Clearwater shale samples increases by approximately 80%. This is attributed to microcrack development and the onset of volumetric dilation, as shown in Figure 15b, in the pre-peak region of the stress-strain behaviour of the highly overconsolidated specimens. With continued strain following peak strength, the permeability decreases. A comparison of Figures 22 and 23 shows that the structure of Sample A (OCR=1.3) is 'blockier' in appearance, with an idealized, aggregated configuration, while that of Sample B has a sharp, disorganized rough surface (OCR=5.2). This may be due to particle realignment as a result of the sample mineralogy (more clay fraction) and its microstructure under effective pressures experienced initially and the subsequent rapid inflow of pressures. Such realignment could initiate greater surface contact and cohesion between particles and a sharp appearance when the specimen is carefully broken apart. It would also change the microstructure of the material fabric, increasing resistance to flow and reducing the measured permeability. This reduction would likely be due to changes in the matrix pore structure occurring at elevated effective stresses, where aggregates are squeezed together so that flow paths becomes more complex and permeability reduces.

## **CONSOLIDATION BEHAVIOUR**

In normally consolidated samples, the present effective stress is the maximum stress to which the sample has been subjected in the past while in overconsolidated samples the present effective stress is less than that which the sample has experienced in the past. The maximum effective past stress is called the preconsolidation stress and the

overconsolidation ratio (OCR) is the ratio of preconsolidation stress and present effective stress. The overconsolidation ratio (OCR) quantifies the ductility or brittleness of the materials. High OCR correlates with brittleness and low OCR with ductility.

**Table 8. Summary of permeability tests results**

		Permeability, k (mD)			
		Max. Confining	Before Shear	At Peak	After Shear
Statistical Analyses	Number of Samples	6	14	6	14
	Maximum	0.0197	0.0228	0.0584	0.025
	Minimum	0.0013	0.0031	0.0103	0.0032
	<b>Average</b>	0.0115	0.015	0.028	0.012
	Standard deviation	0.0077	0.0085	0.021	0.009
	Percentage of Confidence	95%	95%	95%	95%
	Coefficient of Variation (%)	0.67	0.58	0.77	0.8
	Level of Significance (t0.05)	2.45	2.15	2.45	2.15
	Error of Mean (SX)	0.0031	0.003	0.011	0.004
	<b>Confidence Interval for Average (±)</b>	0.004	0.009	0.002	0.0034

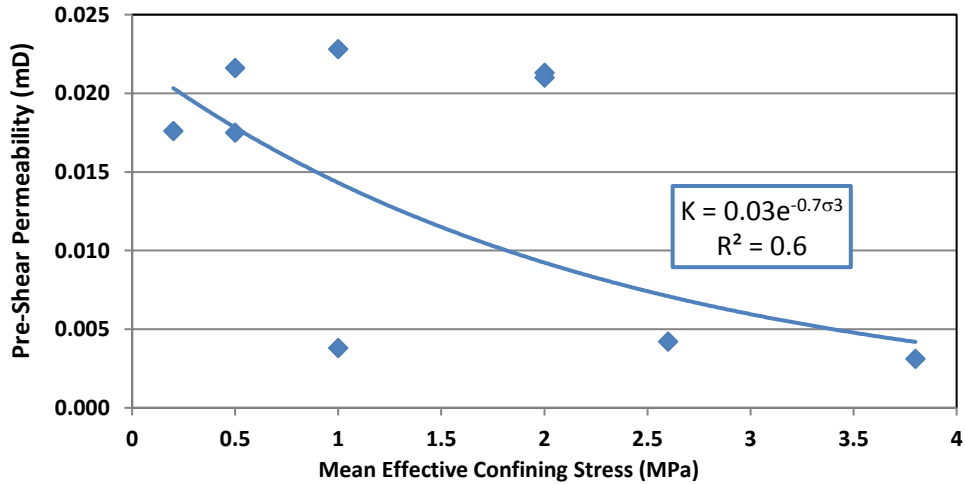


**Figure 20. Pre-shear variation of brine permeability for Clearwater triaxial specimens**

Magnitudes of the preconsolidation stress, compression index, swelling index, and coefficient of compressibility are generally results of one-dimensional consolidation tests (“oedometer tests”). The indices  $\lambda$  and  $\kappa$ , used for mathematical representation of the slope of normal consolidation and swelling lines, respectively, are determined by isotropic compression tests. These two indices are parameters required for the modified Cam Clay constitutive model (MCC) for fine-grained materials.

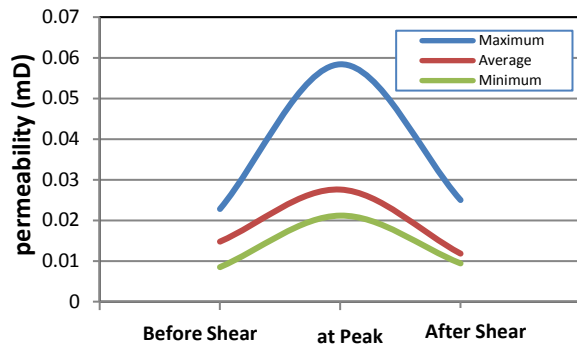


Figure 21. Variation of average brine permeability for Clearwater specimens during the triaxial test

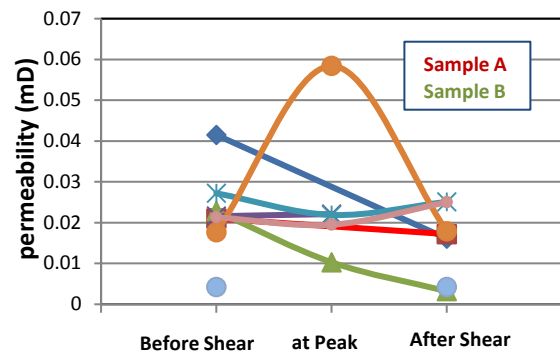
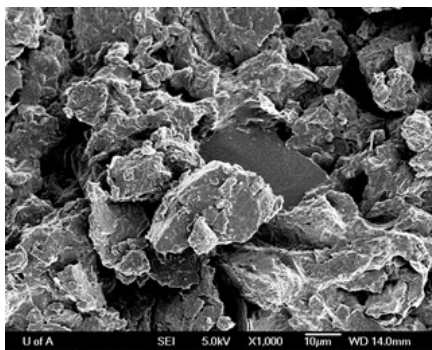
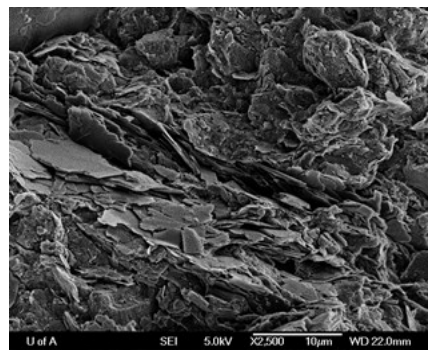


Figure 22. Variation of brine permeability for different Clearwater specimens during the triaxial test



Sample A



Sample B

Figure 23. Comparison of Scanning Electron Microscope (SEM) analysis of two Clearwater clay shale samples with different structures

Seven different tests were completed for evaluating parameters mentioned earlier (3 oedometer tests and 4 isotropic consolidation tests). Preconsolidation stress changed from 5 to 6.1 MPa, and average values of compression index ( $C_c$ ), swelling index ( $C_s$ ), and coefficient of compressibility ( $a_v$ ) are  $0.0764 \text{ (kPa}^{-1}\text{)}$ ,  $0.00545 \text{ (kPa}^{-1}\text{)}$ , and  $0.96 \times 10^{-6}$ , respectively. Table 9 compares the values of compression and swelling indices of different shales.

## SWELLING BEHAVIOUR

Clay and shale have been long known for their tendency to swell and soften when exposed to water. According to Mielenz and King (1955), two mechanisms that govern the swelling of soils are relaxation of effective compressive stress related to an enlargement of capillary films and osmotic imbibition of water by clay minerals that have an expansive

matrix. Swelling phenomena depends on the type of clay minerals (Boulding and Ginn, 2003) and confining pressure (Al-Shamrani and Al-Mhaidib, 2000). The montmorillonite group of silicate clays has the most dramatic shrink-swell capacity, illite has medium to low and, chlorite and kaolinite have low swelling capacity. Al-Shamrani and Al-Mhaidib (2000) performed a series of triaxial swelling tests and oedometer tests to study the vertical and volumetric swelling of compacted expansive soils. They observed that the swelling percentage of the sample decreases when confining pressure increases. Also, as the confining pressure increases, the ultimate volumetric changes due to swelling obtained from the triaxial tests decrease at the same rate as the ultimate vertical swelling measured in the oedometer tests.

To explore the effect of alteration the pore fluid on clay shale, seven swelling tests were performed according to ASTM D4546-03. Samples were consolidated at their in-situ stress condition then unloaded to different desired vertical effective stress levels (0.1, 0.5, 2, 2.1, 2.2, 2.5, and 5MPa) and their strain behavior were monitored during several days (12 -70 days). After samples preparation, filter papers, saturated sintered stainless-steel porous stones, and stainless-steel plate were placed on both ends of the samples and they were put into the confining stainless-steel specimen-ring inside the swelling cell. Stainless-steel ball, spacer, and LVDT were placed on the top of the samples and a seating load of 50 kPa has been applied on them. The swelling box was filled with brine fluid for back saturation of the sample. A data logger was used to record readings from load cell and LVDT. Axial loading has been applied incrementally to reach the in situ normal stress condition and at each increment, the sample consolidated till the vertical displacement was steady. The swelling stage started by draining all brine fluid from the sample and cell and then refilling with distilled water. Samples started swelling at in situ normal stress condition and vertical displacement was recorded. When the change of vertical deformation was negligible or steady, then the normal axial stress was decreased to the next stress level and this was continued until the original seating stress was reached. The whole unloading process was performed at several increments. At each increment, the swelling behavior was monitored. The swelling behaviors changed when the pore fluid was altered. As the vertical effective stress decreased, the swelling was enhanced. A particular stress level where the swelling behavior becomes significant was defined as “potential swelling pressure”.

The swelling behaviors of clay shale at different vertical effective stress are shown in Figure 24. It shows a drastic change as the vertical effective stress decreases below 100kPa, which corresponds to the potential swelling pressure” for these specimens. For the majority of the specimens reported in this study, only small amounts of swelling clay minerals (i.e. montmorillonite) were present, which correlates with the relatively small swelling pressure obtained for these specimens. For specimens having higher contents of swelling clay minerals, the swelling pressure can increase significantly. Wong (2001) showed that the Colorado shales in the Cold Lake region of northeastern Alberta, where the dominant clay mineral was mixed-layer smectite-illite (about 75% smectite and 25% illite layers), the swelling pressure of the shale varied between about 0.7 – 1.2 MPa.

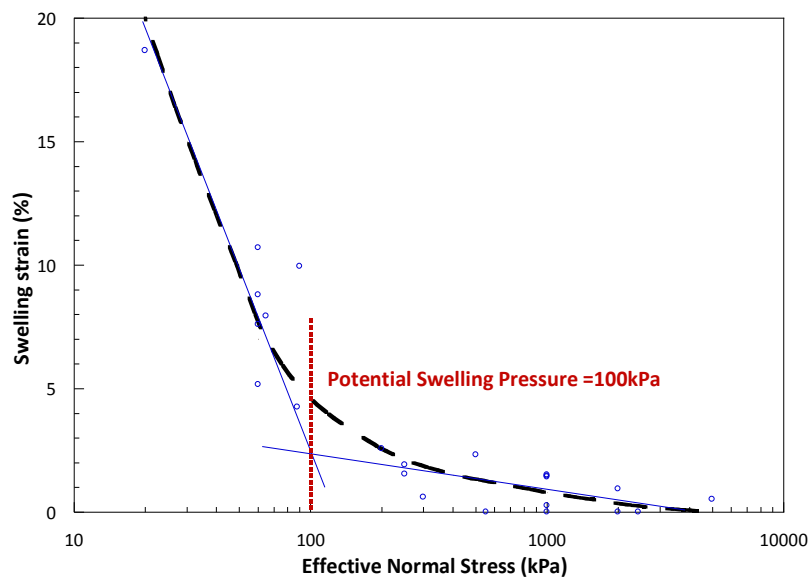


Figure 24. swelling behaviour of Clearwater clay shale

## MODIFIED CAM CLAY CONSTITUTIVE MODEL

The Modified Cam Clay (MCC) constitutive model introduced by Roscoe and Burland (1968) is widely referenced in solving problems in geotechnical engineering practice. It is one of the best matches for representing the geomechanical behavior of fine-grained materials with a significant amount of clay particles such as Clearwater clay shale (Gens and Potts (1988), Yu (1998), Potts and Zdravkovic (1999)).

This model was initially developed for the constitutive behavior expressing the deviation of void ratio  $e$  (volumetric strain  $\epsilon_v$ ) in term of the effective mean stress  $\sigma_m^{\text{eff}}$  in logarithmic

scale, as shown in Figure 25. The parameters mentioned in this Figure are described as follows:

$$\lambda^* = \frac{\lambda}{(1+e)} \quad (1)$$

$$\kappa^* = \frac{\kappa}{(1+e)} \quad (2)$$

$\kappa$  is the slope of swelling line,  $\lambda$  is the slope of NCL (normal consolidation line), and  $e$  is the current void ratio.

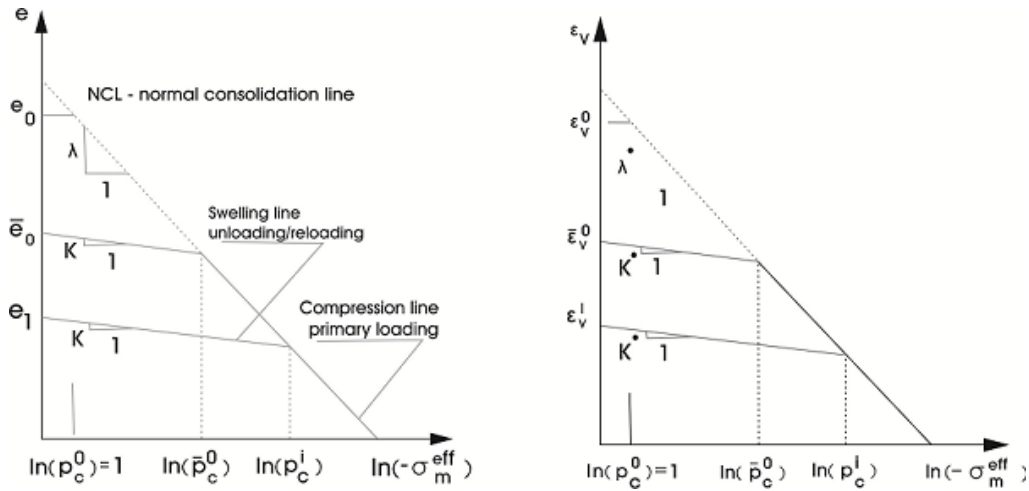


Figure 25. Elastic-plastic behaviour of material in isotropic compression and swelling

The combination of critical state line (CSL) and MCC model provides three different sides of this model, wet side, dry side, and on the CSL. Wet side allows a direct modelling of strain hardening for normally consolidated and lightly consolidated and dry side models strain softening for overconsolidated materials. On the CSL, the plastic volume change is zero, and there is no volume change. MCC Material loaded in shear can be plastically deformed without failure as shown in Figure 26 (Points 1 and 2 for hardening, Point 2 for softening) until it touches the critical state (Point 3 for hardening and Point 2 for softening). Then material deforms in shear under the plasticity theory without the change of  $e$  and  $\sigma_m^{eff}$ . Expansion of the yield surface (hardening/softening) is driven by the recent pre-consolidation pressure  $P_c$ :

$$P_c^{i+1} = P_c^i \exp \left[ \frac{-\Delta \varepsilon_v^{pl}}{\lambda^* - \kappa^*} \right] \quad (3)$$

Where  $P_c^{i+1}$  is current pre-consolidation pressure,  $\Delta \varepsilon_v^{pl}$  is an increment of volumetric plastic strain, and  $e$  is the current void ratio. Apart from parameters  $\kappa$  and  $\lambda$ , and the

Poisson's ratio, the MCC model requires specifying the following three parameters:  $M_{cs}$  (slope of the critical state line), OCR (over-consolidation ratio), and  $e_0$  (initial void ratio). MCC constitutive model used to simulate the clay shale behaviour in this study and the material's constants  $M$ ,  $\lambda$ , and  $\kappa$  are input parameters to be optimized for calibrating the MCC model. All the parameters can be derived from the laboratory tests such as triaxial compression and isotropic consolidation tests as a conventional way of estimation.

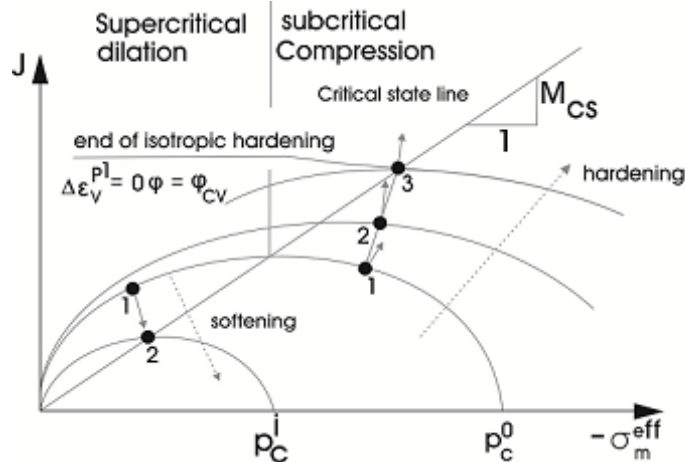


Figure 26. Yield curves as predicted from Cam-Clay constitutive model

Table 10 shows the values of  $\lambda$  (the slope of NCL (normal consolidation line) [ $\text{kPa}^{-1}$ ]) and  $\kappa$  (the slope of swelling line [ $\text{kPa}^{-1}$ ]) calculated from isotropic consolidation curves. Samples were confined isotropically with load/reload phase up to a maximum mean effective stress. Volume and corresponding effective confining stresses were recorded.

Table 9. Summary of values of compression and swelling indices of different shales

Formation	$C_c(\text{kPa}^{-1})$	$C_s(\text{kPa}^{-1})$	Reference
Bearpaw, Canada	0.1-0.14	0.03-0.1	Ringheim (1964), and Peterson (1958)
Taylor	0.05-0.11	0.01-0.07	Cuenca (1988), and Olson (1990)
Bearpaw, USA	0.11-0.14	0.02-0.05	Fleming et al. (1970)
Pierre	0.2-0.37	0.06-0.09	
Claggett	0.07-0.17	0.02-0.16	
Colorado	0.1	0.03-0.08	
Eagle Ford	0.08-0.12	0.02-0.07	Olson (1990)
Clearwater	0.065-0.088	0.002-0.008	

For clay materials, an isotropic consolidation diagram is usually plotted as specific volume against natural logarithm of effective stress as it shows in Figure 27. Since specific volume and void ratio are related ( $v=1+e$ ), it does not affect the calculation of the material constants ( $\lambda$  and  $\kappa$ ). Two further parameters are required to define the position of the normal consolidation and typical swelling lines. For the  $\lambda$ -line,  $N$  should be defined as the

specific volume of a normally consolidated material at  $P'=1$  kPa, thus the  $\lambda$ -line equation for Clearwater shale is:

$$v = N - \lambda \ln P' \quad \rightarrow \quad v = 2 - 0.077 \ln P' \quad \text{OR} \quad e = 1 - 0.077 \ln P' \quad (4)$$

The position of the  $\kappa$ -line is not unique, but depends on  $P'_m$ , the maximum previous stress.

The  $\kappa$ -line equation is:

$$v = v_\kappa - \kappa \ln P' \quad \rightarrow \quad v = v_\kappa - 0.038 \ln P' \quad \text{OR} \quad e = e_\kappa - 0.038 \ln P' \quad (5)$$

$\lambda$ ,  $N$ , and  $\kappa$  are regarded as soil constants. Their values will depend on the particular material.

Table 10. Isotropic compression test results for Clearwater shale

Test No.	Slope of $\lambda$ - and $\kappa$ - lines			
	$\lambda$	$\kappa$ (First rebound)	$\kappa$ (Second rebound)	$\kappa$ (Third rebound)
1	0.07	0.025	—	—
2	0.089	0.055	0.051	0.041
3	0.041	0.034	0.032	—
4	0.073	0.028	0.028	0.021

## THE CRITICAL STATE LINE (CSL) AND YIELD SURFACE

The concept of critical state line originates from the observation that all of the failures of clay material samples which were initially isotropically compressed and then loaded in drained or undrained triaxial compression tests define a single straight line through the origin in  $q$  versus  $p$  space, and a single curved line in  $v$  versus  $p$  space, whose shape is similar to the normal consolidation line.

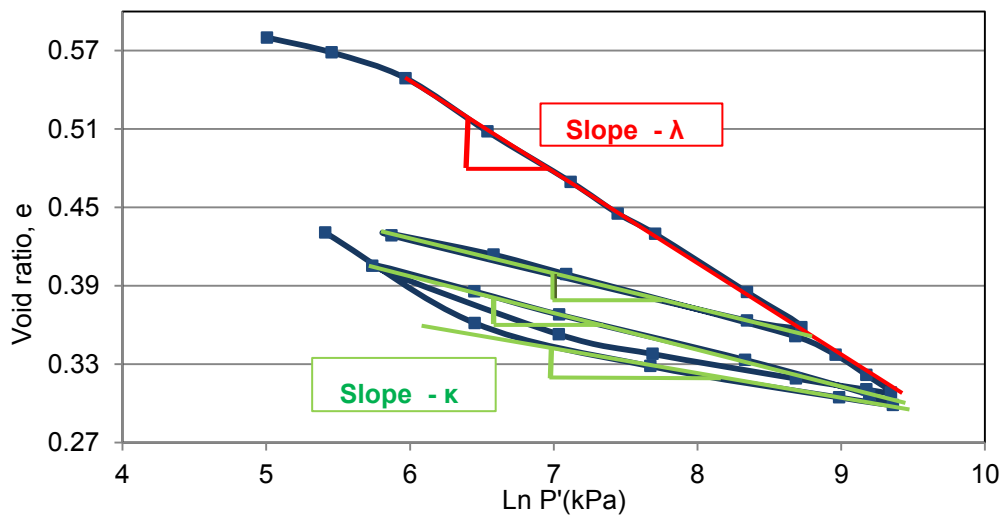


Figure 27. Isotropic compression test results for Clearwater clay shale sample

This single, unique line of the failure points of both drained and undrained tests is defined as the critical state line. Failure is manifested as a state at which large shear distortions occur with no changes in stress or specific volume (void ratio). The projection of the critical state line onto the q versus p plane is described by:

$$q = M p' \tag{6}$$

Figure 28 illustrate  $p'$ - $q$  curves for all drained, and undrained tested samples discussed earlier in shear parameters section. The slope of the critical state line is  $50^\circ$ . Consequently,  $M=1.2$ .

In Table 11, the values of material constants ( $M$ ,  $\lambda$ ,  $N$ , and  $\kappa$ ) of different clays have been compared. The concepts of yield and the state boundary surface included in critical state soil mechanics (CSSM) are often thought to be useful in engineering primarily because they define stress states where loading can take place with relatively little strain occurring, and differentiate those states from ones where irrecoverable large strains occur for natural soils and weak rocks. In fact, the area within the limit state curve defines the zone in which behaviour is elastic.

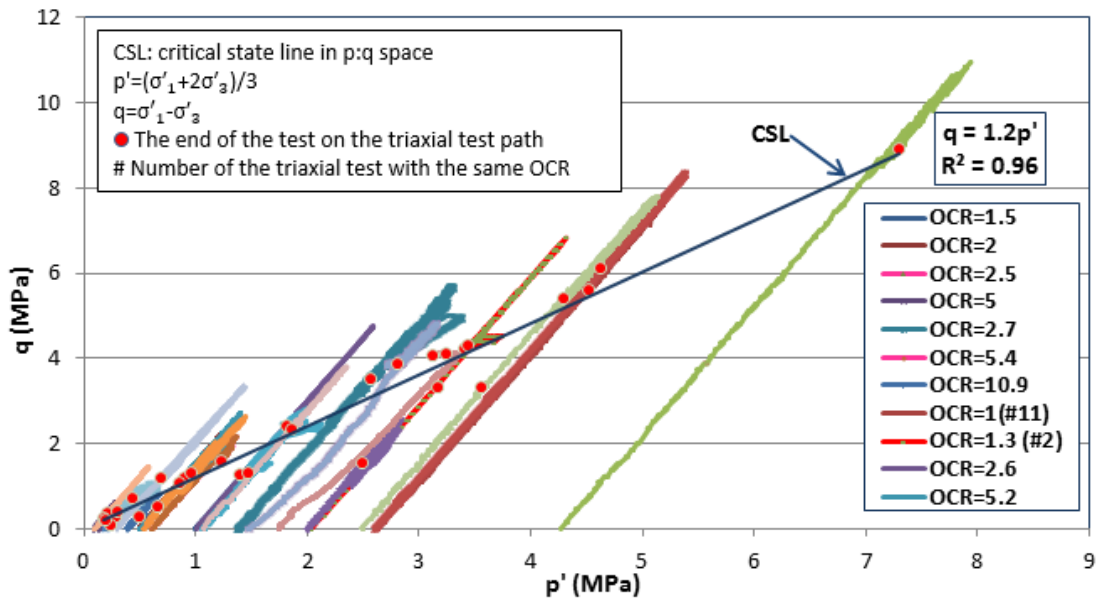


Figure 28. Effective stress path during drained shearing of Clearwater shale for different consolidation stresses and critical state line

When the stress path hits the limit state, it is associated with the development of plastic strains. The plastic strain increments are assumed to be perpendicular to the yield or limit state curve. Figure 27 shows the normalized limit state curves for Clearwater clay shale samples. The  $p'$ - $q$  curves are normalized by  $p'_o$ , the maximum mean pressure.

$$p'_o = \frac{1}{M^2 \times p'} q^2 + M^2 p^2 \quad (7)$$

According to Figure 29, the shapes of the limit state curves of Clearwater clay shales are influenced by the stress ratio prevalent during normal compression. This implies the concept of “kinematic hardening” discussed by Leroueil (1997). He mentioned:” *The fact that the shape of limit state curves depends on effective stress history implies that it evolves depending on the effective stress path followed. This is called kinematic hardening. For natural clay loaded under one-dimensional compression in the normally consolidated range, the shape would remain essentially the same; on the other hand, under an isotropic loading in the normally consolidated range, the shape of the limit state curve would progressively evolve from its shape to a shape corresponding to an isotropic material.*”

**Table 11. Summary of values of soil constants of different Clays**

	Weald Clay	Kaolin	London Clay	Chicago Clay	Clearwater Clay
<b>M</b>	1.2-0.8 (0.95)	1.2-0.8 (1.02)	1-0.6 (0.9)	1.02	1.2
<b>λ</b>	0.2-0.04 (0.093)	0.3-0.1 (0.26)	0.3-0.04 (0.16)	0.08	0.041-0.086 (0.08)
<b>κ</b>	0.04-0.01 (0.035)	0.06-0.03 (0.05)	0.05-0.01 (0.062)	0.019	0.021-0.055 (0.038)
<b>N</b>	2.2-1.8 (2.06)	3.9-3.5 (3.75)	3-2.6 (2.83)	-	2
<b>Reference</b>	<b>Atkinson, Bransby (1978) and Navarro et al. (2007)</b>		<b>Finno et al. (2002)</b>		

The complete state boundary surface consists of the Roscoe, Hvorslev, and tension cut-off surfaces. The first two surfaces meet at the critical state line. The geometry of the Roscoe surface is such that all constant  $v$  sections should be scaled to a single curve if the stresses ( $p'$ - $q$ ) are divided by the equivalent pressure  $p'_e$ , which is the mean normal effective stress on the normal consolidation line at that specific volume.

$$p'_e = \exp\left[\frac{N-v}{\lambda}\right] \quad (8)$$

The Roscoe surface represents the state boundary for normally consolidated to lightly overconsolidated samples. Normalizing the stresses ( $p'$ - $q$ ) by  $p'_e$  for heavily overconsolidated samples, all data lie on a single line space called the Hvorslev space.

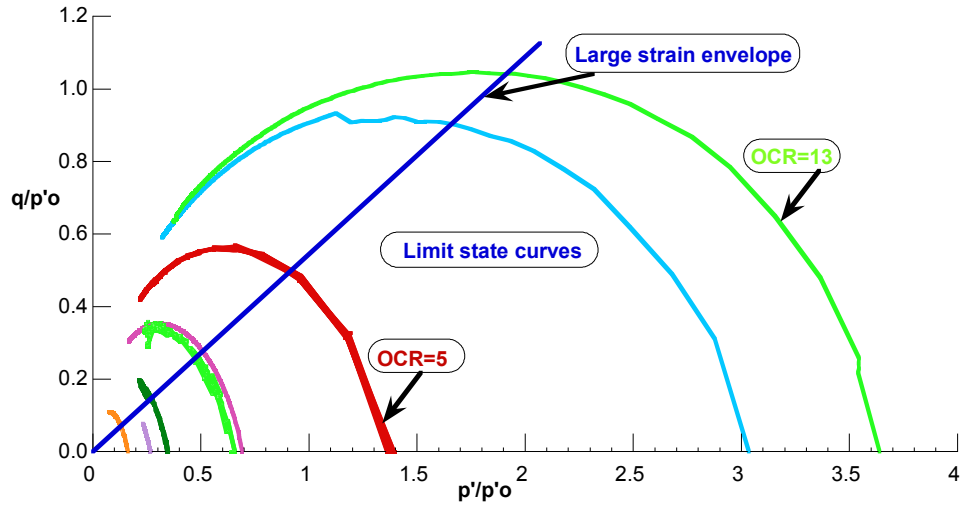


Figure 29. Limit state curves of Clearwater clay shales, for large strain envelope ( $\phi'$  line),  $\phi'=31^\circ$

This line is limited on its right end by the critical state line at the top edge of the Roscoe surface, and on its left end by the tension cut-off line corresponding to the highest value of  $q'/p'$  or tensile failure. Figure 30 summarizes the locus of failure points for Clearwater clay shale. Hence, the complete state boundary surface covers a wide range of behaviours.

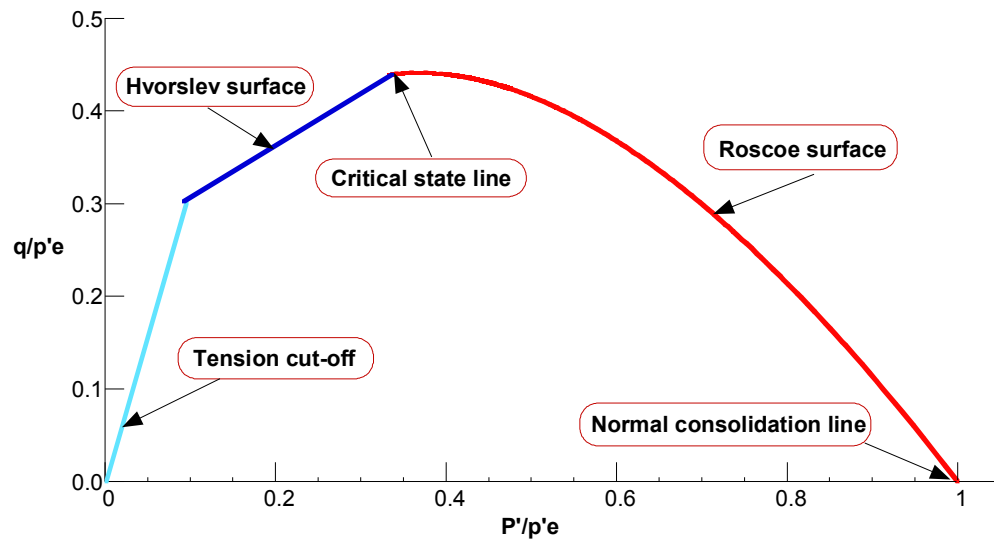


Figure 30. The complete state boundary surface in  $q'/p'_e$  versus  $P'/p'_e$  space

## DISCUSSION

Clearwater clay shales are widely distributed throughout northeastern Alberta and are treated in different enhanced oil recovery projects as caprock. The mineralogy and geotechnical properties of several samples were analyzed to better classify them for engineering purposes. In general, clay shales with higher water content and higher Atterberg limits yield lower strength. Figure 31 shows that Clearwater clay shale is categorized as a high-plasticity material among the various shale formations in western Canada.

From a stress-strain behaviour point of view (Figure 15), the maximum rate of dilatancy occurs immediately after the peak in normally consolidated samples. For lightly overconsolidated samples, a strain softening behaviour is associated with either dilatancy or collapse of the interparticle bonds. Even for high axial strains (10 to 15%), a critical state is likely not reached and volumetric strains are not stabilized. Samples with high OCR show ductile behaviour and low OCR samples indicate brittleness. The bilinear effective stress failure envelope for normally consolidated and overconsolidated samples has been introduced. Moreover, a composite integrated failure envelope for this material was developed.

The direct shear test results conducted parallel to the bedding plane show the peak and residual friction angles for clay shale as 26 and 20 degree with coefficient of regression equal 88% and 82% respectively. El-Ramly (2001) conducted a statistical analysis on the same parameters on 82 specimens of Kc1 depositional unit specifically. The values of the mentioned parameters are reported 19 and 8 degree correspondingly. The reasons for this difference can be related to: 1) the different effective normal stress which was up to 1000 kPa in his study and 4000 kPa in current study and also 2) the specific depositional unit has been considered in his study. Moreover, the scatter of data around the mean trend indicated the high uncertainty in the value of the residual friction angle in his study. Clearwater clay shale is categorized as very low permeable to impermeable material, with average permeability of 0.015 mD. Changes in permeability during the shearing test were monitored. Past effective stresses and current pressure can impact the structure and permeability behaviour of samples. The micro-fabric and microstructure of the samples as well as their mineralogy can effect on their hydro-geomechanical properties as discussed.

It has introduced the critical state line and the complete state boundary surface for this material. State boundary surface indicates the elastic-plastic boundary, which shows the possible and impossible state for a sample. It has been shown that with increasing the OCR during isotropic consolidation, the strength of the material increases thus it leads to a bigger limit state curve.

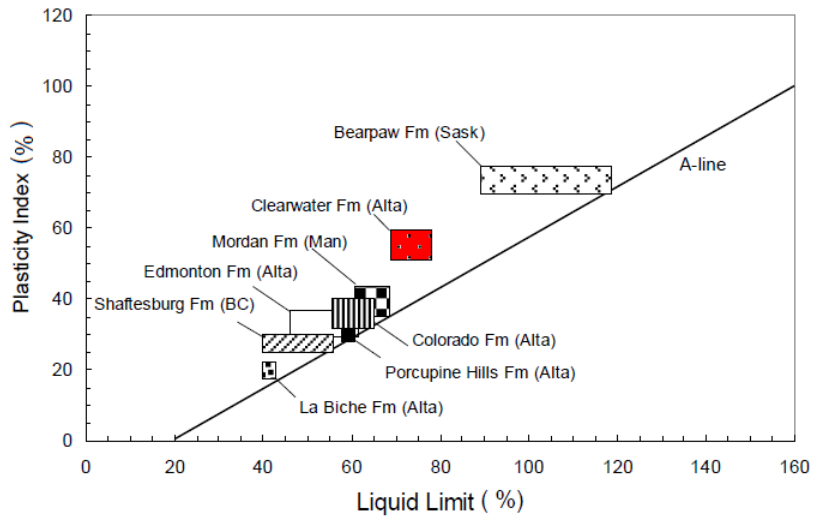


Figure 31. Plasticity of various formations in western Canada (Modified from Wong (1998))

The modified cam clay parameters calculated through these parameters must be calibrated with the triaxial tests, using the inverse method to get the unique set of data. However, this is out of the scope of this study, and will be analyzed and discussed in different papers by the same authors.

## **JOLI FOU CLAY SHALE FORMATION**

Because of the paucity of laboratory data from this formation, the index parameters have been extracted from available reports. One one-dimensional consolidation test has been conducted to extract Cam-Clay constitutive parameters. Results have been calibrated using inverse analyses as will be discussed in the following section.

### **CALIBRATION OF MODIFIED CAM CLAY (MCC) MODEL USING INVERSE ANALYSIS FOR JOLI FOU CLAY SHALE FORMATION<sup>3</sup>**

Abstract: The identification of reliable constitutive model properties used in numerical modelling is often a challenging task. The response of a model to geotechnical actions is defined by the characteristics of the model and the values of its input parameters. Significant challenges are involved in estimating a model's input parameters from the experiments or field data especially when an unacceptable number of experiments are available. Soil models are calibrated using trial-and-error methods, and the accuracy of the conformity between the observational data from experiments and the numerically simulated results is rarely quantitatively evaluated. Inverse analysis techniques were used for developing optimized constitutive model parameters based on experimental data in this paper. The problem is solved with the minimization algorithm based on a gradient method to calibrate the modified cam clay (MCC) parameters extracted from the only oedometer test available and using compression triaxial tests for Joli Fou clay shale samples. The coupling of finite difference code (FLAC) and the optimization algorithm code (UCODE) have been used for calibrating the material's constitutive model.

## **INTRODUCTION**

To simulate material response under complex loading conditions, the constitutive models typically include a large number of parameters. Experimental data sets (field and laboratory) are becoming available for calibration of such constitutive models. Thus, a challenging task is to potentially calibrate some model parameters to satisfactorily match with many data sets simultaneously. Calibration means an evaluation of appropriate values for parameters so that, possibly, the simulated stress-strain relationship of material is consistent with the behavior observed in field or laboratory test. The

---

<sup>3</sup> A version of this section has been submitted to "Computers and Geosciences"

calibration effort can be facilitated by optimization techniques. An optimization procedure systematically searches for a set of model parameters that can simultaneously minimize the difference between a large number of experimental records and the corresponding model simulation results. In simple cases, closed-form solutions to an optimization problem may use so that an optimized set of parameters can be obtained analytically. In more general cases, one has to apply a numerical optimization algorithm. Efforts have been reported in a development of efficient optimization algorithms (DeNatale (1983), Abifadel et al. (1988), Anandarajah et al. (1991), Mattsson et al. (2001), Calvello (2002), Bayoumi (2006)).

In this paper, the calibration of constitutive models is formally handled as an inverse problem. Inverse analysis techniques are powerful tools to improve the conventional observational methods in which monitored data during the first phase of geotechnical engineering projects is used to evaluate the performance of the system for next phases (Keidser and Rosjberg (1991), Ou (1994), Poeter and Hill (1997), Finno and Calvello (2005), Lecampion and Contantinescu (2005)). This quantitative method is used to calibrate modified Cam-Clay (MCC) parameters for the results of drained triaxial compression tests on specimens of Joli Fou clay shale. This approach couples the finite difference code FLAC (Itasca) and the inverse analysis algorithm UCODE (Poeter and Hill 2005) to minimize the differences between computations of stress-strain response and experimental data.

## **INVERSE ANALYSES**

There are two main types of inverse analysis to geotechnical engineering projects; one is optimization by techniques from the field of artificial intelligence, consist of artificial neural networks (Yamagami et al. (1997), Hashash et al. (2006)) or genetic algorithms (Pal et al. (1996), Samarajiva et al. (2005), Levasseur et al. (2007)) and the other one is optimization by iterative algorithms such as gradient methods. These methods are unique by their approach. The artificial neural network is a method that creates by learning phases its constitutive law from geotechnical measurements. Genetic algorithms are global optimization methods, which localize an optimum set of solutions close to the “true” value. The gradient method is a local parameter identification of a specific constitutive law (Hill (1998)).

The classical resolution of a mechanical problem includes the response of mechanical system (R) (to be determined) as a function of (1) its constitutive model (M) and the constitutive model parameters (P), and (2) the action subjected to the system (S), both as known. In contrast, the inverse analysis uses mechanical response provided by experimental data to reconstitute the unknown characteristics of materials using iterative computations that progressively minimize the difference between the experimental data and the simulated ones. Figure 32 shows the definition and identification of an inverse process.

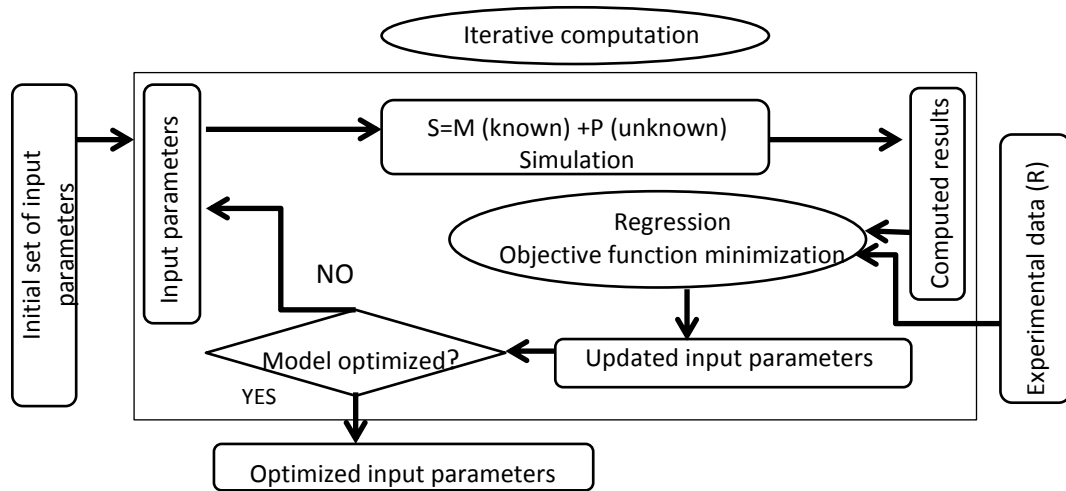


Figure 32. Definition of an inverse process

## GRADIENT METHOD

A gradient algorithm based on the Gauss-Newton's method as available in the program UCODE (Poeter and Hill (2005)) was used in this study. Given models are calibrated by changing input parameters iteratively till the minimum of weighted least-squares objective function is accomplished with respect to the parameter values using a modified Gauss-Newton method or a double-dogleg technique.

UCODE is a universal inverse code for sensitivity analysis, calibration and uncertainty evaluation that has two exclusive attributes. It can be used with any mathematically based models that have numerical ASCII input/output files, and it includes instructive statistics to assess the importance of observations to parameters and the importance of the latter to predictions. All required models are run from a single batch file or script, and simulated values are continuous functions of the parameters values. Thus the observations and simulated equivalents can be compared. Figure 33 shows the inverse analysis algorithm

coupling FLAC and UCODE schematically. Usually, the numerical optimization algorithm of constitutive model parameters consists of the following steps:

1. Material testing that provides experimental data.
2. Providing an initial guess of material parameters.
3. Carrying out a numerical simulation that represents the experiment.
4. Evaluating the magnitude of an objective function, that is, a measure of discrepancy between numerical response and experimental data.
5. Updating the initial guess of parameters using a gradient-based minimization technique if the objective function exceeds a user-specified tolerance (return to step 3 unless the convergence of optimization is achieved).

The weighted least-squares objective function  $S(\underline{b})$  is expressed as:

$$S(\underline{b}) = [\underline{y} - \underline{y}'(\underline{b})]^T \underline{\omega} [\underline{y} - \underline{y}'(\underline{b})] = \underline{e}^T \underline{\omega} \underline{e} \quad (9)$$

where  $\underline{b}$  is a vector containing values of the parameters to be estimated;  $\underline{y}$  is the vector of the observations being matched by the regression;  $\underline{y}'(\underline{b})$  is the vector of the computed values which correspond to observations;  $\underline{\omega}$  is the weight matrix; and  $\underline{e}$  is the vector of residuals. This function represents a quantitative measure of the accuracy of the predictions.

In the inverse procedure, a sensitivity matrix  $\underline{X}$  is computed using a forward difference approximation based on the changes in the computed solution due to slight perturbations of the estimated parameter values. Regression analysis of this non-linear problem is used to find the values of the parameters that result in the best fit between the computed and observed values. This fitting is accomplished with the Gauss-Newton method modified by the addition of a damping parameter and a Marquardt parameter (Hill, 1998).

The normal equations and the iterative process for the modified Gauss-Newton optimization method can be expressed as:

$$(\underline{C}^T \underline{X}_r^T \underline{\omega} \underline{X}_r \underline{C} + \underline{I} m_r) \underline{C}^{-1} \underline{d}_r = \underline{C}^T \underline{X}_r^T \underline{\omega} (\underline{y} - \underline{y}'(\underline{b})) \quad (10)$$

$$\underline{b}_{r+1} = \rho_r \underline{d}_r + \underline{b}_r \quad (11)$$

Where  $r$  is the parameter estimation number;  $\underline{X}_r$  is the sensitivity matrix evaluated at parameter estimates  $\underline{b}_r$  calculated using forward or central differences is equal to:

$$X_{ij} = \partial y_i / \partial b_j \quad (12)$$

$\omega$  is the weight matrix;  $\underline{X}_r^T \omega \underline{X}_r$  is a symmetric, square matrix of NP by NP dimensions (NP is the number of parameters to optimize);  $\underline{C}$  is a diagonal scaling matrix expressed as:

$$C_{ij} = [(\underline{X}_r^T \omega \underline{X}_r)_{ij}]^{(-\frac{1}{2})} \quad (13)$$

$\underline{C}$  produces a scaled matrix with the smallest possible condition number (Forsythe and Strauss (1955), Hill 1998);  $\underline{d}_r$  is a vector with the number of elements equal to the number of estimated parameters, and it is used to update parameter estimates;  $\underline{I}$  is an NP dimensional identity matrix;  $m_r$  is the Marquardt parameter (Marquardt 1963); and  $\rho_r$  is a damping parameter.

Non-linear regression begins with the initially estimated parameter values and ends when one of the convergence criteria has been met. The model is optimized if either the maximum parameter change of a given iteration is less than a user-defined percentage of the value of the parameter at the previous iteration, or the objective function changes less than a user-defined amount for three consecutive iterations.

## NUMERICAL SIMULATION OF TRIAXIAL TESTS

Four drained triaxial tests (samples 1, 2, 3, 5) were chosen to use for simulation as providing the computational points, and one drained triaxial test (sample 4) was chosen to use for verification. Figure 34, schematically, shows the cylindrical specimen modelled as an axisymmetric slice. Triaxial tests simulated under ideal boundary conditions such as frictionless top and bottom platens, which create a homogeneous stress field within the specimen. Therefore, the distribution of stress and strain is identical over the entire specimen. Consequently, any point could represent the stress and strain state in the specimen. Table 12 summarizes the properties and characteristic of the modelled samples. The specimens were isotropically consolidated at different consolidation pressure and then sheared until failure. To evaluate the match between observations from laboratory tests and simulated equivalents from numerical modelling, deviatoric stress curves were digitized from report files and used to calibrate the objective function for the models. Stress- strain curves of the tests were discretized by considering one observation point every 0.5% axial strain up to the maximum of 6%. Given strain levels attained in the tests, UCODE used a total of 48 observation points to calibrate. Calvello (2002) showed that this amount of a number of observation points was sufficient to calibrate the responses.

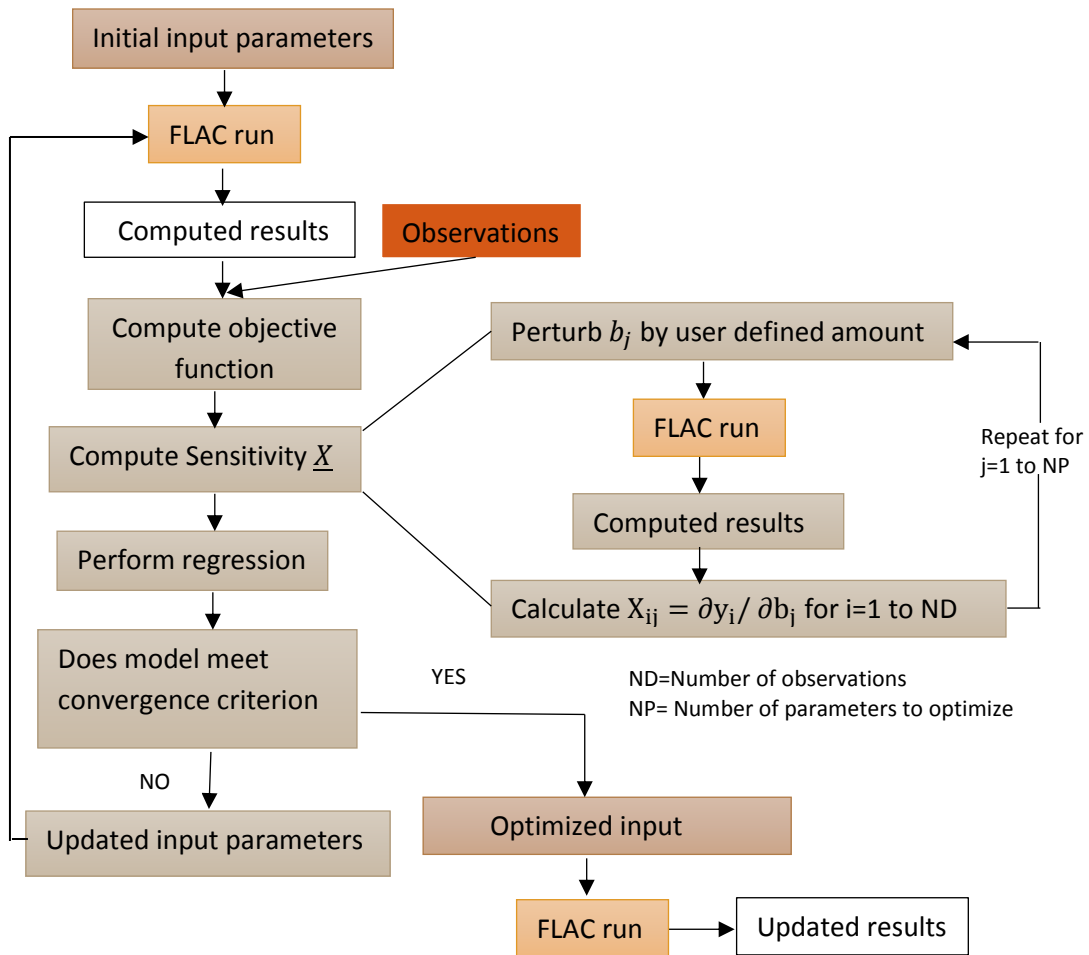


**Figure 33. Inverse analysis coupling UCODE and FLAC**

Modified cam clay model is defined by stress invariants ( $p'$ ,  $q$ ), specific volume or void ratio, and three material's constants  $M$ ,  $\lambda$ , and  $\kappa$  which need to be calibrated. The initial estimation of the material's constants based on the result from one oedometer test conducted on Joli Fou clay shale sample were  $\lambda=0.032$  ( $C_c=0.073$ ),  $\kappa = 0.0022$  ( $C_s=0.005$ ),  $M=0.8$ , the initial void ratio has been considered as 0.49, and the void ratio at reference pressure was equal to 0.91.

### CALIBRATION SCHEME AND INPUT PARAMETERS STATISTICS

Calibrated model is estimated by considering the magnitude of the weighted and un-weighted residuals and their distribution. Different quantities can evaluate the calibrated model. Although the value of the objective function (Eq. (9)) designate calibrated model by the indication of the difference between an optimized model and initial simulation, the

model error variance is a usual indicator of the overall magnitude of the weighted residuals.

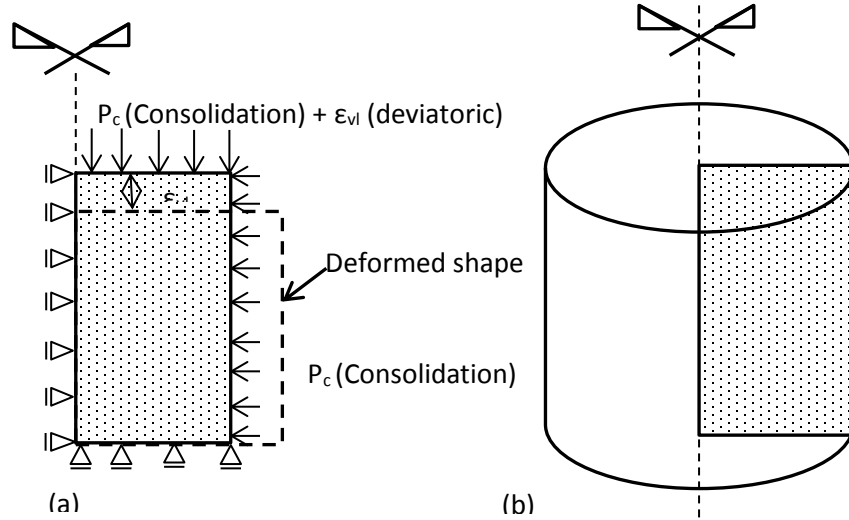


Figure 34. Triaxial test simulation (a) Geometry, boundary conditions and loading, (b) Finite difference mesh

Table 12. Description of the modeled samples

	Orientation	Depth (m)	Diameter (cm)	Length (cm)	P <sub>c</sub> (MPa)	Loading strain rate	Density (g/cm <sup>3</sup> )
LKC1-1	Vertical	383.16	2.54	5.08	5.17	1e-5/s	2.143
LKC1-2	Vertical	383.16	2.54	5.08	4.13	1e-5/s	2.110
LKC1-3	Vertical	383.16	2.54	4.445	3.10	1e-5/s	2.119
LKC1-4	Horizontal	383.16	2.54	5.08	4.13	1e-5/s	2.066
LKC1-5	45 Degree	383.16	2.54	5.08	4.13	1e-5/s	2.111

This parameter expresses as:

$$s^2 = \frac{S(\underline{b})}{ND - NP} \quad (14)$$

Where  $S(\underline{b})$  is the objective function; ND is the number of observations, and NP is the number of estimated parameters.

Different quantities can be used to evaluate the sensitivity of the predictions to parameters changes. In this study, composite scaled sensitivities,  $c_{SS_j}$ , is used since this parameter designates the total amount of statistics provided by the observations for the estimation of one parameter. This sensitivity is defined by:

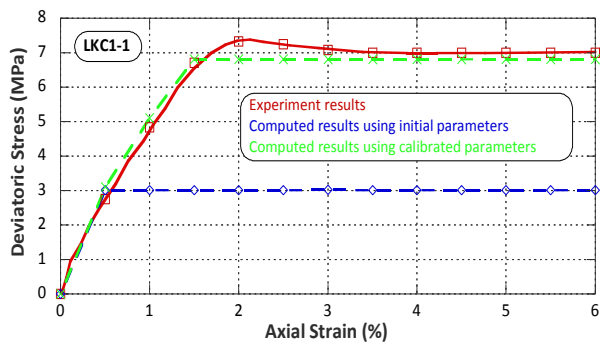
$$c_{SS_j} = \left[ \frac{\sum_{i=1}^{ND} \left( \frac{\partial y_i}{\partial b_j} \right) b_j \omega_{ii}^{1/2}}{ND} \right]^2 \Big|_{\underline{b}} \quad (15)$$

Where  $y'_i$  is the  $i^{\text{th}}$  simulated value;  $y_i/b_j$  is the sensitivity of the  $i^{\text{th}}$  simulated value with respect to the  $j^{\text{th}}$  parameter;  $b_j$  is the  $j^{\text{th}}$  estimated parameter;  $\omega_{ji}$  is the weight of the  $i^{\text{th}}$  observation. The weights assigned to the observations are an important part of the regression analysis because the regression results have been affected by them. UCODE uses a diagonal weight matrix in which the weight of every observation,  $\omega_{ii}$ , is equal to the inverse of its error variance,  $\sigma^2$  (Hill (1998)).

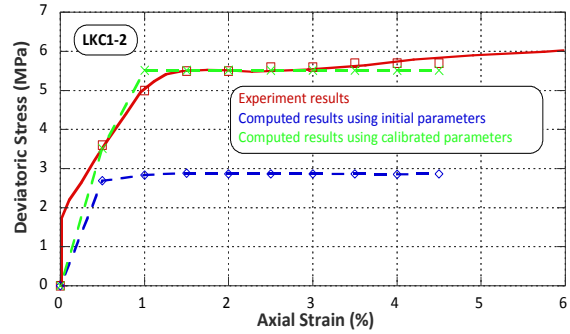
## ANALYSES AND DISCUSSION

Figure 35 shows the comparison between stress-strain curves from experiment results and numerical results for two different cases (1) initial values and (2) calibrated values of parameters under study. The magnitude of these parameters before and after calibration and their statistic parameters are summarized in Table 13. The computed results match the overall experiment results fairly well.

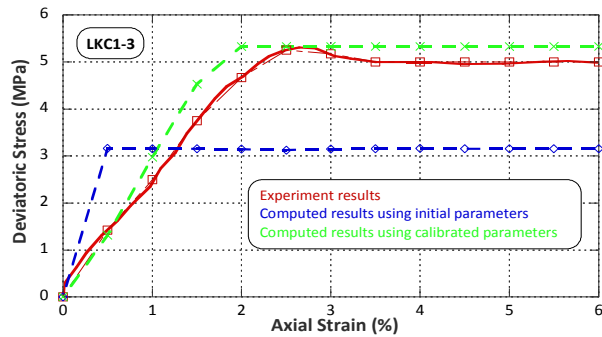
Three quantitative indicators used to evaluate the calibrated model- weighted least-squares objective function (Eq. 10), error variance (Eq. 14), and composite scaled sensitivity (Eq. 15) - show in Figures 36, 37, and 38 respectively with both initial and calibrated input parameters. A noticeable decrease in the values of both objective function and error variance show the better fit to the observational points and improvement of the match between the computed results and experimental data. According to Hill (1998), the absolute value of error variance is a better indicator to show whether the fit achieved by regression is consistent with the data accuracy than the objective function. UCODE uses composite scaled sensitivity to evaluate the importance of different parameters to the response of the system.  $M$  and  $\lambda$  are the parameters that have the substantial effect on simulation results and it can be justified by the fact that during isotropic compression phase of triaxial test, specimens have been reconsolidated to the stresses greater than or equal to the field value of vertical effective stress which is 4.5 MPa (considering the gradient of vertical stress as 20.7 kPa/m), if the preconsolidation pressure has been ignored and assume that the samples are normally consolidated as the behavior of the samples shows from laboratory results, this implies that stress at shearing phase of the test would be very close to the yield, thus the parameters associated with plastic behavior would affect most.



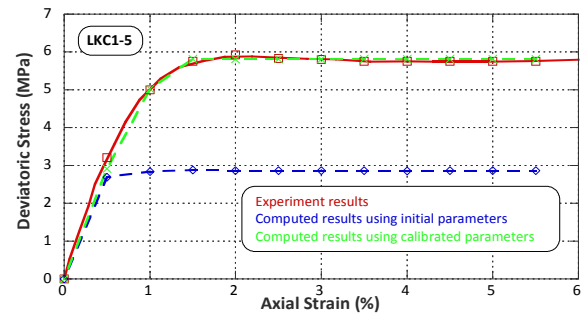
(a) Stress-Strain curve of drained triaxial test for LKC1-1



(b) Stress-Strain curve of drained triaxial test for LKC1-2



(c) Stress-Strain curve of drained triaxial test for LKC1-3



(d) Stress-Strain curve of drained triaxial test for LKC1-5

Figure 35. Stress- Strain curves for drained triaxial tests, comparison between laboratory results and simulated results using initial value of parameters and calibrated ones

Table 13. Initial and calibrated input parameters

Parameters	Initial Values	Calibrated Values
M	0.8	1
$\lambda$	0.032	0.055
$\kappa$	0.0022	0.0035
Correlation Coefficient (%)	36	87

## VERIFICATION AND VALIDATION OF THE PROCEDURE

The previous section, a methodology has been applied to evaluate the best set of clay shale parameters with the data available for further analyses. The final results need to be verified to confirm whether they are reliable and correctly implemented. Validation checks the accuracy of the results. For those purposes, sample LKC1-4 has been modelled using the calibrated parameters and the results show in figure 39 comparing with the laboratory results. It implies that the computed results have a fairly good match with the experimental results. Simulation models are approximate replications of real-world

systems, and they would never exactly imitate it. Thus the calibrated set of parameters is significantly satisfactory as the best fit of MCC input parameters.

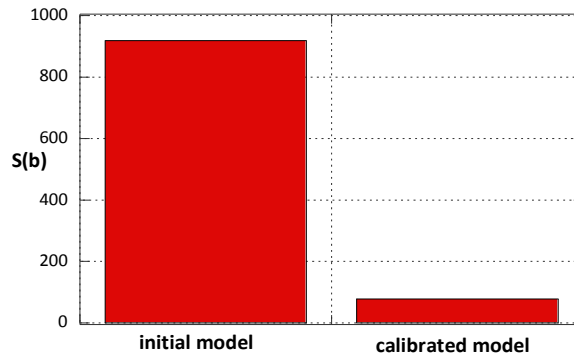


Figure 36. Least square objective function for initial and calibrated models

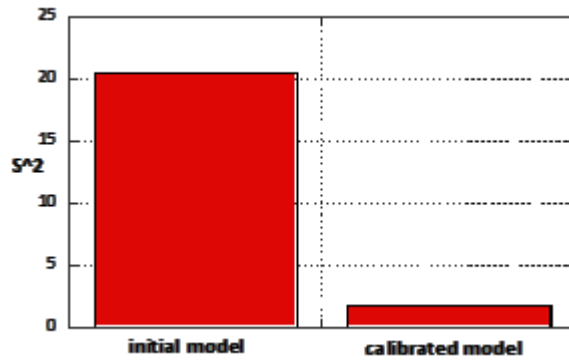


Figure 37. Error variance for initial and calibrated models

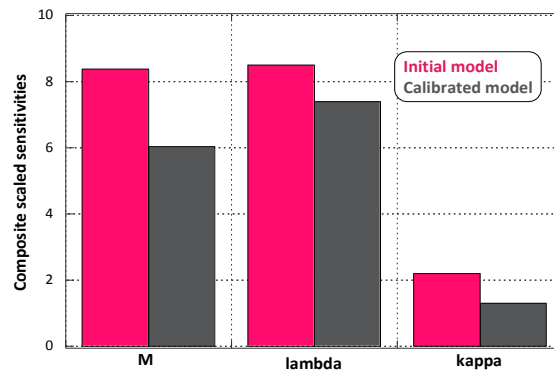


Figure 38. Composite scaled sensitivity for initial and calibrated models

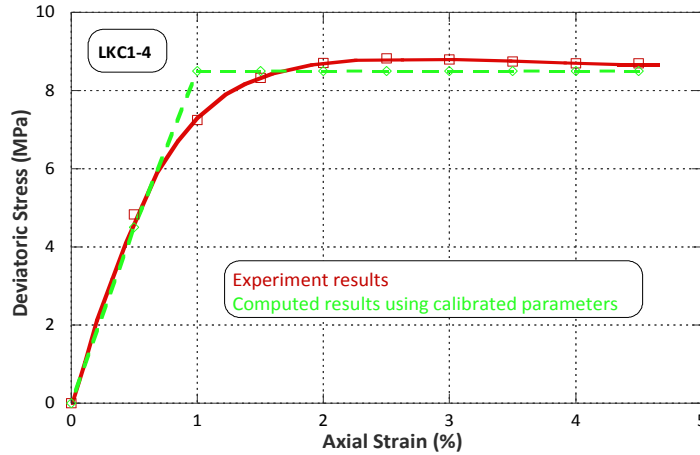


Figure 39. Stress- Strain curves for drained triaxial test, comparison between laboratory results and simulated results using calibrated parameters

## CONCLUSION

The aim of this study was to evaluate the best set of input parameters of MCC constitutive model for Joli Fou clay shale formation with the minimum available data. There was just one oedometer test has been conducted at the University of Alberta Laboratory with its digital data and the rest of data for triaxial tests has been digitized and extracted from the reports and their digital data was not available. Considering the limited amount of information, calibration of Modified Cam Clay parameters from triaxial test results has been conducted successfully using inverse analyses. Coupling finite difference model FLAC and UCODE provides the opportunity for developing this procedure to get the reliable set of input parameters. A comparison between experimental results and simulated results for both initial parameters from oedometer test and calibrated parameters from inverse analysis shows the better fit is achieved.

## **CHAPTER 4 A FLUID-STRUCTURE INTERACTION ANALYSIS OF PRESSURIZING THE PACKER IN SLEEVE FRACTURING TEST**

**DREAMING WHEN DAWN'S LEFT HAND WAS IN THE SKY  
I HEARD A VOICE WITHIN THE TAVERN CRY,  
"AWAKE, MY LITTLE ONES, AND FILL THE CUP  
"BEFORE LIFE'S LIQUOR IN ITS CUP BE DRY."**

**"KHAYYAM"**

## **A FLUID-STRUCTURE INTERACTION ANALYSIS**

The numerical simulation (FSI analyses) of the sleeve fracturing test will be discussed in this chapter. For that purpose, the first step was conducting a sensitivity analysis of the drainage condition as a function of permeability and loading rate to assess the effect of these factors on packer-induced stresses during the sleeve fracturing test in clay shale. The next step before conducting the FSI analyses was calibration of the packer element parameters as a hyperelastic material. In the following section, these topics will be discussed in detail.

### **SENSITIVITY ANALYSIS OF DRAINAGE CONDITIONS AS A FUNCTION OF PERMEABILITY AND LOADING RATE IN PACKER-INDUCED STRESSES DURING MICRO HYDRAULIC FRACTURING TESTS IN CLAY SHALE<sup>4</sup>**

Abstract: Knowing the state of stress in geologic formations is of considerable importance for caprock integrity analyses in any project such as SAGD, CSS, and CCS because of technical management of the operations as well as environmental considerations. The unique behavior of the clay shale caprocks causes diverse problems for geotechnical investigations such as measuring in situ stress. As a first step to understanding these issues, numerical modelling has been conducted on the borehole wall in clay shale. In the model, the packer has been pressurized during either sleeve fracturing or the isolation of the test interval of a hydraulic fracturing test. The modified Cam-clay model is used to describe the geomechanical behavior of clay shale. The complexity of a formation's stress field during a test can cause a variety of drainage conditions, depending on the radial permeability of the formation and the loading rate of the test. Different phenomena during the packer loading process were thus studied numerically. To consider the effects of drainage during the test, packer loading was simulated with various loading rates and permeabilities to investigate the transition zone between undrained, partially drained, and fully drained conditions. Using numerical models, an attempt has been made to quantify these transition zones and drainage conditions based on the permeability of the formation and loading rate.

---

<sup>4</sup> A version of this section is submitted to "Journal of Natural Gas Science & Engineering"

## INTRODUCTION

This study investigates some factors that can affect stresses induced by inflatable packers during sleeve fracturing or hydraulic fracturing tests. Previous research by Kehle (1964), Warren (1980), Evans (1987), Li (1997), Thiercelin (1993), and Atkinson (2001) has revealed that packer behavior is critical to the success of such tests. In particular, the pressure exerted by the packer on the formation must be as close as possible to that in the test interval to avoid initiation or growth of a fracture along the packers during hydrofracturing. Moreover, axial tension in the rock must be minimized to avoid initiation of packer-level transverse fractures that would be detrimental to the test. However, the stress induced by packer pressurization during the first stage of the test (in impermeable plastic materials such as clay shales and mudstones) is fundamental to the accuracy of the final result. It is obvious that a formation's drainage conditions dictate its stress distribution, and consequently its response to the applied pressure. This research has advanced understanding of the relationship between formation response in terms of drainage condition as a function of (1) loading rate and (2) permeability during sleeve fracturing or packer loading for the isolation test interval stage of multiple packer techniques for in-situ stress measurement tests such as micro fracture test. Sleeve fracturing is particularly advantageous in impermeable plastic shales, where hydraulic fracturing often results in fractures that grow along packer elements. This establishes communication between interval and annulus, leading to premature test failure. The packer model considered here consists of an inflatable, reinforced, and initially cylindrical membrane.

It is well recognized that the response of porous media to applied pressure is related to the drainage conditions and permeability of the surrounding formation. The loading rate can produce two extreme drainage states: undrained response if the loading rate is sufficiently high and permeability is extremely low and drained response if the loading rate is sufficiently low and permeability is sufficiently high. There is a range of loading rates between these two extremes in which the formation response is found to be partially drained.

There are very limited studies when it comes to the packer-induced stresses and their effects on any stress measurement test using multiple packer technique such as MDT® (modular dynamic tester) micro fracturing test and RCI® (reservoir characterization

instrument). Unfortunately, among those minimal resources, there is none that refers to hard soil-soft rock materials such as clay shale. Moreover, they did not consider the drainage conditions, permeability, and loading rate and their effects on the materials' response since the material has been considered as hard rocks (elastic behavior) in their studies. The main aim of this paper was parametric study and sensitivity analysis of drainage conditions' influence on packer induced stresses as a function of two main parameters: formation's permeability and test's loading rate.

### **MECHANICAL ANALOGY**

Three main representative elements can be introduced in the rheological model of the geotechnical behavior of materials. The ideal spring is one considered to be operating within its elastic limit, so its behavior can be modelled with Hooke's law. Such a spring is assumed to be massless and to have no damping effects. The dashpot is an ideal viscous damper (damping element) that opposes velocity and can represent delayed strain of the formation, which, in turn, depends on time and can indicate a drained response. The slider describes the strength and refers to time-independent plastic behavior. The function of the sliding element corresponds to that of two blocks lying one on top of the other that may only be displaced relative to each other when the shear stress acting on the contact surface exceeds the shear strength- $\sigma_f$ . This shear strength consists of the components due to the material's constitutive model (failure criteria). To show mechanically the formation response to the drainage condition, loading has been considered purely horizontal in the case under study.

Figure 1 shows a mechanical analogy of the undrained behavior of the material. The model shows a spring and slider system, representing the undrained response of the formation; the spring represents the small elastic deformation, while the slider represents the plastic deformation. The capacity of the slider is governed by a work-hardening relationship. Pressure (P) elastically compresses the spring. This strain is time-independent, reversible, and occurs immediately after application of the external pressure. While external pressure P is smaller than the strength  $\sigma_f$  of the sliding element, only elastic strain occurs in the spring. If the pressure is exceeded, the blocks of the sliding element are displaced relative to one other. The displacements in the sliding element, and the resulting strains in the system are irreversible. The three one-dimensional

substitute systems (I, II, and III) illustrate the stress-strain behavior of the material in three dimensions in an analogous manner. A comparison with the three systems carrying a beam (i.e. a contact element which transfers applied pressure from packer to wellbore wall in the case under study) provides a clear illustration of this case. If the elastic constants of the springs in the three systems are equal (isotropic), they initially experience the same compression under the equal load  $P$  (pressure applied on the wellbore wall by the packer, assumed to be uniform), and the beam does not distribute any load. If it is assumed that the strength  $\sigma_f$  of System II is smaller than that of the two others and  $P$ , plastic strains occur in System II. The beam must bend and distribute load to adjust Systems I and III. Substitute System II continues to change until the stress in the sliding element of the latter is reduced as far as its strength  $\sigma_f$ , so no further plastic deformations occur. As long as Systems I and III can take on additional load and stresses by further compression of springs without exceeding  $\sigma_f$  in their sliding elements, a state of equilibrium is established. Otherwise, the whole system fails.

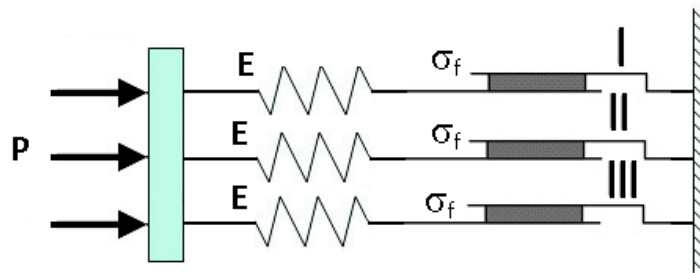


Figure 1. Schematic illustration of equivalent mechanical model for undrained response

Figure 2 shows a spring that represents the elastic deformation that occurs during drained loading. This spring acts in series with a dashpot (Maxwell model), which represents the drainage processes in the formation. The dashpot only serves to delay strain. The strain in the one-dimensional model does not increase beyond all limits immediately but as a function of time. Consequently, for rapid processes, the dashpot does not deform, and there is no drained response.

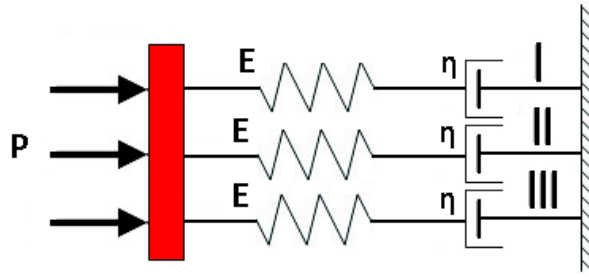


Figure 2. Schematic illustration of equivalent mechanical model for drained response

The partially drained response of a formation can be captured with a combination of these two models that describes both components of time-dependent (drained) and time-independent (undrained) plastic strain (Figure 3).

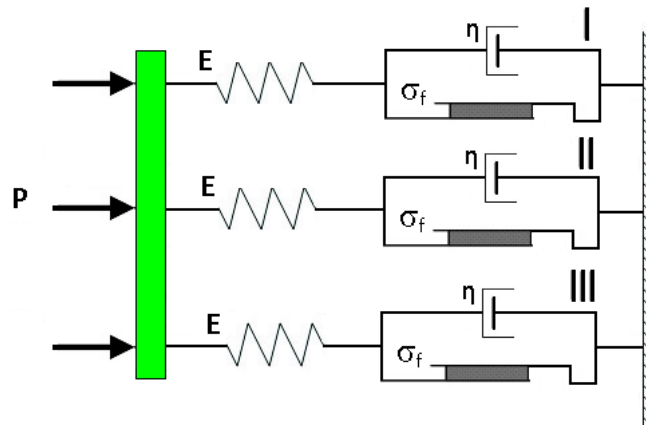


Figure 3. Schematic illustration of equivalent mechanical model for partially drained response

## DESCRIPTION OF MECHANICAL BEHAVIOUR OF THE FORMATION

Poroelastic- MCC plastic constitutive model has been used for simulation of the formation's behavior. A brief review of the poroelastic model is provided below as the MCC (modified cam clay) constitutive model was discussed in Chapter 3.

### MECHANICAL DESCRIPTION OF POROELASTIC FORMATION

In porous media saturated by a fluid, elastic deformation and fluid flow are coupled. Biot (1941) introduced the basic theory of poroelasticity. Since then, many researchers have contributed to its further development. An inclusive review of the theory can be found in Wang (2000), Detournay and Cheng (1993), Rice and Cleary (1976), Coussy (2004), and Zimmerman (1991, 2000). The poroelastic theory is commonly applied to soil mechanics problems where consolidation issues are the primary focus. It is also relevant

to porous soft rock formations where the mechanical behavior of a medium depends on the drainage conditions. Also relevant is the fracture of rocks for enhancing the recovery of oil through hydraulic fracturing. Two crucial parameters that affect the elastic response of porous media are the elastic strain rate and the elastic fluid mass content. The rates of total stress  $\sigma$  and pore-pressure  $p$  through isotropic constitutive equations govern these two most critical parameters. According to Rice and Cleary (1976), the most general form for isotropic material response defines in terms of the strain and stress pairs  $(\epsilon_{ij}, \zeta)$ ,  $(\sigma_{ij}, p)$ ; which by definition, is:

$$\epsilon_{ij} = \frac{\sigma_{ij}}{2G} - \left( \frac{1}{6G} - \frac{1}{9K} \right) \delta_{ij} \sigma_{kk} + \frac{1}{3H'} \delta_{ij} p \quad (1)$$

$$\zeta = \frac{\sigma_{kk}}{3H''} + \frac{p}{R'} \quad (2)$$

where  $\epsilon_{ij}$  is solid strain tensor,  $\sigma_{ij}$  is total stress tensor, parameters  $K$  and  $G$  are bulk and shear modulus of the drained elastic solid respectively,  $\delta_{ij}$  is Kronecker delta,  $p$  is pore pressure which is scalar,  $\zeta$  is variation of fluid content per unit volume of porous medium, and additional constitutive constants  $H'$ ,  $H''$ , and  $R'$  are poroelastic constants that characterize the coupling between the solid and fluid stress and strain.

## DEVELOPMENT OF NUMERICAL MODEL

Numerical modelling of packer loading was performed using the poroelastic-plastic model to predict the stress distribution and excess pore pressure change during borehole wall expansion. During modelling, the formation was considered initially fully saturated. Due to axial symmetry about the  $z$ -axis, and to symmetry on the  $z = 0$  plane, only a quarter of the actual geometry is considered. For the boundary conditions, hinges are imposed along the far-field sides of the model, shown in Figure 4 as a discretization region (vertical displacement was prevented in the bottom and top boundaries, whereas horizontal displacement could develop freely, and horizontal displacement was prevented along the right side of the model). The size of the element increases with the radial distance from the borehole center, where most rapid variations of various parameters with distance are expected to take place. The arrows on the left side indicate the applied pressure along the contact half length. Water flow (flux,  $\phi$ ) was allowed to pass through the left side for

the drained boundary condition, and the amount of it is considered equal to zero for undrained analyses.

The other assumptions are: that the formation is infinite with a circular cylindrical hole in the middle; that initial stresses are applied to the formation according to the depth of the test interval, considered equal to 200m; that K (the horizontal to vertical effective stress ratio) is equal to one and the initial total stresses equal 4.4MPa (a homogeneous state of stress is assumed for better insight about the distribution of induced stresses within the formation due to packer loading); and that pore pressure applied for both drained and undrained conditions is equal to 2MPa. The initial step is one which all pre-defined parameters, in situ stresses and other geomechanical properties such as poroelastic parameters and permeabilities, plastic properties, degree of saturation and initial void ratio have been applied as a static and general step, Geostatic step is the second step to stabilize the model and make sure that model is in equilibrium. Drilling the borehole, stress release and applying mud pressure have been defined in the third step as transient consolidation step with a magnitude of 2.94 MPa. The last step is pressurizing a packer as a transient consolidation step. Only the influence of a single packer has been considered. The problem of the state of stress imposed by a straddle packer arrangement can also be encountered by superposition. For example, the following analysis has been run using the finite element package Abaqus: A packer is inflated to 10 MPa in the wellbore; the porous elastic and cam-clay parameters of the material obtained by laboratory experiments consist of triaxial and isotropic consolidation tests as follows:  $\kappa=0.058$  (logarithmic bulk modulus, unloading-reloading line slope in the  $v-\ln P'$  plane),  $\lambda= 0.125$  (logarithmic hardening modulus, normally consolidation line slope in the  $v-\ln P'$  plane),  $M=1.07$  (slope of critical state line),  $\nu=0.3$  (Poisson's ratio),  $k= 1.355 \times 10^{-10}$  m/s (hydraulic conductivity of the material, isotropic permeability was considered),  $a_0=3000$  kPa (hardening coefficient),  $e_0= 0.51$  (initial void ratio) with preconsolidation stress equal to 6 MPa.

Clay shale around the pressurizing borehole was projected to experience large deformation. Therefore, geometric nonlinearity and updated Lagrangian formulation were considered in the analyses. Two criteria have been reflected as the indicators for developing a plastic zone. The first one was when the stress of any clay shale element reaches the critical state and the second one was when any of the effective principal stresses in a clay shale element reduces.

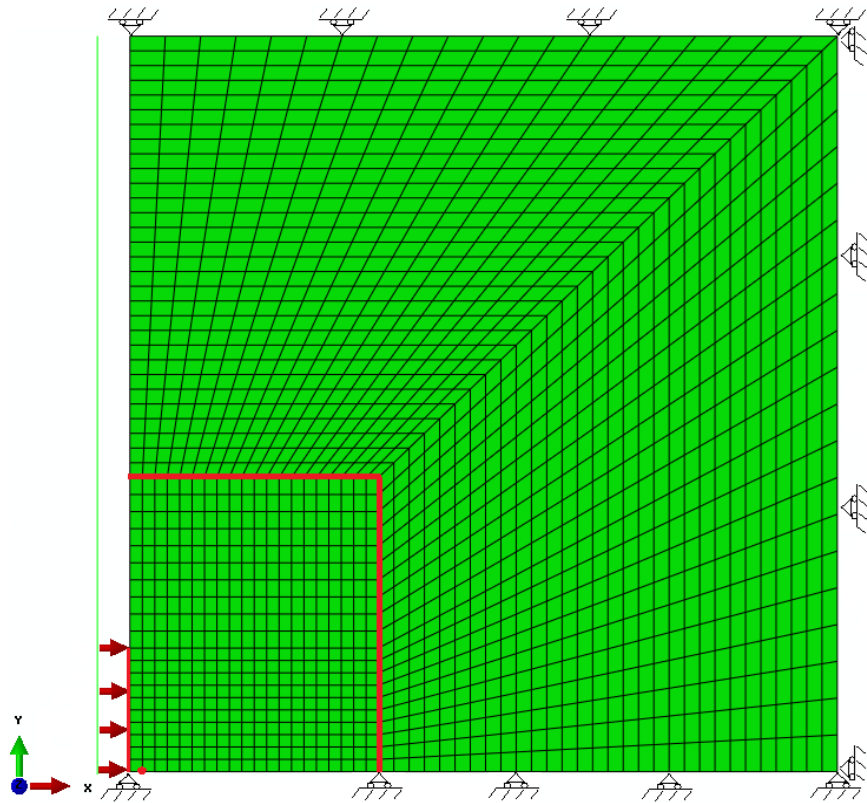


**Figure 4. The finite elements discretization of the region under study, the loading strip, zone of interest and the observational point in 0.1 wellbore radius away from wellbore wall in the middle point of the applied pressure strip**

#### **RESPONSE TO PACKER LOADING WHEN FORMATION FULLY DRAINED VS. PURELY UNDRAINED**

Figure 5 shows the effective radial stress and pore pressure distribution under undrained conditions right after packer loading and dissipation of excess pore pressure. Figure 6 and Figure 7 show the same under drained conditions. It is clear that clay shale behaves completely differently under different drainage conditions. The maximum and minimum effective induced stresses in both conditions remain in compression mode, and this is the result of mud pressure applied at the borehole boundary and of pressure  $P_f$  on a finite strip. The radial effective stress concentration in the undrained case is close to the end point of the packer.

In contrast, the stress distribution seems more uniform for the drained case, with the maximum at the midpoint of the packer/formation interface, as can be seen in the profile

of the completely elastic case. Immediately after applying a constant rate of packer pressure, a lens with high pore pressure appeared behind the strip where packer pressure was acting which dissipated and reached initial pore pressure over time (Figure 7). This is related to the low permeability of the material.

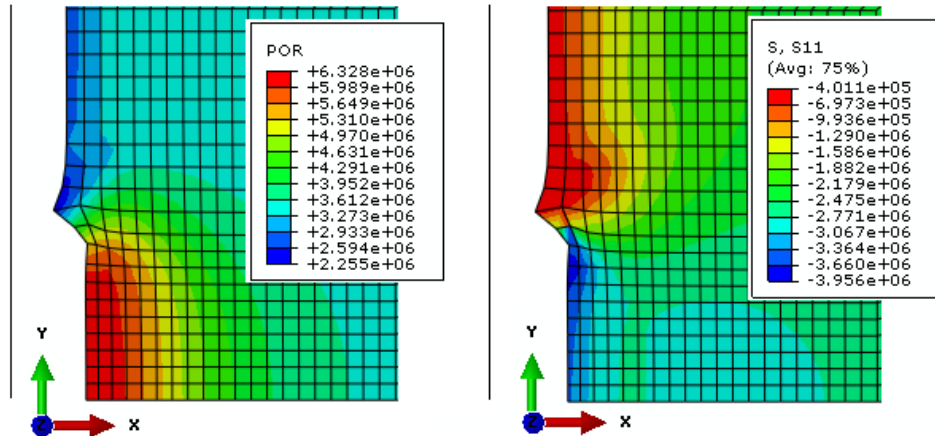


Figure 5. Contours of the resulting pore pressure (Pa) (left) and radial effective stress (Pa) (right) under undrained condition in the formation, with displacement after pressurization of the packer

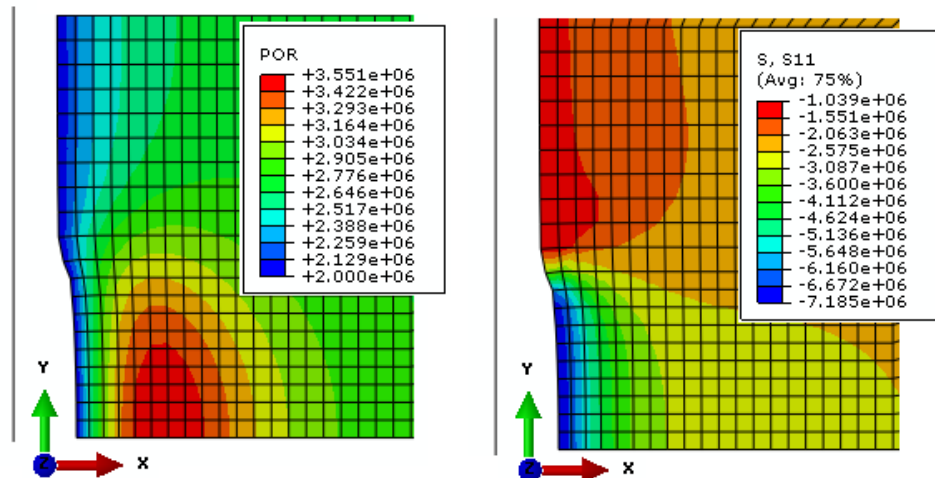


Figure 6. Contours of the resulting pore pressure (Pa) (left) and radial effective stress (Pa) (right) under drained condition in the formation with displacement immediately after packer pressurization

As expected (and similar to results obtained by Rangeard et al. (2006)), the flow of pore water in the radius direction is symmetrical along the centerline of the loading strip and at the middle of the packer/formation interface; it is mainly horizontal. The displacement profiles are completely different under different drainage conditions. Figure 8 illustrates radial displacement ( $u$ ) at the midpoint of the packer/formation interface with initial and deformed mesh. The maximum displacement accrued at this point is  $4.4 \times 10^{-2}$  metres

under undrained conditions,  $4.09 \times 10^{-2}$  metres under drained conditions after applying the packer pressure, and  $6.82 \times 10^{-2}$  metres under drained conditions after excess pore pressure dissipation (which are noticeable in the geomechanical point of view).

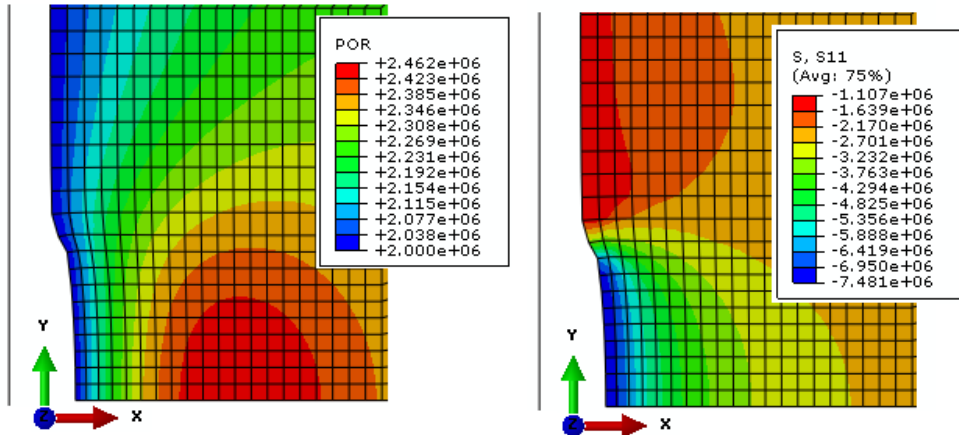


Figure 7. Contours of the resulting radial effective stress (Pa) and pore pressure (Pa) under drained formation condition, with displacement after dissipation of pore pressure

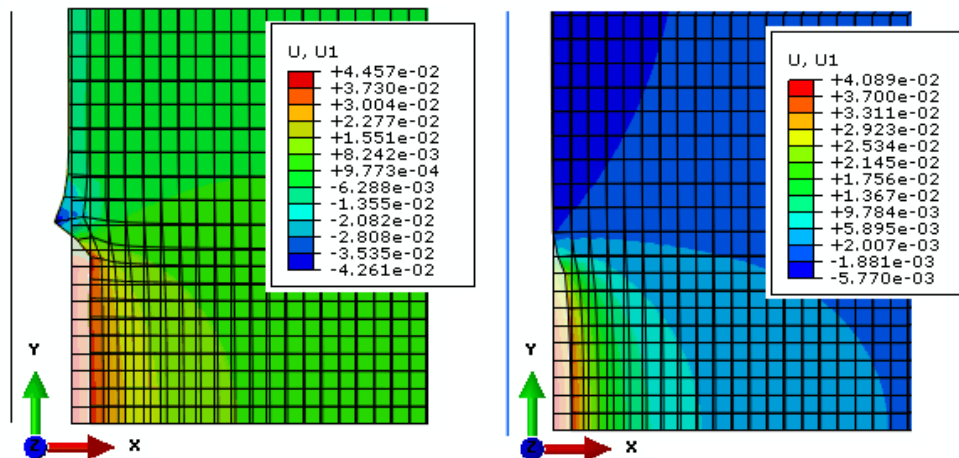


Figure 8. No-deformed and deformed mesh (m) and maximum radial displacement after packer pressurization under undrained (left) and drained (right) conditions at the packer loading step

## ANALYSIS OF DRAINAGE CONDITIONS

Drainage conditions during packer loading depend mainly on the permeability and compressibility of materials. Also, the lower the loading rate, the more fully drained the formation response. At high loading rates, the response is fully undrained. The phenomenon of local consolidation can take place during a sleeve fracturing stage of the

fracturing test, depending on the loading rate at the borehole wall and on formation permeability.

### **Sensitivity to formation permeability**

Formation permeability ( $k$ ) must be taken into account in the packer loading stages of tests. Pressurizing packer(s) generates a non-homogeneous stress field in the formation near the probe, and a formation's permeability can affect its consolidation behaviour around the expanding packer. This is due to different distributions of excess pore pressure, which are, in turn, attributed to partially drained conditions during this stage of fracturing tests. Hence, depending on formation permeability, partial drainage can occur and induce changes of the mechanical properties of the formation under study. For tests under perfectly drained or undrained conditions,  $k$  has no influence on the stress and pore pressure responses, whereas, for tests under partially drained conditions,  $k$  has a considerable effect (Figure 9). The results illustrated in Figure 9 were generated from monitoring the pore pressure, effective and total stresses at an observational point 0.1 times the wellbore radius away from wellbore wall in the middle point of the applied pressure strip (as shown in Figure 4) in different models run with various permeabilities. Figure 9 indicates that permeability has a significant effect on the evolution of pore pressure for values between  $10^{-8}$  and  $10^{-12}$  m/s (i.e., between 10 mD and 1  $\mu$ D), and a minuscule effect for other values, which correspond to either perfectly drained or undrained conditions during the test.

Figure 10 considers the effect of permeability on stress distribution and presents effective stresses including radial, axial, and circumferential stresses and pore pressure distributions along the radial direction for applied packer load equal to 10 MPa at the borehole wall for different representative permeabilities of each region of drainage conditions illustrated in Figure 9. In Figure 10, stresses are normalized by initial in-situ stress, and distance from the centre of the borehole is normalized by borehole radius.

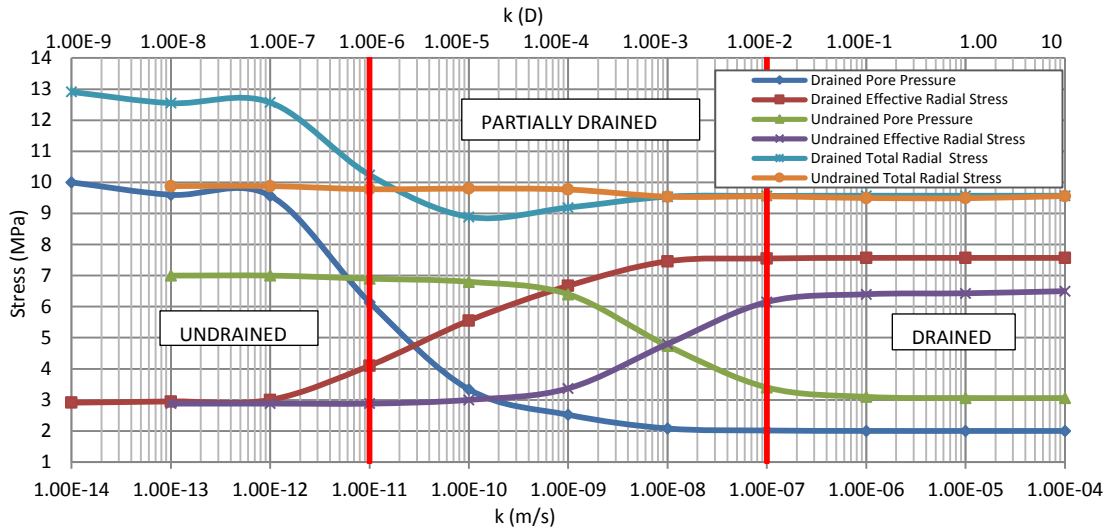


Figure 9. Effects of permeability on radial stress and pore pressure in undrained, partially drained, and drained conditions

The main conclusions to be drawn from these analyses (as shown in Figure 10) are:

- For material with very low to low permeability (undrained condition), in a plastic region (the area between the red and orange vertical lines), the value of effective stresses is constant. For more permeable material, the radial effective stress is higher at the borehole wall and decreases distance from the plastic zone;
- All stresses induced by packer loading reach far-field stresses (in-situ stresses) at a distance of ten times the borehole radius;
- For the value of  $k$  less than  $10^{-8}$ , the distribution of excess pore pressure immediately after the expansion of a borehole wall regarding packer loading is logarithmic, with a radius within the plastic zone and a stabilized value higher than the initial pore pressure.
- Decreases in permeability result in increases in excess pore pressure at the borehole wall, and these changes significantly increase the hydraulic gradient around the borehole wall. Hence, effective stresses, which are directly related to pore pressure, would be significantly affected.
- Figure 10 illustrates that excess pore pressure in the immediate vicinity of the borehole wall for completely undrained conditions is considerably higher than the stabilized value of pore pressure. It also illustrates that decreasing the excess pore pressure could be more drastic under undrained conditions than under partially drained conditions.

- Observed fluctuation in the pore pressure curve indicates a considerable localized redistribution of excess pore pressure in the material around the borehole wall. Collins and Yu (1996) present similar analytical results.
- Under partially and completely drained conditions, an elasto-viscoplastic constitutive model should be considered to analyze the effect of consolidation and creep on the material response; this was discussed in previous sections.

### **SENSITIVITY TO DIFFERENT MONOTONIC LOADING RATES**

It is generally assumed that a material's response in terms of drainage conditions depends directly on the rate of packer loading under test pressurization. The purpose of this parametric study is to clarify the effect of the loading rate on the drainage condition of the formation. Numerical modelling was conducted under drained and undrained conditions with permeabilities ranging from  $1.35 \times 10^{-5}$  to  $1.35 \times 10^{-14}$  m/s and loading rates ranging from 100 to 1500 kPa/min. The loading rate of each subsequent analysis increased by 100 kPa/min ( $\Delta P/\Delta t = 100$  kPa/min for two consecutive analyses). Figure 11 shows that drainage conditions can be determined from loading rates (controlled manually by the hydraulic pump), and material permeability (evaluated in a laboratory test).

Figure 11 also shows the transition points between undrained, partially drained, and fully drained conditions for each loading rate. These were determined by observations of pore pressure and effective radial stress, as done in the previous section. It should be mentioned that for all analyses, the sensitivity of induced radial stress was greater regarding the change of loading rate than for the change of excess pore pressure. Increases in the rate of applied pressure coincided with extremes of transition points for different loading rate shifts to the right. The response of the material suggests that these increases (by a factor of 15 for loading rate) indicate undrained or partially drained conditions (by a factor of 10 for permeability).

Rate effects are discussed separately for undrained, partially drained and fully drained condition ranges:

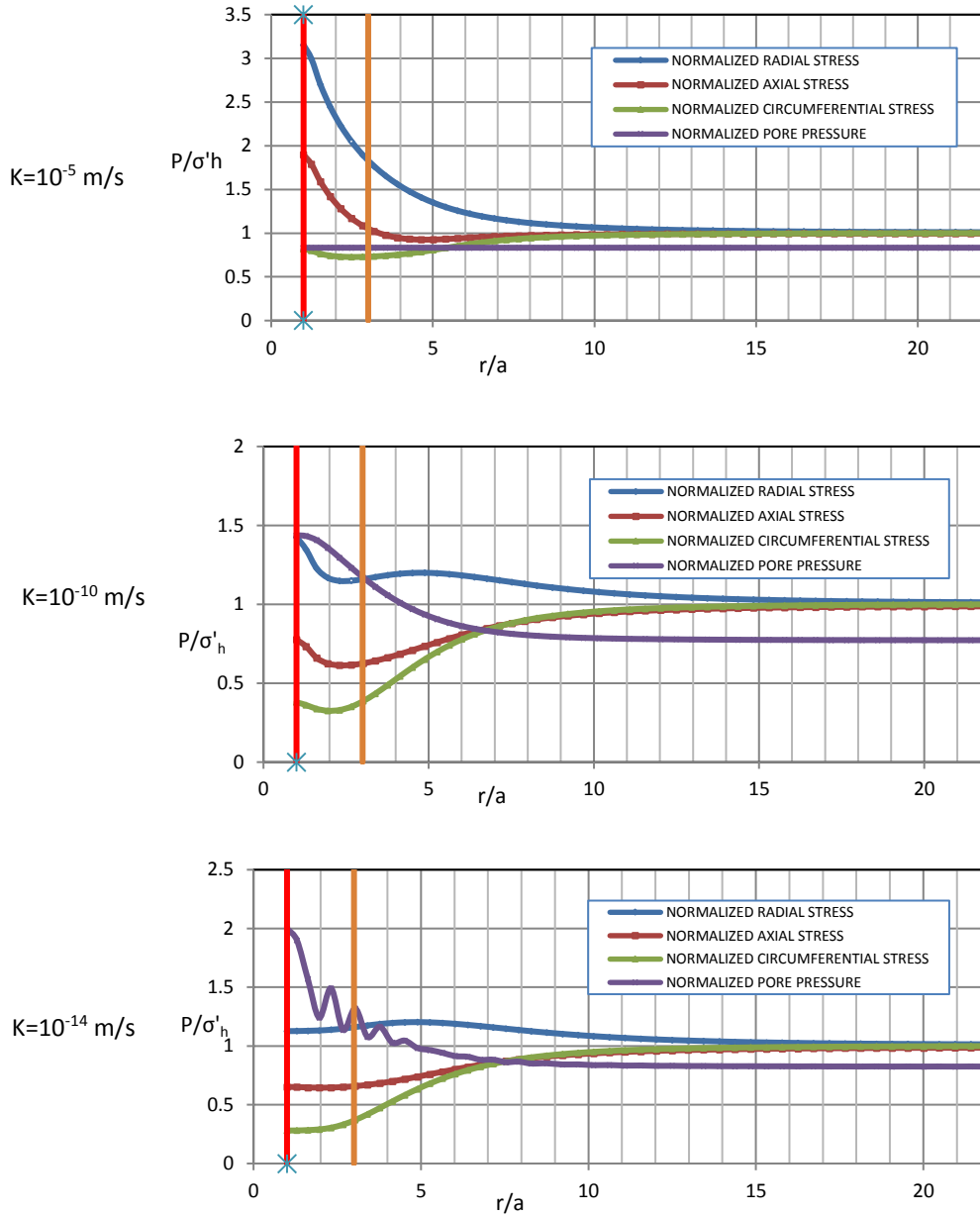


Figure 10. Stress distribution along radial distance from midpoint of packer-formation interface for an applied pressure of 10 MPa and different permeabilities

1) Undrained conditions: the undrained behaviour of clay shale is slightly rate-dependent (i.e. the higher the loading rate, the higher the effective induced radial stress of the material). The average  $\sigma_{rr}$  for a loading rate of 1500 kPa/min under undrained conditions was 7 % higher than that for a loading rate of 100 kPa/min.

2) Partially drained condition: A change from undrained to partially drained conditions during packer pressurization with different loading rates starts to consolidate the formation around the packer.  $\sigma_{rr}$  increases, since during consolidation the larger portion of the applied pressure allows dissipation of pore pressure, and is thus carried by the formation. The change of effective radial stresses and pore pressure under partially drained conditions was examined through the numerical models. It is clear that observation of either pore pressure or radial stress alone does not allow the determination of the transition points at which material behaviour changes from undrained to partially drained or from partially drained to fully drained conditions. This is because of the two offset ranges in which the sensitivity of the change in pore pressure or induced effective radial stress are different at the upper and lower ends of the transition zone. Figure 12 illustrates this effect for the minimum and maximum loading rate. As discussed, the condition change from drained to partially drained condition is in the range of  $k = 10^{-8}$  m/s for the maximum loading rate and of  $k = 10^{-9}$  m/s for the minimum loading rate. However, because the drainage condition is rate-dependent, the changes begin at a higher value of  $k$ , at which effective stresses tend to drop as partially drained condition is approached. However, they actually tend to increase due to loading rate effects. The same phenomenon could be observed in the transition zone from partially drained to undrained conditions. The transitions from undrained to partially drained and drained condition are not clearly defined in pore pressure curves. Therefore, the “partially drained” zone includes an offset range in which conditions may seem undrained or drained. However, transition points are more clearly defined in effective radial stress curves.

3) Fully drained conditions: Results are not affected by variations of loading rate under fully drained conditions. Numerical modelling showed negligible change in the induced effective radial stress and excess pore pressure regardless of the loading rate. The difference between radial stresses under the worst-case scenario is less than 1% for both minimum and maximum loading rates.

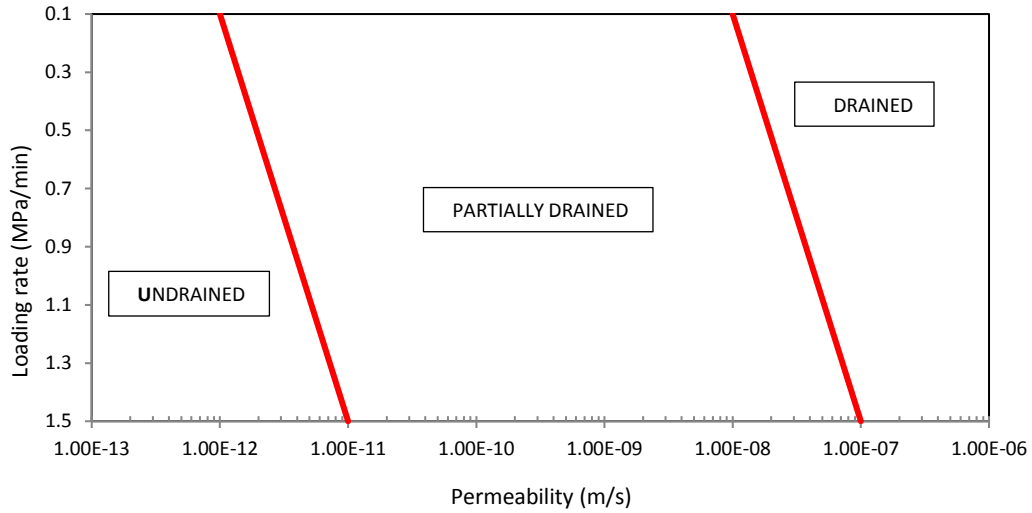


Figure 11. Drainage conditions with regard to permeability and loading rate

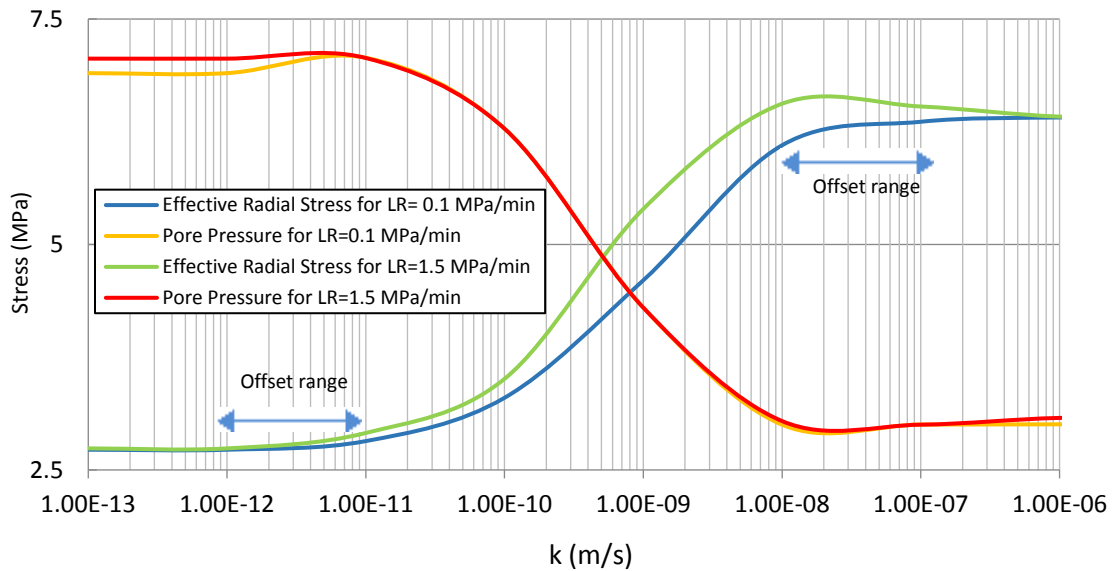


Figure 12. Effect of loading rate on effective radial stress and pore pressure for 0.1 and 1.5 MPa/min loading rates

## CONCLUSIONS

A series of numerical simulations was performed on the first stage of micro hydraulic fracturing test in a clay shale formation to clarify the effects of permeability and loading rate on drainage conditions. The results are summarized as follows:

- To understand the different conditions of drainage, the rheological models have been discussed;

- The drainage condition under a constant loading rate is dependent on the permeability of the surrounding formation. Moreover, the transition zone has been defined;
- The stresses induced as a result of loading the packer reach far-field stresses (in-situ stresses) at a distance of ten times the borehole radius. In other words, the radius of the disturbed zone is equal to ten times that of the borehole radius;
- Drainage condition is dependent on the loading rate. Having the permeability of the formation as well as the loading rate of the test (Figure 11) can be used to determine the drainage condition. If the packer load is applied quickly with respect to the permeability, the pore pressure will go up fast; thus the stiffness of the disturbed zone around the area under loading is greatly increased. The stiffness depends on the rate at which it has been loaded. That causes some misunderstanding in micro-hydraulic fracturing test result's interpretation since instead of measuring the far-field stresses, it shows the magnitude of stresses within the disturbed zone during sleeve fracturing test, which is induced total stresses.

## **INFLUENCE OF PACKER PROPERTIES DURING IN SITU STRESS TESTING<sup>5</sup>**

Abstract: Calibration of any equipment and procedure that is used to measure the magnitude of a field parameter or indicate its value is an essential operation required to obtain the corrected monitoring variable. Ideally, calibration is a simulation of a real test, but with accurately known and controlled boundary conditions, so that the performance of the instrument recording system can be checked. In the absence of calibration during hydraulic fracturing tests for in situ stress measurement, the reference pressure which corresponds to the point at which the fracture starts to initiate in the sleeve fracturing test cannot be identified with sufficient accuracy. Moreover, during the hydraulic fracturing phase of the test, providing the proper sealing to have a successful test directly depends on the optimal difference between packer pressure and test interval pressure otherwise leakage will happen, and pressure will not build up in the test interval to hydraulically propagate or create the fracture. Meaningful interpretation of desired parameters from test data critically depends on an accurate determination of the reference pressure. Micro fracturing testing is almost worthless if proper calibrations of the instruments are not carried out. There are three main groups of calibrations: pressure measuring system (gauges and transducers), compliance of the probe (membrane stiffness and membrane compression), and compliance of the system (volume changes). In this paper, the factors that may affect the compliance of the probe have been investigated and calibration has been done using analytical and numerical methods comparing the available empirical field data.

### **INTRODUCTION**

The micro fracturing test using multiple packer techniques is a common in-situ stress measurement method for evaluation of the stress regime in cap rock for caprock integrity analysis in SAGD, CSS, and CCS projects. MDT<sup>®</sup> (modular dynamic tester) and RCI<sup>®</sup> (reservoir characterization instrument) are two popular instruments using multiple packer techniques for that purpose. An MDT microfrac test will generally have the following steps: leakoff test, sleeve fracture, hydraulic fracture, reopening test, flowback and rebound test. Sleeve fracturing is particularly advantageous in impermeable plastic

---

<sup>5</sup> A version of this section has been submitted to the Journal of Petroleum Science and Engineering

shale, where hydraulic fracturing often results in a fracture that grows along the packer elements and leads to premature failure of the test. During the sleeve fracturing test (Figure 13 (a)), the upper packer is pressurized to the maximum allowable pressure the packer element can tolerate. History plot of pressure versus time is monitored continuously during the test and the breakdown pressure, which is equivalent to slope change in pressure-time plot, can be evaluated. This phenomenon indicates the initiation of the fracture. Since breakdown pressure is interpreted from applied pressure, calibration plays a crucial role.

During hydraulic fracturing tests, the upper packer will be deflated if there is sleeve fracturing phase before. The probe will be moved upward to isolate the test interval by inflating both packers (Figure 13 (c)) and fluid will be injected in the test interval at a constant flow rate for reopening and propagation of the existing (sleeve) fracture or in the case of not having sleeve fracturing stage, initiation and propagation of the hydraulically induced fracture. Providing the proper sealing for the test interval is critical at this stage. Figure 13 (b) shows the lack of appropriate sealing that can cause leakage of the injection fluid and unsuccessful tests which have been reported repeatedly.

Cavity expansion methods can be used to analyze the sleeve fracturing test, as fluid is not yet injected directly into the formation. On the basis of borehole boundary conditions, problems of cavity expansion are generally classified into two categories: (i) displacement-controlled cavity expansion, and (ii) pressure-controlled cavity expansion. The borehole remains cylindrical throughout the former, while spatial distribution of pressure expanding the cavity is uniform throughout the latter and is only a function of time, regardless of borehole deformities. Analytical solutions to displacement-controlled undrained cavity expansion problems may be satisfactory to provide solutions to geotechnical engineering problems such as penetration of cone penetrometers and driven piles. However, packer pressurization during fracturing tests is better categorized as a pressure-controlled cavity expansion problem. Besides the routine calibrations for pressure measuring system and compliance of the system, there are some necessary calibrations related to the packer element, which is elastomeric hard rubber. The constitutive model of the packer element is known as a hyperelastic material, which ideally describes a nonlinear elastic behavior of the special case of a Cauchy elastic material. It has been found that the transferred pressure to the formation during the

sleeve fracturing test or test interval isolation is not equal to the applied pressure which is referred to as the pressure transmissibility of the packer element. In this research, the factors causing this reduction coefficient have been studied, and the properties of the packer element have been calibrated accordingly.

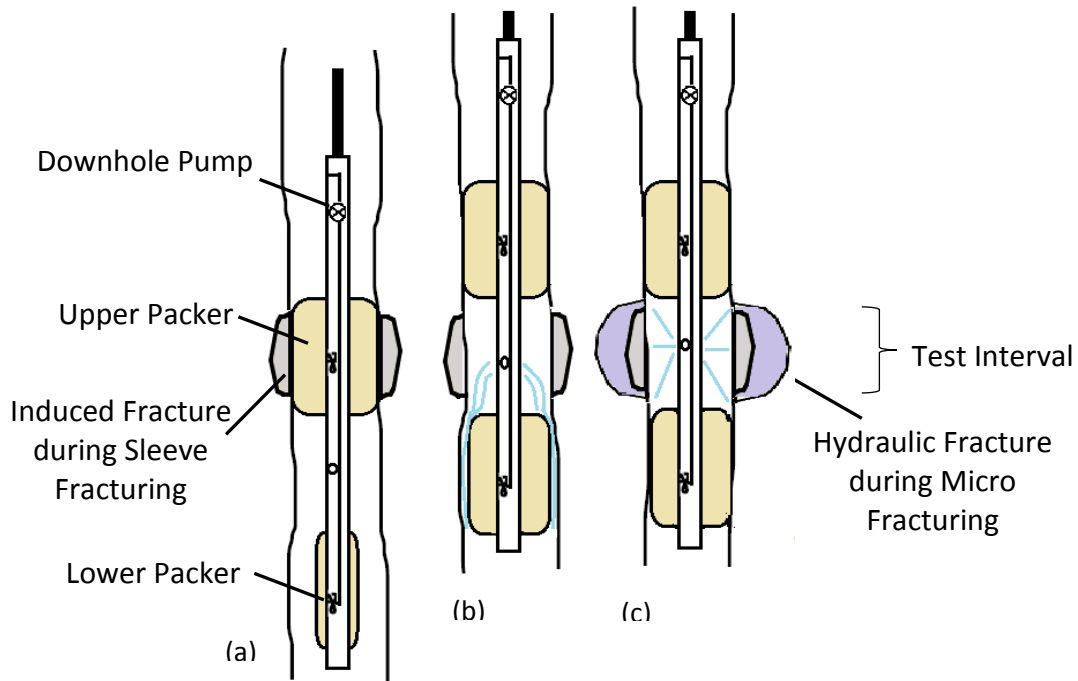
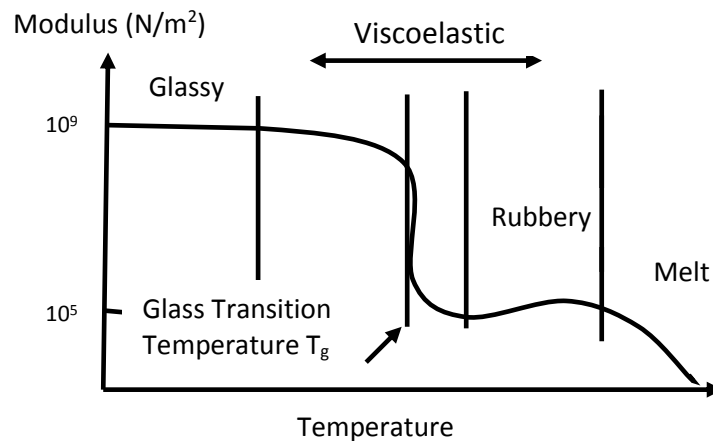


Figure 13. Micro hydraulic fracturing test

## HYPERELASTIC CONSTITUTIVE MODEL

Hyperelastic materials refer to ideally elastic materials, the stress-strain relationship of which is driven from strain energy potential function. The strain energy potential function for this class of elastic materials involves large deformations and consequently large volumetric changes are generally written in terms of principle stretches and their directions, not in closed form expression. The hyperelastic constitutive model represents both the rubbery behavior of a polymeric material and polymeric foam that can be subjected to large reversible deformation. The response of a typical polymer is a function of temperature, strain history, and loading rate. Polymer has different mechanical behavior regimes dependent on increasing temperature, which is known as glassy, viscoelastic, and rubbery.

Figure 14 illustrates the apparent shear modulus as a function of temperature. At lower temperature, the behavior of the polymer is like glass with stiff modulus. As temperature increases, the shear modulus decreases and at a critical temperature known as “the glass transition temperature”, a polymer experiences a dramatic change in mechanical behavior. Near the transition zone, the stress depends strongly on strain rate, at the transition zone, a dramatic decrease of shear modulus happens and beyond this zone, the rubbery behavior of the polymer shows that the behavior is elastic, but the stress is not dependent on strain rate or strain history. At this zone, the stiffness of natural rubber is increasing lightly with temperature. This is called “dynamic stiffening”. Heavily cross-linked elastomer (polymer) is most likely to show ideal rubbery behavior and hyperelastic constitutive model accounts for this behavior.



**Figure 14. Apparent shear modulus of typical polymer as a function of temperature**

Bower (2010) listed the characteristics of rubber behavior as below:

- 1- The material behaves as ideally elastic which means stress should be considered as a function of current strain and it is not history or rate dependent, and the deformation is reversible (network equal zero when material exposed to a closed strain cycle). These facts are applicable when the material deforms at adiabatic/constant temperature.
- 2- It is assumed that the material has negligible compressibility which means under hydrostatic pressure its volume change is avoidable. Its bulk modulus is comparable to that of metals or covalently bonded solids.

- 3- In contrast, its shear modulus is of the order of magnitude of  $10^{-5}$  of most metals, which means it is very compliant in shear.
- 4- It is assumed that material is isotropic.
- 5- The shear modulus is a function of temperature and by increasing temperature, the stiffness of material increases.
- 6- Material discharges heat when stretched.

Malvern explained, for isotropic hyperelastic material, the recoverable strain energy density with respect to the initial, unstressed configuration could be described as a function of the principal invariants of the Cauchy-Green deformation tensor (1969). The complete mathematical process is summarized by Kaliske and Rothert (1997). The key idea is to define a stress energy density function from which the stress can be derived by taking the partial derivatives conjugate to the strain. Hyperelastic material models can be categorized as phenomenological descriptions of observed behavior, mechanistic models deriving from arguments about the underlying structure of the material, and hybrids of phenomenological and mechanistic models. Each group has its subdivision but generally, a hyperelastic model should satisfy the Drucker stability criterion or Valanis-Landel hypothesis and for all models, a stress-strain relation is calculated by differentiating the strain energy density. A comprehensive review and applications of the hyperelasticity theory can be found in Bower (2010), Ogden (1997), Muhr (2005), Friswell (1996), and Green and Adkins (1960).

For this research, the constitutive model of the packer element has been considered as Mooney-Rivlin hyperelastic model, which classifies as one of the phenomenological model group. Considering most rubbers strongly resist volume change, it is a convenient assumption if it is presumed as perfectly incompressible. The strain energy density function for the generalized Mooney-Rivlin model, adopted from Mooney (1940), is described as below:

$$\bar{U} = \frac{\mu_1}{2} (\bar{I}_1 - 3) + \frac{\mu_2}{2} (\bar{I}_2 - 3) + \frac{K_1}{2} (J - 1)^2 \quad (1)$$

The stress-strain relation for incompressible rubber describes as:

$$\sigma_{ij} = \frac{\mu_1}{J^{\frac{1}{3}}} \left( B_{ij} - \frac{1}{3} B_{kk} \delta_{ij} \right) + \frac{\mu_2}{J^{\frac{2}{3}}} \left( B_{kk} B_{ij} - \frac{1}{3} [B_{kk}]^2 \delta_{ij} - B_{ik} B_{kj} + \frac{1}{3} B_{kn} B_{nk} \delta_{ij} \right) + K_1 (J - 1) \delta_{ij} \quad (2)$$

$\mu_1$ ,  $\mu_2$ , and  $K_1$  are material properties. For small deformations, the shear modulus and bulk modulus of the solid are  $\mu = \mu_1 + \mu_2$  and  $K = K_1$  respectively. For incompressible rubber, it should be used with  $K_1 \gg \mu_1$ .

$\bar{I}_1$ ,  $\bar{I}_2$ , and  $J$  are the alternative set of invariants of  $B$  (the left Cauchy-Green deformation tensor) that are more convenient for incompressible materials.  $\bar{I}_1$  and  $\bar{I}_2$  remain constant under a pure volume change. They are defined as:

$$\bar{I}_1 = \frac{I_1}{J^{2/3}} \quad (3)$$

$$\bar{I}_2 = \frac{I_2}{J^{4/3}} = \frac{1}{2} \left[ \bar{I}_1^2 - \frac{B_{ik}B_{ki}}{J^3} \right] \quad (4)$$

$$J = \sqrt{\det B} \quad (5)$$

$$I_1 = \text{trace}(B) = B_{kk} \quad (6)$$

$$B = F \cdot F^T \quad (7)$$

$$B_{ij} = F_{ik}F_{jk} \quad (8)$$

For derivation of stress-strain relation from the strain energy density, check Bower (2010).

## SOURCES OF PRESSURE TRANSMISSIBILITY REDUCTION

From classical physics, energy can neither be created nor destroyed, but in fact, it is always a trade-off between forms of energy. During any man-made energy transformation process, it is almost unachievable to extract the full potential of useful energy from its source, but instead, there are usually energy losses in forms that cannot be fully used. Mechanical energy is perhaps one of the early forms of energy that have been utilized. In its simplest form, when a spring is loaded, there is an “elastic” potential energy, which indicates that the restored energy is fully recoverable. If, on the other hand, a spring is loaded causing some internal changes, some part of the energy is lost in the changing process, which is irrecoverable and will be dissipated during the unloading process. It is the physical explanation of loading the packer element during the sleeve fracturing test although the best rheological representation of rubber materials is the three-parameter Maxwell model instead of spring. For this research, the packer element is considered as an axisymmetric deformable cylindrical membrane of uniform thickness ( $t$ ) composed of an elastic, homogeneous, isotropic and incompressible material possessing a strain energy function  $W(F) = \bar{U}(\bar{I}, J)$  as described in the previous section and reinforced by two families of perfectly flexible and inextensible helical cables. The

packer element is constructed with two layers of hard rubber; the inner runner bladder expands against the outer rubber sheath that has an embedded helical cage of cables. The cables of the two families form constant angles  $\pm \alpha$  with the generators of the undeformed membrane.

Pressure transmissibility is defined as the differential pressure between recorded/applied inflation pressure (pressure within the packer) and pressure acting on the formation (pressure on the borehole wall). Pressure transmissibility is the concept that should be considered when the problem deals with the packer element. In all multiple packer techniques for in situ stress measurement, packer(s) usually use either initiation of a fracture or isolation of the micro fracturing test interval, and since testing equipment works with applied pressure, pressure transmissibility is especially important.

The main sources of pressure transmissibility reduction from the packer element to the formation are:

- 1) membrane stiffness
- 2) membrane compression
- 3) lift-off pressure and touch pressure
- 4) compliance

### ***Membrane stiffness***

Calibration for pressure losses often known as probe calibration or membrane stiffness is undertaken by inflating the packer element in air to obtain the membrane resistance. The rate of expansion of the packer element in the air should be similar to that to be used in the tests on the ground. This can be simply achieved for strain-controlled tests but for stress-controlled tests, which are the case of pressurizing the packer element during the sleeve-fracturing test, the inflation rates during calibration are difficult to match in practice. The membrane resistance depends on the type of material, the membrane thickness, the nature of the reinforcement cables in the surrounding sheath (outer rubber) and temperature. The membrane is inflated following a similar procedure to the in-situ test. Recordings are taken of pressure and volume changes and the calibration curve can be illustrated. The shape of the calibration curve depends on the type of the membrane, age of the membrane, the number of tests carried out with the membrane and temperature.

### ***Membrane compression***

While membrane thinning is the change in thickness of the membrane as it expands due to the change of diameter, membrane compression is the change in its thickness due to an increase in pressure. The former effect should be strongly considered when the radial displacements are the matter of concern, for instance in pressuremeters or dilatometers, but the latter effect is a part of the system compression calibration for volume displacement measuring systems like the sleeve fracturing test or high pressure pressuremeter or dilatometer. It is accomplished by inserting the membrane in a metal cylinder of known geometry and elastic properties and pressurizing it. Readings are taken of pressure versus volume curve, and the slope of the curve combines the stiffness of the system and that of the calibration cylinder.

### ***Lift-off pressure and Touch pressure***

Pressurizing the packer element during the sleeve fracturing or isolation stage for hydraulic fracturing test includes two different parts. The first involves the pressure required to lift the membrane off the body of probe or mandrel and inflate the packer element enough to contact the borehole wall and the second relates to pressurizing the borehole wall. The pressure needed to lift the membrane is lift-off pressure and the pressure taken by the membrane to touch the borehole wall or fill the gap between the outer radius of the membrane and the borehole wall is touch pressure. Therefore, the relative applied pressure acting on the packed off zone on the borehole wall is inflation pressure minus those pressures that are taken by the membrane.

### ***Compliance***

Compliance of the packer element in sliding coupling straddle packer system is another factor affects the reduction of pressure transmissibility. According to Hauck and Baski (1998), *"in sliding coupling packer system for the reason that lower end of the inflatable element moves relative to the packer mandrel, hence in relation to a specific packed off zone of interest in borehole, the effective volume in the packed off zone can change slightly in response to changes of pressure in this zone. This volumetric change can be significant enough to adversely affect the applied pressure on the borehole wall. This effect that the packer can have on zone volume is often referred to as compliance"*.

Furthermore, the sliding end of the inflatable element can move along the packer mandrel and force the inflatable element to expand at a certain amount of inflation pressure and

cause the packer to seize in the well. Reinforcing the packer element in the sliding coupling system can cause less volumetric influence on packed off zones in a borehole due to pressure changes. Low compliance packers have little effect on the volume of a packed off zone as the zone pressures vary. The resistant shear stresses along the lower end coupling and mandrel and also the membrane itself and borehole wall resulting in the sliding of the coupling should be taken into consideration as parameters for reduction of the pressure transmissibility.

### MATHEMATICAL CALCULATION OF PRESSURE TRANSMISSIBILITY

For calculation of the relative pressure transmissibility, consider a tube with pressure inside and a rigid outer wall. Solving for radial stress at the rigid outer boundary and comparing this to the inside pressure, the approximate expression for pressure transmissibility can be obtained. The analysis of a thick wall internally pressurized cylinder under plain strain condition is considered to solve the problem. Figure 15 shows a cross section of the tube in cylindrical coordinates. The symmetry of axisymmetric tube indicates that the principal stress directions are radial ( $\sigma_{rr}$ ), circumferential ( $\sigma_{\theta\theta}$ ), and axial ( $\sigma_{zz}$ ).

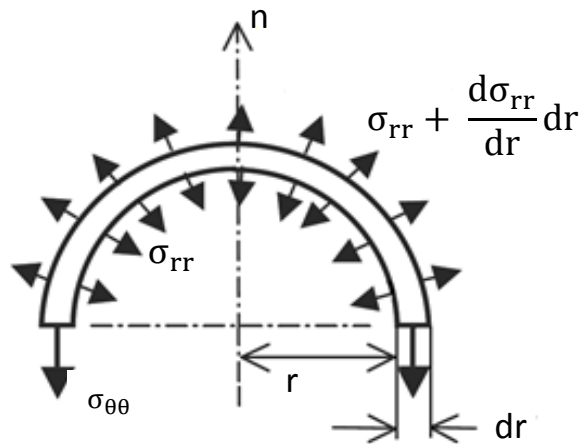


Figure 15. Semi-circular element cut from the tube in cylindrical coordinate system, z-axis is normal to the page

Zero body forces in equilibrium condition in n-direction results in:

$$r \frac{d\sigma_{rr}}{dr} + (\sigma_{rr} - \sigma_{\theta\theta}) = 0 \quad (9)$$

The circumferential strain and radial strain are:

$$\varepsilon_{\theta\theta} = \frac{u}{r} \quad (10)$$

$$\varepsilon_{rr} = \frac{du}{dr} \quad (11)$$

Where  $u$  is the radial displacement of the cylindrical surface of radius ( $r$ ).

Using Hook's law and solve simultaneously to drive equations for stress:

$$\sigma_{rr} = \frac{E}{(1-\nu^2)} (\varepsilon_{rr} + \nu\varepsilon_{\theta\theta}) \quad (12)$$

$$\sigma_{\theta\theta} = \frac{E}{(1-\nu^2)} (\varepsilon_{\theta\theta} + \nu\varepsilon_{rr}) \quad (13)$$

The stress equations (12) and (13) can be substituted into the equilibrium equation (9) to generate Navier equation for axisymmetric case:

$$\frac{d^2u}{dr^2} + \frac{1}{r} \frac{du}{dr} - \frac{1}{r^2} u = 0 \quad (14)$$

By solving this Cauchy-Euler differential equation, the general solution with two constants of integration will be produced:

$$u = c_1 r + c_2 r^{-1} \quad (15)$$

Substituting equation (15) into equations (10)-(13) yields:

$$\sigma_{rr} = \frac{E}{(1-\nu^2)} [(1+\nu)c_1 - (1-\nu)\frac{c_2}{r^2}] \quad (16)$$

The integration's constants  $c_1$  and  $c_2$  must be found using the particular boundary conditions. For this specific problem, we assumed the outer wall is rigid; thus  $u_r = 0|_{r=b}$  and  $b$  is outer wall of the membrane. The second boundary condition is  $\sigma_{rr} = p_i|_{r=a}$  and  $a$  is the inner wall of the membrane. Substituting these boundary conditions into Equations (15) and (16) yields:

$$c_1 = \frac{(1-\nu^2)}{E[(1+\nu)+(1-\nu)\frac{b^2}{a^2}]} p_i \quad (17)$$

$$c_2 = \frac{-b^2(1-\nu^2)}{E[(1+\nu)+(1-\nu)\frac{b^2}{a^2}]} p_i \quad (18)$$

Following this,  $\sigma_{rr}$  at the outer wall can be evaluated as:

$$\sigma_{rr}|_{r=b} = \frac{2p_i}{[(1+\nu)+(1-\nu)\left(\frac{b}{b-t}\right)^2]} \quad (19)$$

where  $b$  is the radius of the borehole or calibration case,  $t$  is the thickness of the packer element, and  $\nu$  is Poisson's ratio of the packer element. For  $b \gg t$  and  $\nu$  tending to 0.5, the pressure exerted on the borehole wall approaches the pressure inside the packer element.

Warren (1980) numerically investigated the packer-induced stresses during hydraulic fracturing test. Evans (1987) studied the mechanical behaviour of two different straddle packer systems, rigid coupling in which the packers were rigidly fixed at both ends to the mandrel, and sliding coupling in which both packer elements were fixed to the mandrel at the upper ends and were free to slide at the lower ends. In his investigation, he used the lengths of steel casing as borehole simulators and pressurized the packer elements in those steel casing instrumented with strain gauges. From the strain histories, the stresses applied to the casing by pressurized packer elements could be monitored. He found, in dual straddle packer system with sliding coupling (same as MDT), the applied pressure into the casing was about 85% of the inflation pressure and referred to it as sealing efficiency.

For a 4-inch-radius borehole, as Evans consider for his experiment, a packer element with 1-inch thickness and 0.35 Poisson's ratio, the pressure exerted on the borehole wall is found to be 80% of the applied inflation pressure according to Equation (19). There are several reasons for this small amount of difference; Evans mentioned that they just calibrated the circumferential strain gages in terms of their actual response to internal pressure, not all of the gages though, in his equation to calculate radial pressure, the axial strain plays a crucial role. Moreover, the thickness and the elastic property have been considered here as the packer element may have a minor difference from the material used in Evans' (1987) experiment.

Atkinson (2001) mentioned for single packer arrangements with two families of cords ( $\alpha=10^\circ$ ), lift-off and touch pressure is of the order of 0.08 MPa out of 10 MPa applied pressure. Kydonieffs (1969) and Atkinson and Peltier (1993) discussed the finite deformation of reinforced membrane. According to their theory, lift-off and touch pressures are calculable directly from Equation (20), provided that the manufacturer properties of packer element are known. Equation (20), which is a nonlinear integral and could be solved using iterative method results from the mapping between the deformed and undeformed shapes of the packer element.

$$\rho \int_1^{\Lambda_2} \frac{d\lambda_2}{\lambda_1 \sin \omega(p_0)} = l_0 \quad (20)$$

where:  $\lambda_1$  is meridian extension ratio and is a function of  $\lambda_2$ :

$$\lambda_1 = \left[ \frac{1}{(\cos(\alpha))^2} (1 - \lambda_2^2 (\sin(\alpha))^2) \right]^{1/2} \quad (21)$$

$2L_0$  is the initial length of the packer element,  $\lambda_2$  is radial extension ratio and  $\Lambda_2$  is packer extension ratio.  $\omega$  is the angle between the tangent of the deformed meridian and the axis of symmetry,  $\rho$  is the wellbore radius,  $\alpha$  is the initial angle between the cords and the cylinder generator, and  $p_0$  is lift-off and touch pressure. Since many parameters are unknown for the understudy case, it is impossible to calculate that part of the pressure transmissibility directly. Considering the boundary conditions applied for this solution, all the pressure transmissibility reduction factors have been considered with the exception of compliance. Compliance and lift-off/touch pressure are discussed in the next section.

## NUMERICAL EXPERIMENTS

A suite of numerical modelling studies has been conducted to evaluate the calibrated properties of the packer elements using Abaqus commercial software. The effect of different reduction factors on pressure transmissibility such as compliance and lift-off and touch pressure have also been investigated. For these purposes, two distinct models have been studied, one with the rigid outer casing to monitor the pressure outside of the packer and another with the steel calibration casing to monitor both the pressure outside of the packer and inside of the casing and the interaction between steel casing and packer element. Figure 16 shows the models with their discretization. Due to the axial symmetry about the z-axis and due to symmetry with respect to the  $z=0$  plane, only a quarter of actual geometry has been modelled.

Some results are presented for 171 mm-diameter packers with a different expansion ratio from 1.1 to 1.3 for evaluation the effect of lift-off and touch pressure on pressure transmissibility. The diameter of the casing varied from 200 to 220 mm. The initial length of the packer element considers 1 m, its initial thickness of 2.5 cm (1 inch), and its strain energy density parameters as Mooney- Rivlin model. These are, to the best of our knowledge, typical parameters for packer elements in MDT tools. For sliding coupling, both static ( $\mu_s=0.3$ ) and static-kinetic exponential decay friction ( $\mu_s=0.3-0.6$ ,  $\mu_k=0.2-0.4$ ) have been considered for tangential behavior of friction formulation on the surface of sliding the coupling on the mandrel at lower end and for the interaction between packer element and casing's wall, the friction coefficient has been changed in different models from 0.2-0.8 for static friction and 0.15-0.5 for kinetic friction according to the literature to study the effect of compliance.

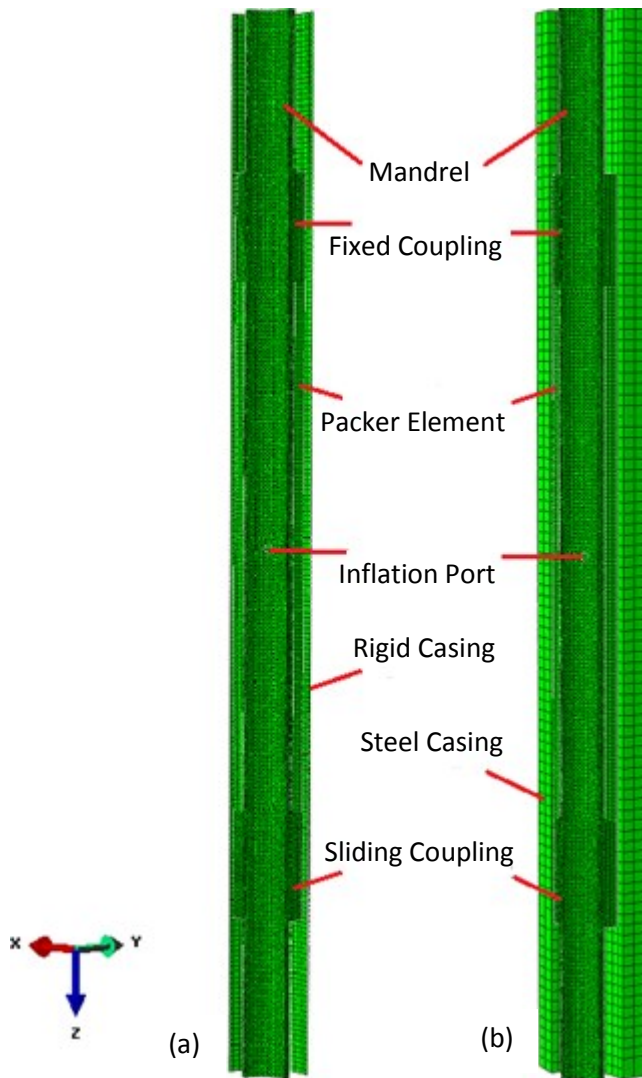
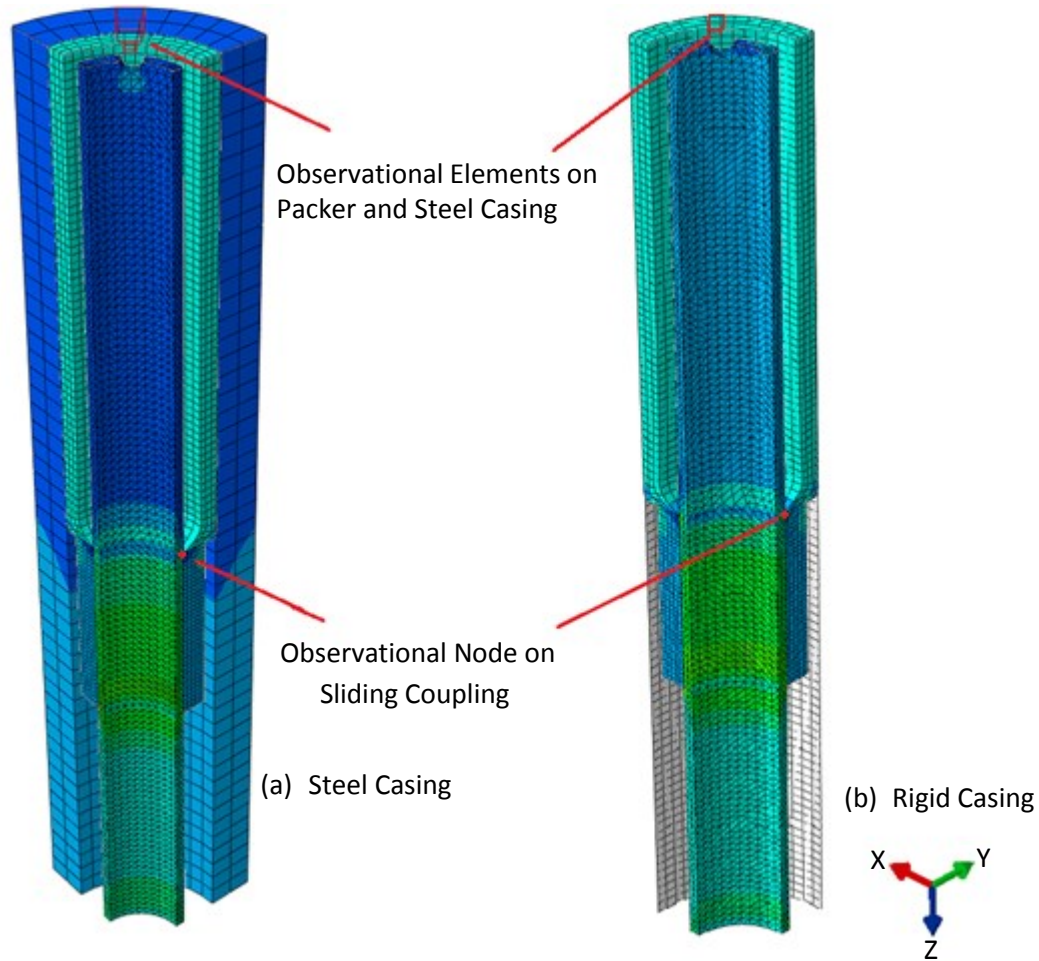


Figure 16. The finite element discretization of the region under study, (a) pressurizing the packer with rigid casing, (b) Pressurizing the packer with steel casing

Applied inflation pressure considered as 20 MPa and 25MPa in different models which are the commonly applied pressures during sleeve fracturing tests for pressurizing the packer element. The observational points have been chosen in the midpoint of the packer/casing interface for both packer and steel casings to monitor the radial/contact pressure, and another observational point has been selected on the sliding coupling for monitoring its displacement while pressurizing the packer. These points are illustrated in Figure 17, for the reason of getting better resolution, the half of the model in deformed shape has been shown.



**Figure 17. Observational elements and point used for monitoring the radial/contact pressure on the packer and casing and displacement on the sliding coupling, shown in deformed shape after pressurizing**

For the purpose of studying the effect of viscoelasticity of the packer element, material properties for membrane were considered as viscoelastic (Prony series parameters) – hyperelastic (Mooney- Rivlin model) material for some models. Parameters  $C_{10}$ ,  $C_{01}$ , and  $D_1$  are equal to  $\frac{\mu_1}{2}$ ,  $\frac{\mu_2}{2}$  and  $\frac{2}{K_1}$  in equation (1) respectively. For the cases where the viscoelastic part has been considered, the parameters  $g_{i(\text{prony})}$ ,  $k_i$ , and  $\tau_i$  have been assigned as 0.3, 0, and 0.1 correspondingly. Case #11 has the maximum expansion ratio (1.3) and for Cases #17 and #18, the friction coefficients of steel on steel have been considered as 0.6 for static friction and 0.4 for kinetic friction, respectively. Table 1 shows the different sets of hyperelastic parameters that have been used for different models. Some of the results of the numerical experiments are summarized in Table 2 and 3 and Figures 18 to 21.

**Table 1. Different sets of Hyperelasticity constitutive model's parameters used for modeling**

	1	2	3	4
$C_{10}$	3.2E6	3.5E6	2.2E6	5E6
$C_{01}$	0.8E6	0.9E6	0.5E6	1.1E6
$D_1$	0	0	0	0

**Table 2. Description of different numerical modeling cases**

Case #	Description of the model
1	First set of hyperelastic constitutive model parameters (Table 1) with viscoelasticity in rigid casing, 25 MPa as inflation pressure, $\mu_s=0.2$ , $\mu_k=0.15$ for packer-casing contact
2	Second set of hyperelastic constitutive model parameters without viscoelasticity in rigid casing, 20 MPa as inflation pressure, $\mu_s=0.2$ , $\mu_k=0.15$ for packer-casing contact
3	First set of hyperelastic constitutive model parameters without viscoelasticity in rigid casing, 20 MPa as inflation pressure, $\mu_s=0.25$ for packer-casing contact
4	Second set of hyperelastic constitutive model parameters without viscoelasticity in rigid casing, 20 MPa as inflation pressure, $\mu_s=0.2$ for packer-casing contact
5	First set of hyperelastic constitutive model parameters with viscoelasticity in rigid casing, 20 MPa as inflation pressure, $\mu_s=0.5$ , $\mu_k=0.3$ for packer-casing contact
6	First set of hyperelastic constitutive model parameters without viscoelasticity in rigid casing, 20 MPa as inflation pressure, $\mu_s=0.8$ , $\mu_k=0.3$ for packer-casing contact
7	First set of hyperelastic constitutive model parameters with viscoelasticity in rigid casing, 25 MPa as inflation pressure, $\mu_s=0.5$ , $\mu_k=0.4$ for packer-casing contact
8	First set of hyperelastic constitutive model parameters with viscoelasticity in rigid casing, 25 MPa as inflation pressure, $\mu_s=0.8$ , $\mu_k=0.5$ for packer-casing contact
9	First set of hyperelastic constitutive model parameters with viscoelasticity in steel casing, 20 MPa as inflation pressure, $\mu_s=0.2$ , $\mu_k=0.15$ for packer-casing contact
10	First set of hyperelastic constitutive model parameters with viscoelasticity in steel casing, 20 MPa as inflation pressure, $\mu_s=0.5$ , $\mu_k=0.25$ for packer-casing contact
11	First set of hyperelastic constitutive model parameters with viscoelasticity in steel casing, 20 MPa as inflation pressure, $\mu_s=0.5$ , $\mu_k=0.25$ for packer-casing contact
12	Third set of hyperelastic constitutive model parameters without viscoelasticity in rigid casing, 25 MPa as inflation pressure, $\mu_s=0.5$ , $\mu_k=0.4$ for packer-casing contact
13	Fourth set of hyperelastic constitutive model parameters without viscoelasticity in rigid casing, 25 MPa as inflation pressure, $\mu_s=0.5$ , $\mu_k=0.35$ for packer-casing contact
14	First set of hyperelastic constitutive model parameters with viscoelasticity in steel casing, 25 MPa as inflation pressure, $\mu_s=0.5$ , $\mu_k=0.4$ for packer-casing contact
15	Third set of hyperelastic constitutive model parameters with viscoelasticity in steel casing, 25 MPa as inflation pressure, $\mu_s=0.5$ , $\mu_k=0.25$ for packer-casing contact
16	Fourth set of hyperelastic constitutive model parameters with viscoelasticity in steel casing, 25 MPa as inflation pressure, $\mu_s=0.5$ , $\mu_k=0.25$ for packer-casing contact
17	Fourth set of hyperelastic constitutive model parameters with viscoelasticity in steel casing, 25 MPa as inflation pressure, $\mu_s=0.7$ , $\mu_k=0.5$ for packer-casing contact
18	Second set of hyperelastic constitutive model parameters with viscoelasticity in steel casing, 25 MPa as inflation pressure, $\mu_s=0.5$ , $\mu_k=0.4$ for packer-casing contact

**Table 3. Summary of the results of the modeling**

case #	P <sub>packer</sub> (MPa)	P <sub>casing</sub> (MPa)	dis <sub>sliding coupling</sub> (mm)	P <sub>lift-off/touch</sub> (MPa)	Pressure Transmissibility
1	20.8	—	3.5	0.75	0.83
2	15.9	—	3.3	0.78	0.8
3	15.8	—	3.36	0.67	0.79
4	16.05	—	3.5	0.83	0.8
5	15.67	—	3	0.67	0.78
6	15.4	—	1.55	0.67	0.77
7	20.8	—	3.6	0.75	0.83
8	20.4	—	1.8	0.63	0.82
9	16	15.95	3.1	0.67	0.8
10	15.86	15.6	2.8	0.67	0.78
11	16.5	16.4	28.7	0.9	0.82
12	21.44	—	4.5	0.5	0.85
13	18.75	—	2.7	1.2	0.75
14	20.85	20.4	3.2	0.63	0.82
15	21.8	21.6	4.05	0.5	0.86
16	18.75	18.6	2.5	0.9	0.75
17	18.75	17.9	2.49	1.13	0.72
18	20.45	18	3	0.68	0.72

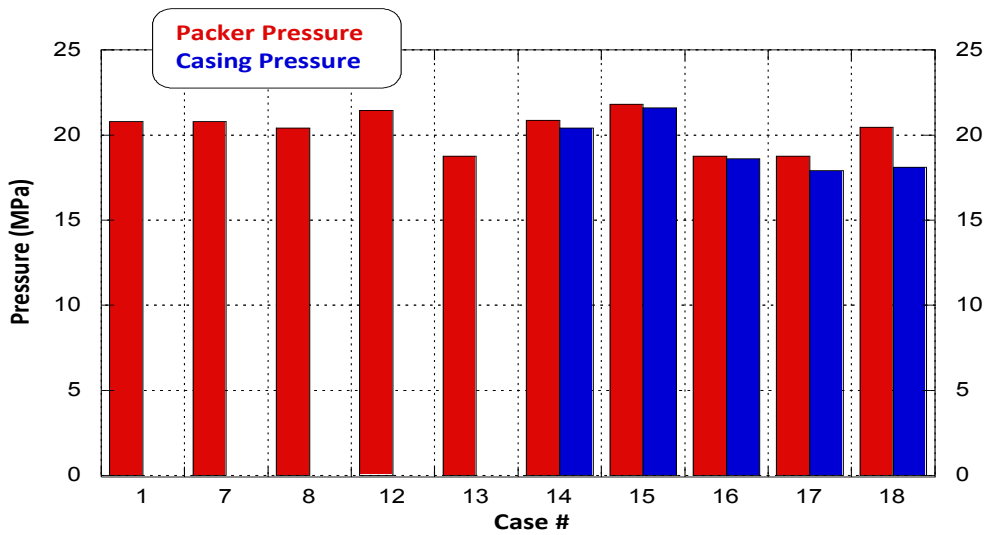


**Figure 18. Packer and casing pressure for different cases with 25 MPa inflation pressure**

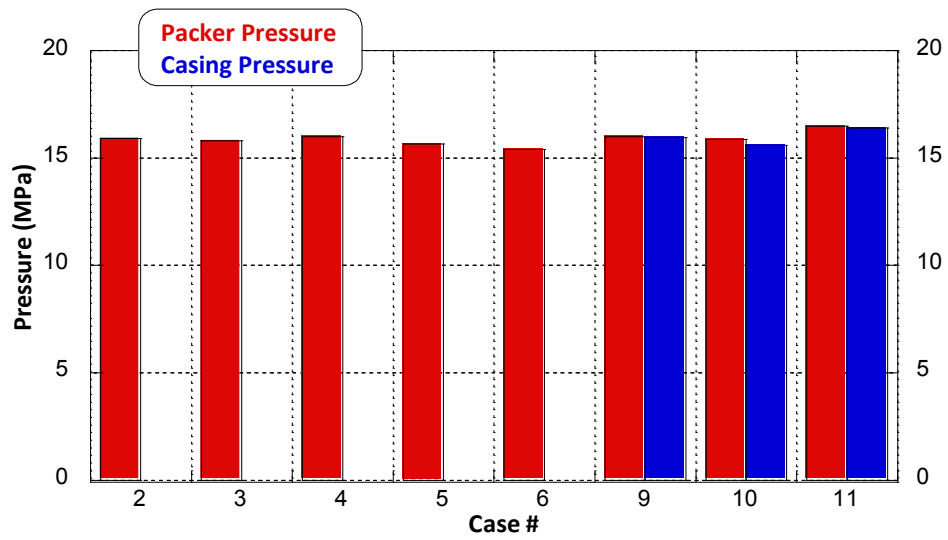


Figure 19. Packer and casing pressure for different cases with 20 MPa inflation pressure

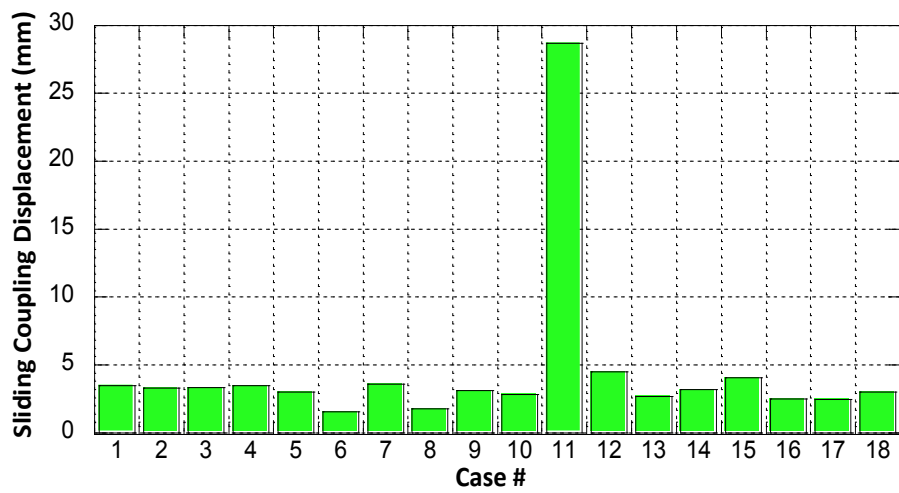


Figure 20. Sliding coupling displacement in different cases

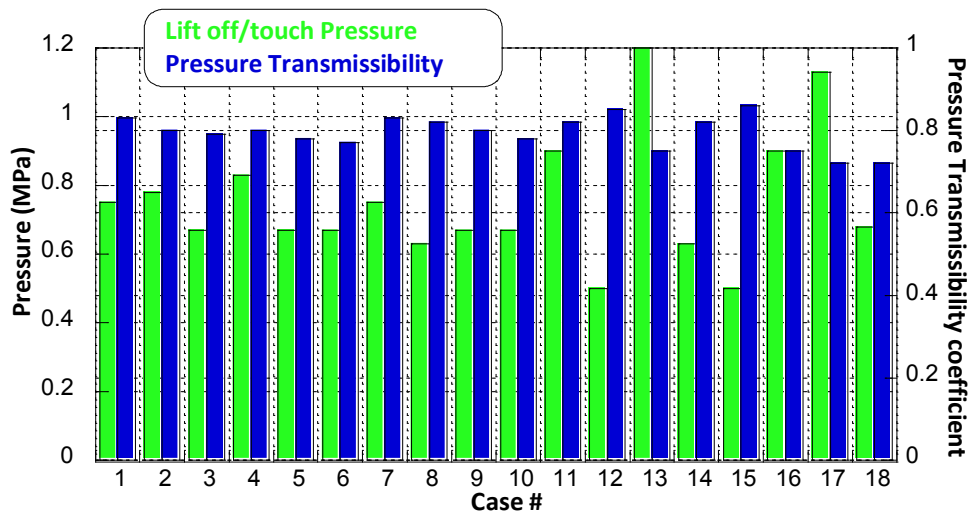


Figure 21. Lift-off/touch pressure and Pressure Transmissibility coefficient for different cases

The main conclusions to be drawn from these analyses are:

- comparing the results of Cases 12 and 13 or 15 and 16 show that pressure transmissibility decreases up to 12% by increasing the membrane properties and enhancement of the strength of the packer element;
- An increase in applied inflation pressure causes increases in pressure transmissibility as it is shown in the results of Cases 1 and 9 with the identical condition but different inflation pressure;
- The results of the analyses show that pressure transmissibility does not have noticeable sensitivity (up to 1%) towards kinetic exponential decay friction for tangential behavior of friction on the surface of packer/calibration casing after packer touched the casing (Cases 2 and 4 or 5 and 10);
- Although at first sight, the viscoelasticity of the membrane seems to play a crucial role in pressure transmissibility, further analyses reveal the fact that the later parameter is not that sensitive (up to 3%) to viscoelastic behavior of the packer element; however, the element age and inflation experience must be taken into account since reduction of pressure transmissibility is attributed to the number of usage of packer element;
- Pressure transmissibility decreases by increasing static/kinetic friction coefficient of the interaction surface of packer and calibration casing up to 5%;
- Lift-off and touch pressure are directly related to the maximum expansion ratio and packer element's properties, by increasing those parameters, lift-off and

touch pressure increases. Case #11 shows the results of the model in which the initial space between packer and calibration casing was 2.4 cm (maximum expansion ratio) comparing with the rest of the models with the initial space of 1.4 cm. Cases #13, 16 and 17 show the results of the models with the maximum value of packer element's properties. Lift-off and touch pressure are 5% of the applied inflation pressure in those cases while for the rest it is 2% to 3% of the applied inflation pressure. Atkinson et al. (2001) mentioned that the touch pressure of 0.079 MPa out of 10 MPa applied pressure for two families of cord with  $\alpha=10^\circ$  which this parameter is 0.075 MPa for just one family of cord and the same applied inflation pressure;

- An important factor that reflects the compliance effect on pressure transmissibility is the amount of displacement of sliding coupling during pressurizing the packer element. The latter parameter directly links with the maximum expansion ratio and the difference between the initial radius of the packer element and the radius of the borehole. The greater this difference, the greater the displacement and consequently the more friction between packer and borehole wall and between sliding coupling and mandrel which causes the larger stress resistance and less pressure transmissibility. Considering this fact, since the magnitude of displacement for the case under study is less than a couple of millimeters out of 1 m of the packer length with the actual expansion ratio of 1.1, the effect of compliance could be ignored for further analyses.
- Figure shows the sliding coupling displacement when the maximum expansion ratio is 1.3 or the difference between the packer element radius and borehole radius is 2.4 cm. Displacement of sliding coupling, under this circumstance, could be up to 3 cm (Case #11);
- Figure 23 shows the contact pressure applied on the steel calibration casing for Case #9. Average pressure on the steel calibration casing is 16 MPa.

With consideration of the results presented above, it is concluded that the best set of parameters for the packer elements that will be used in subsequent analyses are as described in Case 9.

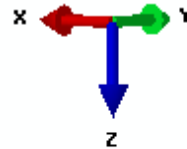
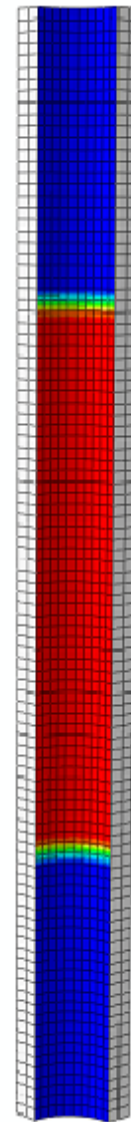
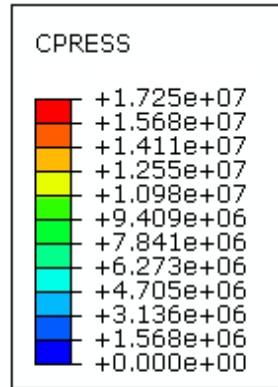
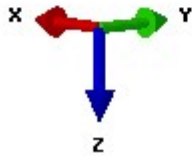
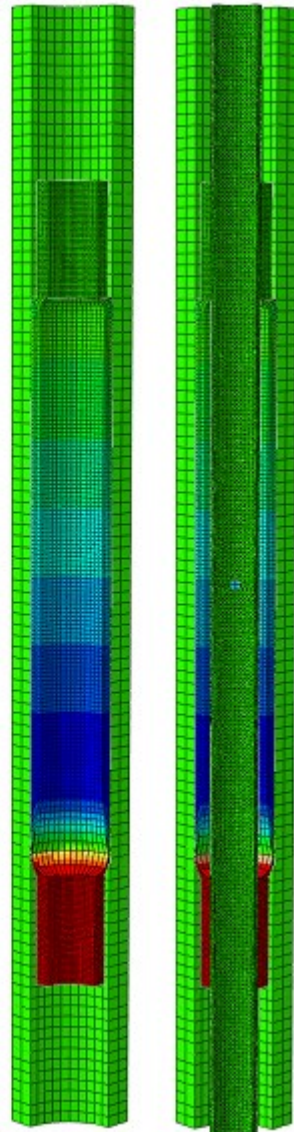
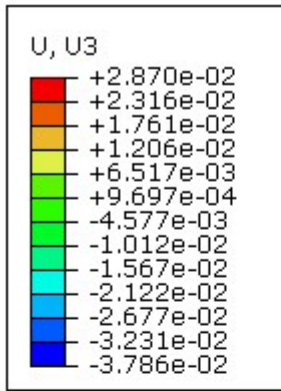


Figure 22. The Z axial displacement of the sliding coupling when the expansion ratio is high ( with (right) and without (left) showing mandrel (case#11), the maximum displacement is about 3 cm

Figure 23. Contact pressure on the steel calibration casing when applied inflation pressure is 20 MPa (case#9), the average value of contact pressure is 16 MPa

## CONCLUSIONS

A series of numerical simulations was performed with the purpose of calibration of the packer element's properties. Sensitivity analyses and parametric study that have been conducted on the parameters have an influence on the pressure transmissibility and the

results have been discussed. The best set of parameters for the packer element has been suggested.

As pressure transmissibility is generally less than unity, this requires that the internal packer pressure increase at a rate greater than the driving interval pressure increases. It has been shown that because pressure transmissibility was typically 0.80 for the packer elements, it is necessary for the packer pressure to increase at rate 1.2 times as great as the relevant interval pressure increase to maintain a seal during the hydraulic fracturing test and to prevent leakage at high interval pressure.

## FLUID-STRUCTURE INTERACTION ANALYSES OF SLEEVE FRACTURING TEST TO EVALUATE HORIZONTAL STRESS COMPONENTS OF CAP ROCK USING INVERSE TECHNIQUE<sup>6</sup>

**Abstract:** Among the methods that have been developed for in situ stress measurements, hydraulic fracturing has been extensively applied by the petroleum industry. MDT micro-fracturing tests with the purpose of stress data collection are very small, over an interval of about 1m, with a limited amount of fluid injection. The common technique for carrying out the stress tests in impermeable and weak rocks like clay shale, is to combine sleeve fracturing with micro- fracturing test where premature initiation of the fracture at the packer level can be avoided. Interpretation of data using micro-fracturing tests, however, reveals illogical magnitudes of minimum stress component in hard soil-soft rock such as clay shales in several cases. In this study inverse analyses have been employed to try and evaluate not only minimum horizontal stress but also the maximum component of horizontal stresses. Fluid-structure interaction (FSI) modeling techniques have been used for calibration of the data from computed pressure versus time curve to the equivalent data from the field, which is the only available and reliable data from in situ test. The packer has been pressurized as a part of a computational fluid dynamics (CFD) domain as well as mechanical domain and the mechanical response of the formation has been monitored and compared with the field data.

### INTRODUCTION

Knowledge of in situ stresses plays an essential role in any SAGD (steam assisted gravity drainage), CSS (cyclic steam stimulation) and CCS (carbon capture and storage) projects as an important factor for designing optimal injection pressure either for steam or CO<sub>2</sub>. Hydraulic-based stress determination tests such as MDT micro hydraulic fracturing are commonly used in petroleum industry. Since caprock need to be chosen for satisfying both mechanical and hydraulic integrity, they should be impermeable shale or clay shale with adequate strength and deformation properties. In any hydraulic-based stress test, the assumption is that rock behaves in a basically linear elastic or poroelastic manner till the point of fracture initiation during the sleeve fracturing or hydraulic fracturing phase.

---

<sup>6</sup> A version of this section was submitted to the Journal of Petroleum Science and Engineering

Clay shales exhibit considerable nonlinear behavior and plasticity and its departure from elasticity or onset of yield occur at significantly different stress and strain levels than the ultimate failure happens. That means this material can support a significant amount of plastic strain sometimes more than 10% without any macroscopic rupture that causes an unreliable indication of initial breakdown and interpretation for maximum and minimum stresses. The main challenge of MDT tests in clay shale is their mechanical behavior, which has a sharp contrast to the assumption of any other hydraulic-based tests. Similarly, the sleeve fracturing phase is difficult to interpret as the rock deforms plastically while the packer inflates and also because the packers induce stresses at the wellbore's wall which are not purely tensile, as will be discussed. Reviewing the mechanical behavior of hard soil- soft rock materials such as clay shale is pointed out that even if inelastic strains dominate the stress-strain relationship, elastic behavior is nevertheless present upon unloading, this elasticity being, most of the times, nonlinear and anisotropic although no technique or calculation model takes into account this particular mechanical behavior for stress measurements. Additional challenges during a test besides the plastic behavior of the formation, these layers include poor packer sealing, fracture by-pass, low fluid filtration, and natural defects which may cause other sources of problems especially in multiple packer techniques such problems of non-uniform strain levels and stress fields around the apparatus. Geotechnical engineers are used to viewing geological materials as either a rock, with engineering behavior primarily controlled by discontinuities or as a soil whose behavior is highly prone to the fabric and water content of the material. However, clay shales are intermediate between rock and soil regarding porosity, strength, and compressibility, and typically exhibit properties of both. These unusual properties of clay shales cause difficulties in analyzing their behavior.

The complex constitutive behavior of the clay shales that comprise the caprock for most SAGD and CSS projects in northeastern Alberta poses diverse problems for geotechnical investigations involving in situ stress measurement testing. It is well accepted that the vertical stress gradient at shallow depths (i.e., less than 500 m) ranges from 20 to 22 kPa/m. Consequently, a properly executed/interpreted MDT micro hydraulic fracturing test should never measure  $\sigma_{Hmin}$  larger than the density-derived  $\sigma_v$ . Yuan (2011) reported some MDT tests conducted for the target shallow reservoir by three different service providers on four different wells. Fracture closure pressures at 24 to 36 kPa/m were

reported to the ERCB (ERCB, 2010). Doubts should be raised about these values because they are larger than the density-derived  $\sigma_v$  around 21 kPa/m. Indeed, subsequent analyses led to a conclusion that most measurements provided data of very low confidence and were deemed inconclusive although one measurement did provide a closure pressure gradient of 20.6 kPa/m. Similar values have been reported by Chevron Canada Resources (2008) at two SAGD shale caprock boreholes and one gas storage shale caprock borehole in which MDT test interpreted fracture closure pressures between 30 and 34 kPa/m were reported. To solve the problem, it needs to well understand what happened during the test. For that purpose, knowing the in situ stresses is one of the important set of input data. From sleeve fracturing phase, the pressure versus time curve has been monitored. Knowing this curve depends on the response of the material towards pressurizing the packer, using inverse analyses, it is possible to evaluate the in situ stresses, which are the aim of this study.

#### **ANALYSIS APPROACH USING FSI ANALYSES**

The sleeve fracturing phase of micro hydraulic fracturing test was the focus for this component of the research. Sleeve fracturing is particularly advantageous in impermeable plastic shales, where hydraulic fracturing often results in a fracture that grows along the packer elements establishing a communication between the interval and the annulus and leading to premature failure of the test. Figure 24 shows the sleeve fracturing test. During the sleeve fracture phase, fluid pumped at a constant rate into the upper packer of MDT up to the maximum allowable pressure of the packer and pressure monitored and constantly recorded during the time of injection. Fracture initiation observes from breakdown or reaching a pressure plateau.

Fully coupled FSI (fluid-structure interaction) analyses have been considered for evaluation of the exact values of horizontal components of in situ stresses since the pressure versus time of the packer element was the only data available. The pressure was a result of injecting the fluid into the packer with a known rate of injection. The pressure versus time was a direct response to interaction between packer and formation while the packer was pressurized. Consequently, a numerical modeling technique is required that can simulate the deformation of the packer as a result of fluid flow into the packer while

at the same time capturing the mechanical deformation of the packer that results in a change in the fluid flow boundary conditions.

A common modeling technique for the numerical simulation of fluid mechanics is Computational Fluid Dynamics (CFD). The governing equations are the Navier-Stokes equations and the continuum hypothesis. Solid mechanics describes the behavior of solid bodies when exposed to external load. Usually, deformation, stresses, and strains of structures are computed using the Finite Element Method (FEM), thus, structural mechanics codes are often simply known as Finite Element codes, although the method is not limited to solid mechanics. The governing equations of solid mechanics problems are the mechanical equilibrium and Newton's laws of motion. These are completed by material equations that describe the behavior of different materials. For this research, packer-injection fluid interactions are studied using the fluid-solid interaction (FSI) co-simulation technique embedded in Abaqus (FEM) and CFD (CFD). Since the model deals with hyperelastic materials known as elastomer as a packer element, strong physics coupling is required resulting in a very complex modeling workflow.

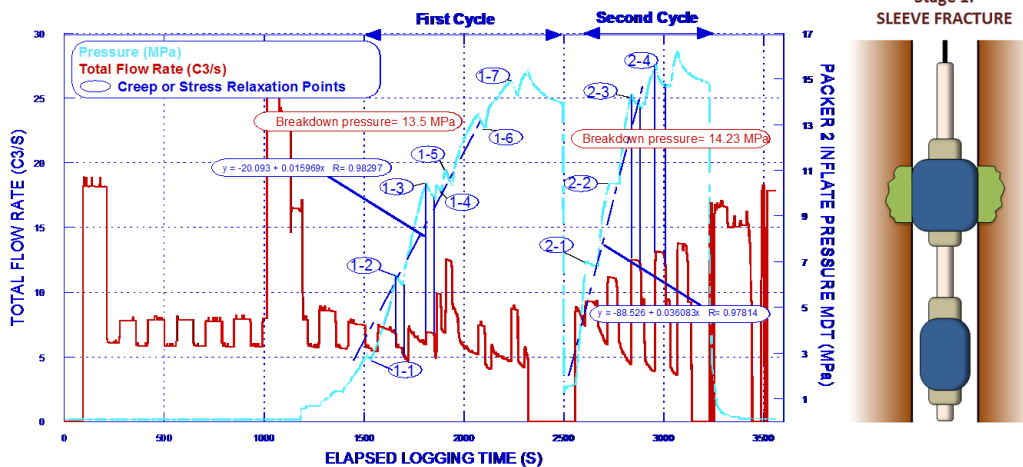


Figure 24. Attempted sleeve fracturing test before micro hydraulic fracturing

In strong physics coupling, each system is solved separately, but data is exchanged during each iteration step. Both codes compute one-time step (the only one in a stationary computation) at the same time. If one code has finished a step of the iteration, it sends its data to the other code, which uses it in its own iteration. Both iterations are continued until both converge, yielding a state that fulfils the governing equation of both physical domains. The only disadvantage in comparison to weak coupling is that convergence is

slower; thus, the computations are slower, but yield more precise results. The other attributes of the FSI analyses are: bi-directional coupling type, algorithm coupling scheme, and time incrementation rendezvousing.

## **DEFINING THE DOMAIN MODELS**

Due to the axial symmetry about the z-axis, only half of the actual geometry has been modelled. The mechanical/structure domain includes the formation and MDT probe. The formation is clay shale, which has been modelled using a Modified Cam Clay (MCC) constitutive model. The MDT probe consists primarily of the deformable packer element. The constitutive model of this elastomeric component has been considered as Mooney-Rivlin hyperelastic model, which is classified as one of the phenomenological model group. Previously in Chapter 4 has discussed the calibration of the mechanical properties of the packer element. The probe also has two couplings and a mandrel with a hydraulic port; the upper coupling is fixed to the mandrel, but the lower one can slide on the mandrel in the z direction. All these parts considered are steel. For sliding coupling static-kinetic exponential decay friction ( $\mu_s=0.5$ ,  $\mu_k=0.3$ ) has been considered for the tangential behavior of friction formulation on the surface of sliding the coupling on the mandrel at the lower end and for the interaction between the packer element and casing's wall. The penalty contact with the coefficient of friction of 0.5 as tangential behavior and hard contact as normal behavior is defined between the packer element and the borehole's wall. The model uses NLGEOM (nonlinear geometric effects) technique to account for non-linearity in the solution. Figure 25 shows details of the mechanical domain.

The CFD domain shown in Figure 26 models the flow region. The flow path includes the empty volume between the mandrel and unpressurized packer before fluid injection, which has been discretized using a volumetric 4-node linear fluid tetrahedron element. A hydraulic port on the mandrel was used as fluid inlet and the model has no outlet. No slip boundary condition has been used for the wall to capture the interaction surface between the mechanical domain and CFD domain. The physics of the CFD domain was boundary nonlinearity, finite volume computational method has been used and the analysis type was treated as laminar transient.

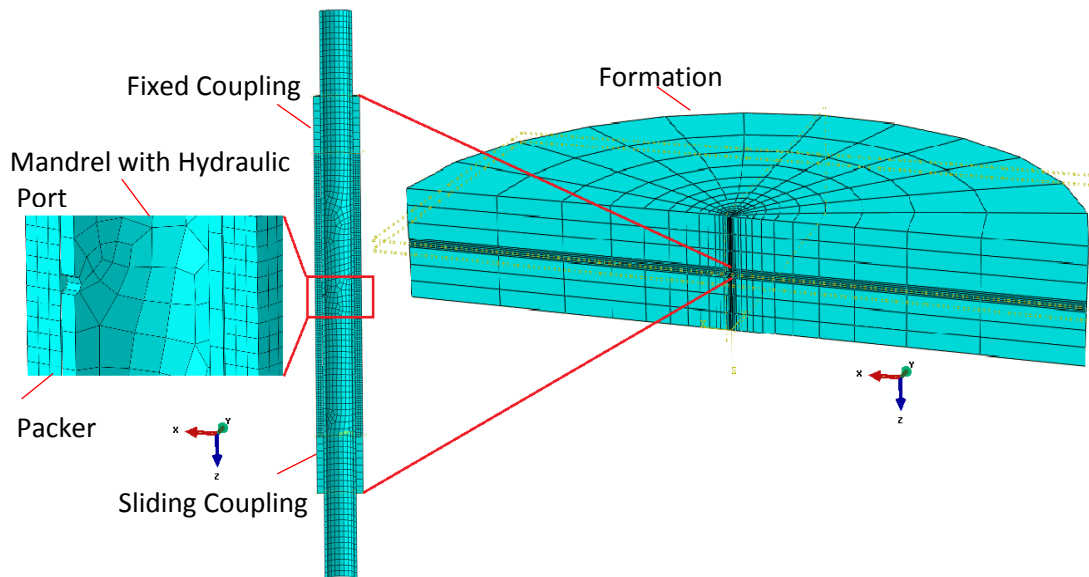


Figure 25. Mechanical Domain in Details

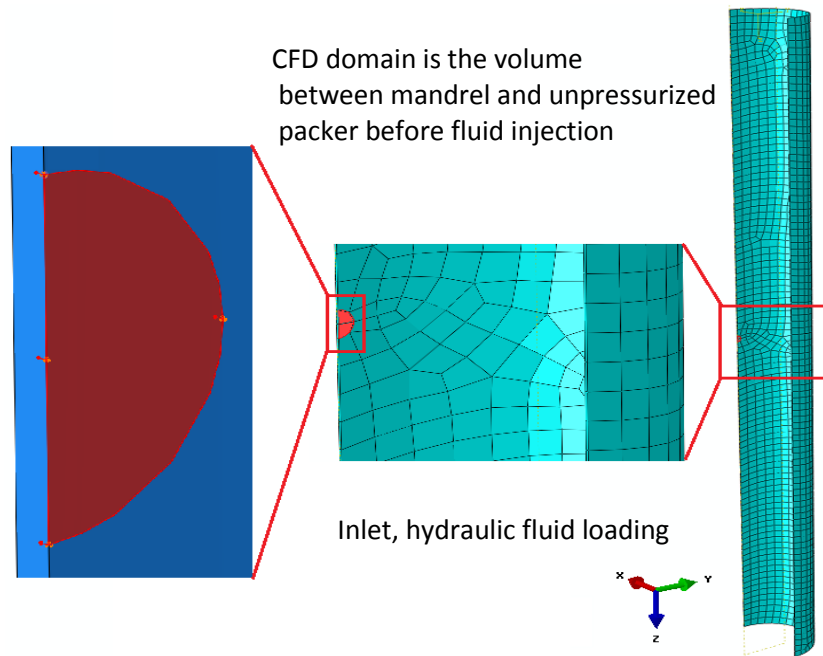
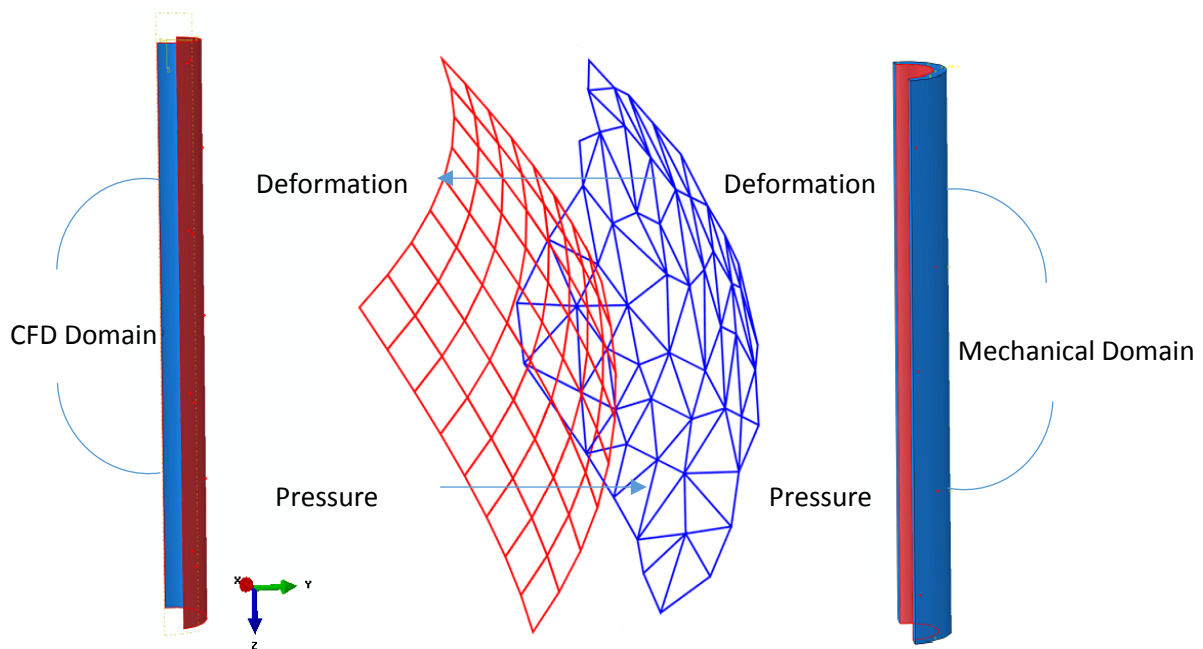


Figure 26. CFD Domain with Details, the hydraulic inlet with and without mesh

After defining the mechanical and CFD sub-domains, the fluid-structure interface must be defined. The interaction definitions include the interaction surfaces and desired solution quantities as illustrated in Figure 27. ABAQUS receives the fluid pressure from CFD and sends the resultant displacement to the CFD using the CSE (co-simulation engine). The inner surface of the packer and the outer surface of the CFD model are the interface or interaction surfaces for the mechanical and CFD domain, respectively. The ALE (Arbitrary Lagrangian-Eulerian) adaptive meshing technique has been used for remeshing during the analyses since both packer and formation are highly deformable.



**Figure 27. Interaction Surface between CFD and Mechanical Domains**

## SOLUTION METHODOLOGY

Sequential inverse analyses have been used to solve the FSI problem to history match the computational pressure versus time curve and equivalent curve monitored from the field test. The inverse analysis uses the mechanical response provided by experimental (measured) data to reconstitute the unknown characteristics of materials using iterative computations that progressively minimize the difference between the experimental data and the simulated ones. For the current problem, the iterative computations have been

done manually since the output data from FSI analyses was impossible to be extracted in a single ASCII file as a readable input file for any optimization code. Numerical iterations in the mechanical domain solves three different steps before the FSI analysis step. The first or initial step is where all pre-defined parameters and in situ stresses and other geomechanical properties such as anisotropic poroelastic parameters and permeabilities in different directions, plastic properties, degree of saturation and initial void ratio have been applied. The second step is called the geostatic step where timesteps are taken to stabilize the model and ensure model equilibrium. The third step involves a transient consolidation stage that involves drilling the borehole, stress release and applying mud pressure. These steps are followed by the FSI analysis, which is defined as dynamic, implicit step. During the simulation, the pressure acting on the packer insert in the fluid domain are mapped and transferred to the mechanical domain via CSE. The mechanical part of the model (i.e. FEM) then solves for the deformation and the resulting stress state in the structure. The interface deformation quantities are mapped and transferred from mechanical domain to the fluid domain via CSE. This process of exchanging solution quantities continues incrementally until the analysis completes. The results of the pressure-time curve of the packer are extracted and compared with the pressure-time curve from the field test.

## **GEOLOGICAL DESCRIPTION OF CSS AND SAGD PROJECTS**

Two different sites have been chosen for FSI analyses to determine the horizontal components of in situ stresses. One is the LP-SAGD project site at a shallow depth (63 m), and the other is a CSS project site at a depth of 337m.

### **LP-SAGD PROJECT SITE**

#### **-GEOLOGY**

In northeast Alberta, bitumen resources are at relatively shallow depths located about 100 meters below ground surface. The stratigraphic section in the project area consists of Devonian, Cretaceous, and Quaternary sediments overlying the Precambrian basement. The Devonian-aged strata underlie the prospective Cretaceous reservoir sediments and are separated by the sub-Cretaceous unconformity. The Cretaceous sediments are in turn overlain by a thin veneer of Quaternary sediments. The characteristics of these stratigraphic units are described in detail by Andriashek (2003), Bachu et al. (1993) and

Porter et al. (1982). The stratigraphic and geomechanical unit of interest is the Clearwater Formation, defined as the caprock for this project, and which is subdivided into the lower Wabiskaw Member and the Clearwater shale. This unit is lower Cretaceous-aged, and conformably overlies the McMurray Formation (reservoir).

According to the project operator (AOS, 2010), the Clearwater shale is pervasive in this area, conformably overlying the Wabiskaw Member, and is unconformably overlain by Quaternary sediments. The top of the Clearwater shale occurs at depths of 10 to 14 meters with the thickness of the Clearwater shale in the Project area typically ranging from 52 to 56 meters. The Clearwater shales are thick and laterally extensive throughout this area and are expected to provide an excellent cap rock for SAGD production.

#### - STRESS POLYGON AND LOCAL FAULTING REGIME

In the Western Canadian sedimentary basin, the regional stress state is dominated by the movement of the North American Plate tectonically (Bell et al., 2010). Zoback and Townend (2001) showed that stress measurements in different places all over the world indicate that the earth's crust is in a state of frictional failure equilibrium and the coefficients of friction are found to be within a relatively small range of 0.6 to 1 (Byerlee's law), and it is independent of the depth. Jaeger and Cook (1971, 1979) mentioned that the friction coefficient is always 0.6. In shale, it is assumed that the friction coefficient might be significantly lower than 0.6 especially at lower depth with lower effective pressure. Byerlee (1978) said in shale, clay particles have a lower friction coefficient due to water layers within crystallographic structure and development of pore pressure while it is deforming. Morrow et al. (1992) and Moore and Lockner (2006) mentioned that the higher the effective pressure is, the higher the frictional strength gets, and it is not just a function of pore pressure but effective pressure as well. Considering this, the friction coefficient of Clearwater clay shale has been reported as 0.5 (Shafie Zadeh and Chalaturnyk (2014)). It is necessary to consider the huge difference between the size of samples used for the experiments in the lab and the size of real faults and the variability of the roughness of the sliding surface. The coefficient of friction should be even higher than the value has been measured in laboratory scale. Assuming that stresses in the earth cannot be exceeded the frictional strength of pre-existing faults; thus, this parameter limits the possible range of stress magnitudes at any given depth and pore pressure. Stress polygon simply estimates the range of possible stress states at any given depth and pore

pressure using Anderson's stress and faulting classification system (1951). It illustrates the range of allowable values for horizontal components of principle stresses for normal, strike-slip, and reverse faulting regime. The local faulting regime for Clearwater clay shale strata of this site is unknown. For this study, it is assumed hydrostatic pore pressure state and not overpressure. Figure 28 shows the stress polygon for Clearwater clay shale at a depth of 63 m, which is the depth of test interval, for coefficients of friction (COF),  $\mu$ , equal 0.2, 0.6 and 1.

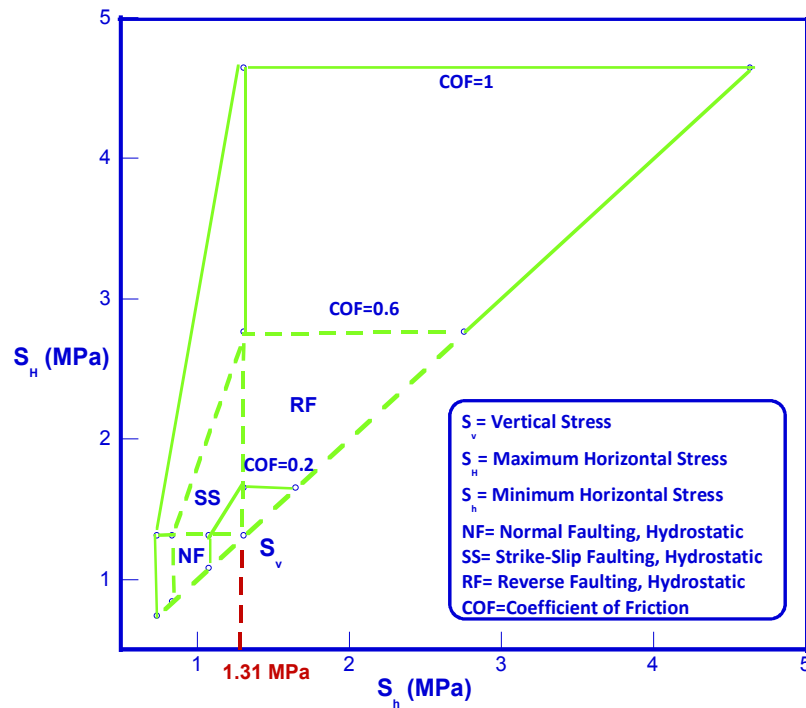


Figure 28. Stress Magnitude constraints for each faulting regime, Clearwater Clay Shale Formation at 63 m

## CSS PROJECT SITE

### -GEOLOGY

The caprock overlying the Clearwater Formation reservoir in this setting comprises the Lea Park Formation, the Colorado Group and Mannville Group consists of the Grand Rapids Formation and non-reservoir Clearwater Formation. The microfrac test intervals are in the first and second last formations of Colorado Group related to the upper Cretaceous.

The Colorado Group is a shale interval with a thickness from 170 to 180 m for wells 11-11 and 11-12 consequently. The variable thickness of these shales is the result of post-Cretaceous erosion combined with subsidence. These shales are the seals for fluids (including gas) in the Clearwater and Grand Rapids Formations. Similarly, they are an effective barrier to communication between any fluids associated with production from or injection into the Clearwater or Grand Rapids and fluids of the Quaternary freshwater aquifers. The Colorado Group consists of the following several units and among them, Joli Fou is the interested unit subjected to the microfrac test. Joli Fou Formation consists of dark gray, noncalcareous shale with very thin interbeds of siltstone and sandstone.

- STRESS POLYGON AND LOCAL FAULTING REGIME

The same methodology has been applied for defining stress constraints in a CSS project site at a depth of 337 m. Vertical stress has been calculated using density log data for each formation overlaid by Joli Fou Formation. Vertical stress calculated equal to 7 MPa and hydrostatic pore pressure state has been considered as 3.3 MPa. Stress polygon for the test interval depth is shown in Figure 29 for different coefficients of friction (COF),  $\mu$ . The faulting regime for this formation has been reported as normal faulting (CNRL, 2014).

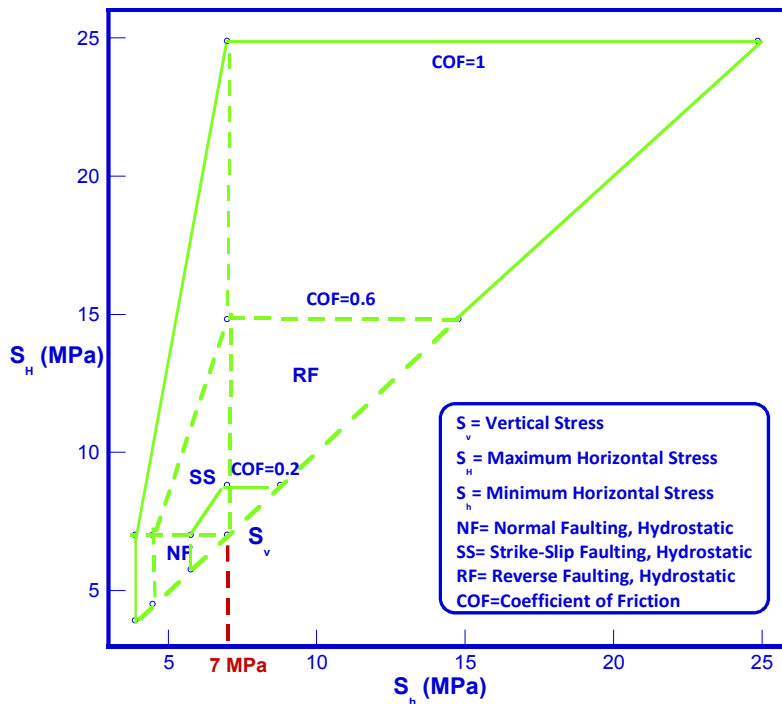


Figure 29. Stress Magnitude constraints for each faulting regime, Joli Fou Clay Shale Formation at 337 m

## RESULTS AND DISCUSSION

Shell Tellus Oil T32 has been used as an injection fluid in the field tests. It is defined as a Newtonian, incompressible fluid with dynamic viscosity as 30.78 cP, kinematic viscosity as 32 mm<sup>2</sup>/s, and density equal 855 kg/m<sup>3</sup>. The velocity of fluid has been calculated by knowing the total fluid volume injected during the specific injection time and the area of the hydraulic port. Laminar and transient flow have been considered for modelling. Material assigned to the couplings and mandrel was steel with the properties summarized in Table 4.

**Table 4. Steel properties used for couplings and mandrel**

	Density (kg/m <sup>3</sup> )	E(GPa)	$\nu$	$\sigma_{Ultim}$ (MPa)
Steel	7800	200	0.3	380

The packer element has been modelled as a hyperelastic material. The constitutive model for the packer element has been considered as Mooney-Rivlin. Parameters adopted from previous analyses are:  $C_{10}=3.2e6$ ,  $c_{01}=0.8e6$  and  $D_1=0$ . Viscoelasticity of the packer element has been considered, the parameters  $g_{i(prony)}$ ,  $k_i$  and  $\tau_i$  have been assigned as 0.3, 0, and 0.1, respectively. The first cycle of both sleeve fracturing tests has been modelled to evaluate the horizontal principal stresses at the two study sites. The following sections provide additional details specific to each study site.

### LP-SAGD PROJECT SITE

The sleeve fracturing test was conducted in Clearwater clay shale. Poroelastic-MCC plasticity model in a transversely isotropic medium is considered for simulating this material. The properties assigned to the model are summarized in Table 5.  $M$ ,  $\lambda$ , and  $\kappa$  are the material's constants that define MCC model,  $P_c$  is pre-consolidation pressure for this material,  $\nu_h$  and  $\nu_v$  are Poisson ratio in a horizontal and vertical direction, respectively and  $e_0$  is the initial void ratio.

**Table 5. Properties used for Clearwater clay shale model (Shafie Zadeh, Chalaturnyk (2015))**

	Poroelastic properties			Plastic properties			
	$\kappa$	$\nu_h$	$\nu_v$	$M$	$\lambda$	$P_c$ (MPa)	$e_0$
Clear water clay shale	0.038	0.4	0.13	1.2	0.077	6	0.51

Permeability has been considered 7.26E-9 m/s and 7.65E-12 m/s in horizontal and vertical directions correspondingly (Thomas (2010)). The density of mud pressure was 1150 kg/m<sup>3</sup>

according to the Schlumberger report (2009); thus, mud pressure with a gradient equal to 11.43 kPa/m has been applied on the borehole wall in the drilling and stress release step. According to the report, the bit size was 158.75 mm and the maximum string diameter for the MDT tool was 127mm. The pressure versus time curve for the sleeve fracturing test at this site is shown in Figure 30.

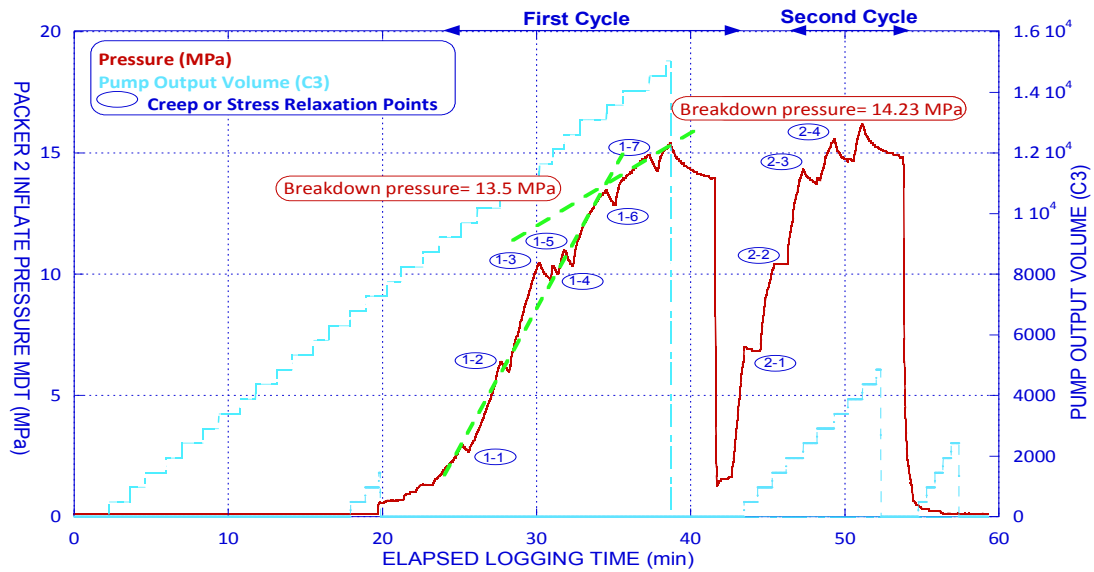


**Figure 30. Pressure versus time curve from in situ stress test for Clearwater clay shale at the depth of 63 m**

Several FSI and inverse analyses have been conducted to evaluate the best match between computed data and the field measured data. Figures 31-38 show some of the results.

The ratio of minimum horizontal to vertical effective stresses is lateral coefficient 1, and the ratio of maximum horizontal to vertical effective stresses is lateral coefficient 2. As little information was available regarding the local fracturing regime; different analyses with a different combination of lateral coefficient 1 and 2 have been conducted. Figure 36 illustrates results from a reverse faulting regime assumption and clearly indicates very little agreement with the field measured data. Figures 37 and 38 show results with a normal faulting regime assumption. These results, while providing a better fit of the field data than the reverse faulting assumption, point towards a strike-slip faulting regime assumption for obtaining the best fit. Consequently, the remainder of the analyses have assumed a strike-slip stress regime. The best match for this site is shown in Figure 39 when

a maximum horizontal stress of 1.61 MPa and a minimum horizontal stress of 0.91 MPa is chosen for the history match analyses. This corresponds to maximum and minimum horizontal stress gradients of 25.5 kPa/m and 14.3 kPa/m, respectively.

The stress distribution around the borehole after applying the pressure and equivalent pressure on the packer illustrate in Figure 40 when the borehole wall experience tensile stress for the first time during the pressurization. It shows the initiation of the crack will happen when the circumferential stress changes its nature from compression to tensile. Considering the tensile strength of the material as zero, the fracture initiation will occur when the packer pressure is about 13 MPa in the direction of maximum horizontal stress. The fracture initiation has been evaluated around 13.5 MPa from the pressure plateau shown in the P-T curve of field data in figure 30. It is another cross check that the current combination of principle stresses matches with the real stress field. The maximum tensile stress on the formation's wall reaches to 1.67 MPa at the end of the test. The formation displacement and plastic strain profiles after pressurizing the packer show in Figure 41. The maximum radial displacement is in the order of magnitude of 2.77 cm for the formation. The displacement profile, velocity contour and pressure contour for CFD domain show in Figure 42.

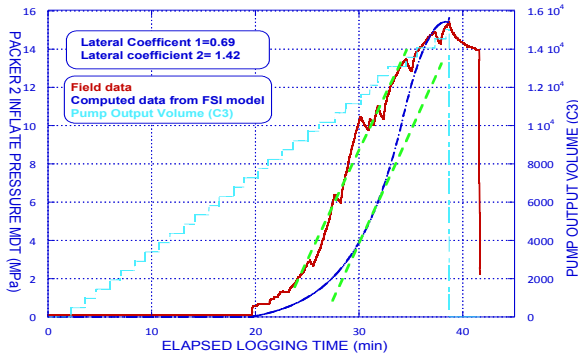


Figure 31. Pressure –Time curve for  $\sigma_H=1.6$  and  $\sigma_h=1.1$

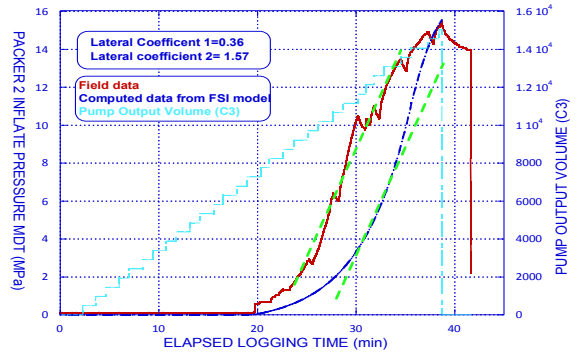


Figure 32. Pressure –Time curve for  $\sigma_H=1.7$  and  $\sigma_h=0.87$

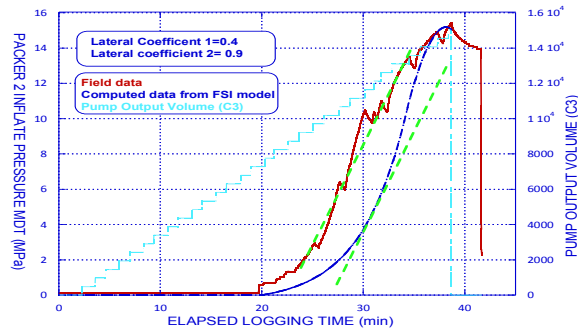


Figure 33. Pressure –Time curve for  $\sigma_H=1.24$  and  $\sigma_h=0.9$

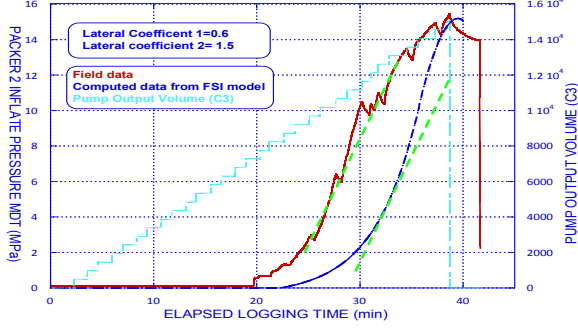


Figure 34. Pressure –Time curve for  $\sigma_H=1.66$  and  $\sigma_h=1$

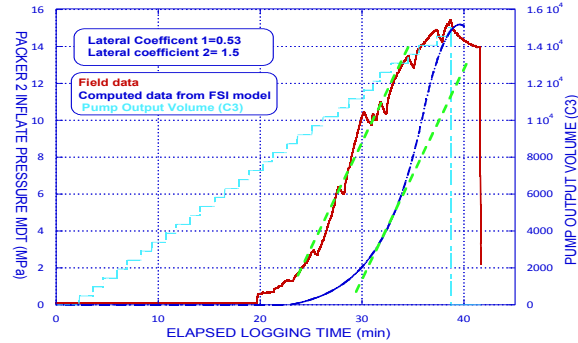


Figure 35. Pressure –Time curve for  $\sigma_H=1.66$  and  $\sigma_h=0.98$

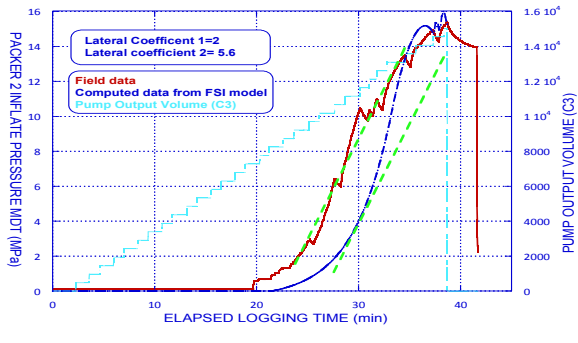


Figure 36. Pressure –Time curve for  $\sigma_H=4.5$  and  $\sigma_h=2$

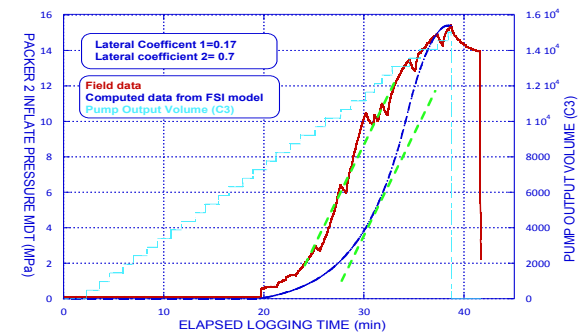


Figure 37. Pressure –Time curve for  $\sigma_H=1.1$  and  $\sigma_h=0.74$

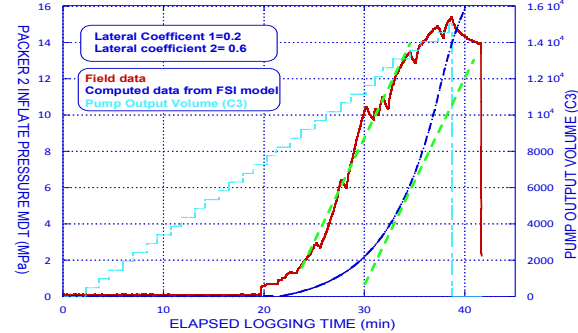


Figure 38. Pressure –Time curve for  $\sigma_H=1.03$  and  $\sigma_h=0.76$

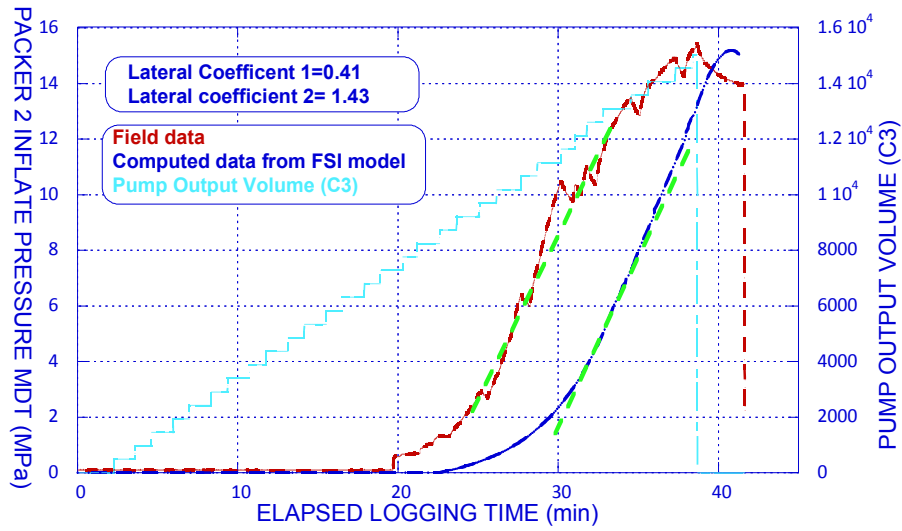


Figure 39. Pressure –Time curve for  $\sigma_H=1.61$  and  $\sigma_h=0.91$

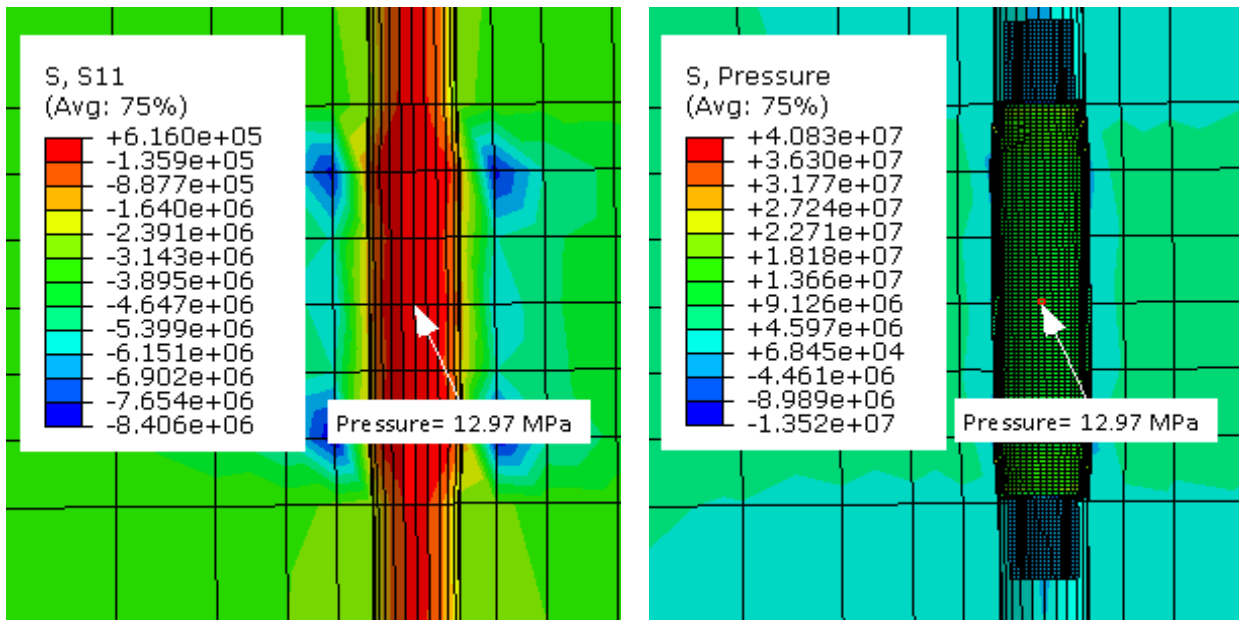


Figure 40. The point that circumferential stress (Pa) changes from compression to tension and its equivalent pressure (Pa) on the packer

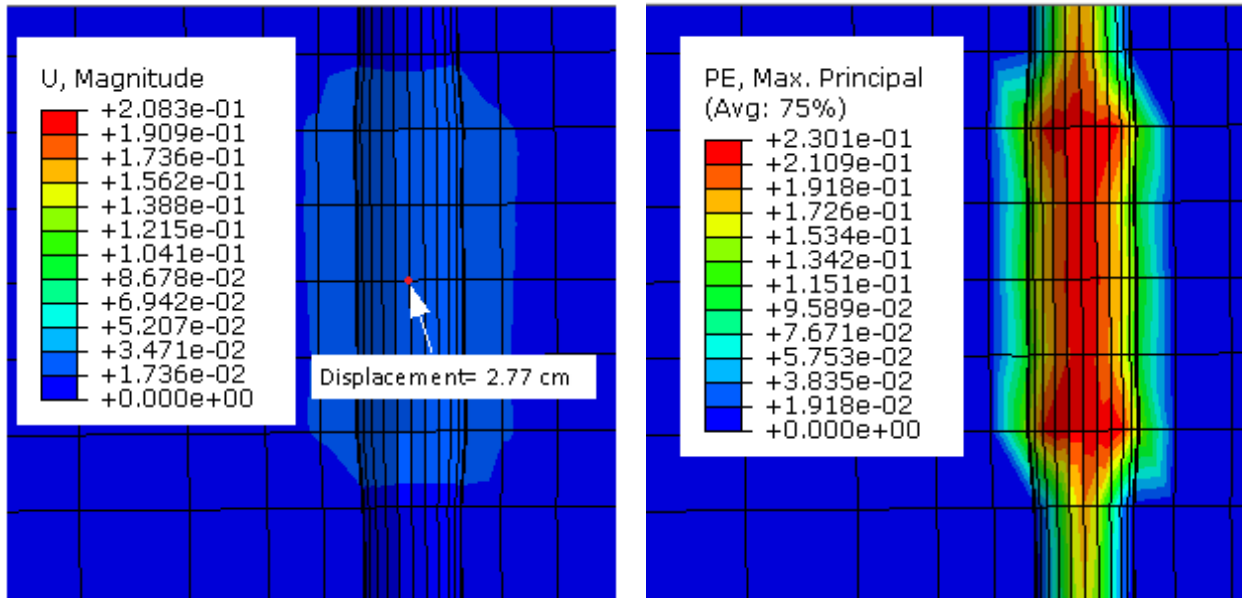


Figure 41. Deformation (m) and plastic strain profile at the end of the sleeve fracturing test at 63 m depth

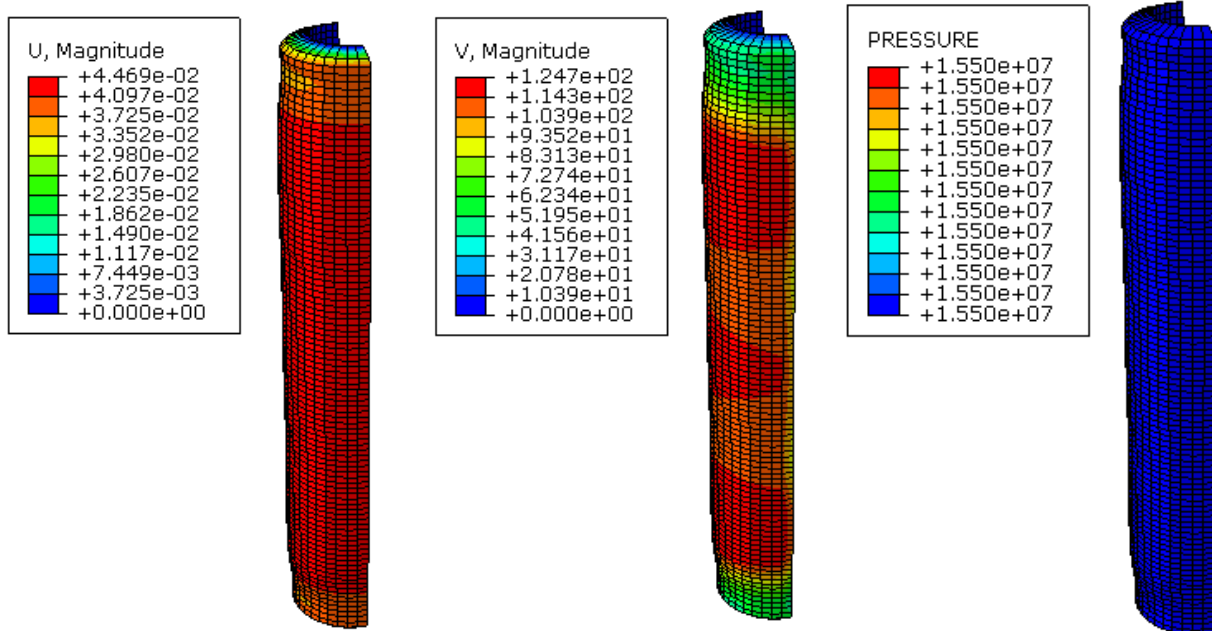


Figure 42. Displacement (m), velocity (m/s) and pressure (Pa) profiles of CFD domain

## CSS PROJECT SITE

One of the main cap rocks for the CSS project is Joli Fou Formation clay shale. Similar to the SAGD project site, the poroelastic-MCC plastic constitutive model in the transversely isotropic medium has been considered for modelling this site. Table 6 summarizes the assigned poroelastic and modified cam clay properties. Permeability in vertical and horizontal direction was considered as  $1.5E-11$  m/s and  $1.2E-8$  m/s respectively (Bachu et al (1993), Hydrogeology Baseline Report (2011)). Mud density applied to this borehole during the operation was  $1080$  kg/m<sup>3</sup> (Schlumberger report (2009)); active mud pressure, therefore, applied on the borehole wall during drilling and stress release step had a gradient equal to  $10.7$  kPa/m. According to the report, the bit size was  $200$  mm and the maximum string diameter for the MDT tool was  $171$ mm. The pressure versus time curve for sleeve fracturing test at this site was shown in Figure 43.

**Table 6. Properties used for Joli Fou clay shale model (Shafie Zadeh, Chalaturnyk (2016))**

	Poroelastic properties			Plastic properties			
	$\kappa$	$\nu_h$	$\nu_v$	M	$\lambda$	$P_c$ (MPa)	$e_0$
Clear water clay shale	0.0035	0.3	0.35	1	0.055	10-11.5	0.49

FSI analyses followed by inverse analyses have been conducted to estimate the far field stress state. Knowing the local fracture regime (CNRL, 2014), the focus of all analyses was on the normal faulting region's upper and lower limits for horizontal principal stresses. The results from this series of analyses are presented in Figures 44 to 51.

As shown in Figure 52, the best history match was obtained when maximum and minimum horizontal stresses were assumed to be  $6.25$  MPa and  $5.25$  MPa consequently. This corresponds to maximum and minimum horizontal stress gradient estimates of  $18.5$  kPa/m and  $15.6$  kPa/m, respectively. Figure 53 shows the circumferential stress, which changes from compression to tension (in the direction of maximum horizontal stress) and the corresponding packer pressure. The formation breakdown pressure, which has been assumed to represent the fracture initiation pressure has been evaluated as  $20$  MPa from field data and as seen in Figure 53, corresponds to a simulated packer pressure of  $18.9$  MPa. The maximum displacement of the packer and formation are illustrated in Figure 54. Figure 55 shows maximum plastic strain on the borehole wall after

pressurizing the packer. The displacement profile, velocity contour and pressure contours for the CFD domain are shown in Figure 56.

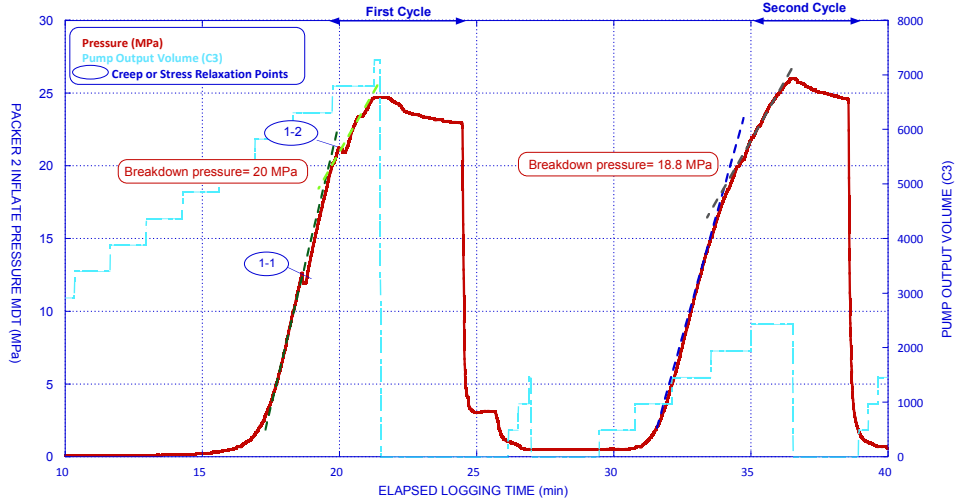


**Figure 43. Pressure versus time curve from in situ stress test for Joli Fou clay shale at the depth of 337 m**

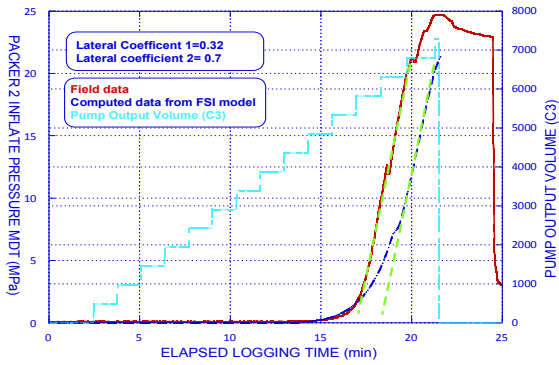


Figure 44. Pressure –Time curve for  $\sigma_H=5.9$  and  $\sigma_h=4.5$

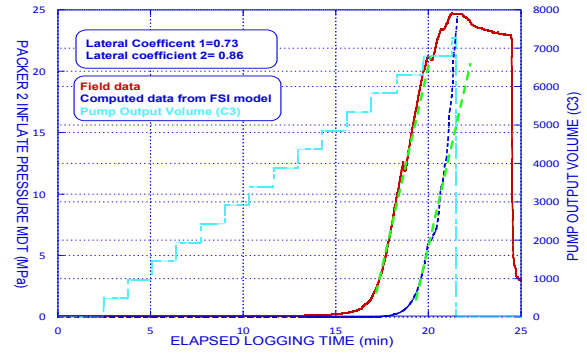


Figure 45. Pressure –Time curve for  $\sigma_H=6.5$  and  $\sigma_h=6$

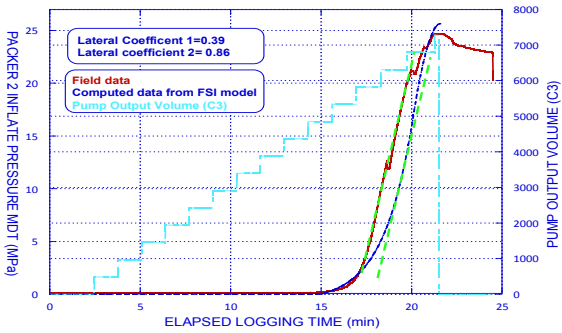


Figure 46. Pressure –Time curve for  $\sigma_H=6.5$  and  $\sigma_h=4.75$

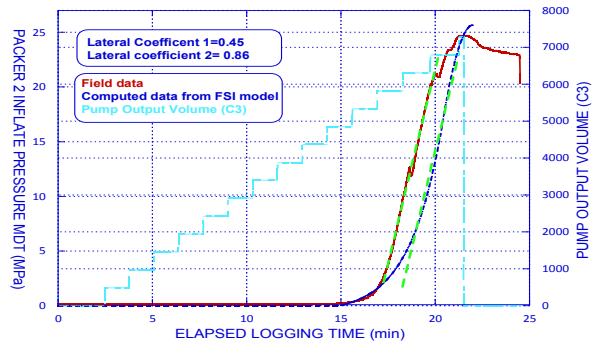


Figure 47. Pressure –Time curve for  $\sigma_H=6.5$  and  $\sigma_h=5$

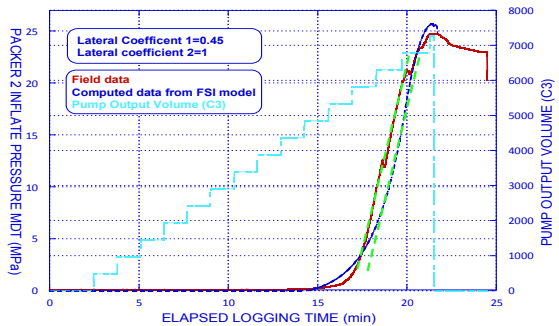


Figure 48. Pressure –Time curve for  $\sigma_H=7$  and  $\sigma_h=5$

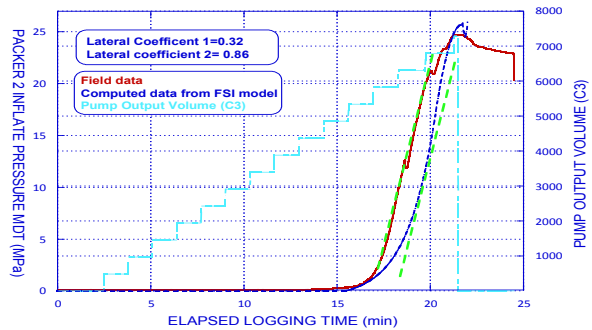


Figure 49. Pressure –Time curve for  $\sigma_H=6.7$  and  $\sigma_h=4.75$

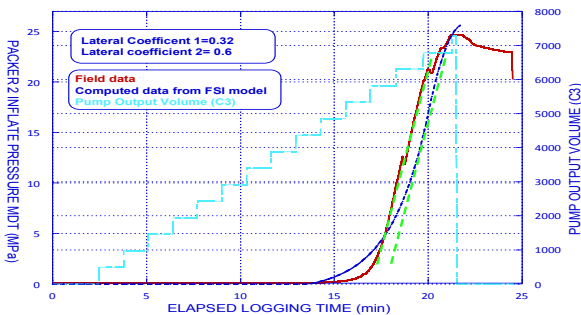


Figure 50. Pressure –Time curve for  $\sigma_H=5.75$  and  $\sigma_h=4.5$

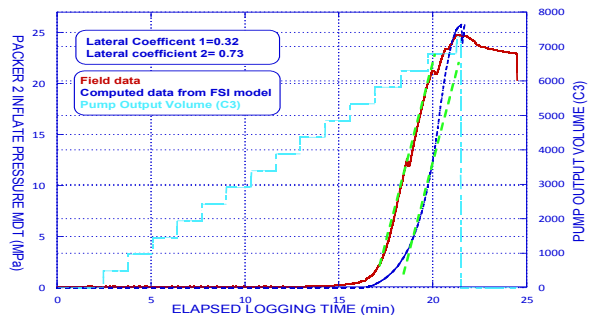


Figure 51. Pressure –Time curve for  $\sigma_H=6$  and  $\sigma_h=4.5$

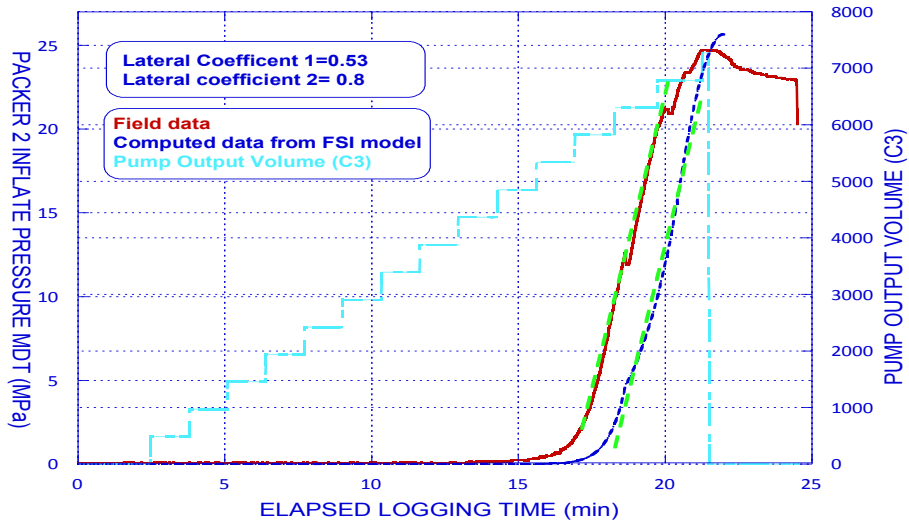


Figure 52. Pressure –Time curve for  $\sigma_H=6.25$  and  $\sigma_h=5.25$

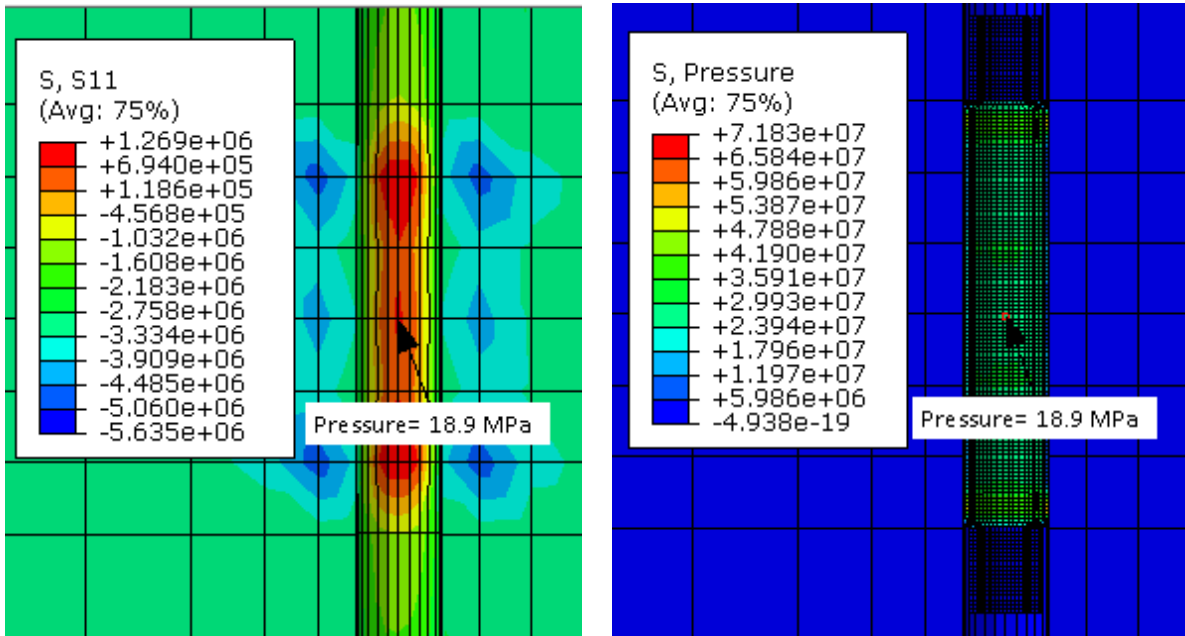


Figure 53. The point that circumferential stress (Pa) changes from compression to tension and its equivalent pressure (Pa) on the packer

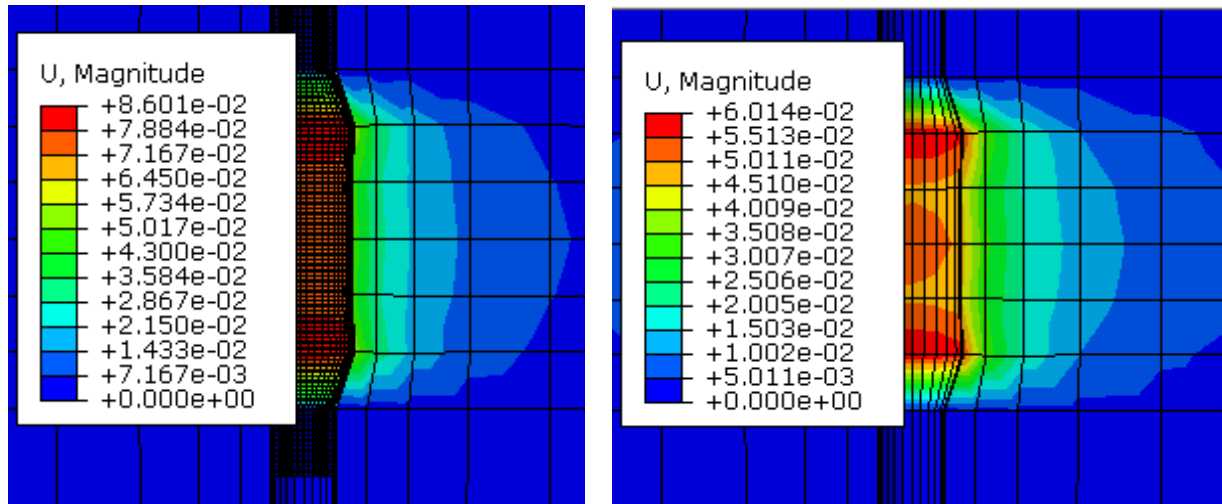


Figure 54. Total deformation (m) of the packer element (left) and formation (right) at the end of the test

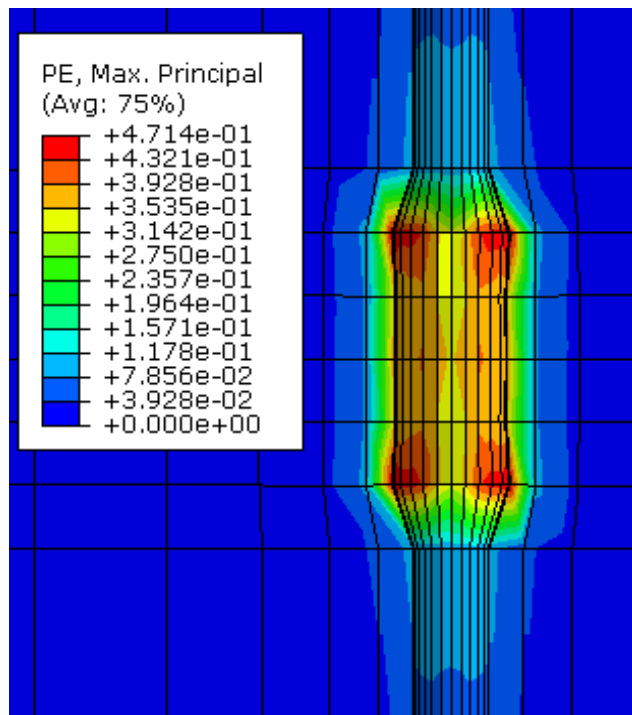
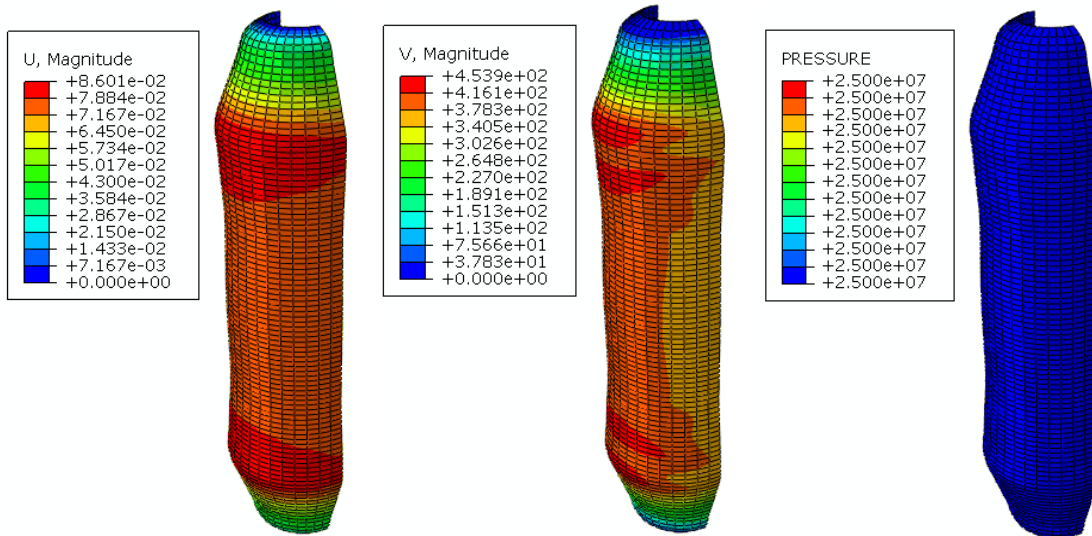


Figure 55. Maximum plastic strain on the borehole wall after pressurizing the packer



**Figure 56. Displacement (m), velocity (m/s) and pressure (Pa) profiles of CFD domain**

## CONCLUSION

Results from sleeve fracturing tests at two different sites in northeastern Alberta have been analyzed to evaluate the in situ stress state. Fluid structure interaction analyses using a co-simulation engine has been used for simulation, and an inverse technique has been adopted to evaluate the best match between computed data and field data. Results show that for shallow depths, the best match was obtained by assuming a strike-slip faulting regime condition. The upper and lower limits for minimum and maximum horizontal principal stresses were analyzed over a range between 1.31-2.76 MPa for maximum horizontal stress and 0.84-1.31 MPa for minimum horizontal stress. The maximum and minimum horizontal stress gradients were estimated 25.5 kPa/m and 14.3 kPa/m, respectively. The starting point of crack initiation - the point that stress changed its nature from compression to tension on the borehole wall - in the simulation was equivalent to the 13 MPa as the pressure on the packer element which has a fairly good agreement with the field data which was 13.5 MPa.

Similarly, analyses have been conducted for CSS project at the deeper level (337 m). The local fracture regime was known from previous studies; therefore, the focus was on the normal faulting boundary condition which was 4.5-7 MPa for both horizontal components of principal stresses. Having the maximum and minimum horizontal stresses as 6.25 MPa

and 5.25 MPa, the best fit between field data and computed data has been achieved. Knowing the depth of the test, the maximum and minimum horizontal stress gradients estimate 18.5 kPa/m and 15.6 kPa/m correspondingly. The initiation of the fracture, for this site, has been evaluated as the point that packer pressure is equal to 18.9 MPa, which is not a great match with the field data which shows the fracture initiation happened when packer pressure was about 20 MPa. One main reason can be addressed here is the difference between the real tensile strength of material which is normally more than 120 kPa as it is shown in Figure 53.

Since for both sites, the minimum component of principal stresses is horizontal, it is expected that any fracture would propagate in the vertical or sub-vertical direction.

**CHAPTER 5 FRACTURE MECHANISUM DURING MICRO HYDRAULIC  
FRACTURING TEST**

**LIKE GOD, IF THIS WORLD I COULD CONTROL  
ELIMINATING THE WORLD WOULD BE MY ROLE  
I WOULD CREATE THE WORLD ANEW, WHOLE  
SUCH THAT THE FREE SOUL WOULD ATTAIN DESIRED GOAL**

**“KHAYYAM”**

## **FRACTURE MECHANISM DURING MICRO HYDRAULIC FRACTURING TEST USING FULLY-COUPLED HYDRAULIC FRACTURING SIMULATION (XFEM)<sup>7</sup>**

Abstract: The extended finite element method (XFEM) is implemented to analyze fracture mechanics during a micro-hydraulic fracturing test in fully saturated, low permeable and poroelastic-plastic materials that exhibits strength/stiffness anisotropy. The propagation of a crack induced by the sleeve fracturing test prior to the hydraulic fracturing test is addressed by adding discontinuous enrichment functions to the standard finite element approach. Analyzing propagation of hydraulically driven fracture in a highly plastic materials such as clay shale with the limited volume of fluid injection during the micro-hydraulic fracture test is a fully coupled problem with at least four main processes: the flow of the injected fluid within the fracture, the flow of injected fluid within the pores, the porous medium response and deformation, and the fracture position and shape. The Abaqus coupled pressure/deformation extend finite element (XFEM) is used to model the propagation of the fracture resulting from the injection of the fluid while pore pressure/deformation continuum finite element (FEM) is used to model porous medium deformation and pore fluid flow. Results show that neither the rate of injection nor the volume of the injected fluid is sufficient within a clay shale formation to propagate fractures far enough away from the borehole to overcome the disturbed zone resulting from drilling and the sleeve fracturing stage of the test. This process has been investigated for two different thermal oil recovery projects (SAGD and CSS) with two different clay shale formations as their caprock.

### **INTRODUCTION**

Unconventional reservoirs, such as shale and tight gas reservoirs, have become significant recoverable hydrocarbon resources due to horizontal drilling and multi-stage hydraulic fracturing. Hydraulic fracturing can be broadly defined as the process by which a fracture initiates and propagates due to hydraulic loading applied by a fluid inside the fracture. Examples and applications of hydraulic fracturing are abundant in geomechanics including large scale hydraulic fracturing for stimulation of the reservoir with low permeability to

---

<sup>7</sup> A version of this chapter has been prepared for submission to the "International Journal of Fracture"

enhance conductivity, improvement of produced water reinjection, cutting reinjection, small scale hydraulic fracturing for in-situ stress measurement, collecting data prior to large scale hydraulic fracturing, and wellbore integrity analysis of drilling operations to prevent drilling fluid loss. Knowledge of the fracture configuration and dimensions as well other important factors is an obligation for the design and integrity of a successful hydraulic fracture operations, thus, different analytical and numerical studies have been developed to analyze fractures in geothermal reservoirs (Legarth et al. (2005), Rutqvist et al. (2008)) or oil and gas industry (Freeman et al. (2011), Vermilyen and Zoback (2011), Fisher and Warpinski (2012), Longuemare et al. (2001), Adachi et al. (2007), Perkins and Kern (1961), Nordren (1972)). Early PKN and KGD models were developed using plane strain geomechanics and assuming simple fracture geometries. Then, the pseudo-3D (P3D) model and the planar 3D model (PL3D) model were proposed for more realistic fracture shapes than those of the PKN and KGD models. These four models provide low computational cost, but they cannot correctly simulate the hydraulic fracturing in shale gas reservoirs. Hydraulic fracturing in shale gas reservoirs requires difficult modelling in fracture propagation and fluid flow, such as tightly coupled flow and geomechanics. Consequently, different algorithms have since been developed for simulating hydraulic fracturing in these class of reservoirs. An algorithm based on the dynamic update of the boundary conditions along the fracture plane based on a node splitting method was developed by Ji et al. (2009). Implementation of shear failure to hydraulic fracturing has been suggested by Nassir et al. (2012) though the effect of the porous medium was not considered. Dean and Schmidt (2009) used Ji's algorithm for tensile fracturing using different criteria based on rock toughness. The node splitting method was introduced first by Fu et al. (2012) based on elastic fracture mechanics. While the Ji algorithm can only be considered for vertical fracturing, Fu's algorithm is not restricted to the vertical fracturing, however, 3D fracturing problems cause more complexity compared with the algorithm suggested by Ji et al. (2009). Ji's method can couple flow and geomechanics for considering leakoff of the injected fluid into the reservoir, but Fu's algorithm allows fluid flow along grid blocks so the leakoff cannot properly be modelled. Extended finite element methods (XFEM) have been studied by Moes et al. (1999) and Borja (2008) in the computational mechanics community with the intention of model discontinuity in displacement. They introduced discontinuous interpolation functions that do not require

remeshing after fracture propagation. Legarh et al. (2005) adopted XFEM to hydraulic fracturing, but the application theoretically has the same difficulties as the method suggested by Fu et al. (2012) and Ji et al. (2009). The significant differences between the results with and without poroelastic effects show that this phenomenon can be substantial for low permeable and high compressible materials such as shale/clay shale with low compressible and viscosity fluid, such as water injection (Kim et al. (2011, 2012)). Therefore the computational modelling of hydraulic fracturing of porous media is a challenging task. The non-linear coupling between governing equations introduces complexity since the process involves at least four different phenomena and their interaction including the flow of the injection fluid within fracture, the flow of injection fluid within the pores, the deformation of the porous medium induced by hydraulic load of the fracture and its response to that, and the fracture propagation which typically occurs in heterogeneous formation subjected to anisotropic in-situ stress field. There are various commercial hydraulic fracturing simulators using for different purposes (Clearly (1980), Meyer (1989), Warpinski et al. (1994)) though they rely on simplified assumptions such as planar and symmetric fractures with respect to the wellbore, Fracture geometries limited with few geometric parameters, The unbounded formation which should be modeled using linear elasticity theory resulting in an integral equation relating fracture opening and fluid pressure, linear elastic fracture mechanics without consideration of poromechanical effects, one-dimensional leakage of injected fluid from fracture into the formation.

To accurately model the micro hydraulic fracturing test under realistic situations, a multi-physics numerical simulator that combines the complex coupling between the injected fluid, the pore fluid, the rock deformation, and the fracture configuration has been chosen. Fully-coupled hydraulic fracturing simulation capabilities that influence (i) the existing Abaqus non-linear soil transient consolidation analysis solver, and (ii) Abaqus extended finite element method (XFEM) for modelling propagating discontinuities have been used for this study. In XFEM, a new tool has been assimilated into the existing Abaqus/Standard coupled pore fluid diffusion and solid stress porous media analysis solver which is an enriched version of the continuum coupled pore fluid diffusion/stress elements. This tool is capable of stimulating arbitrarily oriented discontinuities in

displacements and pore pressures while concurrently the fracturing fluid flow along the fracture can be modelled.

## **ROCK FRACTURE MECHANICS THEORY**

The development of rock fracture mechanics primarily refers to the initiation and propagation of an individual crack or cracks in rock subjected to a particular stress field where those cracks may be pre-existing or induced as a result of applied load/pressure. Fracture mechanics, linear or non-linear elastic fracture mechanics, dynamic fracture mechanics and statistical fracture mechanics has well developed during the past decades for understanding the brittle failure/fracture of artificial man-made high strength materials such as metal alloys and studying crack initiation and propagation in these materials in mechanical engineering world (Rice JR (1968), Hutchinson (1979), Hellan (1984), Lawn (1993), Anderson (1995), Broberg (1999), Sanford (2003), Janssen et al. (2004), Perez (2004), Zehnder (2007)). However, fracture mechanics principles were not well developed with rock mechanics and natural materials such as soils and rocks. Most natural rock/soil structures are mainly subjected to 3D compressive stresses which may vary in magnitude and orientation in position. Moreover, rock and soil themselves should be considered as porous media which add complexity to the theory of fracture mechanics and the analysis of crack initiation and propagation in natural materials when fluid flow and fluid pressure are considered. There are various factors that can distinguish the fracture processes in natural materials from pure fracture mechanics applied in man-made materials. Heterogeneity, discontinuity, anisotropy, in-situ stress field, environmental conditions such as pore pressure, temperature, deviatoric stress, strain rate are such factors.

In rock fracture mechanics, there are two distinct main applications. One is related to prevention of failure in which fracture growth or movement along a pre-existing or induced fracture is prevented from propagating as it relates to the stability improvement of rock structures, slope stability, and underground openings such as caverns, tunnels, under pressure tunnels. The other one is concerned with the generation and propagation of new fracture as in hydraulic fracturing, rock fragmentation by cutting, drilling and blasting optimization. The physics and mechanics of the fracturing process are the same and the applications dictate how the important parameters are used. In the current study,

the primary focus is on the application of rock fracture mechanics for hydraulic fracturing. Rock fracture mechanics and its principles and applications have been extensively discussed by Whittaker et al. (1992).

Hydraulic fracturing involves at least four main processes: porous medium deformation, pore fluid flow, injecting fluid flow and fracture initiation and propagation. The governing equations for each of the coupling processes and the constitutive relations include equilibrium equation and constitutive equation for the porous medium (Biot's theory of poroelasticity), continuity equation for the pore fluid, continuity equation for the injecting fluid, momentum equation for the pore fluid (Darcy's Law), and momentum equation for the injecting fluid (Reynold's Lubrication theory).

In an anisotropic, poroelastic domain experiencing quasi-static deformation, the equilibrium equation enforced by Abaqus in the presence of body forces  $b$  are given by:

$$\sigma_{ij,j} + b_i = 0 \quad (1)$$

Both stress and strain tensors are symmetric.

$$\sigma_{ij} = \sigma_{ji} \text{ and } \varepsilon_{ij} = \varepsilon_{ji} \quad (2)$$

While the poroelastic constitutive relation between stresses and strains is given by:

$$\sigma_{ij} - \sigma_{ij}^0 = 2G\varepsilon_{ij} + \left(K - \frac{2}{3}G\right) \varepsilon_{kk} - \alpha(p - p_0)\delta_{ij} \quad (3)$$

In which  $\alpha$  is Biot's coefficient,  $G$  and  $K$  are Shear modulus and Bulk modulus. Abaqus is formulated in terms of Terzaghi effective stresses,  $\sigma'$ , defined for fully saturated media as (Abaqus 2014, Zielonka et al. 2014):

$$\sigma'_{ij} = \sigma_{ij} + p\delta_{ij} \quad (4)$$

Regarding the latter, the constitutive relation takes the form:

$$\sigma'_{ij} - \sigma'_{ij}^0 = 2G\varepsilon_{ij} + \left(K - \frac{2}{3}G\right) \varepsilon_{kk}\delta_{ij} - (\alpha - 1)(p - p_0)\delta_{ij} \quad (5)$$

Defining effective strains as:

$$\varepsilon'_{ij} = \varepsilon_{ij} - \frac{\alpha-1}{3K}(p - p_0)\delta_{ij} \quad (6)$$

The constitutive relation simplifies to:

$$\sigma'_{ij} - \sigma'_{ij}^0 = 2G\varepsilon'_{ij} + \left(K - \frac{2}{3}G\right) \varepsilon'_{kk}\delta_{ij} \quad (7)$$

The pore fluid continuity equation is given by:

$$\frac{1}{M} p' + \alpha\varepsilon'_{kk} + v_{k,k} = 0 \quad (8)$$

where  $v_k$  is the pore fluid seepage velocity, and  $M$  and  $\alpha$  are Biot's modulus and Biot's coefficient, respectively. These two poroelastic constants are defined by:

$$\frac{1}{M} = \frac{\phi_0}{K_f} + \frac{\alpha - \phi_0}{K_s} \quad (9)$$

$$\frac{1}{K_s} = \frac{1 - \alpha}{K} \quad (10)$$

where  $K_f$  is the pore fluid bulk modulus,  $K_s$  is the porous medium solid grain bulk modulus, and  $\phi_0$  is the initial porosity. According to Darcy's law, pore fluid is assumed to flow through an interconnected pore network as described below:

$$v_i = -\frac{k}{\mu} p_{,i} = -\frac{\bar{k}}{\gamma} p_{,i} \quad (11)$$

In which  $k$  is the permeability,  $\mu$  is the pore fluid viscosity,  $\bar{k}$  is the hydraulic conductivity and  $\gamma$  is the pore fluid specific weight. Merging with the continuity equation, the pore fluid diffusion equation is attained:

$$\frac{1}{M} p' + \alpha \epsilon_{kk}^i = \frac{\bar{k}}{\gamma} p_{,kk} \quad (12)$$

Fluid flow within the fracture is governed by Reynold's lubrication theory defined by the continuity equation:

$$g' + \frac{\partial q_f}{\partial s} + v_T + v_B = 0 \quad (13)$$

The momentum equation for incompressible Newtonian fluids through narrow parallel plates (Poiseuille flow) is as:

$$q_f = -\frac{g^3}{12\mu_f} \frac{\partial p_f}{\partial s} \quad (14)$$

Figure 1 shows the fracture parameters where  $g$  is the fracture aperture,  $q_f$  is fracture fluid flow per unit width across the fracture,  $v_T$  and  $v_B$  are the normal flow velocities of fracturing fluid leaking through the top and bottom faces of the fracture into the porous medium,  $\mu_f$  is the fracturing fluid viscosity, and  $p_f$  is the fracturing fluid pressure along the fracture surface parameterized with the curvilinear coordinate,  $s$ .

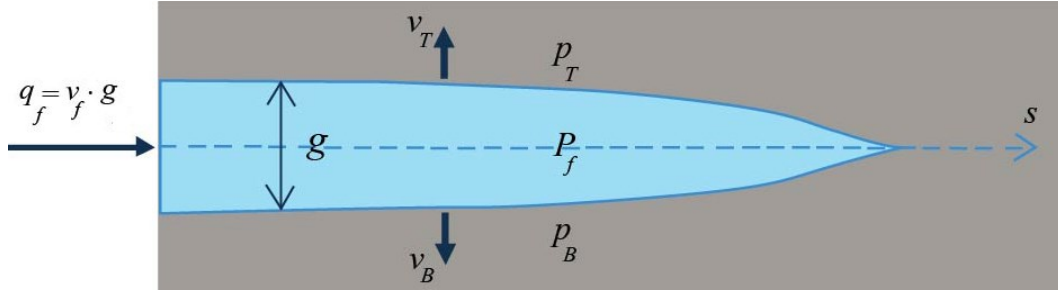


Figure 1. Fracture parameters: aperture, width and fluid flow

$$v_T = c_T(p_f - p_T) \quad (15)$$

$$v_B = c_B(p_f - p_B) \quad (16)$$

where  $p_T$  and  $p_B$  are the pore fluid pressures on the top and bottom surface of the fracture and  $c_T$  and  $c_B$  are the “leakoff coefficients”. This simple leakoff model simulates a layer of filtrate that might accumulate and reduce the effective normal permeability of the fracture surfaces.

Inserting Equation (14) and the simplified leakoff model (Equations (15) and (16)) into the Equation (13) for the fracturing fluid reaches the final form:

$$\dot{g} + c_T(p_f - p_T) + c_B(p_f - p_B) = \frac{\partial}{\partial s} \left( \frac{g^3}{12\mu_f} \frac{\partial p_f}{\partial s} \right) \quad (17)$$

A way to describe the initiation and propagation of a fracture in rock is based on fracture tip stress intensity factors ( $K_N$ ,  $N=I, II$  and  $III$ ), which were introduced by Irwin (1957). Paris and Sih (1965), Johnson et al. (1973), Abou-Sayed et al. (1978), Zoback and Pollard (1978) and Rummel and Winter (1982) suggested different models accordingly for fracture extension and propagation. At the crack tip, the stress field can be broken up into three components, called mode I, II, and III and these are shown in Figure 2. Mode I causes the crack to open orthogonal to the local fracture surface and results in tension or compressive stresses on surfaces. Mode II causes the crack surfaces to slide about each other and results in shear stresses in the direction orthogonal to the crack surface ahead of the crack. Mode-III causes the crack surface to slide about each other in the direction tangential to the crack front and results in shear stresses in that direction ahead of the crack.

The stress intensity factor can be mathematically defined as:

$$K_N = \lim_{|\xi| \rightarrow 0} Z_N \sqrt{2\pi\xi} \quad (N = I, II, III) \quad (18)$$

where  $Z_N$  is Westergaard (1939) stress function.

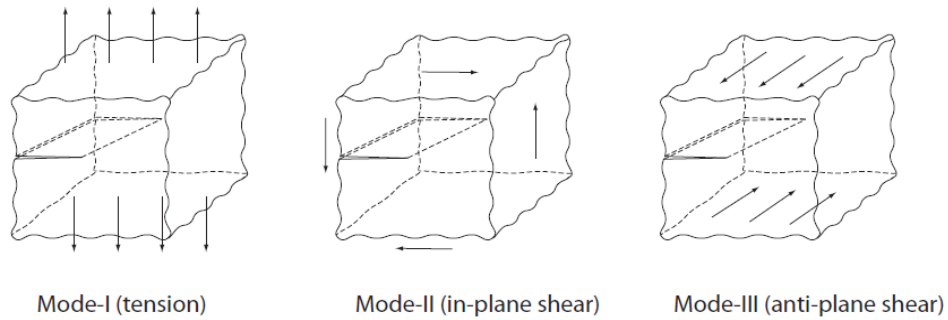


**Figure 2. the three basic modes of loading for a crack and corresponding crack surface displacements**

In many solid mechanics problems the anti-plane shear can be observed but in rock mechanics, mode I or mode II or mixed-mode I-II usually occurs. The local direction of crack propagation is determined by the "kink" angle defined as the angle that the crack will depart from the direction measured in a plane perpendicular to the crack front (Fracture Analysis Consultants Inc. (2010)). The kink angle is the  $\theta$  angle illustrated in Figure 3. In general, there are five different algorithms for determining the kink angle, maximum tensile stress (MTS), maximum shear stress (MSS), maximum generalized stress, maximum strain energy release rate, and planar growth.

Maximum Tensile Stress

The MTS theory expects that a crack will propagate in the direction of maximum circumferential stress,  $\sigma_{\theta\theta}$ . The circumferential stress is related to the resolved mode I stress intensity factor,  $K_I^r$ , given by:

$$K_I^r(\theta) = \sigma_{\theta\theta}\sqrt{2\pi r} = \cos\frac{\theta}{2} [K_I \cos^2\frac{\theta}{2} - \frac{3}{2}K_{II}\sin\theta] \tag{19}$$

The expression for materials with anisotropic stiffness properties is considerably more complex (Banks-Sills et al. (2007)) but can be expressed symbolically as:

$$K_I^r(\theta) = \sigma_{\theta\theta}\sqrt{2\pi r} = f(K_I, K_{II}, K_{III}, \theta, \Theta) \tag{20}$$

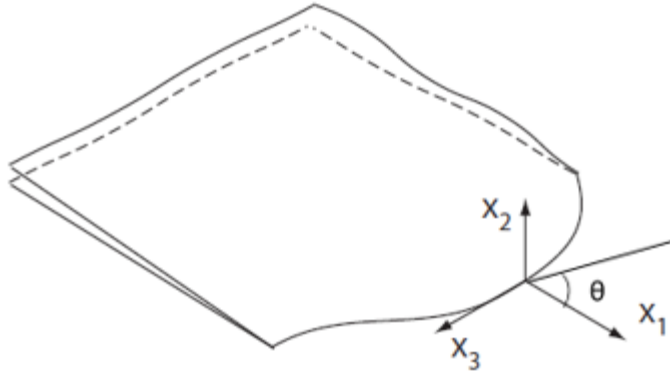


**Figure 3. Schematic illustration of the definition of the kink angle**

where  $\theta$  describes the angle cosines between the material property axes and the local crack-front coordinate system. If an isotropic material toughness is specified (the default behavior), a numerical algorithm is used to find the  $\theta$  angle that maximizes  $K_I^r$  and  $\sigma_{\theta\theta}$  in equation 19 or 20. If anisotropic toughness properties are specified, the kink angle is defined as the angle that maximizes the ratio  $\frac{K_I^r(\theta)}{K_P(\theta)}$ , where  $K_P(\theta)$  is a measure of the materials directionally dependent resistance to crack growth.

#### Maximum Shear Stress

Some materials show crack growth in the direction where shear stress is at its maximum, especially for conditions of high shear loading at the crack front. The MSS theory expects that a crack will propagate in the direction of maximum shear stress. For materials with isotropic stiffness properties, the components of the shear stress are related to the resolved mode II and III stress intensity factors given by:

$$\begin{aligned} K_{II}^r(\theta) &= \sigma_{r\theta} \sqrt{2\pi r} = \frac{1}{2} \cos \frac{\theta}{2} [K_I \sin \theta - K_{II} (3 \cos \theta - 1)] \\ K_{III}^r(\theta) &= \sigma_{z\theta} \sqrt{2\pi r} = K_{III} \cos \frac{\theta}{2} \end{aligned} \quad (21)$$

Symbolic expressions for materials with anisotropic stiffness properties are:

$$\begin{aligned} K_{II}^r(\theta) &= \sigma_{r\theta} \sqrt{2\pi r} = f_{II}(K_I, K_{II}, K_{III}, \theta, \Theta) \\ K_{III}^r(\theta) &= \sigma_{z\theta} \sqrt{2\pi r} = f_{III}(K_I, K_{II}, K_{III}, \theta, \Theta) \end{aligned} \quad (22)$$

where  $\Theta$  characterizes the angle cosines between the material property axes and the local crack-front coordinate system.

If an isotropic material toughness is specified (the default behavior) a numerical algorithm is used to find the  $\theta$  angle that maximizes the expression:

$$K_s^r(\theta) = \sqrt{(\beta_{II}K_{II}^r(\theta))^2 + (\beta_{III}K_{III}^r(\theta))^2} \quad (23)$$

where  $\beta_{II}$  and  $\beta_{III}$  are user supplied parameters that can be used to tailor predicted shear crack growth direction to match assumed or predicted behavior.

If anisotropic toughness properties are specified, the kink angle is defined as the angle that maximizes the ratio  $\frac{K_I^r(\theta)}{K_P(\theta)}$ .

#### Maximum Generalized Stress

The generalized stress criterion expects that the crack will grow in the direction of the higher recognised stress intensity factor from the first or second criterion mentioned above.

#### Maximum Strain Energy Release Rate

The maximum strain energy release rate criterion expects that the direction of the crack growth will be in the direction that the rate of change of potential energy in the system due to crack growth is maximum. For isotropic toughness materials, this angle is determined by numerically maximizing the expression:

$$G(\theta) = (K_I^r(\theta))^2 + (\beta_{II}K_{II}^r(\theta))^2 + (\beta_{III}K_{III}^r(\theta))^2 \quad (24)$$

For materials with anisotropic toughnesses the expression below is maximized:

$$G(\theta) = \left(\frac{K_I^r(\theta)}{K_P(\theta)}\right)^2 + \left(\frac{\beta_{II}K_{II}^r(\theta)}{K_P(\theta)}\right)^2 + \left(\frac{\beta_{III}K_{III}^r(\theta)}{K_P(\theta)}\right)^2 \quad (25)$$

#### Planar

The planar crack growth forces the crack to grow with a zero kink angle (self-similar growth). Abaqus cohesive element method uses this criterion.

### **MICRO FRAC TEST AND FACTORS AFFECTING TEST RESULTS**

A micro frac test is essentially a miniature hydraulic fracturing test conducted at an injection rate of 0.002-0.1 m<sup>3</sup>/min during a short injection time of 3-20 minutes within a one-meter test interval. Except for the injection rate and volume of injected fluid, the theory of hydraulic fracturing and fracture mechanics is applicable for this test.

In order to perform a micro frac test, a portion of the wellbore - test interval - is isolated by inflating the straddle packer arrangement. The interval is then pressurized by pumping fluid until a tensile fracture begins. In an open hole, the fracture initiates and propagates as normal to the minimum stress. In practice, however, such a breakdown (for the non-

sleeved section) is not always observed. After the initial breakdown, the injection is continued until the pressure stabilizes. The injection is stopped and the pressure is allowed to decline to a level that ensures the fracture is closed. The value of the stress acting normal to the fracture surface is determined by monitoring the initiation, propagation, closure, and reopening of the induced fracture.

Factors that affect the results and interpretation of micro frac tests can be categorized into three main groups: reservoir/geological factors, operational factors, and fracture growth pattern.

- Reservoir and Geological Factors

Bush and Meyer (1988) mentioned that the stress magnitude is affected by rock lithology. Lithological factors affecting in situ stress magnitude are the grain size, shape, orientation, strength and type of matrix materials. Geological history imposes various changes such as tectonic, erosion, thermal, chemical or physical weathering on the formation that can affect the state of stresses. Warpinski et al. (1989) found the breakdown and reopening pressures to be higher in sandstones than in shale. Mini-frac tests conducted in a 30-m deep test interval of the McMurray Formation showed the breakdown, reopening, and propagation pressures to be the largest in tar sands, intermediate in interbedded sand and mudstone and the least in mudstone with an identical injection rate. These variations are perhaps caused by a difference in the lithological as well as the geomechanical properties.

In highly plastic rocks like clay shale for which a large part of the deformation is non-elastic, complete fracture closure may occur over a considerable period of time after shut-in while for rocks which are non-porous, and deformation is predominantly elastic, the fracture closure following the shut-in is expected to be instantaneous.

The presence of natural fractures, joints, and cracks is another geological factor that can affect micro frac test results. Natural fractures within the formation subjected to the micro frac test may be closed or open. If they are closed, they may be reopened during fluid injection instead of initiation of hydraulically induced fracture. Thus, instead of breakdown pressure, it is shown the reopening pressure for an existing fracture. If the natural fracture is open, it can serve as an escape path for injected fluid and thereby the pressure would not build up or fracture growth is a compromise between overcoming a stress field and overcoming entrance losses into pre-existing fracture of preferential

permeability (Roegiers et al. (1982), Layne and Siriwardane (1988)). Thus it is possible to extend the natural fractures during the test although they are not aligned perpendicular to the minimum in situ stress direction. That causes inaccuracy of the minimum in-situ stress determination from a micro frac test.

According to Breckels and Eekelen (1981), under-pressured formations generally have lower horizontal total stress than normally pressured or over-pressured formations. Salz (1977) found an exponential decrease in fracture propagation pressure with a reduction in reservoir pore pressure. These examples are only a few of the many studies that have shown that the total stresses in poroelastic media depend on pore pressure.

The poroelastic effect can be important when significant back pressure is generated and this phenomenon can lead the higher closure pressure and instantaneous shut-in pressure, ISIP, and consequently an overestimation of the minimum in-situ stress, if closure stress is used for the minimum in-situ stress determination.

#### - Operational Factors

It is well-understood that breakdown pressure and reopening pressure depend on the viscosity of the injected fluid. The injecting fluid with higher viscosity leads to higher magnitude of mentioned parameters. This effect can be justified by the fact that injecting fluid with higher viscosity causes larger compressive build-up stress since the leakoff coefficient is lower for high viscous fluid.

Another influential factor is injection rate. Morgenstern et al. (1992) studied this effect by conducting laboratory fracturing tests on gypstone, which is low permeability quartz sand cemented with gypsum. Their study proposed high breakdown pressure at high injection rates and a low breakdown pressure at low rates. A rapid injection rate prevents fluid penetration into the formation, causes a large stress concentration, thereby giving rise to a large formation breakdown pressure.

#### - Fracture Growth Pattern

Enever and Woollorton (1982), Hickman and Zoback (1983), Gronseth and Kry (1983) reported fracture propagation continuing after pumping had stopped. Continuation of fracture propagation after shut in causes a decrease in ISIP. Kry (1983) suggested that this decrease in ISIP is due to the propagation and growth of the fracture away from the region of large stress concentration occurring around the wellbore.

Due to stress concentration, damage, cracking, weakness, and anisotropy in the vicinity of a wellbore wall, especially in the sleeved test interval, the fracture may not grow truly perpendicular to the minimum principal stress. Fracture growth non-perpendicular to the minimum in-situ stress may appear on a pressure-time curve as an increase in ISIP and closure pressure.

The possibility of multiple fracture growth is unlikely for micro frac test since the injection rate is too low, however, if the injection rate is large enough and continues for some time after the formation breakdown, or if the injection is carried out in multiple cycles, then an offset in the ratio of the stress magnitude may cause a reversal in fracture growth orientation and even growth of multiple fractures (Roegiers (1989)). It can lead to a change in stress regime and the consequence of this on the results of a micro frac test can be complex. Warpinski (1991) maintains that any complex multiple fracturing may lead to overestimation of closure pressure.

As discussed in the previous section, the stress concentration that occurs at the tip of the fracture can be explained best in terms of stress intensity factor ( $K_I$ ) concept developed in linear elastic fracture mechanics. The fracture will propagate when  $K_I$  reaches a critical value, called the critical stress intensity factor,  $K_{IC}$ , or fracture toughness. Fracture toughness being a measure of the resistance of the rock to crack propagation and being affected by the loading parameters and the geometry of the fracture can affect the ISIP and closure pressure values.

Fracture surface topography is another important factor affects the results of the micro frac test. In theory, it is assumed that the fracture faces are perfectly matched like saw cut surfaces but in reality, any mismatched in fracture faces may result in an uneven closure. The factors can cause any mismatched may be grain crushing, breakage, or slight shearing. The fracture closure may be slow; hence, the fracture would be more compliant in this case. A sharp drop in the pressure seen as closure pressure may not be visible in pressure versus time curve. Thus an accurate estimate of closure can be difficult.

## **XFEM THEORY**

The extended finite element method (XFEM) based on the partition of unity method (PUM) was introduced by Moes et al. (1999) as a new approach to representing fracture surfaces and to capture their evolution within a standard Galerkin-based method. The

basic concept of XFEM is a numerical technique that combines the conventional finite element method (FEM) approach with the solutions to differential equations with discontinuous functions. XFEM is the methodology that represents the fracture by applying an improvement to the space of shape functions by specialized enrichment functions that can duplicate the discontinuous and singular elastic fields related to the crack. These enrichment functions are limited to elements near the fracture and its tips, while field variables in the solid medium can be characterized by standard polynomial basis functions. Therefore, fracture propagation can be modelled even on a structured mesh by dynamically correcting the enrichment process to integrate the location of the moving fracture tips without remeshing to be needed to update the crack path (Richardson et al. (2009), Ahmed (2009), Gordeliy and Peirce (2013, 2014), Zielonka et al. (2014), Abaqus documentation (2014), Hattori et al. (2015)). The XFEM is implemented within Abaqus using the “phantom node” approach (Abaqus (2014)). In this approach, each enriched pressure diffusion/stress element has another corner phantom node in addition to its original nodes, as described in Figure 4. The original nodes are shown with full circles and hollow circles represent corner phantom nodes. Before damage happens, only the original nodes of the element are active. Once damage takes place, the displacement and pore pressure degrees of freedom associated with both original and corner phantom nodes are activated and both copies of the element can deform independently, pore pressures can diffuse independently, and a traction-separation cohesive law has been developed for creating interface behavior. To solve the fracturing fluid flow equations, new “edge-phantom nodes” (depicted as orange triangles in Figure 4) are integrated into enriched elements. These nodes interpolate the fracturing fluid pressure within the fracture. The pore fluid pressure  $p_T$  and  $p_B$  at the top and bottom faces of the fracture are interpolated from the pore pressure degrees of freedom at the corner real nodes and phantom nodes. The difference in the fracturing fluid pressure  $p_f$  is the driving force controlling the leakage of fracturing fluid into the porous medium that interpolated at the edge-phantom node.

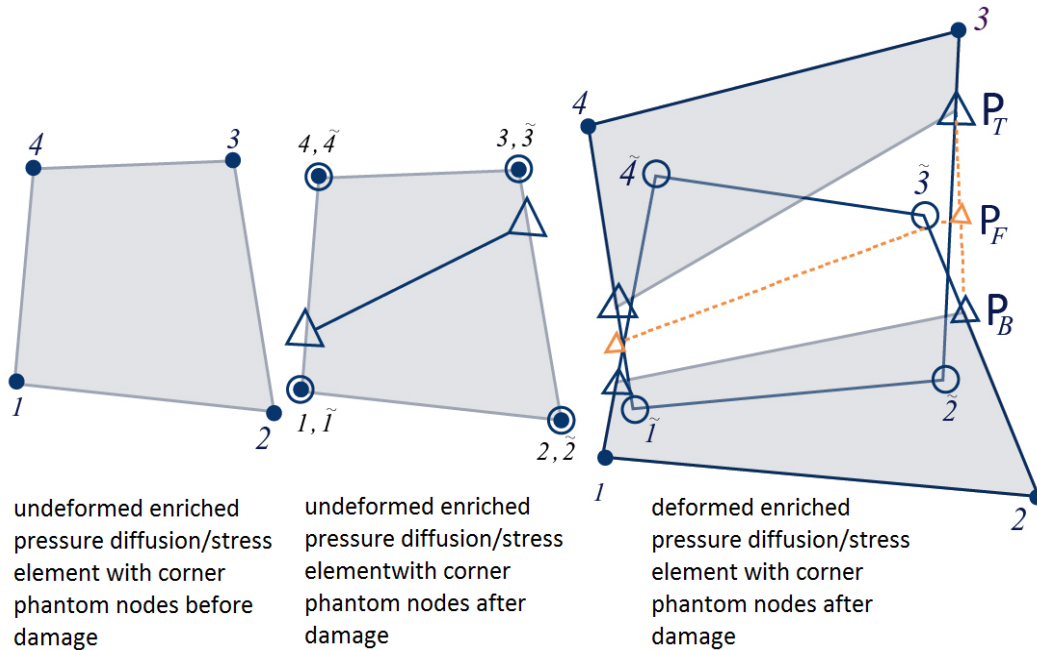


**Figure 4. Concept of phantom nodes in XFEM**

Two main approaches have been considered as the criterion in Abaqus XFEM for studying crack initiation and propagation: traction-separation cohesive behavior and linear elastic fracture mechanics (LEFM). The former criterion has been adopted for this research. The concept of this approach is that fracturing can be hypothesized as the transfiguration between two limiting states: the undamaged state and the fully damaged state. Undamaged state is described as a state with continuous displacements and non-zero tractions in all directions while damaged state is identified by the presence of a discontinuous displacement along a material interface with zero tractions in the direction normal to the interface. In Abaqus, this process is modelled as a progressive degradation of cohesive strength along a zero-thickness interface whose orientation and extent is either predefined (cohesive element method) or calculated during the simulation (extended finite element method). An interface traction/interface separation relation or cohesive law is developed for defining this gradual loss of strength in the interface with increasing separation (Abaqus 2014, Ortiz 1999).

A traction-separation cohesive law with linear softening (Figure 5) is defined by the cohesive energy  $G_c$  and the cohesive strength  $N_0$ .  $G_c$  represents the area under the softening part of the traction-separation curve. Assume the maximum tensile strength at damage initiation is  $N_0$ . During the damage process, the interface cohesive traction



MDT. In the previous section, the in situ stress state prior to running the MDT micro fracture test has been evaluated using the FSI and inverse techniques. Knowing the stress state and other parameters, the micro hydraulic fracture models have been constructed for both SAGD and CSS project sites. The models for these two project configurations are provided in the next sections.

### LP-SAGD PROJECT SITE

After two cycles of sleeve fracturing, two cycles of fracturing fluid injection directly into the test interval between the two packers is undertaken. The micro hydraulic fracturing test operation has been summarized in Table 1.

**Table 1. Micro hydraulic fracturing test operation data for SAGD**

	Injection time (s)	Volume of injecting fluid (cm <sup>3</sup> )	Injection rate (cm <sup>3</sup> /s)	Maximum pressure (MPa)
First cycle	684	11970	17.5	3
Second cycle	1008	9274	9.2	3

Clear water clay shale geomechanical properties and injecting fluid properties for this site have been provided in Chapter 4. The formation has been discretized with enriched coupled pore fluid diffusion/stress C3D8P elements. As for initial conditions, the medium is assumed to be fully saturated with confining stresses of 1.31 MPa, 1.61 MPa and 0.91 MPa for vertical, maximum horizontal and minimum horizontal in situ stresses respectively as discussed in Chapter 4. Initial pore pressure has been applied equal to 0.62 MPa and formation initial void ratio has been considered as 0.51. Abaqus requires an explicit specification of the set of enriched elements where the fracturing fluid flow equations will be initially solved. The numerical analyses have been conducted over 10 different steps: Geostatic stress equilibrium, drilling and applying mud pressure, sleeve fracturing- first cycle- loading and unloading, sleeve fracturing- second cycle- loading and unloading, and two hydraulic fracturing with their injection and shut in times. All the steps beside geostatic are simulation steps involving transient consolidation. Fracture criterion considered as maximum principal stresses (MAXPS) with damage evolution equal 0.002 and damage stabilization equal 10e-6. To crosscheck the results, the maximum displacement in the XFEM model during the first sleeve-fracturing test (2.76 cm), as shown in Figure 6, is in good agreement with the FSI results, as shown in Figure 41 (previous chapter). The opening of the initial crack after injection is illustrated in Figure 7,

in a Z-plane and X-plane view cut. Figure 8 shows the crack element in the enriched region within the model in a Z-plane and X-plane view cut. Figure 9 shows the length of the region (on an x-plane view) that has been disturbed during drilling, the application of mud pressure and two cycles of sleeve fracturing test from FSI analysis discussed in the previous chapter.

The area that has been affected just by drilling and the application of mud pressure in the non-sleeve station is around 30 cm from the wellbore wall. The cracked element area in the enriched region affected by fluid injection is about 45 cm (Figure 7, right), while the disturbed zone after the sleeve-fracturing tests, which caused stress redistribution around the wellbore, is 90 cm (Figure 9). Based on the size of the disturbed zones, it is clear that the injection of a total of 21,244 cm<sup>3</sup> of fracturing fluid during the two cycles of the hydraulic fracturing test, the initial crack can barely extend and propagate past the disturbed zone resulting drilling and mud pressure and/or sleeve fracturing test in sleeved stations. Moreover, the minimum redistributed stress at the cracked element in the enriched region equals to 2.26 MPa (36 kPa/m) for the first element and 1.65 MPa (26 kPa/m) for the second element in FSI model, as illustrated in Figure 10. These results suggest that the interpretation of the results from the MDT tests, as discussed in Chapter 2, correctly determined the minimum stress for the region of fracturing – the disturbed zone – but not the far-field minimum in situ stress.

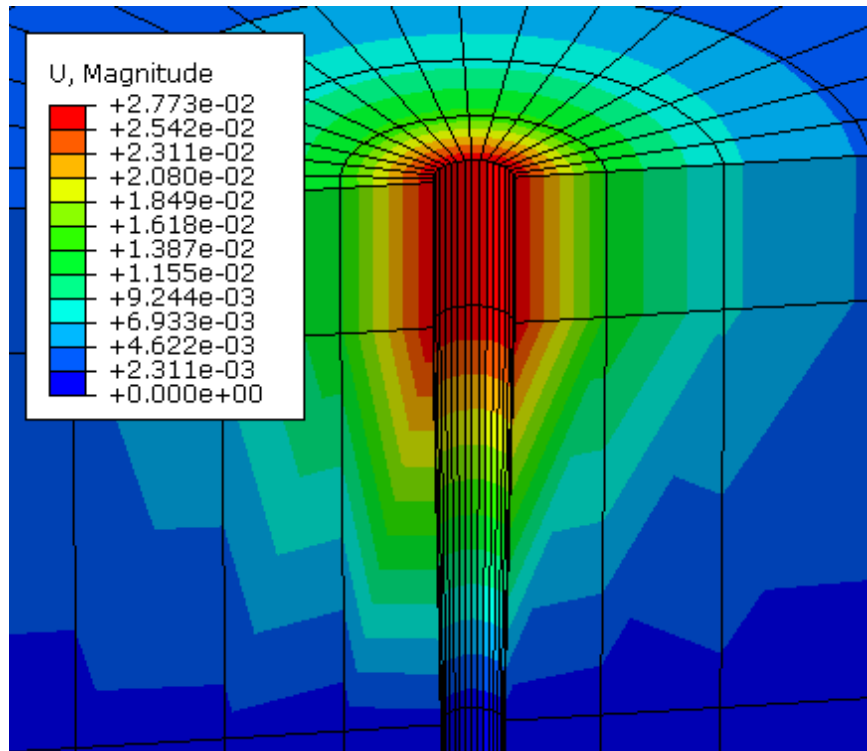


Figure 6. Maximum formation displacement (m) after first cycle of sleeve fracturing loading step, X-plane view cut, in XFEM model

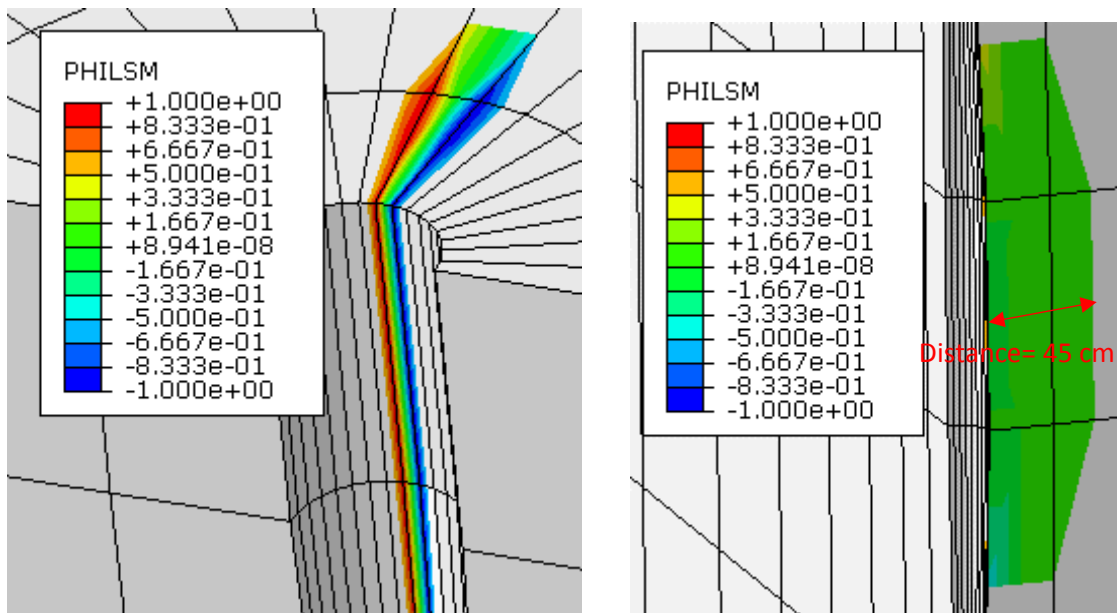


Figure 7. Fracture opening of enrichment element after 2 cycles of injection, SAGD project, opening in X-plane view cut (left), opening in Z-plane view cut (right)

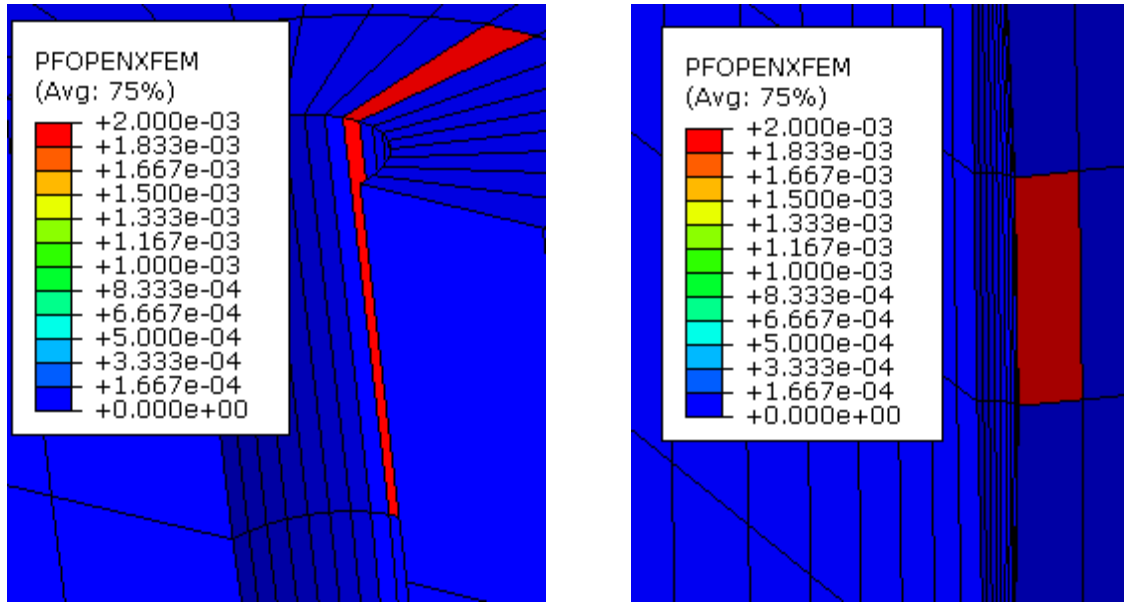


Figure 8. Crack element in the enriched region, SAGD project, Crack element in X-plane view cut (left), Crack element in Z-plane view cut (right)

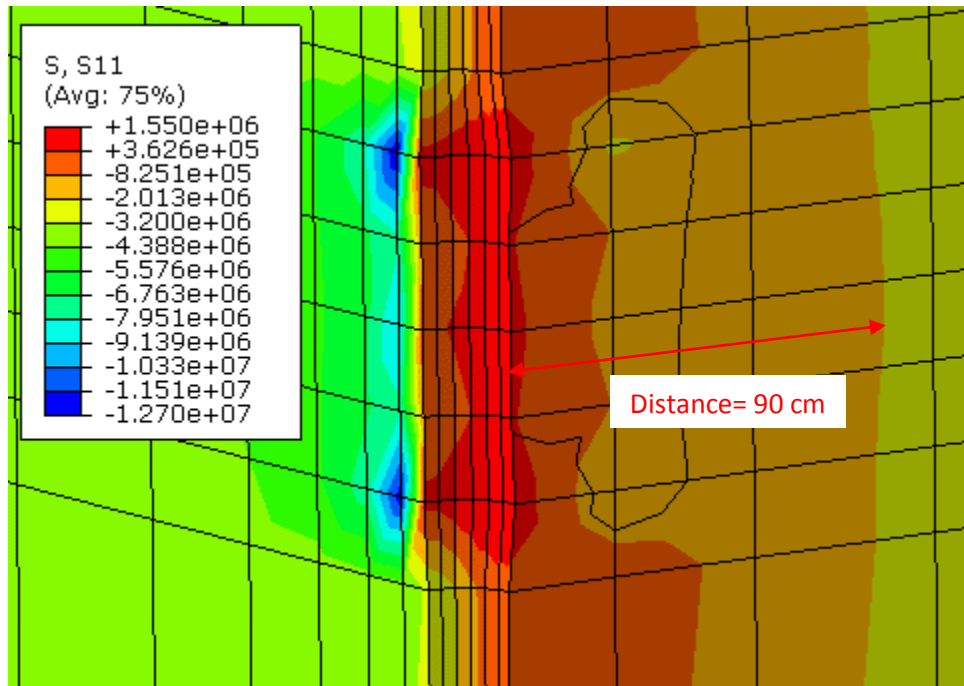


Figure 9. The length of the disturbed zone during the drilling and sleeve fracturing test, SAGD project

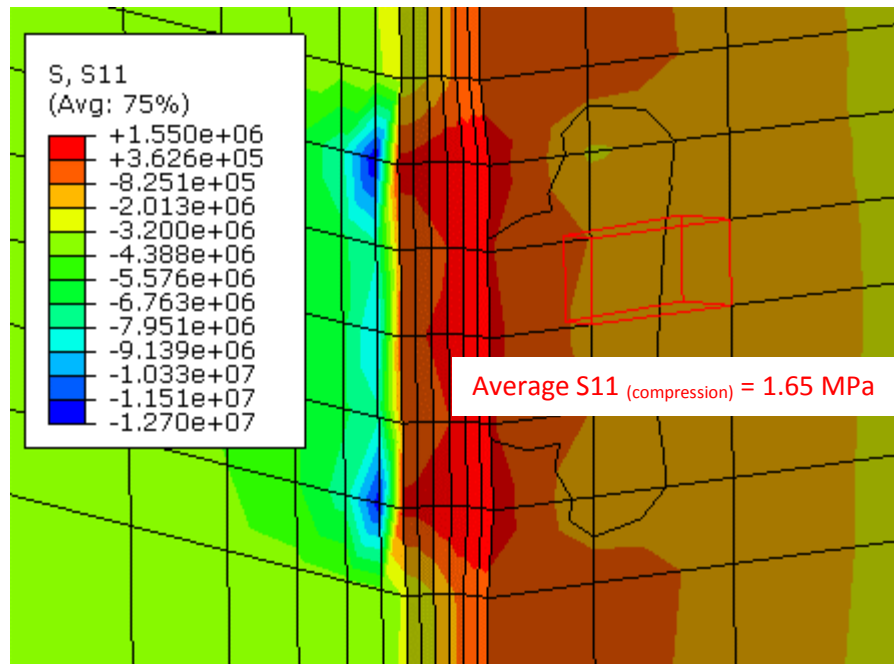
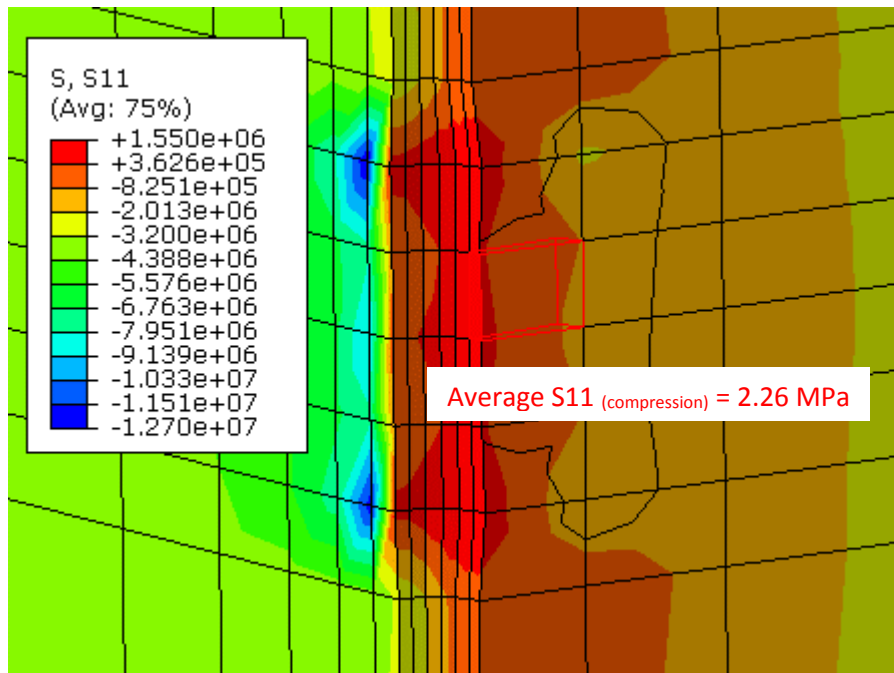


Figure 10. Minimum redistributed stress for the first and second element at the cracked element in the enriched region in FSI model

## CSS PROJECT SITE

For this project site, four different cycles within the hydraulic fracturing test have been conducted after the execution of two cycles of sleeve-fracturing. Over the four cycles, a total of 7,005 cm<sup>3</sup> of fracturing fluid has been injected and the operational data is summarized in Table 2.

**Table 2. Micro hydraulic fracturing test operation data for CSS project**

	Injection time (s)	Volume of injecting fluid (cm <sup>3</sup> )	Injection rate (cm <sup>3</sup> /s)	Maximum pressure (MPa)
First cycle	576	2494	4.33	15.1
Second cycle	612	3060	5	14.26
Third cycle	36	479	13.3	11
Fourth cycle	72	972	13.5	11.42

Similar to the SAGD project modelling approach, 14 different steps have been considered to model the MDT tests conducted in the CCS project site: Geostatic stress equilibrium, drilling and applying mud pressure, sleeve fracturing- first cycle- loading and unloading, sleeve fracturing- second cycle- loading and unloading, and four hydraulic fracturing with their injection and shut in times. All the steps beside geostatic are simulation steps involving transient consolidation. The same fracture criteria used in the previous analyses (SAGD project) have been considered for this site. Joli Fou clay shale properties mentioned in the previous chapter are used for XFEM simulations and the fracturing fluid remains the same as used in the FSI analyses. The initial condition for this model is: the formation is fully saturated, initial far field in situ stresses are 7 MPa, 6.25 MPa and 5.25 MPa for vertical, maximum horizontal and minimum horizontal orientations, respectively. Initial pore pressure has been applied equal to 3.3 MPa and the formation initial void ratio was 0.49.

Figure 11 shows the maximum formation displacement of 5.23 cm after the first sleeve fracturing step, which reasonably agrees with the FSI analysis results shown in Figure 54 (previous chapter). On Z-plane and X-plane orientations, Figure 12 shows the opening of the initial crack after injection. The crack element in the enriched region within the model in Z-plane and X-plane view cut is shown in Figure 13. Figure 14 shows the length of the region that has been disturbed during drilling, application of mud pressure and two cycles of sleeve fracturing test. The boundary where hoop stress changes from

tension to compression after two cycle of sleeve fracturing test can be observed clearly in Figure 15.

The cracked element area in the enriched region affected by injection the fracturing fluid is about 45 cm (Figure 12, right). The disturbed zone after the sleeve fracturing test which caused stress redistribution around the wellbore is 98.5 cm (Figure 14). By injecting a total of 7005 cm<sup>3</sup> fracturing fluid during four cycles of hydraulic fracturing test, the initial crack cannot propagate and pass the disturbed zone resulting drilling and mud pressure and/or sleeve fracturing test in sleeved sections. Moreover, the minimum redistributed stress at the cracked element in the enriched region is equal to 13.15 MPa (39 kPa/m) for the first element and 11.36 MPa (33.7 kPa/m) for the second element in FSI model (Figure 16) which indicates that the field data interpretation summarized in the second chapter are actually showing the minimum stress measured within the disturbed zone but not the minimum component of far-field stresses.

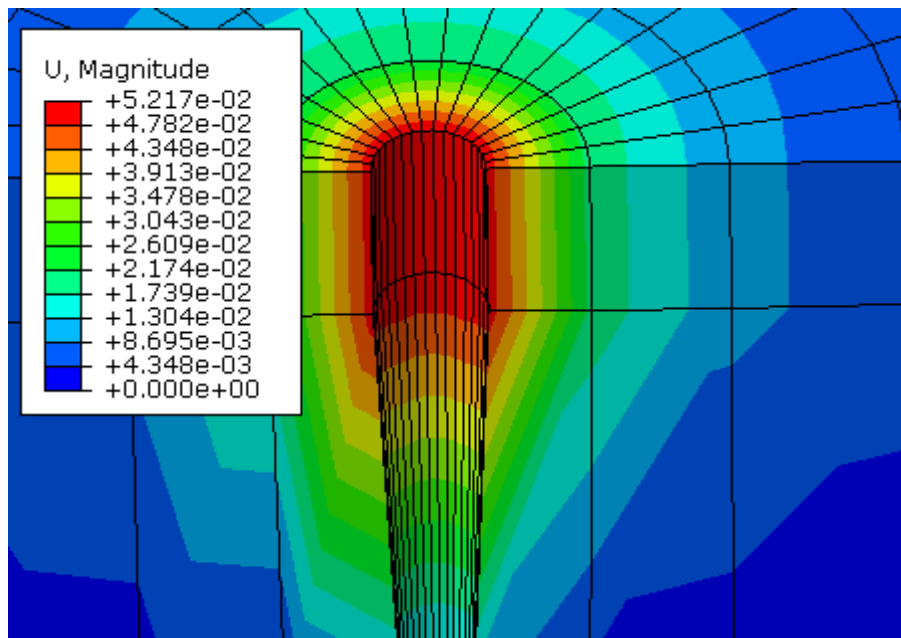


**Figure 11. Maximum formation displacement (m) after first cycle of sleeve fracturing loading step, CSS Project**

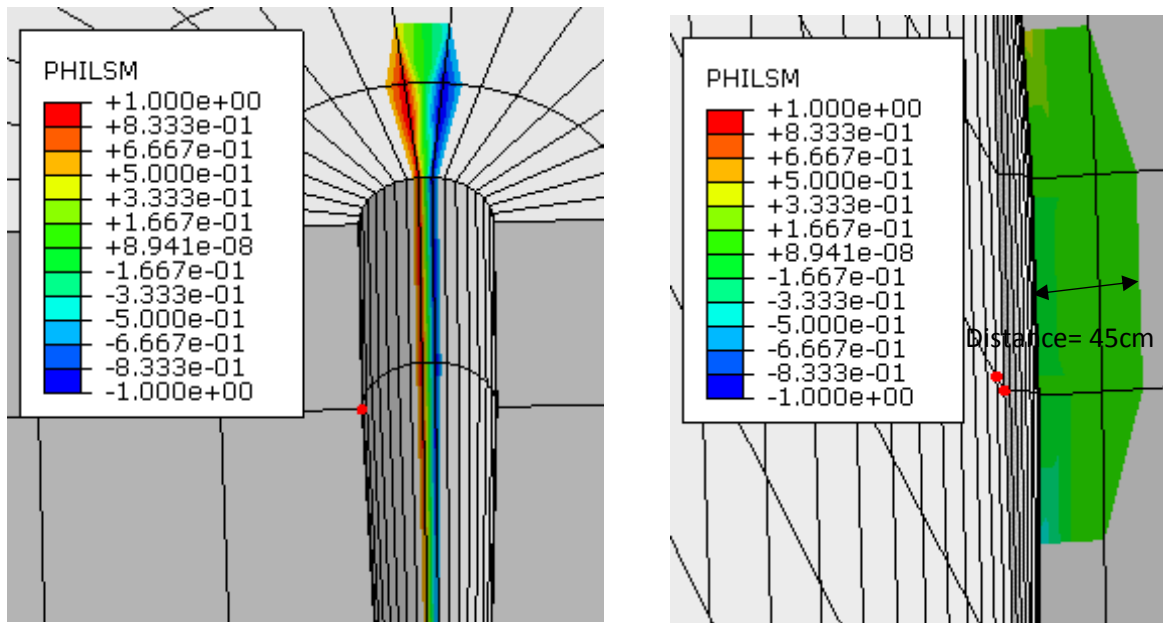


Figure 12. Fracture opening of enrichment element after 2 cycles of injection, CSS project, opening in X-plane view cut (left), opening in Z-plane view cut (right)

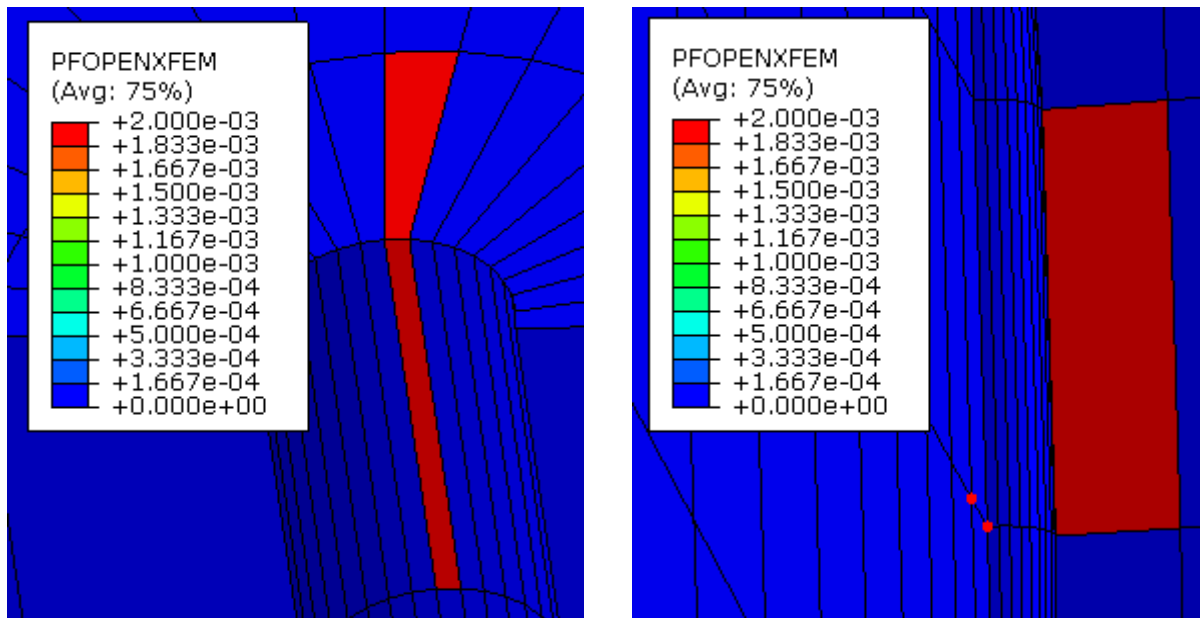


Figure 13. Crack element in the enriched region, CSS project, Crack element in X-plane view cut (left), Crack element in Z-plane view cut (right)

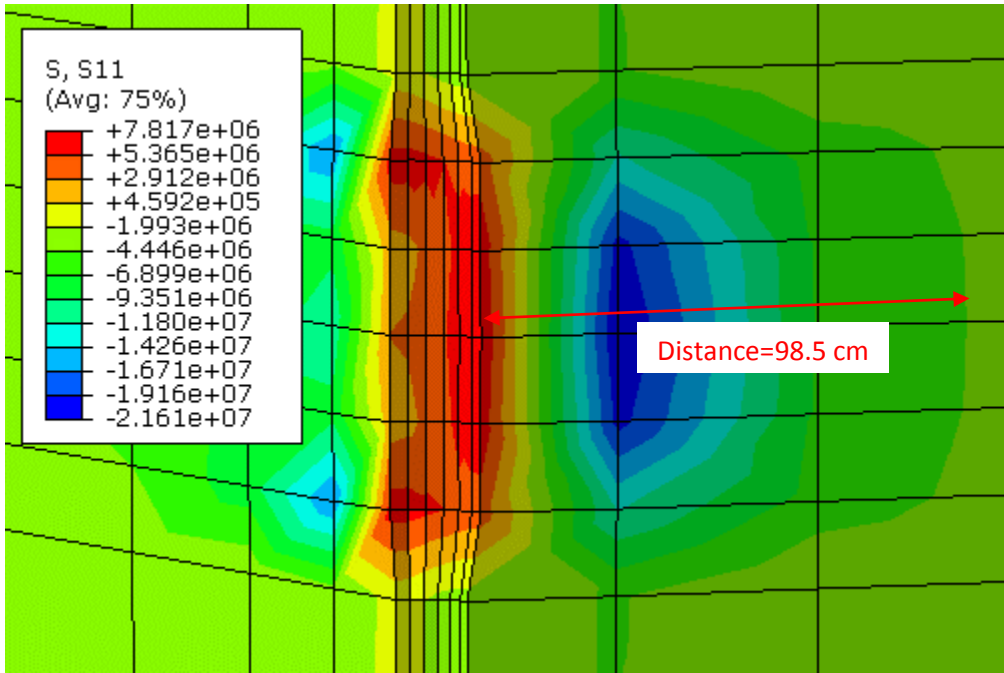


Figure 14. The length of the disturbed zone during the drilling and sleeve fracturing test, CSS project

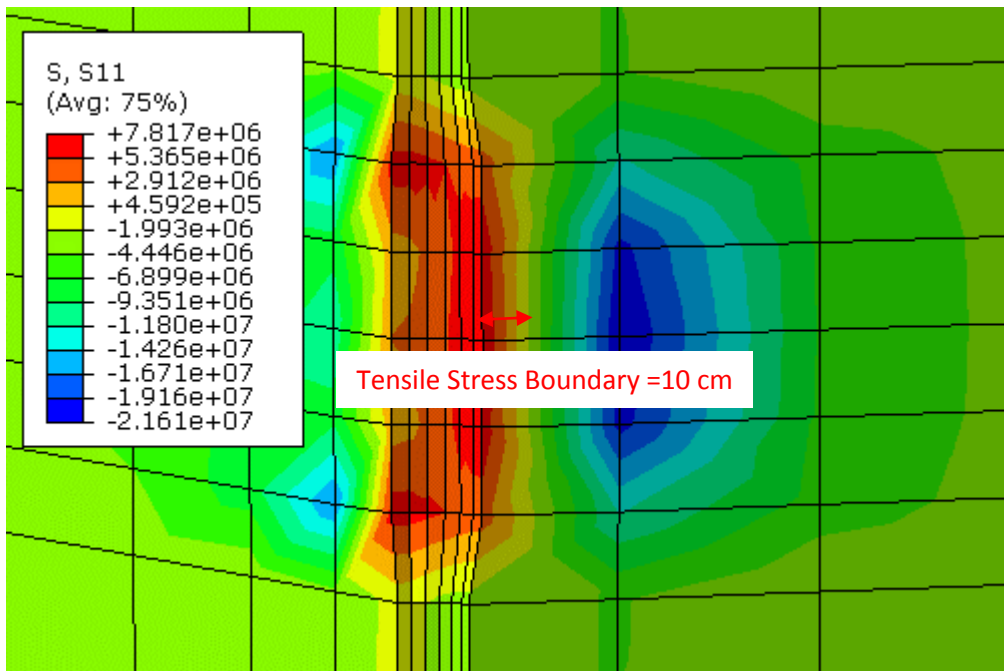


Figure 15. Boundary that the nature of loop stress changes from tension to compression during sleeve fracturing test, the length of tensile crack , CSS project

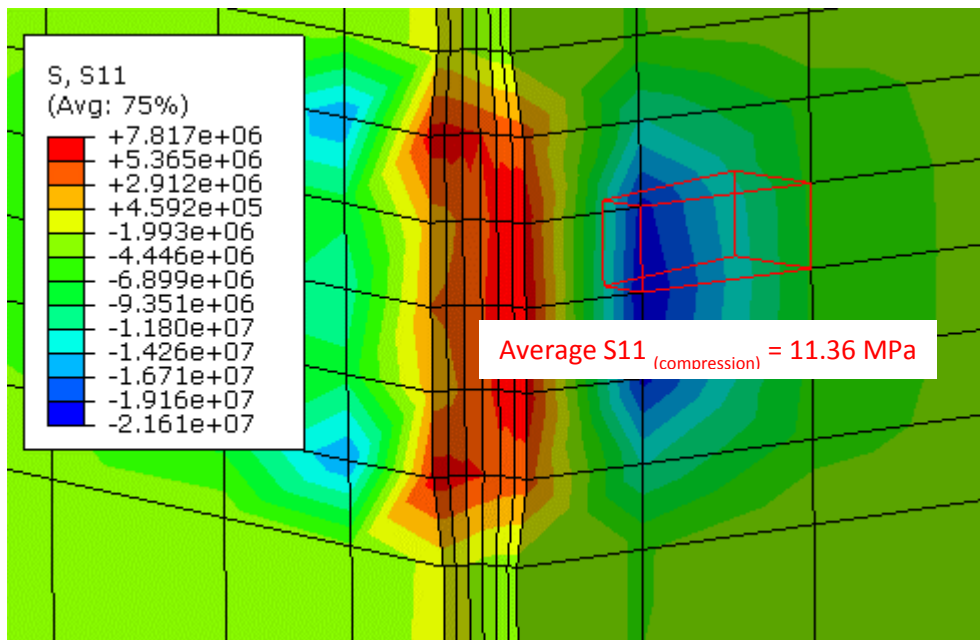
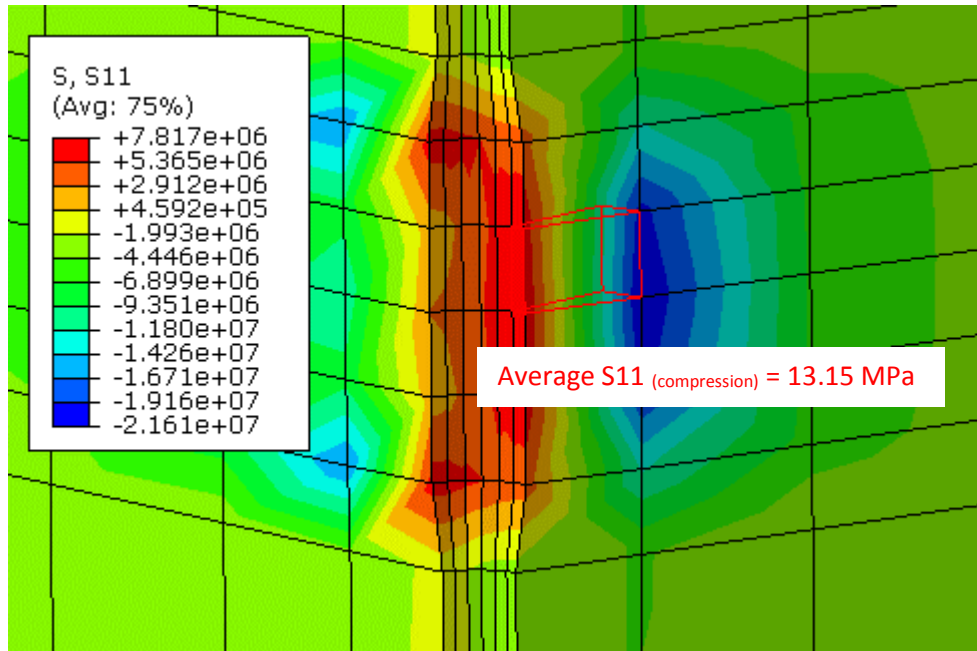


Figure 16. Minimum redistributed stress for the first and second element at the cracked element in the enriched region in FSI model

## DISCUSSION

Formations, such as clay shale, are known as caprocks for reservoirs and can support substantial plastic strains without any macroscopic rupture. Micro hydraulic fracturing test conducted on two different clay shale formations has been simulated and discussed. The test intervals over which the micro frac tests were conducted were initially exposed to a sleeve-fracturing test. In addition, the wellbore wall was disturbed while drilling and the application of mud pressure providing substantial opportunity for stress redistribution around the borehole wall and the development of a “new” local state of stress. This disturbed zone is further expanded when the test interval is a sleeved fractured. A very limited volume of fracturing fluid is usually injected during micro-frac tests. As discussed in the previous section, that small amount of fluid was insufficient to propagate a hydraulic fracture beyond the disturbed zone resulting in measurements that were only sensitive to and measuring the altered stresses in a localized region around the borehole. To show this fact, the same model has been used for CSS project with the identical steps and rate of injection for each step has been used to model the harder material used by Haddad and Sepehrnoori (2014). The properties of material were summarized in Table 3. They used Drucker-Prager plastic constitutive model for quasi-brittle shale as the reservoir and used cohesive zone approach to model multi-stage hydraulic fracturing.

**Table 3. Quasi-brittle shale properties used by Haddad and Sepehrnoori (2014)**

Properties	Reservoir Layer
Poisson's ratio	0.27
Young's Modulus [ $10^9$ Pa]	20
Drucker Prager friction angle, $\phi$ [deg]	36
Drucker Prager dilation angle, $\Psi$ [deg]	36
Formation Grain Bulk Modulus [ $10^9$ Pa]	14.9
Formation Density [kg/m <sup>3</sup> ]	2263

Figure 17 shows the propagation of the initial crack after the fourth cycle of hydraulic fracturing. The length of the fracture is 2.44 m and at that distance from wellbore wall, the far field stresses can be reached. The highlighted point is the volume of injected fluid and the rate of injection is the same as it has been used for Joli Fou clay shale formation. The only factor changed was properties of the material. This rate of injection can definitely be useful for brittle material with high elastic properties. On the other hand, if

ductile materials are subjected to the micro hydraulic fracturing test, it is will be required to consider the higher rate and volume of injection.

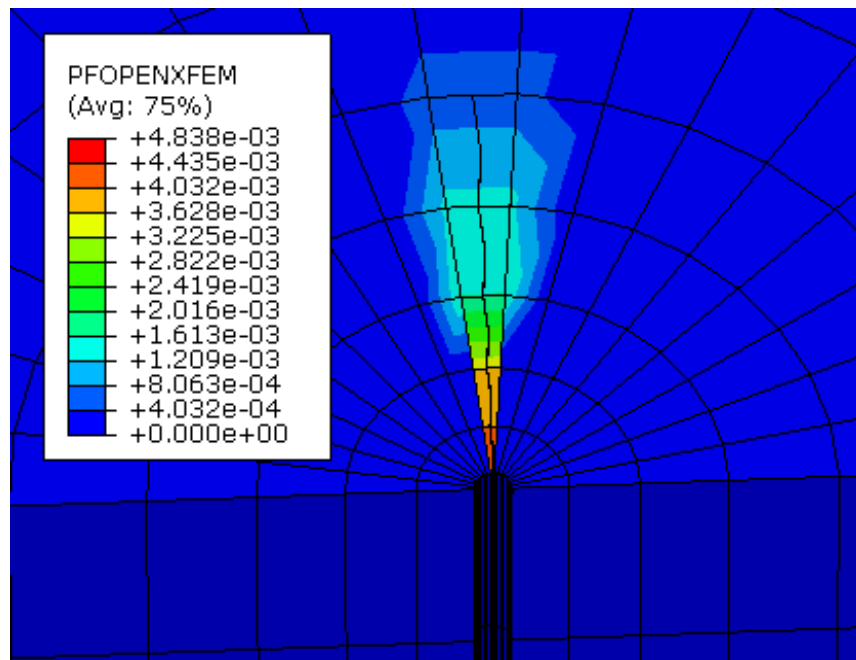
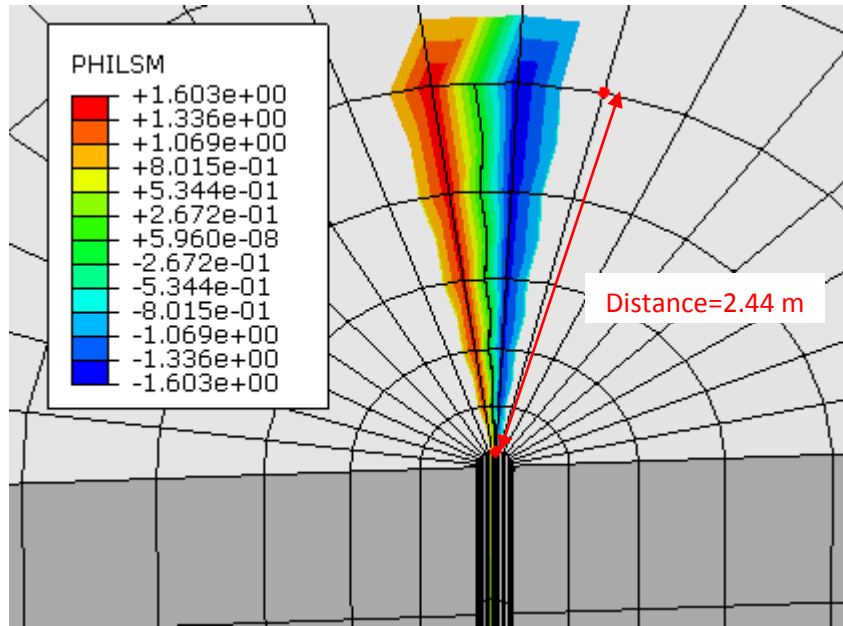


Figure 17. Fracture propagation and opening in micro hydraulic fracturing test in quasi-brittle shale

## **CHAPTER 6 CONCLUSION**

**GOOD AND EVIL, OUR MORAL PRISON,  
JOY AND SORROW PASSING LIKE SEASON,  
FATE IN THE WAY OF LOGIC AND REASON  
IS THE VICTIM OF FAR WORSE TREASON.**

**“KHAYYAM”**

## SUMMARY AND CONCLUSION

Micro hydraulic fracturing test is one of the multiple packer techniques for in situ stress measurement that is commonly used in the petroleum industry. It has repeatedly been reported that micro-frac test conducted using the MDT in clay shales leads to unrealistic estimates of the minimum in situ stress. This research explored the hypothesis that the complex constitutive behavior of the hard soil-soft rock (HS-SR) material such as Clearwater clay shale and Joli Fou clay shale is the main source of the inconsistent results. These materials are highly plastic and can bear a significant amount of plastic strain before generating any macroscopic rupture. This behaviour has a sharp contrast with conventional assumptions of elastic rock behavior in any hydraulic-based test for in situ measurement. The premise that the limited volume of the fracturing fluid injected in an MDT test is insufficient to initiate or propagate the fracture beyond the packer influenced region was also studied in this research.

Numerical studies were undertaken to better understand the mechanism of micro hydraulic fracturing tests conducted in HS-SR materials and to examine the interaction behavior between the MDT probe and formation to evaluate the principal components of in situ stress. Drainage condition in terms of permeability of the material and loading rate, material properties, the representative constitutive model for the material, and packer elements' properties were considered as critical parameters in the analyses.

The first step in the research was a comprehensive analysis of laboratory results and field data. Chapter 2 summarized the extensive analyses conducted on field data using all the available conventional interpretation methods to evaluate the minimum component of the principal stress tensor, which is the aim of micro hydraulic fracturing test. These analyses showed that special attention needs to be considered when interpreting the results of MDT tests. Potential issues associated with the incorrect estimation of the minimum component of far field stresses were identified as stress distribution and alteration near wellbore region resulting from wellbore drilling, skin effect and wellbore storage, low permeability of the material and low injection volume of the fracturing fluid. From the analysis of available laboratory data, parameters were extracted for a representative constitutive model for the behaviour of clay shale. Two different formations have been considered for this study, the Clearwater Formation and the Foli Fou Formation. Sufficient information was available for the Clearwater clay shale, to

compute the parameters required for a modified Cam Clay model used in the simulation studies. The lack of sufficient laboratory test data for the Joli Fou Formation lead to inverse analyses for calibration of the constitutive model parameters. Considering the limited amount of information, calibration of Modified Cam Clay parameters from triaxial test results has been conducted successfully using inverse analyses. Coupling of the finite difference model FLAC and the inverse analysis code UCODE established a new methodology and created a unique tool for calibration and optimization of the geomechanical parameters to demonstrate the behavior of the materials with the minimum amount of laboratory testing and yet generate a consistent set of input parameters.

Clay shales have low permeability so that the loading rate (from the packer) is a crucial factor in determining the drainage response within the formation. The transition zone between different drainage conditions as a function of permeability and loading rate has been suggested. If the loading rate of the packer is high, total stress is increasing abruptly along with an associated increase in pore pressure which creates a stiffer distributed zone around the loading area. This contributes to some misunderstandings in micro-hydraulic fracturing test results' interpretation.

The lack of knowledge about packer's mechanical properties lead to another parametric study and sensitivity analyses. Packer properties have been calibrated and as a result of this part of the study the packer pressure transmissibility was determined. Unfortunately, many unsleeved sections of the micro hydraulic fracturing tests fail. One of the main reasons for these failures is an improper amount of packer pressure regarding the relevant interval pressure that should be used to isolate the test interval. It was shown that for proper isolation, the packer pressure should be at least 1.2 times of interval pressure to maintain an efficient seal to prevent leakage and unsuccessful hydraulic fracturing test.

A novel methodology using fluid-structure interaction (FSI) analysis has been developed to evaluate the principal stress components of caprock in two different projects, LP-SAGD project and CSS project. Separated by approximately 350 km, the SAGD project belongs to Athabasca deposit and the CSS project relates to the Cold Lake deposit area. FSI analyses using a co-simulation technique was successfully conducted to evaluate the in situ stress state using inverse analysis. Sleeve fracturing data, the only reliable data for

these analyses, has been used. Results show that for the shallow depth SAGD project, the local faulting regime is strike-slip and the upper and lower limits for minimum and maximum horizontal principal stresses were analyzed over a range between 1.31-2.76 MPa for maximum horizontal stress and 0.84-1.31 MPa for minimum horizontal stress. The maximum and minimum horizontal stress gradients were estimated 25.5 kPa/m and 14.3 kPa/m, respectively. The initiation of the crack on wellbore wall from numerical simulation and the breakdown pressure from field data were in good agreement. For the CSS project, maximum and minimum horizontal stresses of 6.25 MPa and 5.25 MPa, respectively, provided the best fit between field data and computed data. This corresponds with estimated maximum and minimum horizontal stress gradients of 18.5 kPa/m and 15.6 kPa/m, respectively.

The last phase of the research was modelling the micro hydraulic fracturing stage of the MDT test. XFEM, a very powerful method for the simulation of hydraulic fracturing was utilized even though it was mainly developed for solid mechanics application of fracture mechanics. Results of modelling micro hydraulic fracturing test in clay shale have been compared with the same model with harder material. As a result of the injection of a limited amount of fracturing fluid, it is almost impossible to propagate fractures beyond the disturbed zone which was the result of drilling and mud pressure effects in unsleeved section and the disturbed zone around wellbore wall in sleeved or packer section. For this reason, it is likely that a fracturing fluid with a higher viscosity and/or a larger volume of fracturing fluid at higher injection rates is required to obtain a reasonable estimate of the far field in situ stresses. As an alternative for in situ stress measurement in hard soil soft rock, which can usually tolerate a considerable amount of plastic strain, it is recommended to focus on strain- rate tests such as dilatometer instead of the test based on fluid pressure.

## **RECOMMENDATIONS FOR FURTHER RESEARCH**

Packer elements play a critical role in process of stress measurement. The lack of knowledge about its mechanical properties can create a high level of uncertainty for numerical modeling studies. It is essential to study its behavior by conducting a proper set of experiments to extract its representative constitutive parameters.

An extensive investigation needs to be conducted to evaluate the optimal volume of the injecting fluid to pass the disturbed zone and reach the far-field stress zone. The ideal injection rate under partially drained condition also needs to be studied. As well, the properties of injected fluid during micro-hydraulic fracturing test and its effect on the test results need to be better understood.

## REFERENCES

- Abaqus Documentation and manual, 2014
- Abifadel N, Klisinski M, Sture S, Ko HY. Unconstrained optimization for the calibration of an elasto-plastic constitutive model. Report, Department of Civil, Environmental, and Architectural Engineering, University of Colorado, Boulder: U.S. Army Engineer Waterways Experiment Station, Contract DACA 39-83-C-0012, 1988; 65
- Abou-Sayed, A.S., 1978, An experimental technique for measuring the fracture toughness of rocks under downhole stress conditions, VDI-Berichte, No.313, 819-824
- Adachi J., Siebrits E., Peirce A., and Desroches J. 2007. Computer simulation of hydraulic fractures. *International Journal of Rock Mechanics and Mining Sciences* 44:739–757.
- Advanced Geotechnology, 2001, “Geological and Geomechanical Characterization of the Lea Park Formation, Colorado Group, and Upper Mannville Group Cap rocks”, Volume 1
- AGI (American Geological Institute), 1984, Dictionary of geological terms, Edited by R., Bates, J.J., Doubleday, New York, 571P.
- Ahmed, A., 2009, eXtended Finite Element Method (XFEM)- Modeling arbitrary discontinuities and Failure analysis, Dissertation, Istituto Universitario di Studi Superiori di Pavia
- Alberta Energy and Utilities Board, Statistical Series 2002-98, Alberta’s Reserves 2001 and Supply/Demand Outlook 2002-2011.
- Alberta Oil Sands Inc., (2010), “Application for Alberta Oil Sands Inc. Clearwater West LP-SAGD Pilot Project”, Website:<http://www.aboilsands.ca>
- Al-Shamrani, M.A. and Al-Mhaidib, A.I., 2000, Swelling behavior under oedometric and triaxial loading conditions. *Advances in Unsaturated Geotechnics*, Geotechnical Special Publication No. 99. ASCE. pp. 344-360
- Anandarajah A, Agarwal D. Computer-aided calibration of a soil plasticity model. *International Journal for Numerical and Analytical Methods in Geomechanics* 1991; 15(12):835–856.
- Andriashek, L.D., (2003), “Quaternary geologic setting of the Athabasca oil sands in situ area, Northeast Alberta”, EUB/AGS Earth Sciences Report, 2003-03, 83 p.
- Anderson, E. M. (1951). *The Dynamics of Faulting and Dyke Formation with Applications to Britain*. Edinburgh, Oliver and Boyd.
- Anderson TL (1995), *Fracture Mechanics Fundamentals and Applications*, CRC Press, 2nd Ed.
- Andriashek, L.D., (2003), “Quaternary geologic setting of the Athabasca oil sands in situ area, Northeast Alberta”, EUB/AGS Earth Sciences Report, 2003-03, 83 p.

- Atkinson, J.H., Sallfors, G., 1991, Experimental determination of stress-strain-time characteristics in laboratory and in situ tests, Proc. 10<sup>th</sup> Eur. Conf. Soil Mech. Fdn Engng, Florence, Vol. 3, 915-958.
- Atkinson, C., Desroches, J., Eftaxiopoulos, D. A., Thiercelin, M., 2001, Wellbore stresses induced by the nonlinear deformation of an inflatable packer, *Journal of Engineering Mathematics* Vol. 41: 305–327
- Atkinson, C., Peltier, B., 1993, the finite deformation of a reinforced packer, membrane theory, *Journal of Engineering Mathematics*, 27:443-454
- Attewell, P.B., Farmer, I.W., 1976, *Principles of Engineering Geology*, Wiley & Sons, Inc., 497 P.
- Aversa, S., Evangelista, A., Leroueil, S., Picarelli, L., 1993, Some aspects of the mechanical behavior of structured soils and soft rock, *Geotechnical Engineering of Hard Soils-Soft Rocks*, Athens, Greece, (Ed. Anagnostopoulos, A.G. et. al.), Balkema, 359-366.
- Bachu, S., U nderschultz, J.R., Hitchon, B., Cotterill, D., (1993), "Regional-scale subsurface hydrogeology in Northeast Alberta", Bulletin No.6, Alberta Geological Survey (AGS), Alberta Research Council (ARC), 49 p.
- Banks-Sills, Wawrzynek, Carter, Ingraffea, and Hershkovitz, 2007, "Methods for computing stress intensity factors in anisotropic geometries: Part II – arbitrary geometry," *Engng. Fracture Mech.*, 74, 9, 1293-1307
- Barree, R.D, V.L. Barree and D.P. Craig, 2009. Holistic Fracture Diagnostics: Consistent Interpretation of Prefrac Injection Tests using Multiple Analysis Methods. *SPE J. Production and Operations*, SPE 107887, pp. 396-406.
- Bertuccioli, P., Lanzo, G., 1993, Mechanical properties of two Italian structurally complex clay soils, *Geotechnical Engineering of Hard Soils-Soft Rocks*, Athens, Greece, (Ed. Anagnostopoulos, A.G. et. al.), Balkema, 383-389.
- Bell, J.S., Gough, D.I., 1983, The use of borehole breakouts in the study of stress, proceeding of the workshop on hydraulic fracturing stress measurement, Monterey, California, 201-209.
- Bell, J.S., Price, P.R., Mclellan, P.J., 2010, In situ stress in the Western Canada Sedimentary Basin, Chapter 29, *Geological Atlas of the Western Canada Sedimentary Basin*.
- Bieniawski, Z.T., 1973, Engineering classification of jointed rock masses, *Transactions of the South African Institution of Civil Engineers*, Vol. 15, 335-344.
- Biot, M. A. (1941). "General theory of three dimensional consolidation." *J. Appl. Phys.*, 12(2), 155-164.
- Biot, M.A. (1962). "Mechanics of deformation and acoustic propagation in porous media." *J. Appl. Phys.*, 33, 1482–1498.

- Bjerrum, L. 1967, Progressive failure in slopes of overconsolidated clay and clay shales, *J. Soil Mech. Found, ASCE*, Vol. 93, No. SM5, 1-49.
- Breckels, I.M. and van Eekelen, H.A.M., 1981, Relationship Between Horizontal Stress and Depth in Sedimentary Basins, SPE 10336, Paper presented at the 56<sup>th</sup> Annual Fall Technical Conference and Exhibition of the Society of Petroleum Engineers of AIME, held in San Antonio, Texas, Oct. 5 -7, 1981.
- British Standard Institution BSI (1981), Code of practice for site investigation, BS 5930. HMSO, London.
- Braudeau, E., Costantini, J. M., Bellier, G., Colleuille, H., 1999, New device and method for soil shrinkage curve measurement and characterization, *Soil Science Society of America Journal*, 63 (3), 525-535.
- Bredehoeft, J.D., Wolf, R.G., Keys, W.S., Shuter, E., 1976, hydraulic fracturing to determine the regional in situ stress field, Piceance Basin, Colorado. *Geological Society of American Bulletin*, 87:250-258.
- Borja R.I. 2008. Assumed enhanced strain and the extended finite element methods: A unification of concepts. *Computer Methods in Applied Mechanics and Engineering* 197: 2789–2803.
- Botts, M.E., 1986. The Effects of Slaking on the Engineering Behaviour of Clay Shales, PhD Thesis, University of Colorado
- Boulding, J. R., Ginn, J. S., 2003, *Practical Handbook of Soil, Vadose Zone, and Ground-Water Contamination: Assessment, Prevention, and Remediation*, Second Edition, CRC Press, ISBN: 9781566706100, PP. 728
- Bower, A.F., 2010, "Applied mechanics of solids", Taylor&Francis Group, ISBN 978-1-4398-0247-2, 794 pages
- Burland, J.B., 1990, On the compressibility and shear strength of natural clays, *Géotechnique*, 40(3), 329-78.
- Burland, J.B., Rampello, S., Georgiannou, V.N., Calabresi, G., 1996, A laboratory study of the strength of four stiff clays, *Géotechnique* 46(3), 491-514.
- Bush, D.D. , Meyer, B.S., 1988, In-situ stress magnitude dependency on lithology, in Proc. of the 29<sup>th</sup> U.S. Symposium of Rock Mechanics: Key questions in rock mechanics. Cundall, P.A., Sterling, R.L., and Starfield, A.M, Eds.
- Butler, R.M., 1994, "STEAM-ASSISTED GRAVITY DRAINAGE: CONCEPT, DEVELOPMENT, PERFORMANCE AND FUTURE", *Journal of Canadian Petroleum Technology*
- Butler, R.M., 1994, Horizontal wells for the recovery of oil, gas and, bitumen, Monograph No. 2, Petroleum Society of CIM
- Byerlee, J. D. (1978). "Friction of rock." *Pure & Applied Geophysics*, 116, 615–626.

- Calvello M., 2002, Inverse analysis of a supported excavation through Chicago glacial Clays, PhD thesis, Northwestern University, Evanston, IL
- Cantini, S., Desroches, J., Fourmaintraux, D., Goff, C., Detailed in situ stress measurements above the reservoir for safety assessment of underground gas storage, OMC 2005, Proceeding offshore marine conference, Ravenna, Italy, 2005.
- Carlson, M., 2003, SAGD and Geomechanics, JCPT, Vol. 42, No.6, 19-25
- Castillo, J.L., (1987), "Modified fracture pressure decline analysis including pressure-dependent leakoff", SPE 16417, 9 p.
- Chappell, B.A., 1976, Deformation response of differently shaped and sized test pieces of shale rock, International Journal Rock Mechanics Mining Science, Vol. 11, 21-28.
- Chandler, R.J., 1970, Shallow slab slide in the Lias clay near Uppingham, Rutland, Géotechnique, Vol. 20, 253-260
- Carlson, M., 2003, SAGD and Geomechanics, JCPT, Vol. 42, No.6, 19-25
- Clark, J.B., 1949, A hydraulic fracture process for increasing the productivity of wells, Transactions, AIME, 186:1.
- Clearly M. P., "Comprehensive Design Formulae for Hydraulic Fracturing," Society of Petroleum Engineers SPE-9259-MS, 1980.
- Clough, W.G., L.J. West, and L.T. Murdock, (1978). Pit Slope Performance in Shale, Wyoming, U.S.A. Rockslides and Avalanches, Elsevier Publishing, Amsterdam, The Netherlands pp. 667-690.
- CNRL Report, 2014, "Primrose Flow to Surface Causation Report".
- Colback, P.S.B., Wiid, B.L., 1965, The influence of moisture content on the compressive strength of rocks, *Proc. 3rd Can. Rock. Mech. Symp.*, Toronto: 55-83.
- Collins, I.F., and Yu, H.S., (1996). "Undrained cavity expansion in critical state soils." International Journal for Numerical and Analytical Methods in Geomechanics, 20(7): 489-516.
- Collins, P.M., 2007, Geomechanical Effects on the SAGD Process, SPE 97905
- Collins, P.M., Walter, D.A., Perkins, T., Kuhach, J.D., Veith, E., 2011, Effective caprock determination for SAGD projects, CSUG/SPE149226.
- Conly, F. M., Crosley, R. W., and Headley, J. V. 2002. Characterizing sediment sources and natural hydrocarbon inputs in the Lower Athabasca River, Canada. Journal of Environmental Engineering and Science 1:187.
- Coussy, O. (2004). Poromechanics, John Wiley & Sons Ltd., Chichester, United Kingdom ISBN-13: 9780470849200.

- Cuccovillo, T., Coop, M.R., 1993, The influence of bond strength on the mechanics of carbonate soft rocks, *Geotechnical Engineering of Hard Soils-Soft Rocks*, Athens, Greece, (Ed. Anagnostopoulos, A.G. et. al.), Balkema, 447-455.
- Cuenca, F. A., 1988, *Stability of reinforced embankments constructed of high plasticity clays*, PhD Dissertation, The University of Texas at Austin, United States
- Deen, R.C., 1981, The need for a schema for the classification of transitional (shale) materials, *Geot. Test. J.*, Vol. 4, No. 1, 3-10.
- DeNatale JS. On the calibration of constitutive models by multivariate optimization. Ph.D. Dissertation, University of California, Davis, 1983.
- Deo, P., 1972, *Shales as embankment materials*, Joint Highway Research Project, Purdue University, W. Lafayette, Ind.
- Detournay, E., and Cheng, A. H-D. (1993). "Fundamentals of poroelasticity." *Comprehensive rock engineering: Principles, practice and projects*, Vol. 2, J. A. Hudson, ed., Pergamon, Oxford, UK, 113–171.
- Detournay, E., Carbonell, R., 1994, "Fracture mechanics analysis of the breakdown process in minifrac or leak-off tests", *Proc. of the joint ISRM/SPE conference Eurock'94 2*, 9-31, August 1994, Delft, The Netherlands. 399-407, Rotterdam: Balkema.
- Desroches, J, and A. Kurkjian, 1999. "Applications of Wireline Stress Measurement", *SPE Reservoir Eval. & Eng.*, Vol 2, No. 5, SPE 58086, pp. 451-461.
- Desroches, J., Marsden, J.R., Colly, N.M., 1995, Wireline open hole stress test in a tight gas sandstone, *Oil and Gas Journal, Drilling and Production*, Cannes, France, November 6-9.
- Desroches, J., Thiercelin, M., 1994, Estimating the in situ state of stress and rock properties using small scale hydraulic fracturing, 5<sup>th</sup> Brazilian Petroleum Congress and Conexpo Arpel.
- Doe, T., Hustrulid, W.A., Leijon, B., Ingevald, K., Strindell, L., 1983, Determination of the state of stress at the Strip Mine, Sweden, *Proceeding of the workshop on Hydraulic fracturing stress measurements*, Monterey, California, 119-129.
- Dubost, F.X. Zheng, S.Y. Corbett, P.W.M., (2004), "Analysis and numerical modelling of Wireline pressure tests in thin bedded turbidites", *Journal of petroleum science and engineering*, pp. 247-261.
- Dunlap, I.R., 1963, Factors controlling and direction of hydraulic fracture, *Journal of the institute of Petroleum*, 49.282-288
- Edmunds, N.R., and Suggett, J.C., Design of a Commercial SAGD Heavy Oil Project, Paper SPE 30277 presented at the International Heavy Oil Symposium, Calgary, June 19–21, 1995.
- Encver, J.R. and Woollorton, B.A., 1982, Experience with hydraulic fracturing as a means of estimating in-situ stress in Australian coal basin sediments, *Proc. of the Workshop on*

Hydraulic Fracturing Stress Measurements, U.S. Nat. Comm. on Rock Mech., Washington, D.C.

ERCB Investigation Report, 2013, "CNRL Primrose East Bitumen Emulsion Release"

Elliot, G.M., Brown, E.T., 1985, Yield of soft high porosity rock. *Géotechnique* 35, 4, 413-423.

Esu, F., 1977, Behavior of Slopes in Structurally Complex Formation, in Proceeding of the International Symposium on the Géotechnique of structurally complex formation, Capri, AGI, Vol. 2, 292-304.

Evans. K.F., (1987). "Laboratory study of two straddle packer systems under simulated hydrofrac stress measurement conditions." *Journal of Energy Resources Technology*, 109, 180-190.

Finno, R. J. , Bryson, L. S. , and Calvello, M. ,2002, "Performance of a stiff support system in soft clay." *J. Geotech. Geoenviron. Eng.* 128 (8), 660-671

Fisher K. and Warpinski N. 2012. Hydraulic fracture-height growth: real data. *SPE Production & Operations* 27(1): 8–19.

Finno RJ, Calvello M. Supported excavations: the observational method and inverse modeling. *J Geotech Geoenviron Eng ASCE* 2004, in press.

Fleming, R.W., Spencer, G.S., Banks, D.C., 1970, Empirical study of behavior of clay shale slopes, U.S. Army Eng. Nuclear Cratering Group Tech. Report No. 15, Vol. 1 and 2

Franklin, J.A., and Chandra, R., 1972, The slake- durability test, *Intl. J. Rock Mech. Min. Sci.*, v. 9, 325-341.

Freeman C.M., Moridis G.J., and Blasingame T.A. 2011. A numerical study of microscale flow behavior in tight gas and shale gas reservoir systems. *Transport in Porous Media* 90: 253–268.

Friswell MI., 1996, "The derivatives of repeated eigenvalues and their associated eigenvectors", *Journal of Vibration and Acoustics (ASME)* 1996; 118:390–397

Forsythe, G.E. and Strauss, E.G., 1955, on best conditioned matrices: American mathematical Society proceedings, v. 10, no. 3, p. 340-345.

Fu P., Johnson S.M., and Carrigan C.R. 2012. An explicitly coupled hydro-geomechanical model for simulating hydraulic fracturing in arbitrary discrete fracture networks. *International Journal for Numerical and Analytical Methods in Geomechanics*

Gay, N.C., 1980, THE STATE OF STRESS IN THE PLATES, IN Dynamics of plate interiors. Geodynamics Series. Edited by Bally, Bender, American Geophysics Union and the Geological Society of America, vol. 1, 145-154.

Gamble, J.C. (1971). Durability-plasticity classification of shales and other argillaceous rocks, Ph.D. Thesis, Geology, University of Illinois, Urbana.

- Gillott, J.E., 1987, *Clay in Engineering Geology*, Developments in Geotechnical Engineering, 41, Elsevier, Amsterdam
- Gordeliy, A., Peirce, A, 2013, Coupling schemes for modeling hydraulic fracture propagation using the XFEM, *Comput. Methods Appl. Mech. Engrg.* 253 (2013) 305–322
- Gordeliy, A., Peirce, A, 2014, Enrichment strategies and convergence properties of the XFEM for hydraulic fracture problems, *Comput. Methods Appl. Mech. Engrg.*
- Grainger, P. 1984, The classification of mudrocks for engineering purposes. *Quaternary Journal and Engineering Geology*, 17(4), 381-387.
- Gens, A., and Potts, D. M. (1988). "Critical state models in computational geomechanics." *Engrg. Comp.*, 5, 178-197.
- Geological Atlas of the Western Canada Sedimentary Basin, Cretaceous Mannville Group of the Western Canada Sedimentary Basin, AGS, Chapter 19, 317- 335.
- Glass, D.J. (editor) 1997. *Lexicon of Canadian Stratigraphy*, vol. 4, Western Canada including eastern British Columbia, Alberta, Saskatchewan and southern Manitoba. Canadian Society of Petroleum Geologists, Calgary, 1423 p. on CD-ROM. ISBN 0-920230-23-7
- Green, A. E., Adkins, J. E., 1960, "Large elastic deformations and non-linear continuum mechanics", Clarendon Press, Oxford, 1960
- Haddad, M., Sepehrnoori, K., 2014, Simulation of Multiple-Stage Fracturing in Quasibrittle Shale Formations Using Pore Pressure Cohesive Zone Model, Unconventional Resources Technology Conference, URTEC: 1922219
- Hattori, G., Rojas-Díaz, R., S´aez, A., Sukumar, N., Garc´ia-S´anchez, F, 2015, New anisotropic crack-tip enrichment functions for the extended finite element method, *Computational Mechanics*
- Hauck, E., Baski, H.A., 1998, "Fix head inflatable packer with fully reinforced inflatable element and method of fabrication", USA Patent, Patent number: 5778982
- Hawkins, A.B., Pinches, G.M., 1992, engineering description of mudrocks. *Quarterly Journal of Engineering Geology* 25, 17-30.
- Haimson, B.C., Fairhurst, C., 1970, In-situ stress determination at great depth by means of hydraulic fracturing, proceeding of the 11<sup>th</sup> US Symposium on Rock Mechanics, University of California, Berkeley, pp.559-584.
- Haimson, B.C., 1975, deep in-situ stress measurement by hydraulic fracturing, *Tectonophysics*, Vol. 29, 41-47
- Haimson, B.C., 1978, the hydro-fracturing stress measurement method and recent field results, *international Journal of Rock Mechanics and Mining Science*, 1594:167-178

- Haimson, B.C., 1981, Confirmation of hydrofracturing results through comparison with other stress measurements, proceeding of the 22th US Symposium on Rock Mechanics, Cambridge, Massachusetts, 409-415.
- Haimson, B.C., 1983, a comparative study of deep hydrofracturing and overcoring stress measurements at six locations with particular interest to the Nevada test site, proceeding of the workshop on hydraulic fracturing stress measurement, Monterey, California, 107-118.
- Haimson, B.C., 1984, the state of stress at Nevada test site, proceeding of the International Symposium, Zurich, Edited by K.Kovari, 115-126
- Haimson, B.C., Voight, B., 1977, Crustal stresses in Iceland, Pure and application Geophysics, 115,153-190.
- Hanna, A., and T.E. Little, 1992," An estimate of rebound potential of the Shatesbury shales at a damsite in British Columbia, Canada", Geotech. J., 29:375-92.
- Hashash Y.M.A., Marulanda C., Ghaboussi J., Jung, S. 2006. Novel approach to integration of numerical modeling and field observation for deep excavation. Journal of geotechnical and geoenvironmental engineering, Vol. 132(8), pp.1019-1031
- Hein, F.J., March, R.A., and Boddy, M.J. ,2007, Overview of oil sands and carbonate deposit of Alberta: Regional geological framework and influence of salt-dissolution effects, extended abstract prepared for AAPG Hedberg conference, "Heavy oil and bitumen in Foreland basins – from processes to products", September 30 – October 3, Banff, Alberta, Canada.
- Hellan K (1984), Introduction to Fracture Mechanics, McGraw-Hill.
- Henkel, D.J., 1971, "The relevance of laboratory measured parameters in field studies". Proc. Roscoe Mem. Symp., Cambridge, publ. Foulis, pp.669-75.
- Henshell R.D. and Shaw K.G. 1975. Crack tip finite elements are unnecessary. International Journal for Numerical Methods in Engineering 9: 495–507
- Hickman, S.H., Zoback, M.D., 1983, the interpretation of hydraulic fracturing pressure time data for insitu stress determination,, proceeding of the workshop on hydraulic fracturing stress measurement, Monterey, California, 44-54.
- Hill, M.C., 1998, Methods and guidelines for effective model calibration: U.S. Geological Survey Water-Resources Investigations Report 98-4005, 90 p
- Hubbert, M.K., Willis, D.G., 1957, Mechanics of hydraulic fracturing Transaction of AIMMPE, 210,153-168
- Hutchinson JW (1979), A Course on Nonlinear Fracture Mechanics, Department of Solid Mechanics, The Technical University of Denmark
- Hydrogeology Baseline Report, 2011, Appendix 4-IV, Westwater Environmental Ltd.

- Hyett, A.I., Hudson, J.A., 1990, A photoelastic investigation of the stress state close to rock joints. Proc. Conf. on rock Joints (ed. Barton N. and Stephansson F.), Balkema, 227-233
- Hoshino, K., 1984, Effect of geological factors on mechanical properties of rocks, Proc. 6<sup>TH</sup> Symp. Rock Mechanics, Japan, 145-150.
- IAEG. ,1979, Report for the commission on engineering geological mapping. Buletin IAEG 19, 364-371.
- Ingram, R.L., 1953, Fissility of mudrocks, Bull. Geol. Soc. Amer., v. 64, No. 8, 869-878.
- International Society for Rock Mechanics ISRM, 1982, Suggested Methods: Rock Characterization, Testing and Monitoring. Edited by Brown, E.T. Oxford
- Irwin, G.R. 1957, analysis of stresses and strains near the end of crack, J. Appl. Mech., 24, p361
- Isaac, B.A., Dusseault, M.B., Lobb, G.D., and Root, J.D., 1982. Characterization of the Lower Cretaceous overburden for oil sands surface mining within Syncrude Canada Ltd. Leases 17 and 22. Proceedings, 4th International Congress of the International Association of Engineering Geology, New Delhi, India.
- Ito, T., Hayashi K., (1993), "Analysis of crack reopening behavior for hydrofrac stress measurement", Int. J. Rock Mech. Min. Sc. Geomech. Abs. , 30, 7: pp. 1235-1240.
- Jaeger, J. C. and Cook, N. G. W. (1971). Fundamentals of Rock Mechanics. London, Chapman and Hall.
- Jaeger, J. C. and Cook, N. G. W. (1979). Fundamentals of Rock mechanics, 2nd edn. New York, Chapman and Hall.
- Janssen M, Zuidema J, and Wanhill R (2004), Fracture Mechanics, Spon Press, London and New York, 2nd Ed.
- Jardine, R.J., Potts, D.M., St.John, H.D., Hight, D.W., 1991, Some practical applications of a non-linear ground model, Proc. 10<sup>th</sup> Eur., Conf. Soil Mech. Eng., Florence, Vol. 1, 223-228.
- Jaworski, G.W., 1979, An experimental study of hydraulic fracturing, PHD thesis, University of California, Berkeley.
- Jaworski, G.W., Duncan, J.M., Seed, H., Bolton, 1981, Laboratory study of hydraulic fracturing, ASCE Journal of the geotechnical engineering division, 107 (GT6): 713-732
- Ji L., Settari A., and Sullivan R.B. 2009. A novel hydraulic fracturing model fully coupled with geomechanics and reservoir simulation. SPE Journal 14(3): 423–430
- Johnson, J.N., Clifton, R.J., Simonson, E.R., Green, S.J., 1973, Analysis of fracture for hollow cylindrical and spherical rock specimens subjected to internal pressure with application to underground contamination, Terra Tek report, Salt Lake, Utah

- Johnson, S.J., 1969, Report of Chairman of Specialty Session No: 10, Engineering properties and behavior of clay shales, Proc., 7th Intl. Conf. Soil Mech. Found. Eng., Mexico City, Vol. 3, p. 483
- Kaliske, M., Rothert, H., 1997, "On the finite element implementation of rubber-like materials at finite strains", Engineering Computations, Vol. 14, No. 2, pp216-232
- Keidser A, Rosjberg D. A comparison of four inverse approaches to groundwater flow and transport parameter identification. Water Resour Res 1991; 27(9):2219–32.
- Kehle, R.O., (1964). "Determination of tectonic stresses through analysis of hydraulic well fracturing." J. Geophysics Res., 69:259.
- Kim, K., Prezzi, M., and Salgado, R., 2006, Interpretation of cone penetration tests in cohesive soils, FHWA/IN/JTRP-2006/22, SPR-0622, Joint Transportation Research Program, Purdue University, USA
- Kim J. and Moridis G.J. 2012. Analysis of fracture Propagation during hydraulic fracturing operations in tight/shale gas systems
- Kim J. and Moridis G.J. 2012. Gas flow tightly coupled to elastoplastic geomechanics for tight and shale gas reservoirs: material failure and enhanced permeability. SPE Unconventional Resources Conference, Pittsburgh, PA, SPE 155640.
- Kim J., Moridis G.J., Yang D., and Rutqvist J. 2012. Numerical Studies on Two-way Coupled Fluid Flow and Geomechanics in Hydrate Deposits. SPE Journal 17(2): 485–501.
- Kim J., Sonnenthal E., and Rutqvist J. 2012. Formulation and sequential numerical algorithms of coupled fluid/heat flow and geomechanics for multiple porosity materials. International Journal for Numerical Methods in Engineering 92: 425–456.
- Kim J., Tchelepi H.A., and Juanes R. 2011. Rigorous coupling of geomechanics and multiphase flow with strong capillarity. SPE Reservoir Simulation Symposium, the Woodlands, TX, SPE 141268.
- Kim J., Tchelepi H.A., and Juanes R. 2011. Stability and convergence of sequential methods for coupled flow and geomechanics: Drained and undrained splits. Computer Methods in Applied Mechanics and Engineering 200: 2094–2116.
- Kim J., Tchelepi H.A., and Juanes R. 2011. Stability and convergence of sequential methods for coupled flow and geomechanics: Fixed-stress and fixed-strain splits. Computer Methods in Applied Mechanics and Engineering 200: 1591–1606.
- Kry, P.R. and Gronseth, J.M., 1983, In-situ stresses and hydraulic fracturing in deep basin. Journal of Can. Petrol. Tech., pp. 31-35.
- Kydoniefs, A.D., 1969, Finite axisymmetric deformations of an initially cylindrical membrane reinforced with inextensible cords, Journal of Mechanics and Applied Math, Vol. XXIII, Pt.4

- Kurkjian, A., Detournay, E., Khodaverdian, M., Guo, Q., Mclennan, J., 1995, 'A study of injection between dual packers prior to fracture initiation", Internal report, Schlumberger Houston Product Center, Sugar Land, TX
- Lambe, T.W., Whitman, R.V., 1969, Soil Mechanics, New York: John Wiley & Sons Inc., 553 p.
- Lashkaripour, G.R., Ghafoori, M. 1999, Predicting mechanical properties of shale from index parameters, *Proc. 2nd Asian Symp. on Engineering Geology and the Environment*, Bangi, Malaysia: 2-35 to 2-39.
- Layne, A.W., and Siriwardane, H.J., 1988, Insights into hydraulic fracturing of a horizontal well in a naturally fractured formation, Paper SPE 18255.
- Lawn B (1993), *Fracture of Brittle Solids*, Cambridge University Press, Cambridge, New York, 2nd Ed.
- Lecampion B., Contantinescu A. 2005. Sensitivity analysis for parameter identification in quasi-static poroelasticity, *International Journal for Numerical and Analytical Methods in Geomechanics*, Vol.29, pp.163-185 Lecampion B, Constantinescu A,
- Lefebvre, G., 1970, Contribution a l etude de la stabilite des pentes dans les argiles cimentees. PhD thesis, Universite Laval, Quebec
- Legarth B., Huenges E., and Zimmermann G. 2005. Hydraulic fracturing in a sedimentary geothermal reservoir: Results and implications. *International Journal of Rock Mechanics and Mining Sciences* 42: 1028–1041.
- Lee, M.Y., Haimson, B.C., (1989), "Statistical evaluation of hydraulic fracturing stresses measurement parameters, *Int. J. Rock Mech. Min. Sci., Geomech. Abstr.* Vol.26, No.6, pp. 447-456.
- Leroueil, S., 1997, Critical state soil mechanics and the behaviour of real soils, *Symposium on Recent Development in Soil and Pavement Mechanics*, June 25-27, pp.1-40, Rio De Janeiro, Brazil
- Levasseur S., Malécot Y., Boulon M., Flavigny E., 2007. Soil parameter identification using a genetic algorithm. *International Journal for Numerical and Analytical Methods in Geomechanics*, in press.
- LO, K.W., Chua, K.H., Tamilselvan, T., 1993, A fractured mechanical model for hard soil, *Geotechnical Engineering of Hard Soils-Soft Rocks*, Athens, Greece, (Ed. Anagnostopoulos, A.G. et. al.), Balkema, 647-652.
- Li Fang-quan, 1983, Experiments of in situ stress measurements using stress relief and hydraulic fracturing techniques, *proceeding of the workshop on hydraulic fracturing stress measurements*, Monterey, California, 130-134.
- Massarsch, K.R., Holm, B.G., Fredriksson, A., 1975, Measurement of horizontal in situ stress , *proceeding of the American Society of Civil engineering*, Raleigh, Vol. 1, 266-286.

- Malvern, L.E., (1969), "Introduction to the Mechanics of a Continuous Medium", Prentice-Hall, New York
- Mattsson H, Klisinski M, Axelsson K. Optimization routine for identification of model parameters in soil plasticity. *International Journal for Numerical and Analytical Methods in Geomechanics* 2001; 25(5):435–472.
- Marslan, A., 1971, The shear strength of stiff fissured clays, Building Research Station, Department of Environmental, England.
- Martens, S.N., 2000.Characterizing the operational strength of Discontinuous stiff clays and mudstones, Master Thesis, University of Alberta
- Meyer B.R. "Three-Dimensional Hydraulic Fracturing Simulation on Personal Computers: Theory and Comparison Studies," Society of Petroleum Engineers, SPE 19329, 1989.
- McLennan, J.D., Roegiers, J.C., (1981), "Do ISIP accurately represent the minimum principal stress?", USGS Workshop on hydraulic fracturing stress measurement, Monterey, California. 11 p.
- McNeilan, T. W., and Bugno, W.T. 1985. Cone Penetration Test Results in Offshore California Silts, *Strength Testing of Marine Sediments: Laboratory and In-Situ Measurements*, ASTM, San Diego, CA, USA, 55-71.
- Merci, G., Cepeda-Diaz, A.F., 1986, Residual shear strength of clays and shales, *Géotechnique*, 36, 269-74
- Mielenz, R.C., and King, M.E., 1955. Physical-Chemical Properties and Engineering Performance of Clays. Bull., California, Division of Mines, No.169.
- Mroz, Z. and Norris, V. A., 1982, Elastoplastic and viscoplastic constitutive models for soils with anisotropic loading, In *Soil mechanics-transient cyclic loads*, Eds. G. N. Pande and O. C. Zienkiewicz, Wiley (Chichester), pp. 219-252
- Moes N., Dolbow J., and Belytschko T. 1999. A finite element method for crack growth without remeshing. *International Journal for Numerical Methods in Engineering* 46:131–150.
- Moore, D. E. and Lockner, D. A. (2006). Friction of the smectite clay montmorillonite: A review and interpretation of data. *The Seismogenic Zone of Subduction Thrust Faults, MARGINS Theoretical and Experimental Science Series*. C. M. and T. Dixon. New York, Columbia University Press. 2.
- Morrow, C., Radney, B. et al. (1992). Frictional strength and the effective pressure law of montmorillonite and illite clays. *Fault Mechanics and Transport Properties of Rocks*, Academic, San Diego, Calif.
- Morgenstern, N.R., Scott, J.D., Guo, F., and Wang, Y., 1992, Report produced at the large scale hydraulic fracturing workshop held at the University of Alberta, March 19.

- Morgenstern, N.R., Eigenbrod, K.D., 1974, Classification of argillaceous soils and rocks, Proceeding American Society Civil Engineers, Journal Geotechnical Engineering Division, Vol. 100, 1137-1156.
- Morgenstern, N.R., Cruden, D.M., 1977, Description and classification of geotechnical complexities, in Proceeding of the International Symposium on the Géotechnique of structurally complex formation, Capri, IGA, Vol. 2, 195-203.
- Morgenstern, N.R., 1979, Geotechnical behavior of clay shales, an overview, In Proceeding of the International Symposium on Soil Mechanics, Oaxaca. Vol. 1, 29-52.
- Morgenstern, N.R., Blight, G.E., Janbu, N. and Resendiz, D., 1977. Slopes and excavations, state-of-the-art report, Proceedings 9th International Conference Soil Mechanics Foundation Engineering, Vol.2, p. 547-604, Toyko, Japan
- Muhr, A. H., 2005, "Modeling the stress-strain behavior of rubber", Rubber chemistry and technology, 78(3), 391-425
- Nassir M., Settari A., and Wan R. 2012. Prediction and optimization of fracturing in tight gas and shale using a coupled geomechanical model of combined tensile and shear fracturing. SPE Hydraulic Fracturing Technology Conference, The woodland, TX, SPE 152200
- Navarro, V., Candel, M., Barenca, A., Yustres, A., Garcia, B., 2007, "Optimization procedure for choosing Cam clay parameters", Computers and Geotechnics, 34, 524-531
- Navidi, W., 2010, Statistics for Engineers and Scientists, third edition, ISBN-13: 978-0073376332
- Olson, R.E., 1990, Preliminary laboratory testing, samples from Superconducting Super Collider project, Final Report to the Earth Tech. Corp., CA.
- Ogden, R.W., 1997, "Non-linear elastic deformations", General Publishing Company, Ltd., ISBN 0-486-69640-0, 532 pages
- Nelson, R.A., 1985, Geologic analysis of naturally fractured reservoir, Gulf publication Co., Houston
- Niandou, H., Shao, J.F., Henry, J.P., Fourmaintraux, D., 1997, Laboratory investigation of the mechanical behavior of Tournemire shale, International Journal Rock Mechanics Mining Science, 34, 3-16.
- Nguyen Minh D. 2002. Parameter identification for lined tunnels in viscoplastic medium, International Journal for Numerical and Analytical Methods in Geomechanics, Vol. 26, pp. 1191-1211.
- Nobari, E.S., Lee, K.L., Duncan, J.M., 1973, Hydraulic fracturing in zoned earth and rock fill dame, office of Research Services, University of California, Berkeley, Report TE 73-1, VOL 9, NO 8, 17-23.

- Nordren R.P. 1972. Propagation of a vertical hydraulic fracture. SPE Journal 12(8): 306–314. SPE 7834
- Notle, K.G., (1982), “Fracture design considerations based on pressure analysis”, SPE Production Engineering. February, SPE 10911, pp. 22-30.
- Notle, K.G., (1979), “Determination of fracture parameters from fracturing pressure decline”, paper SPE 8341. 16 p.
- Olsson, W.A., 1991, the compressive strength of tuff as a function of strain rate, Inter. J. Rock Mech. Min. Sci. & Geomech. Abstr., 28, No:1, 115-118.
- O’Kelly, B.C., 2013, Atterberg limits and remolded shear strength- water content relationships, ASTM Geotechnical Testing Journal, Vol. 36, No. 6,939-947
- Ottis, M.E., 1998, Effects of Slaking on the Strength of Clay Shales: A Critical State Approach, Proceedings of the 2nd International Symposium on the Geotechnics of Hard Soils / Soft Rocks, Vol. 1, Naples, Italy.
- Ou CY, Tang YG. Soil parameter determination for deep excavation analysis by optimization. J Chin Inst Eng 1994; 17(5):671–88.
- Palmgren, C., Waltker, I., Carlson, M., Uwiera, M., Torlak, M., 2001, Reservoir design of a shallow LP-SAGD project for *in situ* extraction of Athabasca Bitumen, WHOC11-520
- Pal S., Wathugala G.W., Kundu S. 1996. Calibration of constitutive model using genetic algorithms. Computers and Geotechnics, Elsevier, Vol. 19(4), pp.325-348
- Paris, P.C., Sih, G.C., 1965, STRESS ANALYSIS OF CRACKS, astm stp 391, pp 309-381
- Patton, F.D., 1966, Multiple modes of shear failure in rock, In Proceeding of the International Symposium on Soil Mechanics, Lisbon, Vol. 1, 509-513.
- Perkins T.K. and Kern L.R. 1961. Widths of hydraulic fractures. Journal of Petroleum Technology 13(9): 937–949. SPE 89.
- Perez, N., 2004, fracture mechanics, Kluwer Academic Publisher, ISBN: 1-4020-7745-9, P. 299
- Petly, D.J., 1984, Shear strength of overconsolidated fissured clay, In Proceeding of the International Symposium on Landslides, University of Toronto, Toronto, Vol. 2, 167-172
- Petly, D.J., 1999, Failure envelopes of mudrocks at high confining pressures, In Muds and Mudstones, Physical and Fluid-flow Properties, Edited by A.Aplin, A.Fleet, J.MacQuaker, The Geological Society, Special Publication, No.158.
- Peterson, R., 1954, Studies of Bearpaw shale at a damsite in Saskatchewan. Proceedings, Am. Soc. Of Civil Engineers, 80: 1-28
- Peterson, R., 1958, Rebound in Bearpaw Shale, Western Canada, Bulletin of the Geol. Soc. of Am., 69, 1113-1124

- Picarelli, L., Olivares, L., 1998, Ingredients for modeling the mechanical behavior of intensely fissured clay shales. Proc. 2nd Int. Symp. On the Geotechnics of Hard Soils and Soft Rocks, Napoli, Balkema
- Potts, D.M., Zdravković, L.T. 1999. Finite element analysis in geotechnical engineering: Theory. Thomas Telford Limited, London.
- Poeter, E. and Hill, M. 1998. UCODE, a computer code for universal inverse modeling. U.S. Geological survey.
- Poeter EP, Hill MC. Inverse methods: a necessary next step in groundwater modeling. Ground Water 1997; 35(2):250–60.
- Porter, I.W., Price. R.A., McCrossan, R.G., (1982), “The Western Canadian Sedimentary Basin: Philosophical transactions of the Royal Society of London, Series A, V: 305, pp. 169-182.
- Powless, K., 2013. The Use of Pressure Transient Analysis Tools To Interpret Mini-Frac Data in Alberta Oilsands Caprocks. SPE Heavy Oil Conference, SPE 157843, Calgary, 8 p.
- Pyrak-Nolte, L.J., Nolte, D.D., Myer, L.R., Cook, N.G.W., 1990, Fluid flow through single fractures, Proc. Conf. On Rock Joints, Balkema, Rotterdam, 405-412.
- Rangear, D., Zentar, R., Abriak, N.E., (2006). “Numerical study of pressuremeter strain and stress holding test.” Numerical Methods in Geotechnical Engineering, 141-146.
- Rangear, D., 2002, Identification des caractéristiques hydro-mécaniques d’une argile par analyse inverse des essais pressiométriques. Thèse de l’Ecole Centrale de Nantes et l’Université de Nantes
- Ratigan, J.L. (1992), “The use of fracture reopening pressure in hydraulic fracturing stress measurements”, Rock. Mechanics and Rock Engineering, Vol. 25, No. 4, pp. 225-236.
- Richardson, C.L., Hegemann, J., Sifakis, E., Hellrung, J., Teran, J.M., 2009, An XFEM method for modelling geometrically elaborate crack propagation in brittle materials, Int. J. Numer. Meth. Engng 2009; 1:1, P41
- Rice JR (1968), Mathematical analysis in the mechanics of fracture, in Liebowitz H (ed.) Fracture An Advanced Treatise, vol. 2, chap. 3, Academic Press, New York, 191–311.
- Rice, J.R., Cleary, M.P., 1976, Some basic stress diffusion solution for fluid saturated elastic porous media with compressible constituents, Geophysics and Space Physics, 14 92), 227-241.
- Ringheim, A.S. 1964, Experiences with the Bearpaw shale at the South Saskatchewan River Dam, 8<sup>th</sup> International Congress on Large Dams, Edinburgh, G.B., 1, 529-549.
- Rodríguez, E., Orjuela, J., 2004, FEASIBILITY TO APPLY THE STEAM ASSISTED GRAVITY DRAINAGE (SAGD) TECHNIQUE IN THE COUNTRY’S HEAVY CRUDE-OIL FIELDS, CT&F Ciencia, Tecnología y Futuro, diciembre, año/vol. 2, número 005, Bucaramanga, Colombia, 7-22

- Roegiers, J.C. 1974, the development and evaluation of field method for in situ stress determination using hydraulic fracturing, PhD thesis, University of Minnesota, Minneapolis.
- Roegiers, J.C., McLennan, J.D., and Murphy D.L., 1982, Influence of pre-existing discontinuities on the hydraulic fracturing propagation process, First U.S./Japan Tech. Sem. on Hydraulic Fracturing, Tokyo, Japan (November).
- Roegiers, J.C., 1989, Elements of rock mechanics, in Economides, M.J. and Nolte, K.G., Eds., Reservoir Stimulation, Prentice Hall, Englewood Cliffs, second edition.
- Roscoe, K. H., and J. B. Burland, Stress-strain Behavior of 'Wet Clay', Engineering Plasticity, J. Heyman and F. A. Leckie, Editors, Cambridge University Press, 1968.
- Rummel, F., Winter, R.B., 1982, Application of laboratory fracture mechanics data to hydraulic fracturing field tests, Proc. 1st Japan-USA Symp. On fracture mechanics approach, hydraulic fracture and geothermal energy, Sendai, Japan, pp 495-501
- Rutqvist J., Freifeld B., Min K.B., Elsworth D., and Tsang Y. 2008. Analysis of thermally induced changes in fractured rock permeability during eight years of heating and cooling at the Yucca Mountain Drift Scale Test. International Journal of Rock Mechanics and Mining Sciences 45: 1375–1389
- Safdar Khan, Hongxue Han, Sajjad Ansari and Nader Khosravi, 2011, Geomechanical Modeling to Assess Caprock Integrity in Oil Sands, energy environment economy, CSPG CSEG CWLS Convention
- Safdar Khan, Sajjad Ansari, Hongxue Han, Nader Khosravi, 2011, Importance of Shale Anisotropy in Estimating In-Situ Stresses and Wellbore Stability Analysis in Horn River Basin, CSUG/SPE 149433
- Safdar Khan, Hongxue Han, Sajjad Ansari, Morteza Vishteh, Nader Khosravi, 2011, Caprock Integrity Analysis in Thermal Operations: An Integrated Geomechanics Approach, WORLD HEAVY OIL CONGRESS, EDMONTON, ALBERTA, WHOC11-609.
- Salz, L.B., 1977, Relationship between fracture propagation pressure and pore pressure, SPE 6870, paper presented at the 52<sup>nd</sup> Annual Fall Technical Conference and Exhibition of SPE held in Denver, Colorado, Oct. 9-12.
- Samarajiva P., Macari E.J., Wathugala W. 2005. Genetic algorithms for the calibration of constitutive models of soils. International Journal of Geomechanics, Vol.5 (3), pp. 206-217
- Sanford RJ (2003), Principles of Fracture Mechanics, Prentice Hall
- Schofield, A., Wroth, C. P., Critical State Soil Mechanics, McGraw-Hill, 1968
- Scheidegger, A.E., 1962, Stresses in the earth's crust as determined from hydraulic fracturing data, Geology, 27 (2).

- Sinclair, S.R. and E.W. Brooker, 1967, "The shear strength of Edmonton Shale, Proc. Of Geotechnical Conf., Oslo, 1:295-99.
- Schlumberger, 2009, "Final report, mini stress test, 1AA/12-22-088-08 W4M, MODULAR FORMATION DYNAMIC TESTER".
- Schlumberger, 2009, "Final report, mini stress test, 1AA/111106703W400, MODULAR FORMATION DYNAMIC TESTER".
- Scott, J.S. and Brooker, E.W. 1968. Geological and engineering aspects of Upper Cretaceous shales in Western Canada. Geological Survey of Canada, Paper 66-37.
- Scott, J.D., Morgenstern, N.R., 1987, Stress deformation and strength properties of Athabasca oil sand, progress report on geotechnical and thermal testing of oil sands submitted to AOSTRA, Edmonton, Alberta
- Shafie Zadeh, N., Chalaturnyk, R.J., 2015, "Geotechnical Characterization of Clearwater Clay Shale and Comparison of the Properties with Other Cretaceous Clay Shales in North America", JCPT, SPE-178916-PA, 54, 394-411
- Shafie Zadeh, N., Chalaturnyk, R.J., 2016, "Influence of Packer Properties during In Situ Stress Testing", UNDER REVISION
- Shafie Zadeh, N., Chalaturnyk, R.J., 2016, "Calibration of modified cam clay (MCC) model using inverse analysis for Joli Fou clay shale Formation", UNDER REVISION
- Shamburger, J.H., Patrick, D.M., Lutten, R.J. ,1975, Survey of problem areas and current practices, Design and Construction of Compacted Shale Embankments, v. 1, Federal Highway Administration, FHWA-RD-75-61, Washington, D.C.
- Skempton, A.M., and Hutchinson, J.N., 1969, Stability of natural slopes and embankment foundations, Proc. 7th Intl. Conf. Soil Mech. Found. Eng., State-of-the-Art Volume, Mexico City, p. 291.
- Skempton, A.W., Petley, D.J., 1967, The strength along structural discontinuities in stiff clay, Proc. Geot. Conf., Oslo, 2, 3-20.
- Skempton, A.W., 1964, Long-term stability of clay slopes, Fourth Rankine Lecture, Géotechnique, Vol. 14, p. 77
- Smart, G.D., Rowlands, N., Isaac, A.K., 1982, Progress towards establishing relationships between the mineralogy and physical properties of Coal Measures rocks, International Journal Rock Mechanics Mining Science and Geomechanical Abstracts, 16, 81-89.
- Smith, P.R., 1992, the behavior of natural high compressibility clay with special reference to construction on soft ground, PhD thesis, Imperial College, University of London.
- Spears, D. A., 1980, towards a classification of shales, J. geol. Soc. London 137, 125-30
- Syfan, F.E., Newman, S.C., Meyer, B.R., Behrendt, D., (2007), "Case history: G-Function analysis proves beneficial in Barnett shale application", SPE 110091, 10 p.

- Ridharan, A., PRAKASH, K. 1998. Characteristic water contents of a fine-grained soil-water system. *Géotechnique*, 48 (3), 337-346.
- Stallebrass, S. E., and Taylor, R. N., 1997, The development and evaluation of a constitutive model for the prediction of ground movements in overconsolidated clay, *Géotechnique*, Vol. 47, No. 2, pp. 235-254
- Steiger, R.P., Leung, P.K. 1990, Predictions of wellbore stability in shale formations at great depth. In: Maury, V. & Fourmaintraux, D. (eds), *Rock at great depth*, Balkema, Rotterdam: 1209-1218.
- Tandanand, S., 1985, Moisture adsorption rate and strength degradation of Illinois shales, *Proc. 26<sup>th</sup> US Symp. On Rock Mech.*, Rapid City: 595-600.
- Tavenas, F.A., Blanchette, G., Lerouil, S., Roy, M., Larochelle, 1975, difficulties in the in situ determination of  $K_0$  in sensitive clay, proceeding of the American Society of Civil engineering, Raleigh, Vol. 1, 450-476.
- Terzaghi, K., 1936, Stability of slopes of natural clay, *Proc. Intl. Conf. Soil Mech.*, Harvard, v. 1, 161-165.
- Till, R. & Spears, D. A. 1969. The determination of quartz in sedimentary rocks using an X-ray diffraction method, *Clays Clay Miner*, 17, 323-7
- Thiercelin, M., Desroches, J., Kurkjian, A., 1994, Open hole stress tests in Shales, SPE 28144, Proceedings of the joint SPE/ISRM Conference on Rock Mechanics in Petroleum Engineering, Eurock 94, Delft, The Netherlands, 921-928.
- Thomas, S., and Sands, I. S.O., 2010, Re: Project Update for Alberta Oilsands Inc. Clearwater West LP- SAGD Pilot Project.
- Torp, T.A., Gale, J. 2004, Demonstrating storage of CO<sub>2</sub> in geological reservoirs: The Sleipner and SACS projects. *Energy*, 29 (9, 10):1361-69.
- Total E&P Canada Ltd., 2010, Surface Steam Release of May 18, 2006 Joslyn Creek SAGD Thermal Operation ERCB Staff Review and Analysis
- Underwood, L. B. 1967. Classification and identification of shales, *Prec. Am. Soc. Civ. Eng., J. Soil mech. Foundn Div.* 93 SM6, 97-116.
- Uwiera-Gartner, M.M.E., Carson, M.R., Walter, D., Palmgren, C.T.S., 2011, Geomechanical simulation of caprock performance for proposed, low pressure, Steam-Assisted Gravity Drainage pilot project, CSUG/SPE148886.
- Vallejo, L.E., 1987, Influence of fissures in a stiff clay subjected to direct shear, *Géotechnique*, 37 (1), 69-82
- Van Eeckhout, E.M. 1976, the mechanisms of strength reduction due to moisture in coal mine shales. *Int. J. Rock Mech. Min. Sci. & Geomech. Abstr.* 13: 61-67.
- Venter, J.P., 1981, the behavior of some South African mudrocks due to temperature and humidity changes, with particular reference to moisture content and volume change.

- Proceeding International Symposium Weak rock- soft, fractured and weathered Rock, Tokyo, Akai, K., Hayashi, M., Nishimatsu, Y. (Eds.), A.A.Balkema, Rotterdam, 1, 205-212.
- Vermeylen J.P. and Zoback M. 2011. Hydraulic fracturing, microseismic magnitudes, and stress evolution in the Barnett Shale, Texas, USA. SPE Hydraulic Fracturing Technology Conference, The woodland, TX, SPE 140507.
- Vinay K. Mishra, Peter Lywood, Cosan Ayan, 2011, Application of Wireline Stress Testing for SAGD Caprock Integrity, CSUG/SPE 149456
- Von Schonfeldt, Hilmar, A., 1970, An experimental study of open-hole hydraulic fracturing as a stress measurement method with particular emphasis on field test. PhD thesis, University of Minnesota, Minneapolis,
- Vukadin, V., 2007, modeling of the stress-strain behavior in hard soils and soft rocks. *Acta Geotechnica Slovenica* 2, 1, 33-43.
- Warpinski, N.R., 1989, determining in-situ stress from hydraulic fracturing through perforations. *Int. J. Rock Mech. Min. Sci & Geomech. Abstr.* 26(6), pp. 523-531.
- Warpinski, N.R., 1991, Hydraulic fracturing in tight, fissured media, *J. of Petrol. Tech.*, February, pp. 146-152 and 208-209.
- Warpinski N.R., Moschovidis Z.A., Parker C.D., Abou-Sayed I.S., 1994, "Comparison Study of Hydraulic Fracturing Models," Society of Petroleum Engineers, SPE-25890-PA. Warren, W.E (1980). "Packer-induced stresses during hydraulic well fracturing." *Journal of Energy Resources Technology.* 103: 336-343.
- Witcher, L., 1979, on the geotechnical properties of Jurassic clay shale, proceeding 4<sup>th</sup> International congress society rock mechanics, Montreux, A.A.Balkema, Rotterdam, 319-328.
- Wentworth, C.K., 1922, *Geology*, W.C. Putnam, Oxford University Press, Inc., NY.
- Wesley, L.D., 1975, "Influence of stress-path and anisotropy on behavior of a soft alluvial clay", PhD dissertation, Univ. of London,
- Westergaard, H.M., 1939, Bearing pressure and cracks, *J. Appl. Mech.*, 61, A49-53
- Widjaja, H., Duncan, J.M., Seed, H.B., 1984, Scale and time effects in hydraulic fracturing ,report prepared for the US army corps, Geotechnical laboratory, waterways Experiment Station, Vicksburg, 189P.
- Widodo, S., Ibrahim, A.M., Hong, S., 2014, Analysis of different equations of undrained shear strength estimations using Atterberg Limits on Pontianak soft clay, *Challenges of modern technology* 2082-2863 08/2012; 3(3):46-50
- Whitehead, W.S., Gatens III, J.M., Holditch, S.A., 1989, "Determination of in situ stress profile through hydraulic fracturing measurements in two distinct geologic areas, *Int. J. Rock Mech. Min. Sci., Geomech. Abstr.* Vol.26, No.6, PP.637-645.

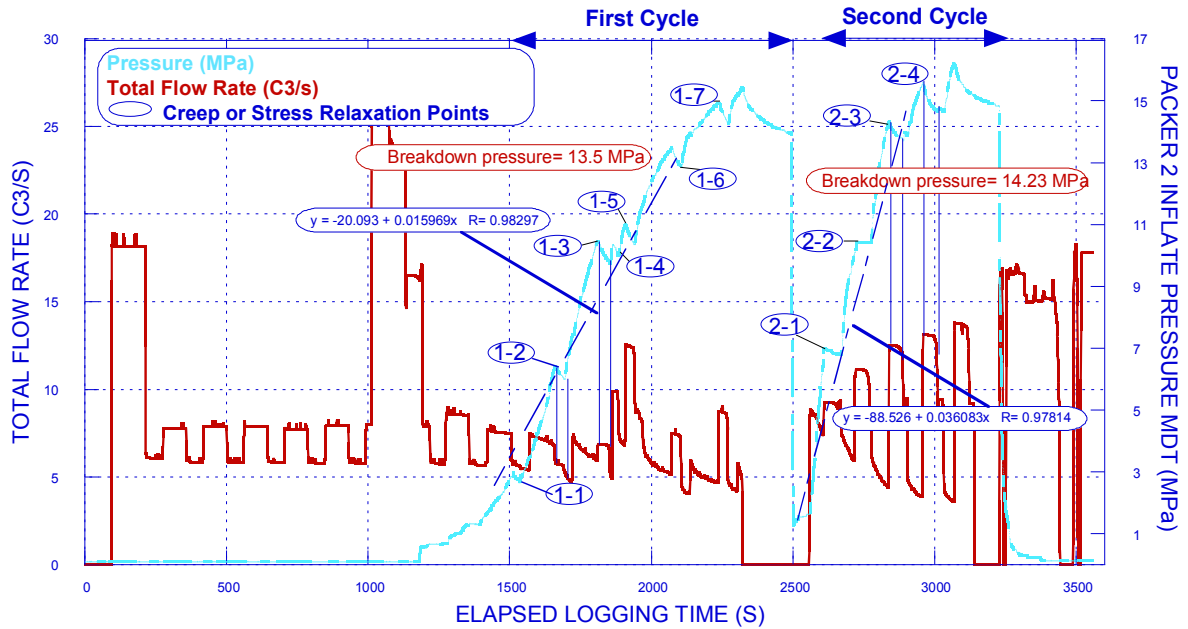
- Whittaker, B.N., Singh, R.N., Sun, G., 1992, Rock Fracture Mechanics, principle, design and application, Elsevier science publisher, ISBN: 0-444-896848, P:570
- Wang, H.F. (2000). "Theory of linear poroelasticity with application to geomechanics and hydrogeology." Princeton University Press, Princeton, New Jersey, United States of America ISBN: 9780691037462.
- Wong, R.C.K., Wang, E.Z., 1997, Three dimensional anisotropic swelling mode for clay shale- a fabric approach, International Journal Rock Mechanics Mining Science, 34, 187-198.
- Wong, R., 2001. Analysis of Swelling and Softening of Shale (Colorado Group) Near a Drilled Hole Subjected to Water Invasion. Journal of Canadian Petroleum Technology, Vol. 40, No. 12, pp. 49-54.
- Wong, G.Y., 2007, Geomechanical characterization for Clearwater formation clay shale, Master Thesis, University of Alberta
- Yamagami T., Jiang J.C., Ueta, Y. 1997. Back calculation of strength parameters for landslide control works using neural networks. Proceedings of the 9th Int. Conf. on Computer methods and advances in geomechanics, Wuhan, China.
- Yanguang Yuan, Baohong Yang, Bin Xu, 2011, fracturing in the oil-sands reservoirs, CSUG/SPE149308
- Yanguang Yuan, Bin Xu, BitCan, Claes Palmgren, 2011, Design of Caprock Integrity in Thermal Stimulation of Shallow Oil-Sand Reservoirs, CSUG/SPE 149371
- Yoshida, N, Morgenstern, N.R. , Chan, D.H., 1991, Finite element analysis of softening effects in fissured overconsolidated clays and mudstone, Canadian Geotechnical Journal, 28, 51-61.
- Yong, R. N. & Wamxntin, B. P. 1975. Properties and behaviour. Developments in Geotechnical Engineering, 5. Elsevier, Amsterdam.
- Yu, H. S. (1998). "CASM: A unified state parameter model for clay and sand.", Int., J., Numer. Anal. Methods Geomech., 22(8), 621-653
- Yuan, Yanguang, Baohong Yang, Bin Xu, 2011, fracturing in the oil-sands reservoirs, CSUG/SPE149308
- Yuan, Yanguang, Bin Xu, BitCan, Claes Palmgren, 2011, Design of Caprock Integrity in Thermal Stimulation of Shallow Oil-Sand Reservoirs, CSUG/SPE 149371
- Zaruba, Q., Bukovanky, M., 1965, Mechanical properties of Ordovician shale of central Bohemia, proceeding 6<sup>th</sup> International Conference Soil Mechanics Foundation Engineering, Montreal, 3,421-424
- Zehnder, A., T., 2007, Lecture notes on fracture mechanics, Cornell University, Ithaca, NY 14853
- Zentar R., Hicher P.Y., Moulin G. 2001. Identification of soil parameters by inverse analysis. Computer and Geotechnics. Vol.28, pp.129-144

- Zhiyl, L., Jinfeng, W. 1993, Engineering properties of Chongqing Mudstone, China. Proc. 26th Annual Conf. of the Eng. Group of the Geol. Soci., The Engineering Geology of Weak Rocks, Cripps et al. (eds), Leeds: 101-107.
- Zielonka, M.G., Searles, K.H., Ning, J., Buechler, S.R., 2014, Development and Validation of Fully-Coupled Hydraulic Fracturing Simulation Capabilities, 2014 SIMULIA Community Conference
- Zimmerman, R.W. (1991). "Compressibility of Sandstones." Elsevier Science Publishers B.V., Amsterdam, The Netherlands.
- Zimmerman, R.W. (2000a). "Coupling in poroelasticity and thermoelasticity." *Int. J. Rock Mech. & Min. Sci.*, 37, 79–97.
- Zimmerman, R.W. (2000b). "Implications of static poroelasticity for reservoir compaction." *Pacific Rocks 2000*, Girard, J., Liebman, M., Breeds, C., and Doe, T., eds., Proc. Pacific Rocks, Balkema, Rotterdam, ISBN 90 5809 155 4, 169–172.
- Zoback, M. D. and Townend, J. (2001). "Implications of hydrostatic pore pressures and high crustal strength for the deformation of intraplate lithosphere." *Tectonophysics*, 336, 19–30.
- Zoback, M.D., 1978, a simple hydraulic fracturing technique for determining rock fracture toughness, proc. 19th USA Symp. On rock mechanics, University of Nevada, Reno, pp83-85

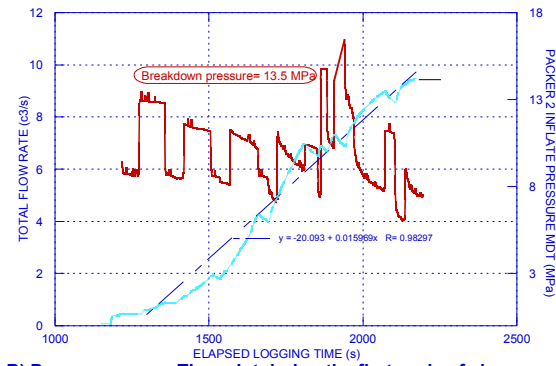
APPENDIX I

AOS MICRO-FRAC TEST AT THE DEPTH OF 63 M IN WELL AA/03-22-088-08W4

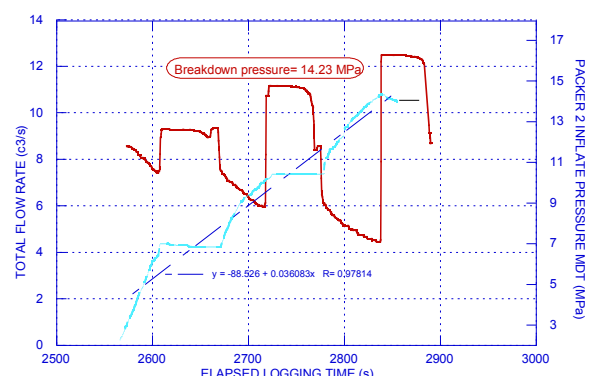
1) Sleeve fracturing test:



A) Pressure versus Time history plot during sleeve fracturing test



B) Pressure versus Time plot during the first cycle of sleeve fracturing, a slope change can be observed at around 13.5 MPa



C) Pressure versus Time plot during the second cycle of sleeve fracturing, a slope change can be observed at 14.2 MPa

Figure A.I.1. Record of Field Data: a) history of pressure and flow rate versus time, b) first cycle breakdown pressure and c) second cycle breakdown pressure

## 2) Micro-hydraulic fracturing test:

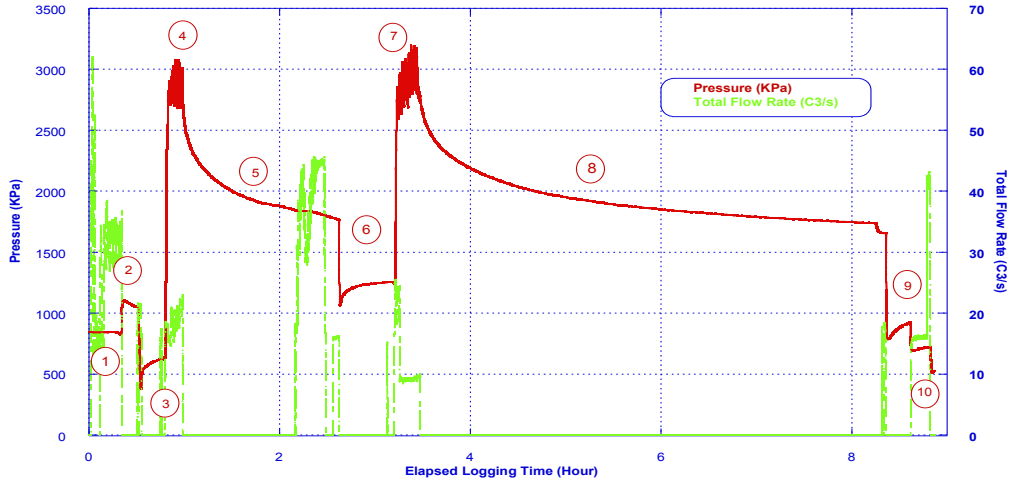
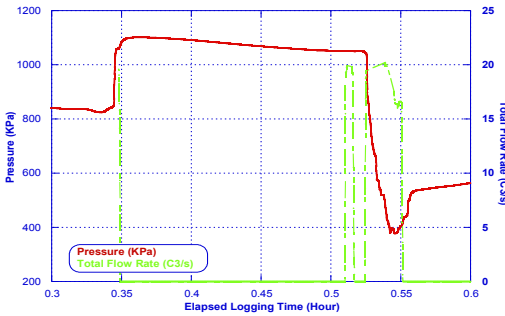
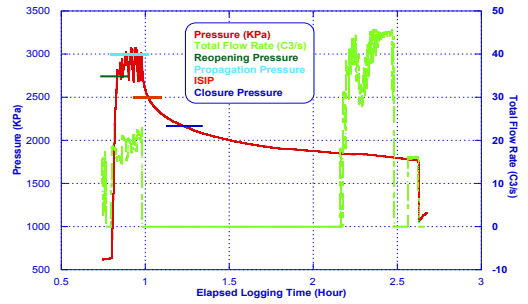


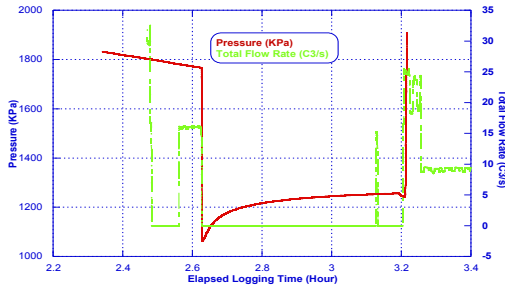
Figure A.I.2- Recorded pressure history during the mini-frac test in ClearWater Clay Shale at 63 m:1-Inflate, 2- Leakoff test, 3- Draw Down, 4- First propagation (First Cycle), 5- First Falloff, 6- Flowback, 7- Second propagation (Second Cycle), 8- Second Falloff, 9- Flowback, 10- Deflate



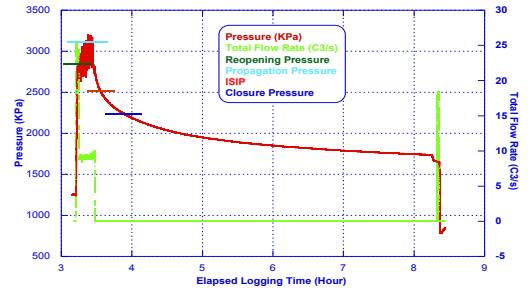
A.I.3. Recorded pressure history during the micro-frac test in Clear Water Clay Shale at 63 m: Leakoff test



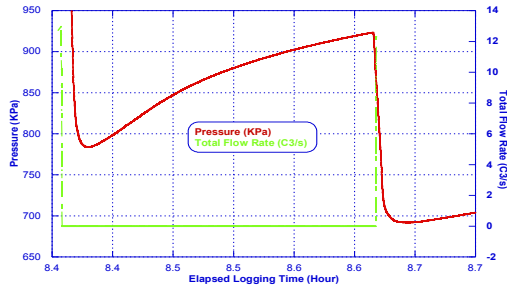
A.I.4. Recorded pressure history during the micro-fractest in Clear Water Clay Shale at 63 m- First Cycle



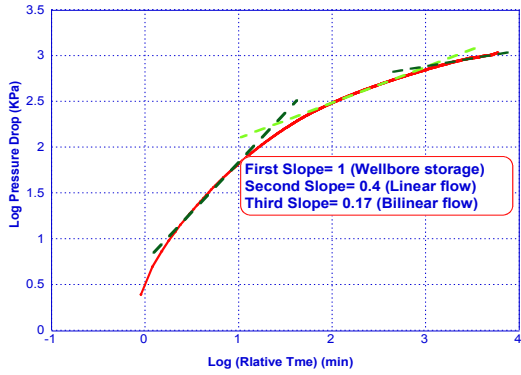
A.I.5. Recorded pressure history during the micro-frac test in Clear Water Clay Shale at 63 m - First Flowback



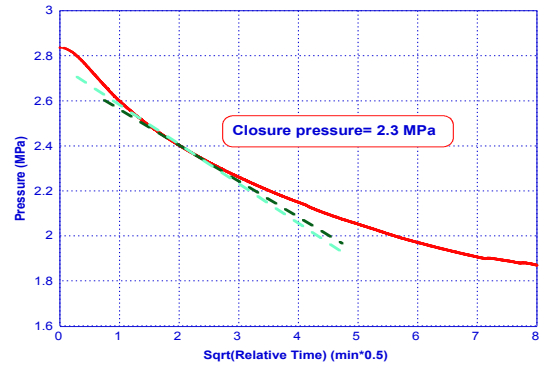
A.I.6. Recorded pressure history during the micro-fractest in Clear Water Clay Shale at 63 m- Second Cycle



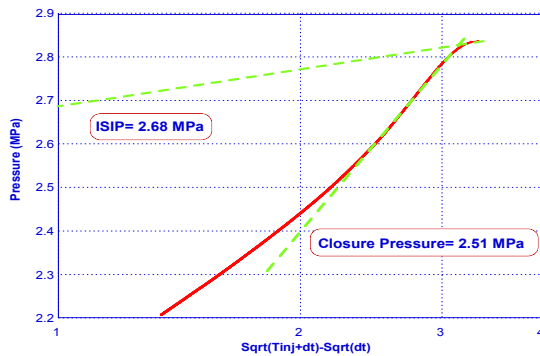
A.I.7. Recorded pressure history during the micro-frac test in Clear Water Clay Shale at 63 m- Second Flowback



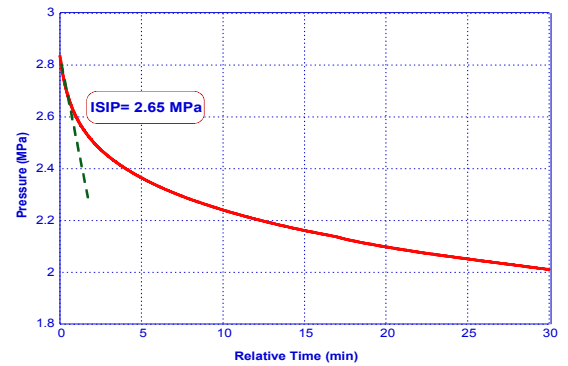
A.I.8. Schematic plot of micro-frac pressure fall-off data showing various flow regimes- first cycle



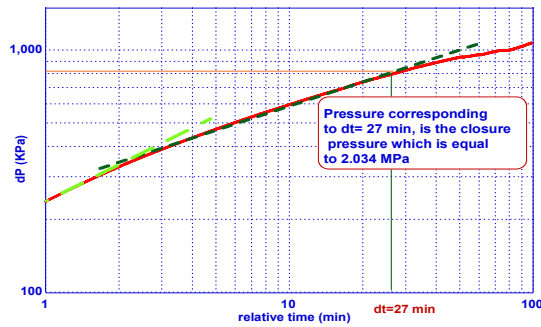
A.I.9. Interpretation of closure pressure from the change in slope of pressure versus square root of shut-in time- first cycle



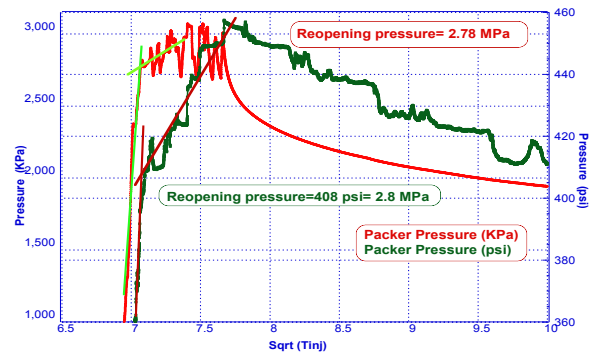
A.I.10. Change in slope following shut-in of the injection corresponds to closure pressure or minimum in-situ stress- first cycle



A.I.11. Interpretation of ISIP from change in slope of pressure versus shut-in time



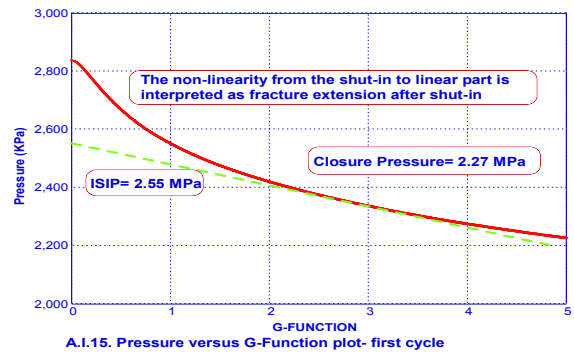
A.I.12. Log-log scale of  $dP$  versus  $dt$ , closure pressure corresponds to a value where fracture linear flow deviates from a straight line- first cycle



A.I.13. Determination of fracture reopening pressure- first cycle



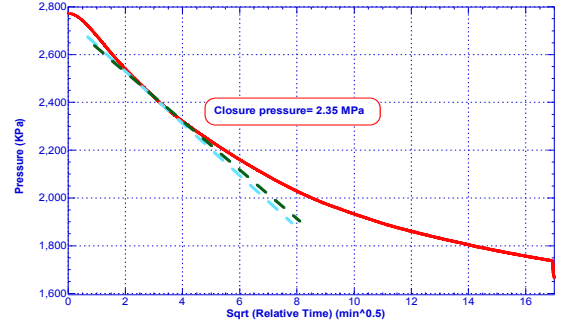
A.I.14. Determination of in-situ minimum stress from the slope of a Horner plot- first cycle



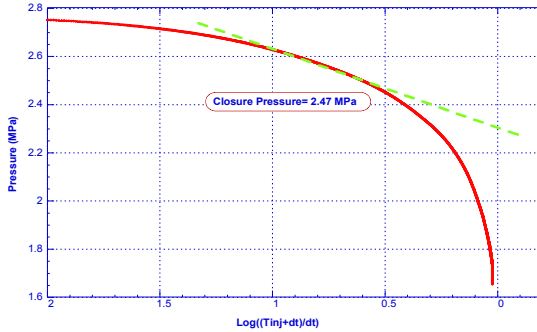
A.I.15. Pressure versus G-Function plot- first cycle



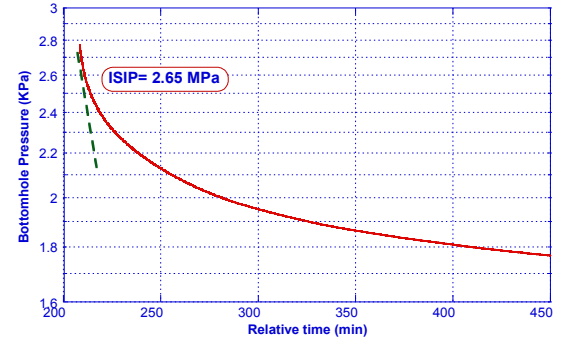
A.1.16. Schematic plot of micro-frac pressure fall-off data showing various flow regimes-second cycle



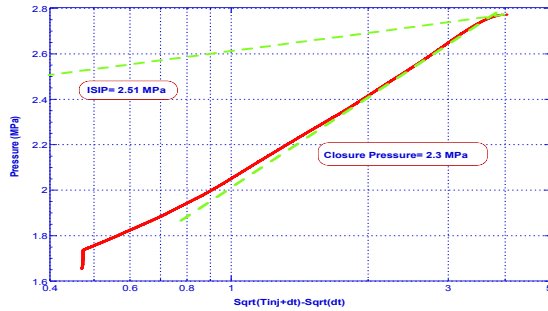
A.1.17. Interpretation of closure pressure from the change in slope of pressure versus square root of shut-in time-second cycle



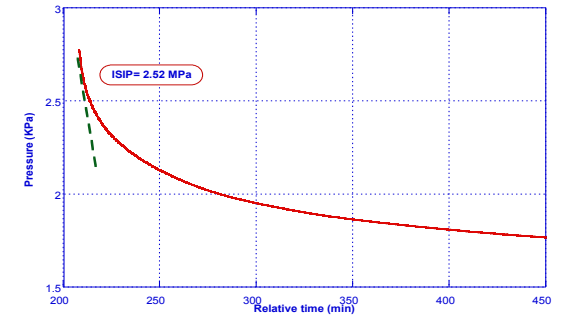
A.1.18. Determination of in-situ minimum stress from the slope of a Horner plot-second cycle



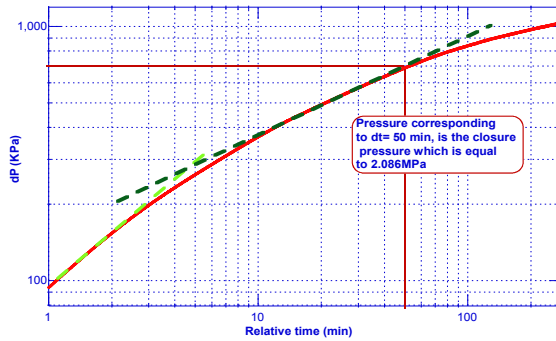
A.1.19. Determination of ISIP from Log P versus Relative Time-first cycle



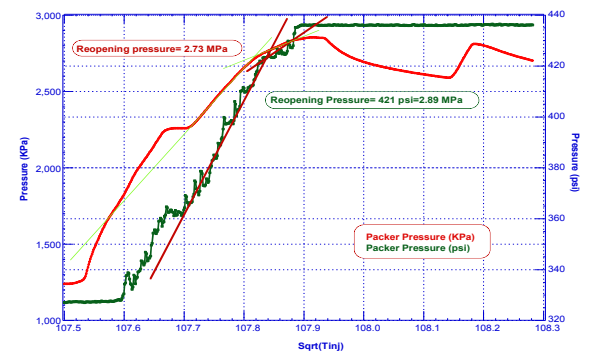
A.1.20. Change in slope following shut-in of the injection corresponds to closure pressure or minimum in-situ stress-second cycle



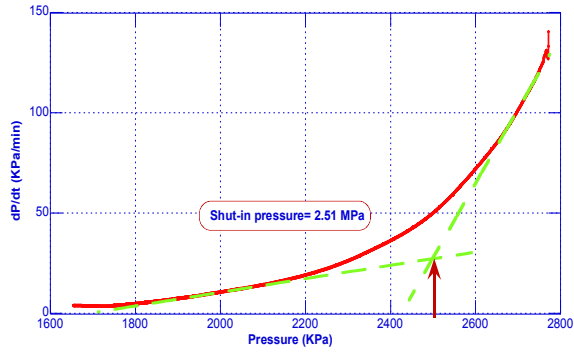
A.1.21. Determination of ISIP from Log P versus Relative Time-second cycle



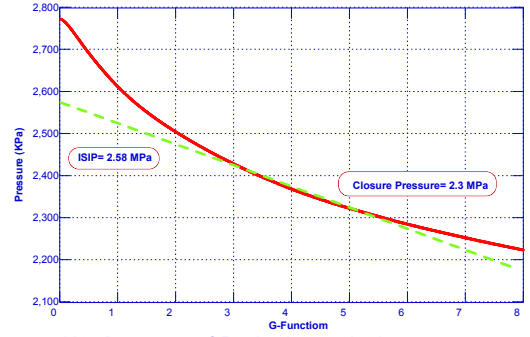
A.1.22. Log-log scale of dP versus dt, closure pressure corresponds to a value where fracture linear flow deviates from a straight line-second cycle



A.1.23. Determination of fracture reopening pressure-second cycle



A.I.24. Shut-in pressure determination using bi-linear pressure-decay rate method- second cycle



A.I.25. Pressure versus G-Function plot- second cycle

## APPENDIX II

### CNRL MICROFRACTURE AT 337 M IN WELL 11-11-67-3W4

#### 1) Sleeve fracturing test

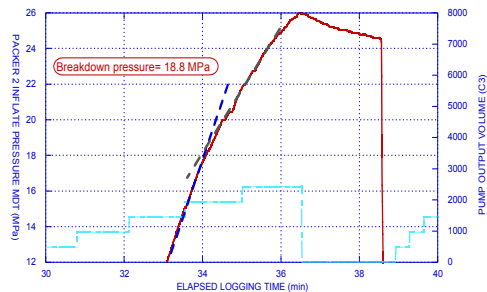
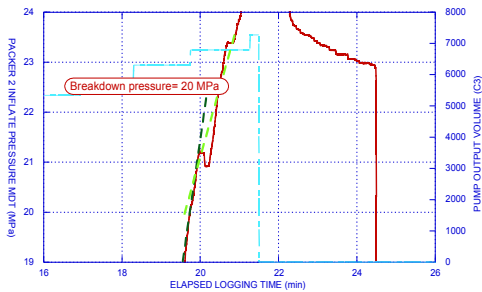
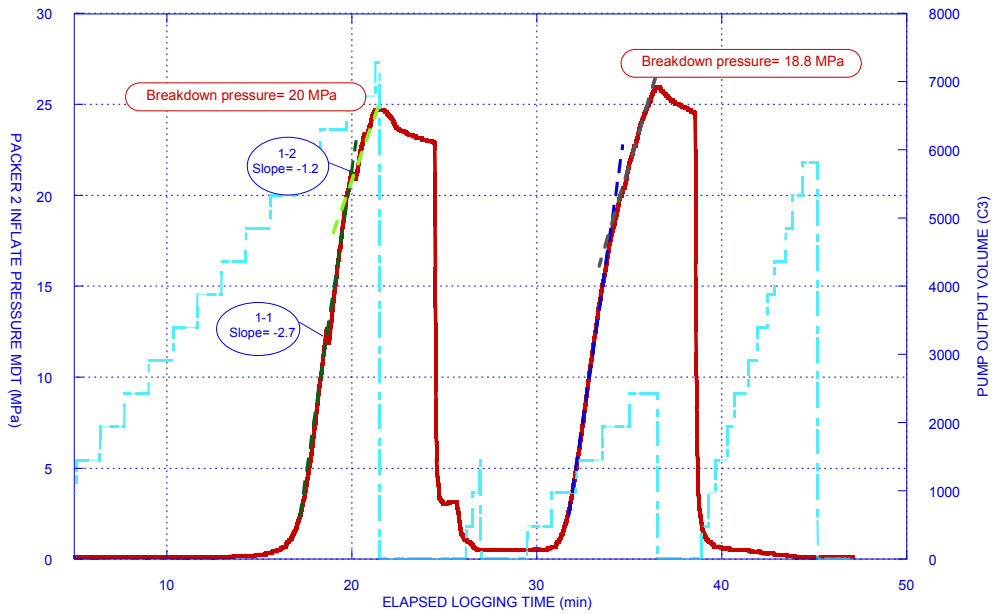


Figure A.II.1. Record of Field Data: a) history of pressure and flow rate versus time, b) first cycle breakdown pressure and c) second cycle breakdown pressure

2) Micro hydraulic fracturing test:

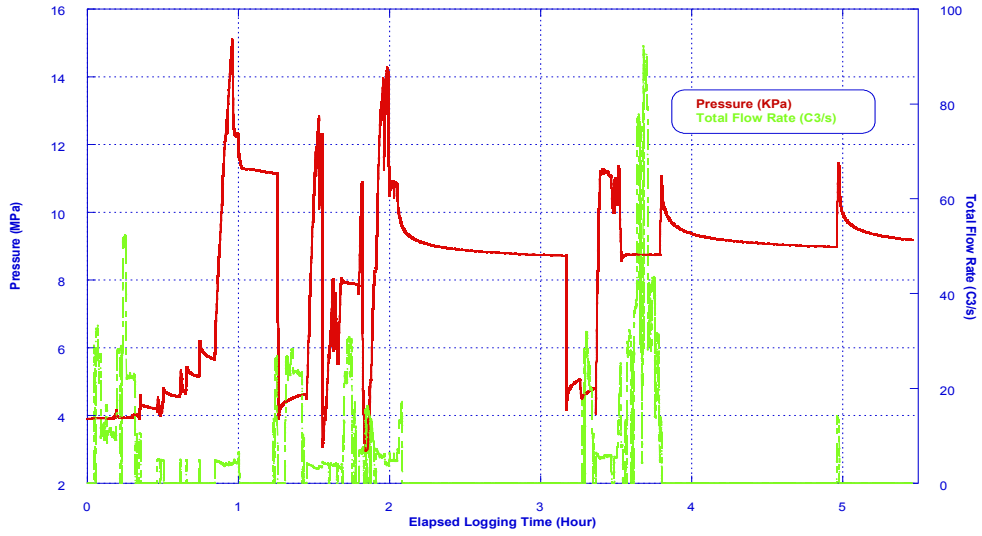


Figure A.II.2. Recorded pressure history during the mini-frac test in Joli Fou Formation at 337 m

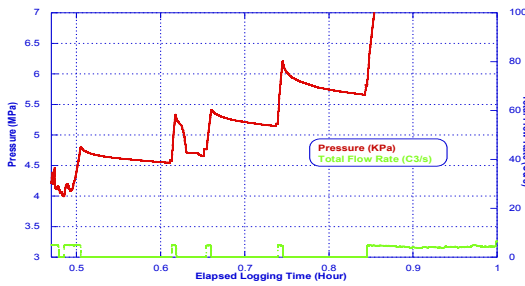


Figure A.II.3. Recorded pressure history during the micro-frac test in Joli Fou Formation at 337 m: Leakoff tests

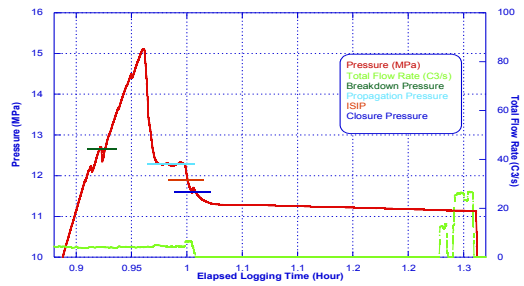


Figure A.II.4. Recorded pressure history during the micro-frac test in Joli Fou Formation at 337 m: first cycle

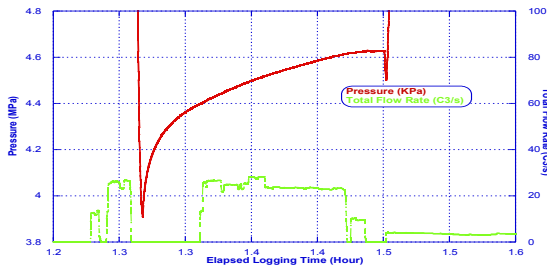


Figure A.II.5. Recorded pressure history during the micro-frac test in Joli Fou Formation at 337 m: first flowback

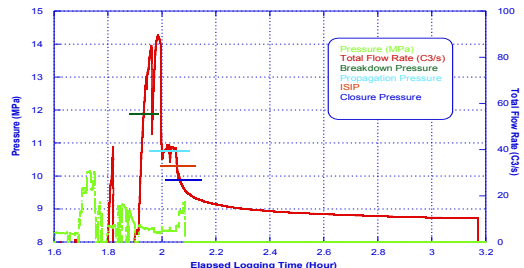


Figure A.II.6. Recorded pressure history during the micro-frac test in Joli Fou Formation at 337 m: second cycle

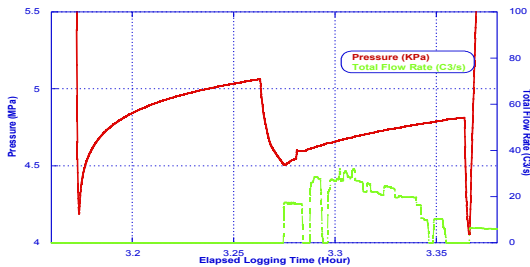


Figure A.II.7. Recorded pressure history during the micro-frac test in Joli Fou Formation at 337 m: second flowback

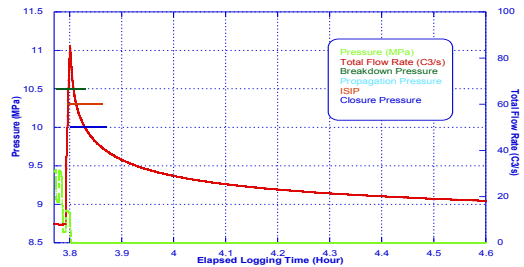


Figure A.II.8. Recorded pressure history during the micro-frac test in Joli Fou Formation at 337 m: third cycle

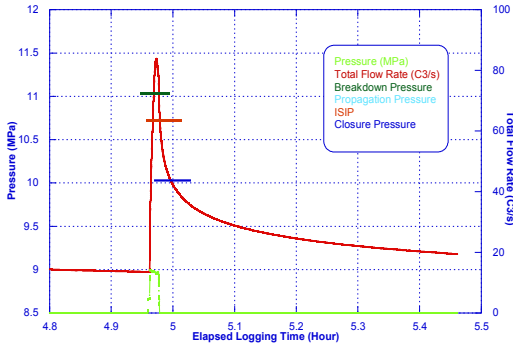


Figure A.II.9. Recorded pressure history during the micro-frac test in Joli Fou Formation at 337 m: fourth cycle

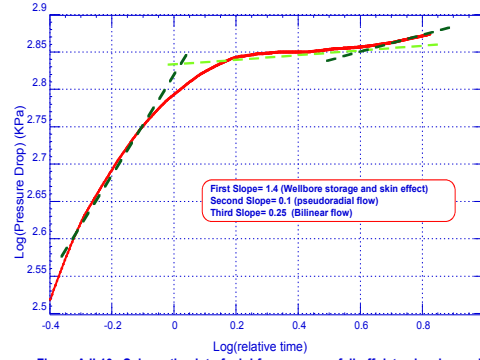


Figure A.II.10. Schematic plot of mini-frac pressure fall-off data showing various flow regimes- first cycle

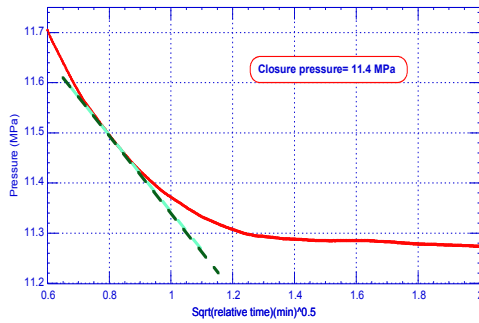


Figure A.II.11. Interpretation of closure pressure from the change in slope of pressure versus square root of shut-in time- first cycle

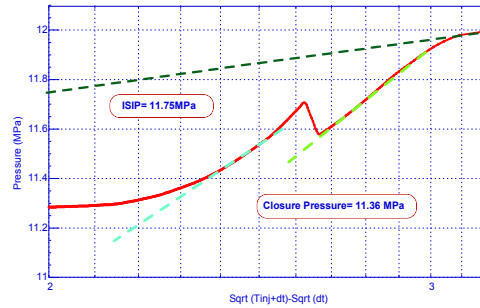


Figure A.II.12. Change in slope following shut-in of the injection corresponds to closure pressure or minimum in-situ stress- first cycle

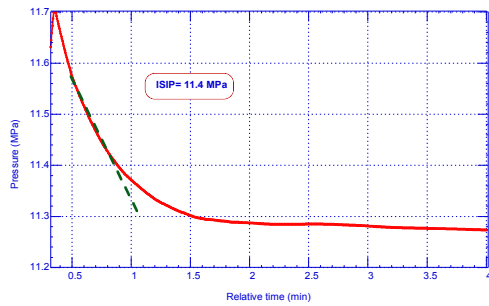


Figure A.II.13. Interpretation of ISIP from change in slope of pressure versus shut-in time- First Cycle

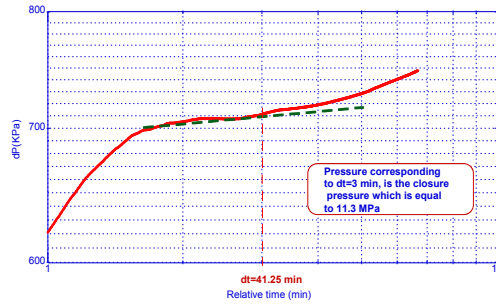


Figure A.II.14. Log-log scale of  $dP$  versus  $dt$ , closure pressure corresponds to a value where fracture linear flow deviates from a straight line- first cycle

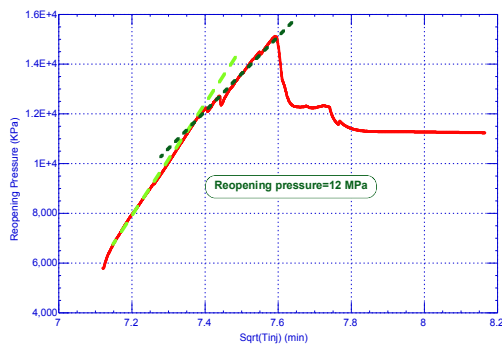


Figure A.II.15. Determination of fracture reopening pressure- first cycle

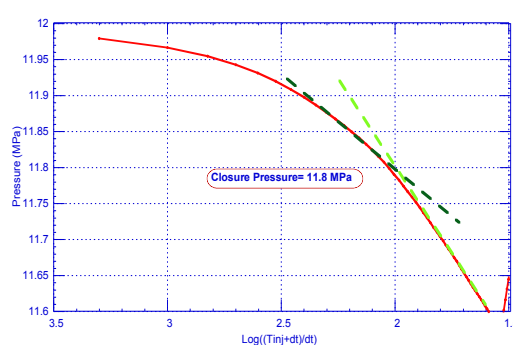


Figure A.II.16. Determination of in-situ minimum stress from the slope of a Horner plot- first cycle

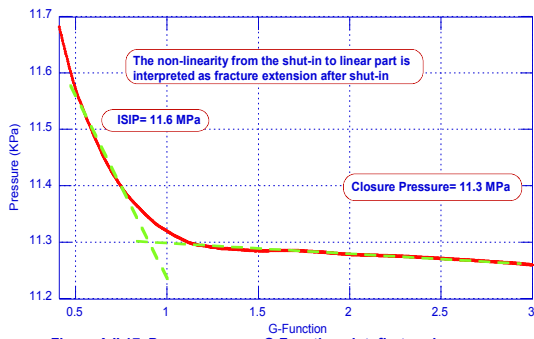


Figure A.II.17. Pressure versus G-Function plot- first cycle

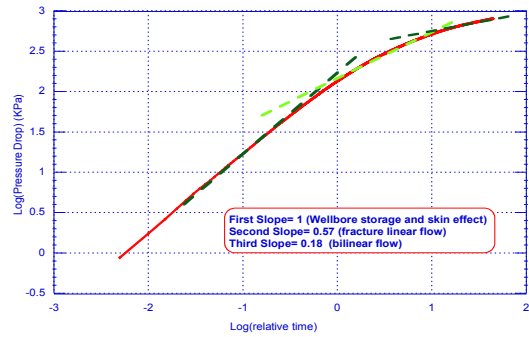


Figure A.II.18. Schematic plot of mini-frac pressure fall-off data showing various flow regimes- second cycle

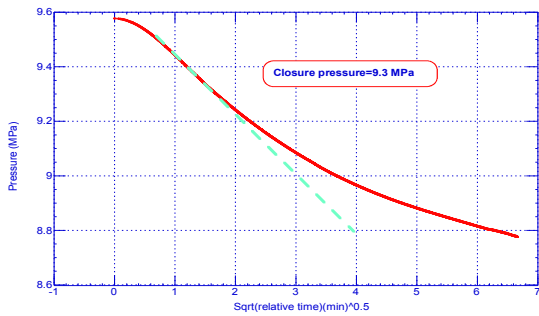


Figure A.II.19. Interpretation of closure pressure from the change in slope of pressure versus square root of shut-in time- second cycle

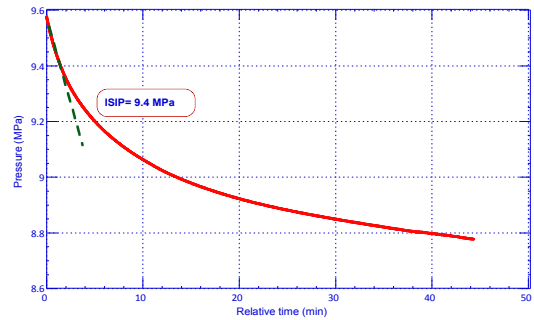


Figure A.II.21. Interpretation of ISIP from change in slope of pressure versus shut-in time- second cycle

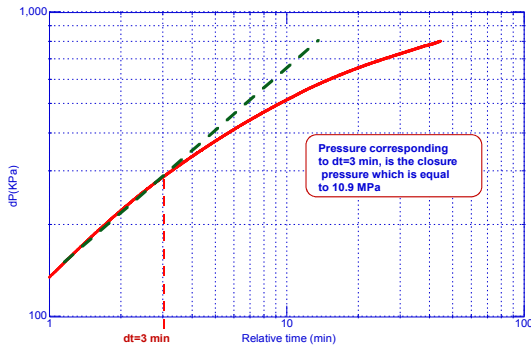


Figure A.II.22. Log-log scale of  $dP$  versus  $dt$ , closure pressure corresponds to a value where fracture linear flow deviates from a straight line- second cycle

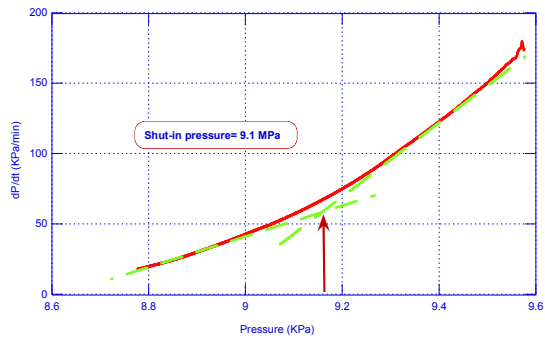


Figure A.II.23. Shut-in pressure determination using bi-linear pressure-decay rate method- second cycle

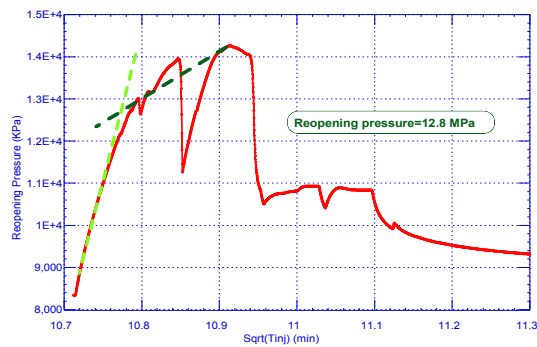


Figure A.II.24. Determination of fracture reopening pressure- second cycle

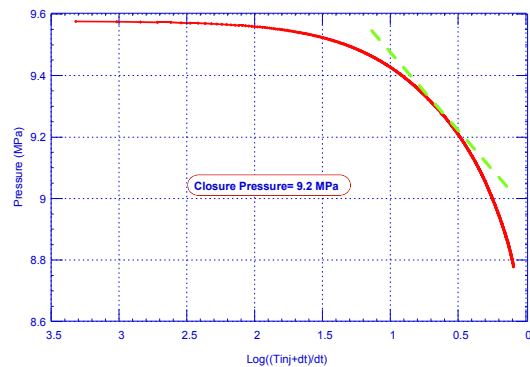


Figure A.II.25. Determination of in-situ minimum stress from the slope of a Horner plot- second cycle

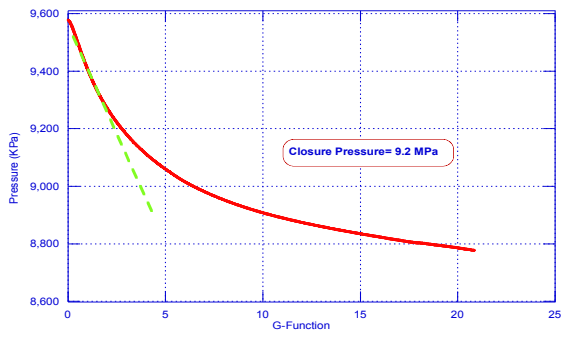


Figure A.II.26. Pressure versus G-Function plot-second cycle

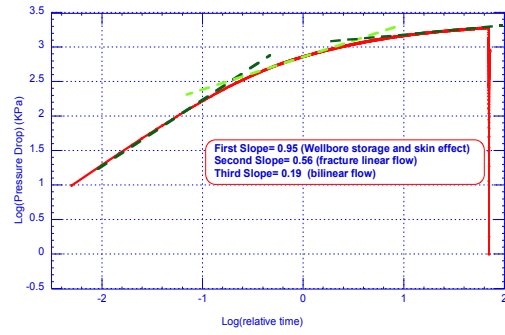


Figure A.II.27. Schematic plot of mini-frac pressure fall-off data showing various flow regimes- third cycle

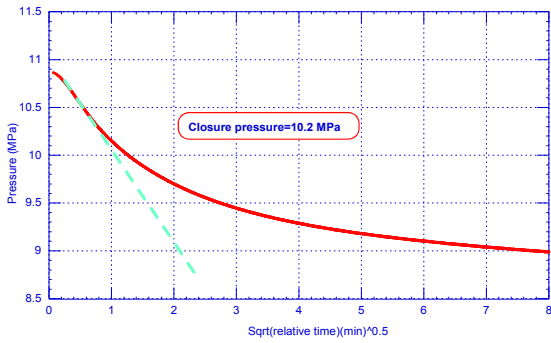


Figure A.II.28. Interpretation of closure pressure from the change in slope of pressure versus square root of shut-in time- third cycle

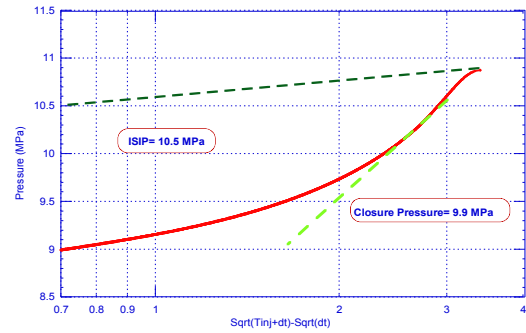


Figure A.II.29. Change in slope following shut-in of the injection corresponds to closure pressure or minimum in-situ stress- third cycle

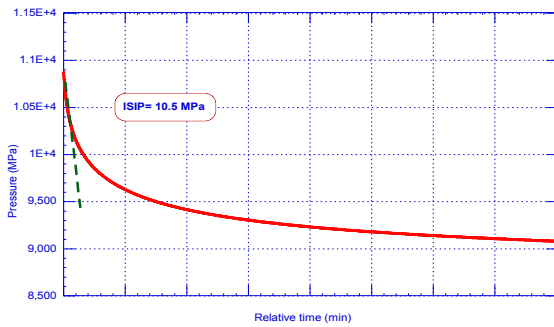


Figure A.II.30. Interpretation of ISIP from change in slope of pressure versus shut-in time- third Cycle

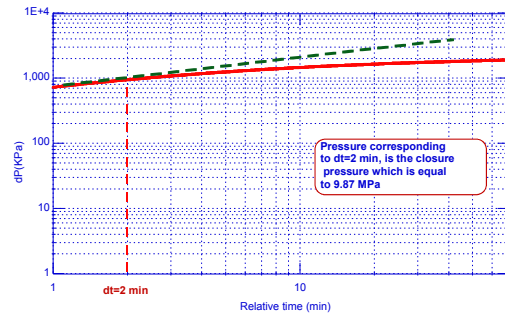


Figure A.II.31. Log-log scale of  $dP$  versus  $dt$ . closure pressure corresponds to a value where fracture linear flow deviates from a straight line- third cycle

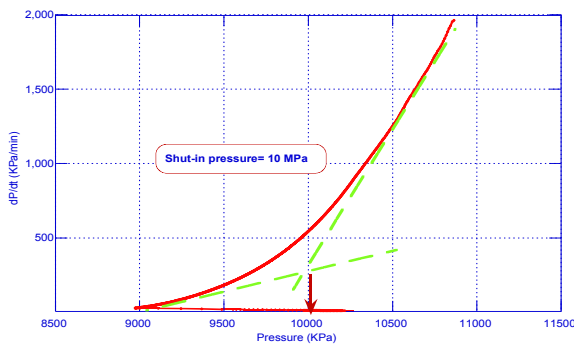


Figure A.II.32. Shut-in pressure determination using bi-linear pressure-decay rate method- third cycle

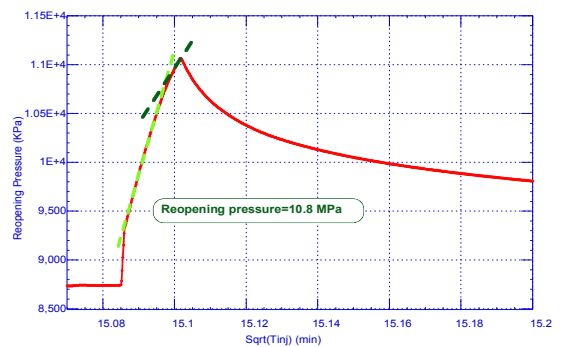


Figure A.II.33. Determination of fracture reopening pressure- third cycle

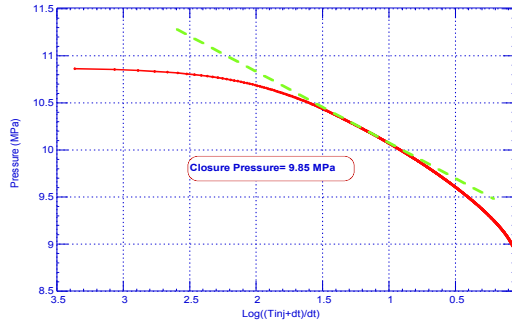


Figure A.II.34. Determination of in-situ minimum stress from the slope of a Horner plot- third cycle

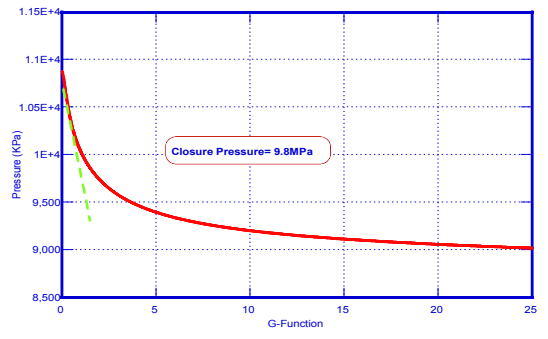


Figure A.II.35. Pressure versus G-Function plot-third cycle

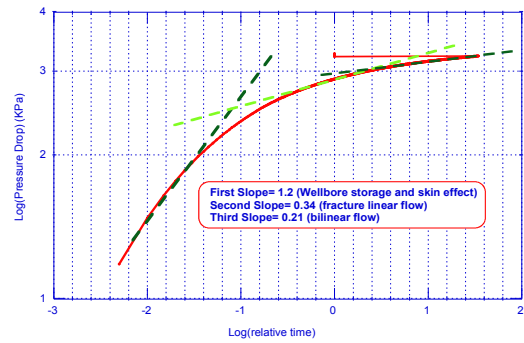


Figure A.II.36. Schematic plot of mini-frac pressure fall-off data showing various flow regimes- fourth cycle

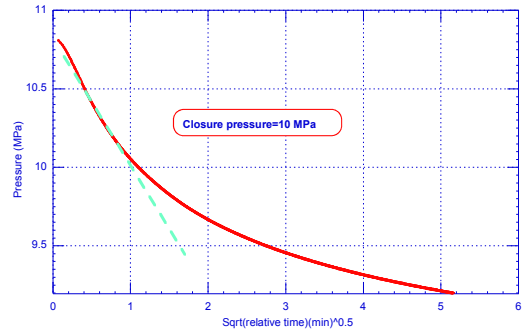


Figure A.II.37. Interpretation of closure pressure from the change in slope of pressure versus square root of shut-in time- fourth cycle

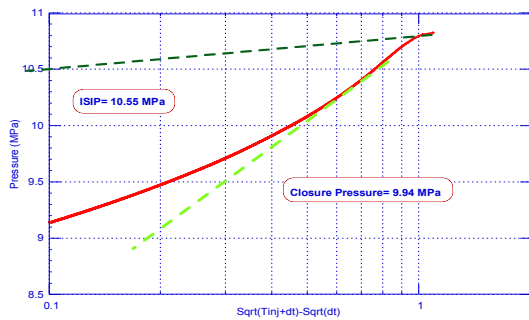


Figure A.II.38. Change in slope following shut-in of the injection corresponds to closure pressure or minimum in-situ stress-fourth cycle

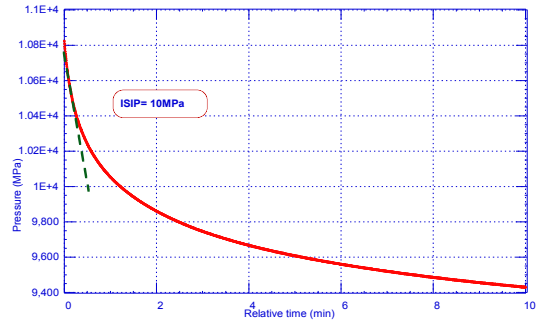


Figure A.II.39. Interpretation of ISIP from change in slope of pressure versus shut-in time- fourth cycle

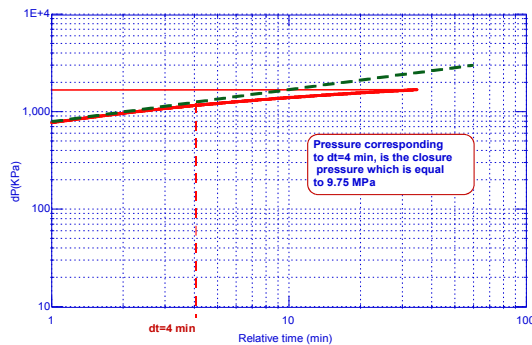


Figure A.II.40. Log-log scale of dP versus dt, closure pressure corresponds to a value where fracture linear flow deviates from a straight line-fourth cycle

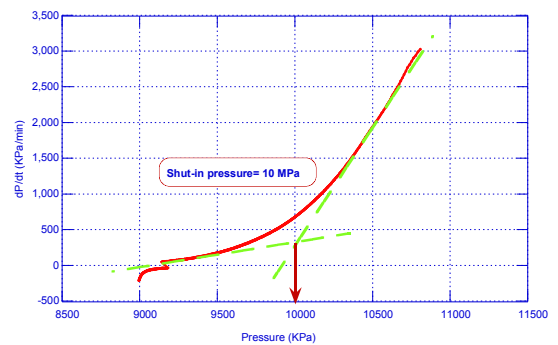


Figure A.II.41. Shut-in pressure determination using bi-linear pressure-decay rate method-fourth cycle

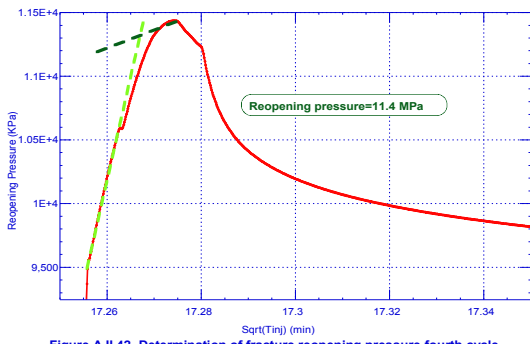


Figure A.II.42. Determination of fracture reopening pressure-fourth cycle

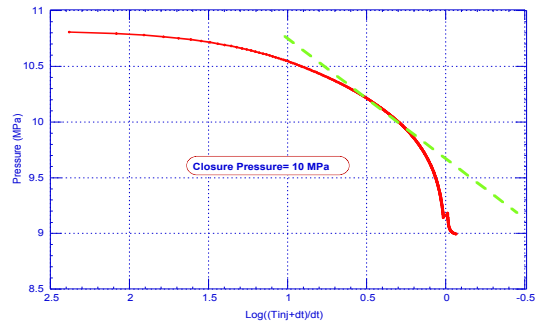


Figure A.II.43. Determination of in-situ minimum stress from the slope of a Horner plot-fourth cycle

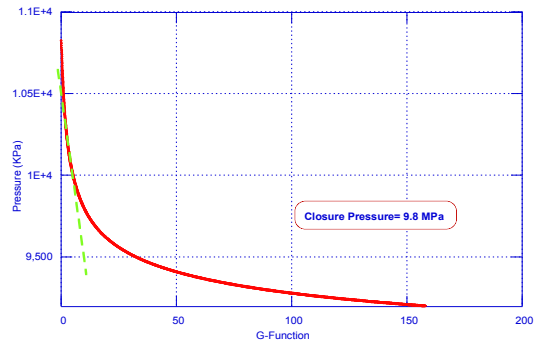


Figure A.II.44. Pressure versus G-Function plot-fourth cycle

